Proposal for Deposition Mechanism of Diamond and Cubic BN

Yukio Ichinose
Nagaoka University of Technology, Nagaoka, Niigata 940-21, Japan

Abstract

Deposition mechanism of diamond and/or cubic BN from gas phases was considered with reviewing the previous data containing ours. Especially the developmental history of several types of plasma CVD apparatus by ourselves told that it is essential how high energy to introduce into the gas plasma for excitation electromagnetically and thermally and then how much atomic hydrogen to produce for etching out sp^2 materials like graphite and hexagonal BN or for suppressing their deposition in the CVD under the low vacuum. Conclusively, a key for the formation of diamond and/or cBN from gas phases is to excite raw material species up to higher energy states beyond kTe (electron temperature of plasma) corresponding to activation energy Usp^3 of sp^3 materials and to let them come flying just on the substrate with not losing their energy by collision or recombination. Thus, a new general concept for the deposition mechanism of diamond and/or cBN has been proposed in relation to the atomic potentials with sp^2 and sp^3 electron orbitals.

1. Introduction

Once the synthesis of diamond and cubic boron nitride (cBN) required extremely high pressure and high temperature[1]. Now, some new processes have been investigated for the chemical vapor deposition (CVD)[2,3,4,5] or the physical vapor deposition (PVD)[6,7,8,9] of diamond and cBN from gas sources at low pressure. In such techniques, a tungsten hot filament and/or an r.f.induction are often used to excite the gas plasma to higher energy states. The hot filament method at first reported by NIRIM group[2] is usually used for the deposition of diamond. This method needs such some requirements as follows; much amount of H_2 near or over 99% to methane(CH_4), hot filament heating over 2000 ˚C and very short distance under 5mm between filament and substrate. The reason is possibly that hot filament heating over 2000 ˚C dissociates H_2 to atomic H and that this atomic H plays an important role to etch graphite out and resultantly to form diamond at such some trap-sites as steps or kinks on the surface of substrate. However, it cannot be immediately said that the formation mechanism of diamond was understood. As for the cBN composed of two different elements of B and N, it is much more difficult to understand a cBN formation mechanism.

With the aim to clear a cBN formation mechanism, we[4] have also developed some types of CVD apparatus until now. On the development, it was found that the essential requirement conditions are to introduce a high energy into the reaction space electromagnetically and thermally for plasma excitation and to produce much atomic H for decrease of turbostratic or amorphous BN (tBN or aBN) and increase of cBN. This can be same in the diamond formation. Whereas, it is said that the atomic H is needed in the CVD process but not needed in the PVD process. For example, in the ion beam deposition[6] or in the laser beam sputtering[7] Ar gas is mainly used and (Ar + H_2) or (Ar + N_2) gas mixture is occasionally used. Why is that? This is one important problem. Meanwhile, there is other very important problem relating to plasma energy. It was found from our detailed plasma spectroscopic study that the synthesis of cBN by plasma CVD method requires a very high gas plasma energy for the chemical bonding of zinc-blende type cBN. How high energy is needed for the formation of cBN? This is another important problem. It is thought that an answer to these problems is a key to clear the formation mechanism of diamond and cBN. In this report, our developmental history of plasma CVD apparatus for the formation of cBN will be presented and then the problems described above will be considered from the experienced points, followed by the necessary conditions and the possible mechanism for the synthesis of diamond and cBN.

2. Development of plasma CVD apparatus for synthesis of cBN

Recently, CVD techniques for diamond and cBN deposition have been advanced widely. We have also developed some CVD apparatus to study the formation factors of cBN. They are schematically shown in Fig.1[4]. Our developmental history of plasma CVD apparatus is divided into three generations.

An apparatus set in the first generation was of the simplest horizontal furnace type using an r.f.power of 13.56 MHz(Fig.1(a)). By this furnace, no cBN was deposited but only a tBN was deposited on a substrate placed at the center of furnace.

A redesigned apparatus in the second generation was of a unique type using both an r.f. electromagnetic field and tungsten filament heating. In this method, the tungsten filament plays a key role for the formation of cBN. For the purpose of cBN synthesis, we made two types of apparatus; one is the vertical type (Fig.1(b)) and the other is the horizontal type (Fig.1 (c)). When the filament is not heated, i.e. only the r.f.induction is used, cBN cannot be formed but only tBN or aBN. For the synthesis of cBN, the first success was attained by the additional thermal assistance of the tungsten filament. Source material gases put into the plasma chamber were first excited into the plasma state by the usual r.f. induction of 13.56MHz at 100W and additionally excited by heating the tungsten filament over 1600 ˚C. The source gases used were diborane (B_2H_6) and ammonia (NH_3), which were diluted to 1% in volume with hydrogen gas. A silicon wafer substrate placed just behind the filament was heated to a constant temperature of 800 ˚C by an electric furnace. By this method, cBN was found to be co-deposited with a tBN structure by about 20% in the volume fraction. The cBN was also formed with the horizontal type apparatus, where solid

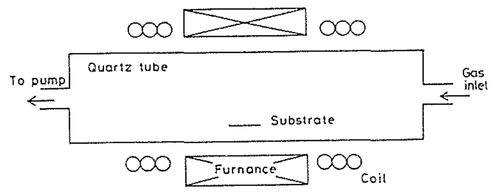

(a) Horizontal-type (Volume Fraction : 1)

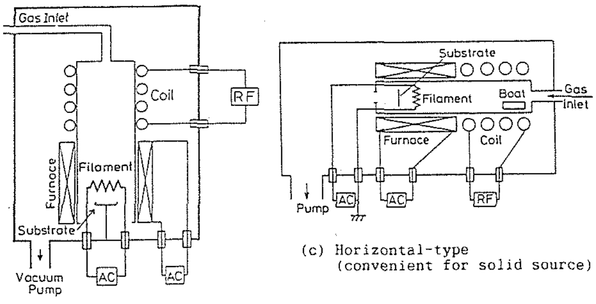

(c) Horizontal-type (convenient for solid source)

(b) Vertical-type (Volume Fraction : ~1/50)

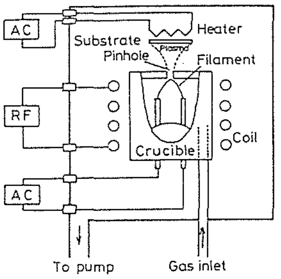

(d) Crucible-type (Volume Fraction : ~1/500)

Fig. 1. Progress of plasma CVD apparatus developed in our laboratory.

state raw materials can be used.

In the third generation, a new type of CVD apparatus like a Knudsen cell as shown in Fig.1(d) was devised with the aim to improve the yield of cBN. This apparatus is in principle similar to the apparatus in (b) and (c). Here, solid raw materials such as $NaBH_4$ or H_3BO_3 are placed in the crucible and the reactive carrier gas, NH_3, is introduced into a crucible containing a tungsten filament. The vaporized and reactive carrier gases are excited into a plasma in the crucible by r.f. induction and then are activated by the filament. The reacted gas product, BN, is ejected from a small central pinhole of the cap covering the crucible out. With this apparatus, the BN film was deposited with a relatively high rate of about 1000 Å s^{-1}. By the IR spectroscopy and transmission electron microscopy, the deposited BN film was examined to be mostly composed of cBN. The reaction process of cBN synthesis in this method is essentially as well as in the earlier methods. Our developmental history of plasma CVD apparatus tought us that it is important how high energy level to excite up the gas plasma to. The reaction space of the crucible type apparatus is about 1/500 of that in the first generation apparatus, while the reaction space in the second generation apparatus is about 1/50 of that in the first generation apparatus. This means that the plasma energy can be highly concentrated in the reaction space of the third generation apparatus.

3. Pressure-temperature diagram for diamond and cBN synthesis conditions

We learned from our past experiments that it is most of importance how high energy level the reactive gas plasma should be excited to. Then, we attempted first to examine the formation conditions of cBN already reported in various PVD and CVD methods. Some other data plots on the diagram of plasma pressure vs temperature (p-T) as shown in Fig.2[1,4,6-12] suggested that it is essential for the synthesis of cBN to activate reactive gas species beyond the electron temperature(Te) of plasma. This can be undoubtedly same in the case of diamond synthesis. Figure 3[13-19] is the p-T plots of diamond which apparently shows the same results as that of cBN. Meanwhile, it is found from the previous studies on the formation of diamond and cBN that much amount of atomic hydrogen is absolutely needed in the CVD process but not in the PVD. In the present report, these facts described will be considered from the physical point of the "mean free path" and then the potential energy distribution diagram will be proposed for the formation mechanism of sp^2 and sp^3 materials.

According to our experiments[4,5], the cBN could be formed on the Si substrate by means of the r.f. plasma CVD technique with hot filament. The result of in-situ plasma spectroscopic analysis told that a great number of H atoms and N_2^+ ions co-exist. Especially for the generation of atomic H, it is found that the atomic H increases with increase of hot filament temperature. Also, the formation of diamond and cBN is strongly dependent on the gas pressure. That is, the CVD process in the low vacuum is used for diamond deposition against the PVD process in the high vacuum for i-C (ion-beam deposited carbon). Figure 4 shows the potential curves for sp^2 and sp^3 materials. The energy difference Usp^3-vdw represents the transformation energy from the sp^2 to sp^3, e.g. graphite to diamond. In the deposition process, gas species such as atoms or molecules are shifted to the higher energy level by collision of high speed electron with high energy, and then they should be holding or not be losing their potential energy just by reaching the substrate for the diamond and cBN deposition. The reaction for the formation of the sp^2 or sp^3 must occur just on the surface of substrate, and then only the radicals having high energy beyond one threshold value must form a sp^3 material. "This is closely related to the degree of vacuum." Actually in the BN deposition experiment, the deposition of the sp^2 material is dominant under the relatively high gas pressure (low vacuum) though the sp^3 material is dominant under the relatively low gas pressure (high vacuum). This means that the major species reached the substrate have lost energy and have become inactive. It is supposed that the radicals can always lose their energy by collision and recombination with other species or electrons especially in the relatively low vacuum. If the radicals could fly in the relatively short mean free

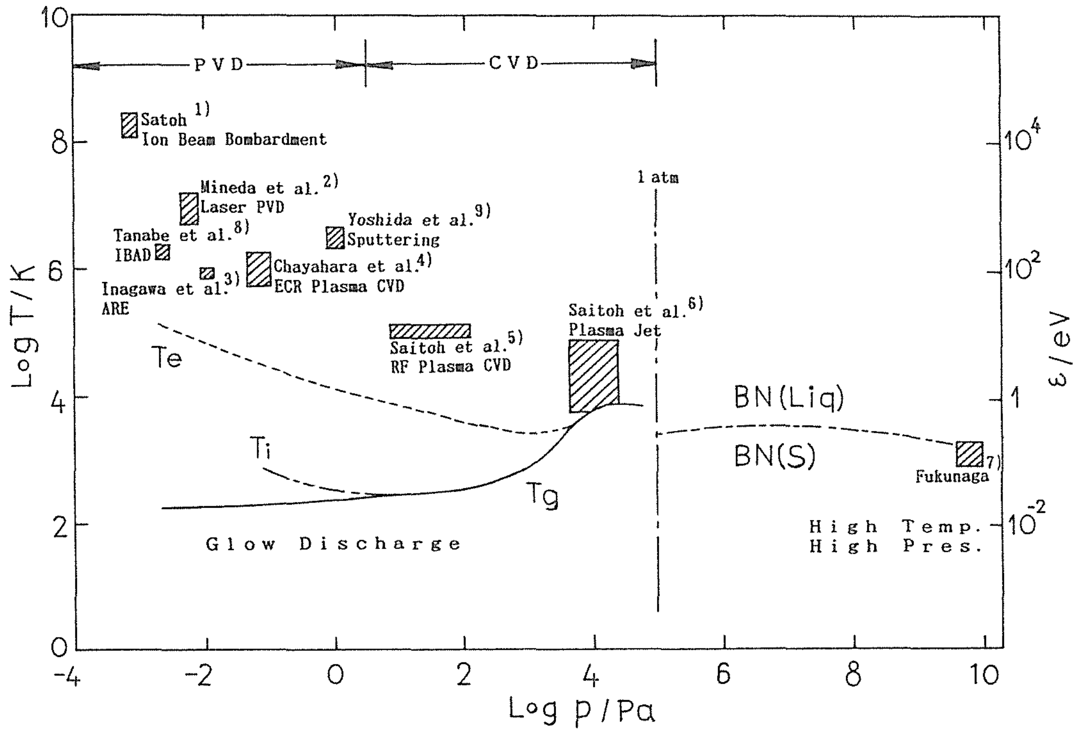

Fig. 2. Illustration of log p - log T diagram for the BN system: 1) ref. 6; 2) ref. 7; 3) ref. 8; 4) ref. 9; 5) ref. 10; 7) ref. 1; 8) ref. 11; 9) ref. 12.

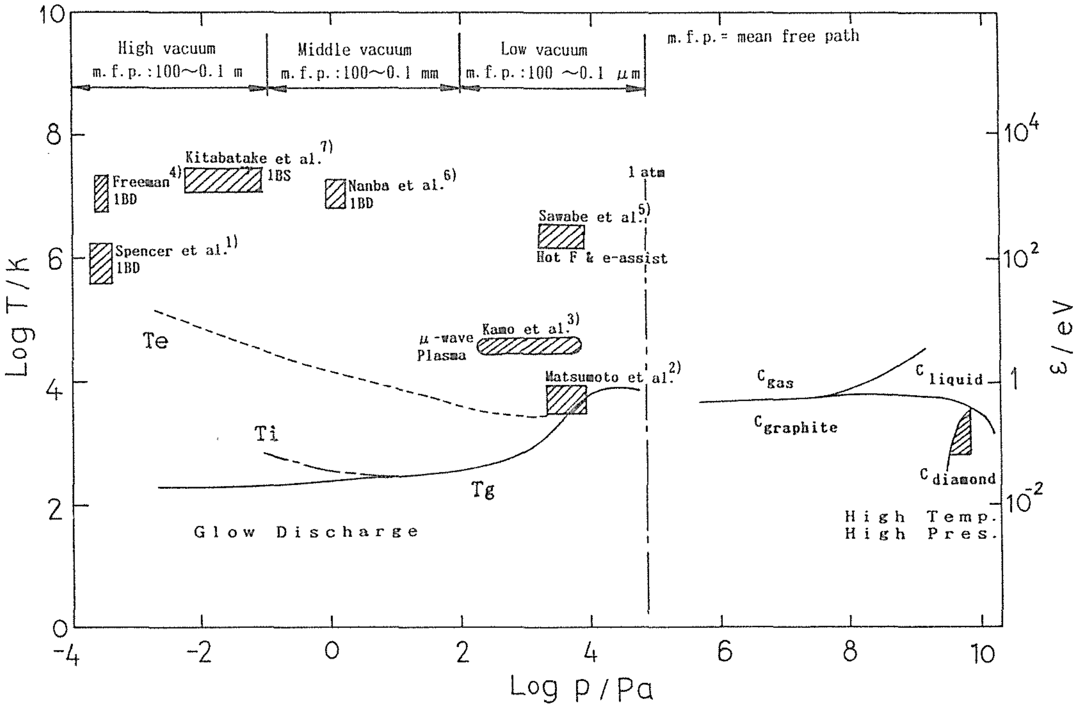

Fig. 3. Illustration of log p - log T diagram for the diamond system: 1) ref. 13; 2) ref. 2; 3) ref. 3; 4) ref. 14; 5) ref. 15; 6) ref. 16; 7) ref. 17.

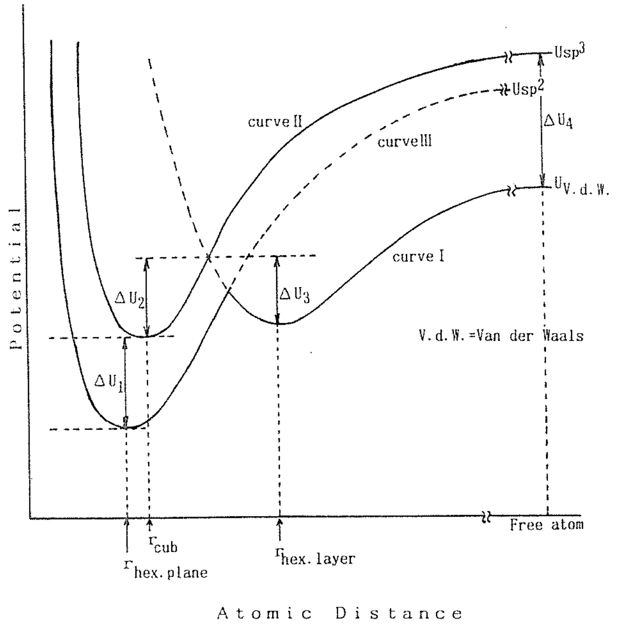

Fig. 4. Interatomic potentials for graphite and diamond; curve I (van der Waals' force), curve II (sp^3) and curve III (sp^2).

path, they might form only the sp^2 materials. From the physical point of the "mean free path", it can be said that the CVD process is short but the PVD process is long. For the formation of the sp^3 material by means of the CVD process, therefore, a great amount of atomic H must be needed to remove the sp^2 material out and the distance between the filament and the substrate must be as short as possible. On the point of view mentioned, the CVD apparatus already succeeded for diamond deposition must be so well devised as not to lose energy by collision or recombination. Namely, the substrate must be set very near the filament for the hot filament CVD and also just at the center of gas plasma for r.f.- or micro-wave CVD. Also in the plasma jet or plasma torch method, the energized particles can come flying onto the substrate with not losing their energy by means of ejecting the high pressure gas plasma from the fine nozzle. Thus, each of methods talked above is applicable to the deposition of diamond along the interatomic potential curve as already shown in Fig. 4. On the other hand, the synthesis of cBN is much more difficult than that of diamond as compared because the cBN is composed from two elements of B and N against diamond of monoatomic C. Then, the two ideal methods of cBN synthesis expected best are a PVD by NIT group[20] having a characteristics of exciting B and N near on the substrate by high speed electron shower in the high vacuum and a CVD by NIRIM group[21] having a characteristics of energizing B and N by means of laser irradiation just on the surface of substrate.

4. Considerations

The above description tells that the most important problem is how high energy the flying particles onto substrate have. For the deposition of sp^3 material, the flying particles must be excited beyond the electron temperature(Te) of plasma and brought to substrate with holding activation energy over kTe corresponding to Usp^3 in Fig.4. This is easy in the PVD process but hard in the CVD process because the mean free path is very long in the former but very short in the latter. This means that some special requirements are needed in the CVD process for the formation of sp^3 material; much amount of H_2 near or over 99% to CH_4, hot filament heating over 2000 °C and extremely short distance between filament and substrate. Now, the possible mechanism for the synthesis of diamond and cBN will be considered and discussed.

(1) Activation energy of flying particles onto substrate

We are talking about which material of sp^2 or sp^3 is deposited from gas phase by using our vertical-type plasma CVD apparatus as shown in Fig. 1(b). A simple concept of the reaction at that time is shown in Fig.5. The raw material gases like atoms or molecules introduced from the top inlet are firstly inductively excited to plasma state by the r.f. coil in the upper room and then thermally assisted to much higher energy state by the hot filament in the lower room. Thus, the raw material gases are dissociated and the sp^2 or sp^3 material is deposited on the substrate placed just under the hot filament. Then, a key for the formation of sp^3 material is that the high energy particles formerly excited must reach the substrate with not losing energy by recombination. Here, the activation energy of flying particles must be beyond kTe which can be mainly given by *high* speed electrons thermally or electromagnetically accelerated. As for the flying particles below kTe, only the sp^2 materials can be deposited but the sp^3 ones cannot be done. Of course, it is natural that the energy loss of flying particles by recombination is fairly dependent on the degree of vacuum, and so even if the

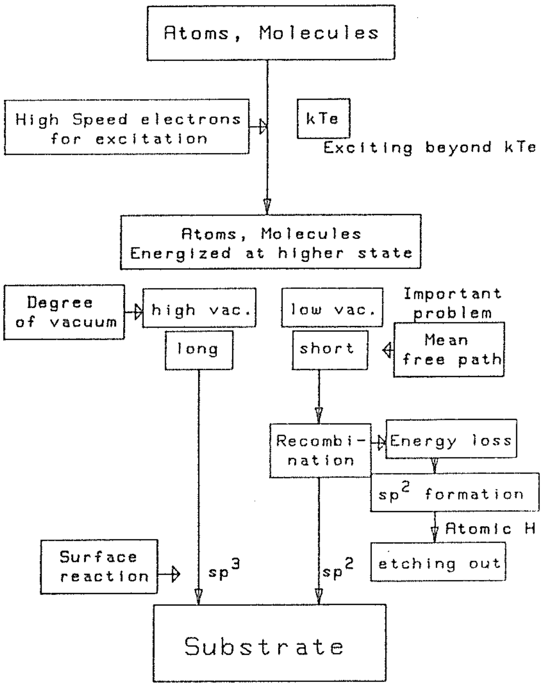

Fig. 5. A new concept for the formation mechanism of sp^3 material like diamond and cBN.

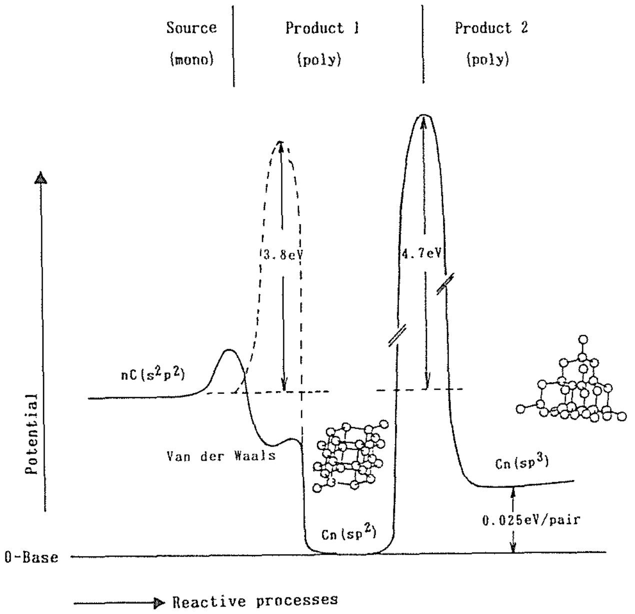

Fig. 6. A new model in the chnages of potential dependent on reactive processes form source to products. (Example; graphite and diamond.)

flying particles can be excited beyond kTe, they may easily lose their energy by recombination, especially in the CVD process of the low vacuum. Indeed, it is well known that the visible light of gas plasma is emitted when the excited particles lose their energy by recombination. Then, the flying particles which lost their energy immediately fall down into the more stable state, i.e. the sp^2 material like graphite or hBN. The deposition of such sp^2 material as graphite or hBN has a tendency to suppress the formation of the sp^3 material like diamond or cBN. Therefore, much amount of atomic H is needed to evaporate out the sp^2 material as a gas phase from a reactive system. The CVD process for the formation of the sp^3 material like diamond or cBN is said to need much amount of atomic H which is catalytically generated from H_2 molecule by heating W-filament beyond 2000 °C.

(2) Potential barrier between graphite and diamond ; hBN and cBN

It is well known that graphite is easy to be formed but diamond is hard. This fact is also same in the relation between hBN and cBN. Why ? This answer can take us to the best way to deposit or form the sp^3 material like diamond or cBN from gas phase.

In the following, the changes of potential barriers to reactive processes will be discussed by using the model as shown in Fig. 6. This shows the changes of the potential dependent on the reactive processes from source to product in the case of carbon (graphite and diamond). Here, the source of raw material is a free carbon atom or molecule like CH_4 in the ground state, the product 1 is a graphite structure composed of a few atoms, at least 4, characterizing graphite, and the product 2 is a diamond structure composed of the minimum number 8 atoms. In the reaction from source to product 1, the potential barrier B1 between the ground state $nC(s^2p^2)$ and the excited state $Cn(sp^2)$ is so high as about 3.8 eV by theory but in fact is very small, maybe at most 0.1 eV, because the van der Waals' force (long-distance force) between hexagonal planes strongly affects the formation of graphite structure. This fact can be read from Fig. 4. Next, talking about the reaction from source to product 2 via product 1, the potential barrier B2 between $nC(s^2p^2)$ and $Cn(sp^3)$ is 4.7 eV for diamond corresponding to kTe in Fig. 4, but that between $Cn(sp^2)$ and $Cn(sp^3)$, i.e. graphite and diamond, is supposed to be so much higher. In the PVD process each carbon atom or molecule energized beyond barrier B2 can construct the diamond structure, but in the CVD process the graphite structure is as usual dominant to the diamond. Here, the former, once if deposited, tends to suppress the deposition of the latter. The reason is that the potential barrier from $Cn(sp^2)$ to $Cn(sp^3)$ should depend on a few atoms (cluster), at least 4, and that the potential energy is estimated about 6 eV for the transformation of $C_4(sp^2){\cdot}C_4(sp^2)$ to $C_8(sp^3)$ as shown in Fig. 7.

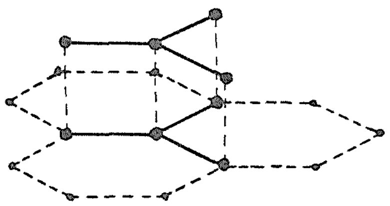

$$(1)\ \underset{(\text{mono})}{nC(s^2p^2)} \Rightarrow \underset{(\text{poly})}{Cn(sp^2)} \Leftrightarrow \underset{(\text{poly})}{Cn(sp^3)}$$

$$\uparrow \text{ low barrier} \qquad \uparrow \text{ high barrier}$$

$$(2)\ C_4(sp^2)/C_4(sp^2) \underset{\underset{\approx 6\text{ eV}}{\uparrow}}{\Rightarrow} C_8(sp^3)$$

Fig. 7. A consideration relating to the changes of $nC(s^2p^2)$ to $Cn(sp^2)$ and $Cn(sp^2)$ to $Cn(sp^3)$.

5. Conclusion

The synthesis of cBN from the gas phase has been studied by a new plasma CVD apparatus using an r.f. plasma and tungsten filament heating, and the formation mechanism of cBN has been described by a p-T (pressure vs. temperature) diagram in which the experimental data on cBN formation are plotted. These facts can be quite same to the formation of diamond.

With respect to the formation of diamond and cBN, it is most important how much energy the flying particles onto the substrate have. Namely, for the deposition of sp^3 material, the flying particles must be excited beyond the electron temperature of plasma and brought to the substrate with holding activation energy over kTe corresponding to Usp^3. This is easily attained in the PVD process of the high vacuum but hardly in the CVD process of the low vacuum, because the mean free path is very long in the former but very short in the latter. Conclusively, for the formation of the sp^3 material like diamond or cBN by means of the CVD process, much amount of atomic H is needed to evaporate out the sp^2 material like graphite or hBN which was formed as the result of recombination.

Therefore, we have proposed a new concept for the formation of diamond or cBN.

References

1. O. Fukunaga: Abst. 3rd Dia. Symp., 1989, Jpn. Dia. Forum Ass., p.47, (in Japanese)
2. S. Matsumoto et al: Jpn. J. Appl. Phys., 21(1982), L183
3. M. Kamo et al: J. Cryst. Growth, 62(1983), 642.
4 .Y. Ichinose et al: Surf. and Coat.Tech., 43/44(1990), 116.
5.Y. Ichinose et al: Proc. 11th Symp. on ISIAT, Tokyo, 1987, p.469.
6. M. Satoh et al: Jpn. J. Appl. Phys., 22(1983), L171.
7. S. Mineda et al: Seimitsu-Kougakukaishi, 53(1987), 1532, (in Japanese).
8. K. Inagawa et al: Proc. 9th Symp. on ISIAT, Tokyo, 1985, p.299.
9. A. Chayahara et al: Proc. ISPC-8, Tokyo, p.2440.
10. H. Saitoh et al: Ext. Abst. Carbon Conf., Penn State, 1989, p.428.
11. A.Tanabe et al: Abst. 4th Dia. Symp., 1991, Jpn. Dia. Forum Ass., (in Japanese).
12. T. Yoshida et al: Jpn. J. Appl. Phys., 29(1990), L1175.
13. E. G. Spencer et al: J. Appl. Phys. Lett., 29(1976), 118.
14. J. H. Freeman: Vacuum, 34(1985), 305.
15. A. Sawabe et al: Appl. Phys. Letter, 46(1985),146.
16. Y. Nanba et al: J. Vac. Sci. and Tech., A3(1985), 319.
17. M. Kitabatake et al: J. Appl. Phys., 58(1985), 1963.
18. S. Matsumoto et al: Appl. Phys. Letter, 51(1987), 737.
19. Y. Hirose et al: Electronic Mater., No.8(1989), 45, (in Japanese).
20. M. Murakawa et al: Surf. and Coat. Tech., 43/44(1990), 128.
21. S. Komatsu et al: J. Appl. Phys., 71(1992), 5654.

CVD Diamond Growth: Gas Compositions and Film Properties

P.K. Bachmann, H.J. Hagemann, H. Lade, D. Leers, D.U. Wiechert and H. Wilson
Philips Research Laboratories, P.O. Box 1980, D-52021 Aachen, Germany

Abstract

The influence of various deposition parameters on rate, crystallinity and phase purity of CVD diamond deposits is discussed. Emphasis is on microwave plasma CVD of diamond from C/H-, C/H/O-, C/H/F-, C/H/Cl- and C/H/N-gas mixtures.

The manufacture of wear-resistant diamond thin films, diamond vacuum window membranes and thick diamond heat spreader plates are used as examples to outline the influence of various deposition parameters on the performance of finished products and to describe the use of our ternary gas phase compositional diagrams as tools for minimization of process and product optimization efforts.

Introduction

Since the revitalization of diamond chemical vapor deposition by the ground-breaking publications of B.V. Spitsyn et al [1], and M. Kamo, S. Matsumoto, Y. Sato and N. Setaka at NIRIM, Japan [2,3], numerous CVD processing variants were added to the list of possible ways to grow diamond films (see, e.g., [4,5] for an extensive list of references and a critical comparison of the methods). The driving force of inventing new ways of diamond making was and is to grow better quality diamonds on larger substrate areas at higher rates and lower deposition temperatures. While some of the methods are merely of scientific interest, others, especially hot filament deposition, microwave plasma, DC arc jet, or RF plasma CVD technology emerged into industrially applicable manufacturing technologies with potential for scale-up and volume production of high quality material.

In addition to new methods of initiating the CVD reactions, new gas compositions were tested in order to improve the quality and phase purity of the deposit, to reduce the thermal load on the substrate and to increase the deposition rates (see [4-6] for references). Additives to the carbon carrier gases as well as their concentrations were often selected by trial-and-error or are directly connected with the deposition process used (e.g., combustion flame technology [7]).

The scientific as well as the patent literature of the 1980s contain a wealth of methods and recipes to grow diamond from the vapor phase. Our analysis of such data along with the results of our own experiments resulted in the development of a C/H/O - gas phase compositional diagram [6] that provides a common roof for all diamond CVD methods known to date and helps to explain, optimize and correlate deposition conditions, experimental results and film properties.

Diamond CVD Gas Phase Compositional Diagrams

The principles of constructing the C/H/O-diagram and the resulting predictable trends of the experiments are outlined in ref. [6]. In its first version, the triangular diagram comprises a wedge-shaped region where diamond growth is, at least with respect to the gas composition, feasible. This "diamond domain" extends along the H-CO tie line of the diagram and is limited by a region of oxygen-rich gas compositions from which no deposit forms and by a region of carbon-rich gas mixtures that result in the deposition of dominantly amorphous, non-diamond carbon phases. The basic principles of this diagram stood the test of time and the existence of the diamond domain was confirmed by many authors [8-10]. Its position and shape can even be explained by thermodynamical calculations [11]. However, additional experiments in previously unexplored regions of the diamond domain led to modifications of its shape and revealed additional trends [8]. If solely based on microwave plasma CVD experiments at 1.5 kW and 50-110 mbar performed on the same deposition unit, the diamond domain exhibits a lens shape as shown in Fig.1 [8].

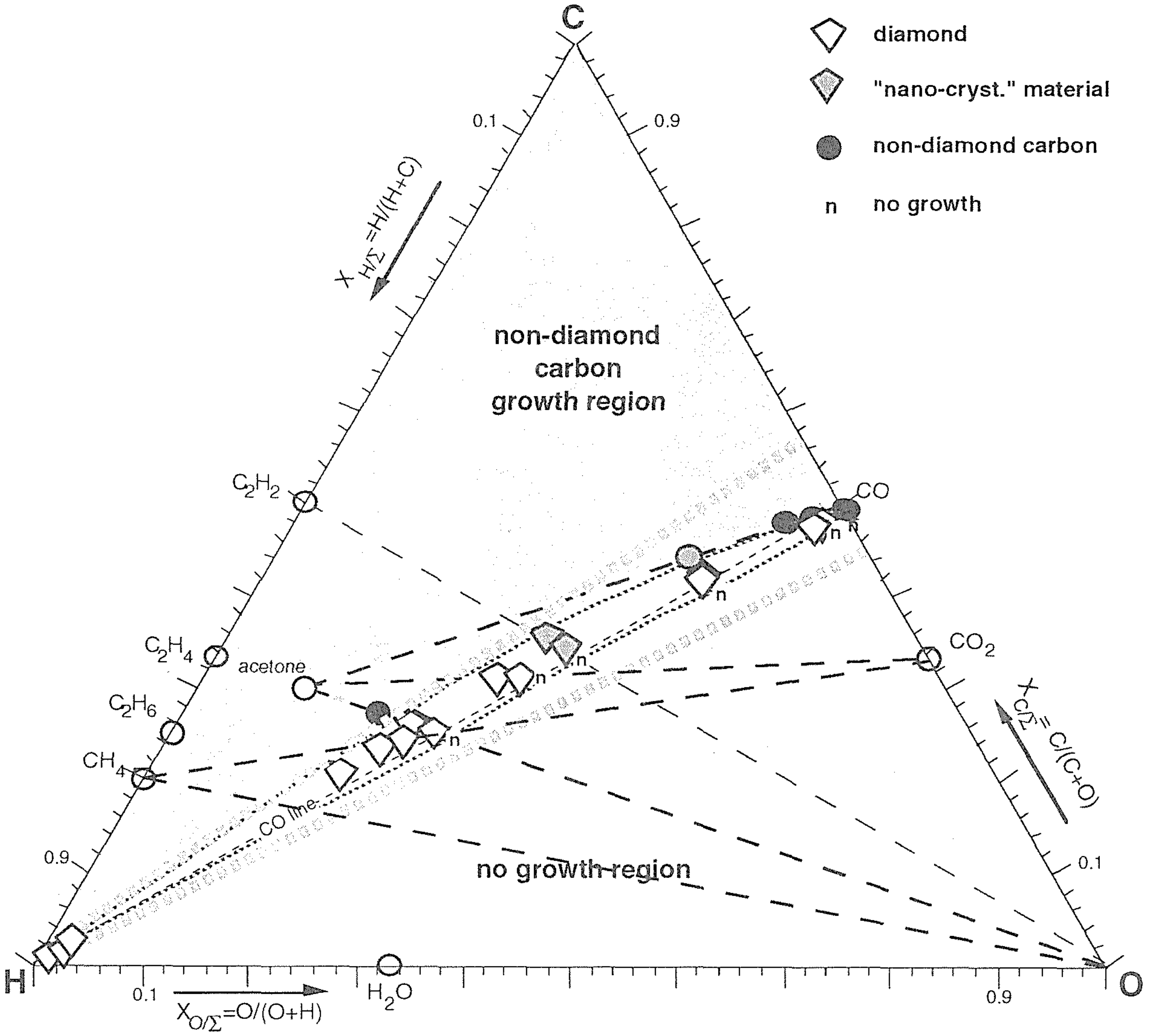

Fig. 1: Updated C/H/O-gas phase compositional diagram of diamond CVD [8] showing a lens-shaped diamond domain.

The most import modifications compared to the earlier version [6] of this diagram are:

- a lens-shaped rather than a wedge-shaped diamond domain. This includes the fact that the domain narrows down to a single point at its right side. Carefully performed experiments indicate that diamond growth without any source of hydrogen in the system is not feasible and at least 0.5% H needs to be present in the C/H/O-mixture to allow for diamond to grow.
- the straight oxygen-rich border of the diamond domain is very close to the CO-H-tie line of the diagram. Its position was not only confirmed in many growth experiments but is also nicely illustrated by the complete vanishing of any C-related optical plasma emission when crossing over from the diamond domain into the no-growth region of the diagram.Interestingly, both the sharpness of the oxygen-rich domain border as well as the lens shape of its C-rich border are confirmed by thermodynamics calculations. For high power densities, calculated and experimental domain shape seem to match even closer than for low power/low pressure plasmas [21] indicating that at least under high power density conditions the system can be close to thermodynamical equilibrium.

Of course, the correct gas phase composition is not the only requirement for diamond CVD. If no energy is provided to the system in order to sufficiently radicalize the gas phase, diamond growth will not proceed, i.e. the diamond domain will disappear. For microwave energies of only 500 W, the domain is narrower than indicated in Fig.1 and does not extend over the full width of the triangular diagram, as shown by P. Paroli [9]. Nevertheless, the diamond domain indicates where to search for diamond and hence provides a strategy tool to optimize the deposition process and the quality of the deposit. In connecting the experimental results of over 30 years of worldwide research, it also illustrates that specific starting materials are not required for diamond growth and that many CVD diamond patents related to gas phase compositions are most likely obsolete.

It is, of course, possible to construct other ternary gas phase compositional diagrams. In order to evaluate the proposed [12] benefits (lower deposition temperature and higher rates) of adding halogen compounds to the diamond CVD gas phase, we performed a series of microwave plasma deposition experiments using C/H/Cl- and C/H/F-gas mixtures [13]. We were able to confirm diamond growth from both gas systems and plotted our results along with literature data into C/H/Cl- and C/H/F-gas phase compositional diagrams. The hydrogen-rich corner of the C/H/Cl-diagram is shown in Fig. 2 [13]. The respective diamond domain is limited to an area very close to the H-corner of the diagram. High chlorine concentrations seem to foster the deposition of non-diamond carbon phases. In our microwave experiments we were, however, unable to locate a region inside the C/H/Cl-growth domain that would provide an advantage in terms of rate, phase purity or deposition temperature over C/H/O-gas compositions. This along with the problems associated with the handling of chlorine-containing gas mixtures, forced us to terminate further exploration chlorine-assisted diamond CVD.

In the case of fluorine-assisted diamond CVD, evaluation of the literature and our own experimental data in the form of a C/H/F-diagram indicates that the diamond domain extends

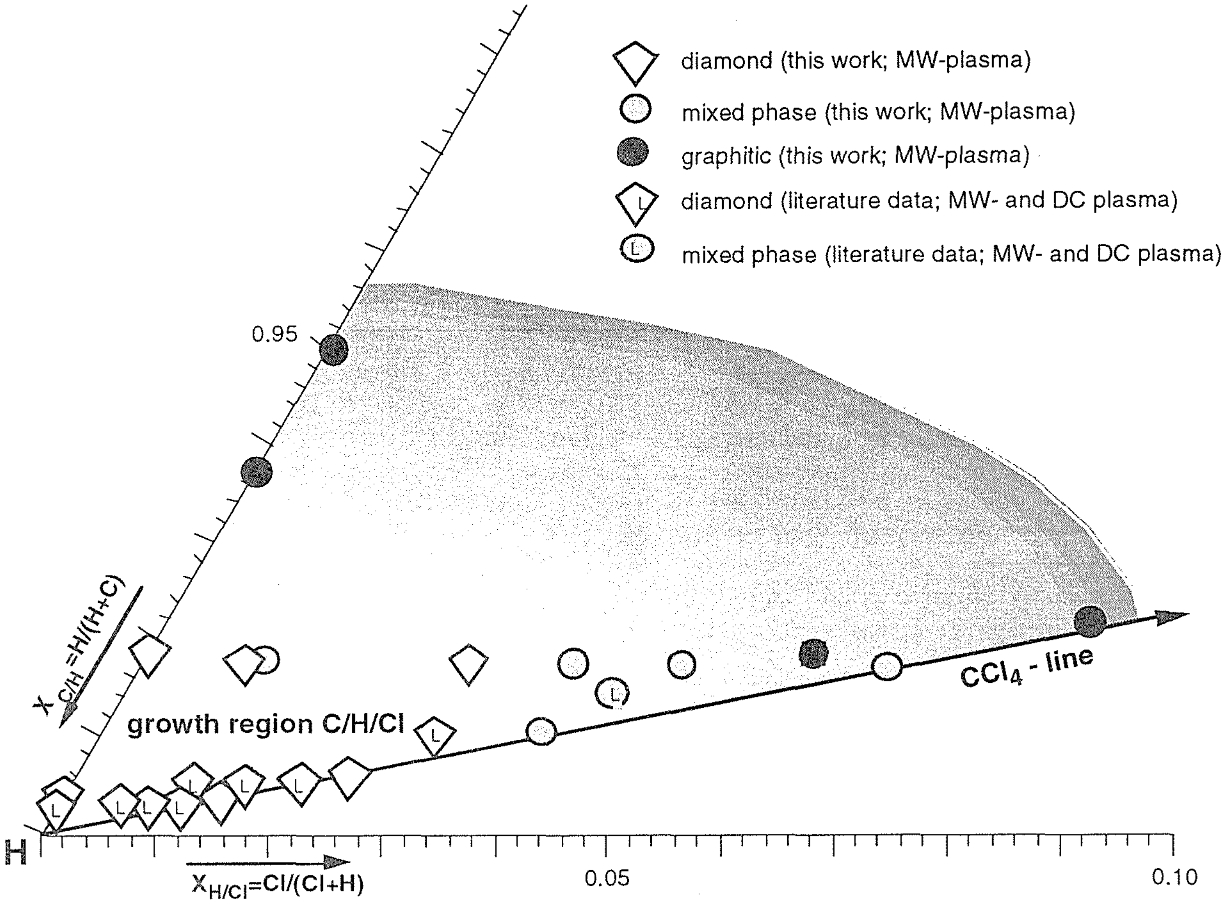

Fig. 2: H-rich corner of the C/H/Cl-gas phase compositional diagram of diamond CVD [24].

well into the fluorine-rich region of the ternary system and is positioned next to the H-CF_4 tie line. However, again we could not find any advantage of fluorine-assisted diamond CVD over growth from C/H/O-mixtures and, in addition, the use of fluorine severely restricts the type substrate materials. Silicon, e.g, is always damaged, even if only small quantities of fluorine are present in the plasma activated gas phase. We, therefore, terminated further investigation of halogen-containing diamond CVD gas mixtures.

A C/H/N-gas phase compositional diagram is not worth plotting, because diamond growth is basically limited to a region very close to its C/H- side line. Addition of only 1% nitrogen gas to a mixture of 1% CH_4/H_2 results in severe deterioration of the crystalline structure and poor phase purity of the deposited material [14]. As detected by emission spectroscopy, nitrogen-containing compounds in the source material were also responsible for the poor quality of our microwave plasma deposited films grown from acetylen-oxygen mixtures [8] (see Fig.1).

Film Properties

The C/H/O- or C/H/X-diagrams are not only helpful in exploring new gas compositions or to optimize the start-up or shut down procedure of deposition experiments, but also minimize the effort needed to optimize the properties of the deposit and hence of the final product.

In the course of developing vacuum windows based on thin diamond membranes [15], we were able to clearly correlate the occurrence of membrane damage during the required wet etching procedure with the CVD gas phase composition. Attempts to correlate the membrane destruction with crystal size, texture, phase purity, thickness, or other deposition parameters failed. TEM data of our films [16] indicate that, although the crystalline perfection of individual diamond grains grown from gas mixtures with high oxygen levels, i.e. in the center of the C/H/O-diagram, is better and the dislocation densities are lower than for C/H-grown material, connectivity between the grains seems to be a problem and small pores are likely to form. These O-induced structural differences seem to be responsible for the observed film damage.

Wear resistant coatings can be grown from C/H- and C/H/O-gas mixtures. We were able to demonstrate that if the nucleation density is high enough, a layer of only 50 nanometer of CVD diamond grown from either acetone/oxygen- or from methane/hydrogen-mixtures converts the wear performance of the soft surface of a silicon wafer to that of a tungsten carbide cutting tool insert [17]. In this case, optimization of the film properties along the diamond domain is not required and the deposition rate advantage of C/H/O- over C/H-gas mixtures can be fully exploited. However, choosing the proper position <u>across</u> the width of the diamond domain allows to optimize the wear performance of a film versus its friction properties. While high friction, well-facetted material grows closer to the oxygen-rich border, low friction, fine grain material precipitates closer to the C-rich border of the diamond domain.

Gas phase induced crystallinity and phase purity changes also affect the thermal and optical properties of the deposit: the thermal conductivity of C/H/N-grown diamond is usually low and the presence of nitrogen in the CVD gas phase quenches the diamond A-band luminescence at 445 nm.

Preliminary results of a comparison of thermal diffusivity data of a large number of our C/H- and C/H/O-grown diamond thin and thick films reveals that it is difficult to grow high quality heat sink material from oxygen-containing gas mixtures. Although we were able to grow 250 µm thick white diamond disks with a thermal conductivity of 22±2 W/cm K, the thermal conductivity of material grown from gas mixtures with high oxygen partial pressures never exceeded 10 W/cm K [18].

Conclusion

The composition of the CVD gas phase plays a vital role for the diamond deposition process, its optimization with respect to rate, phase purity, substrate temperature and substrate material. It is equally important for the mechanical, optical, thermal and electrical properties of the deposited material. Ternary gas phase compositional diagrams are not only scientifically interesting but are helpful tools that provide a strategy to minimize the effort needed for optimization and thus reduce diamond CVD process and product development costs.

Acknowledgements

Support of this work by the German Ministry of Research and Technology is gratefully acknowledged.

References

[1] B.V. Spitsyn, L.L. Bouilov, and B.V.Derjaguin, J. of Crystal Growth, 52, 219 (1981).

[2] S. Matsumoto, Y. Sato, M. Kamo, and N. Setaka, Jpn. J. of Appl. Phys. 21, L183 (1982).

[3] M. Kamo, Y. Sato, S. Matsumoto, and N. Setaka, J. of Crystal Growth, 62, 642 (1983).

[4] P.K. Bachmann, in "Thin Film Diamond" edited by A. Lettington and J.W. Steeds, Chapman and Hall Royal Society London, ISBN 0-412-49630-5 (1994).

[5] P.K. Bachmann, W. v. Enckefort, Diamond and Related Materials, Vol.1, 1021 (1992).

[6] P.K. Bachmann, D.Leers, and H. Lydtin, Diamond and Related Materials, Vol. 1, No.1, 1 (1991).

[7] Y. Hirose, S. Ananuma, N. Okada, K. Komaki, "1st Intl. Symp.on Diamond and Diamond-Like Films", The Electrochem. Soc. Pennington, NJ, Proceedings,Vol. 89-12, 80 (1989).

[8] P.K. Bachmann, D. Leers, and D.U. Wiechert, presented at DIAMOND 1992, paper 4.2 (Book of Abstracts), Aug. 31-Sept. 4, 1992, Heidelberg, Germany

[9] P. Paroli,presented at, ADC´93, 2. Intl. Conference on the Applications of Diamond Films and Rel. Materials Aug. 25-27, 1993, Omiya, Saitama, Japan.

[10] M. Fryda, C.P.Klages,Diamond and Rel. Mat.,in press,(1994)

[11] N.A. Prijaya, J. C. Angus, P.K. Bachmann Diamond and Related Materials, Vol. 3, N0.1-2, 129 (1993)

[12] D.E. Patterson, B.J. Bai, C.J. Chu, R.H. Hauge,and J.L. Margrave in "New Diamond Science and Technology", edited by R.F. Messier, J.T. Glass, J.E. Butler, and R. Roy, Mater. Res. Soc. Pittsburgh, PA, 433 (1991).

[13] P.K. Bachmann, H.J. Hagemann, H. Lade, D.Leers, F. Picht, D.U. Wiechert, presented at "Diamond Films´93", paper 2.2, Albufeira, Portugal, Sept. 20-24, 1993

[14] P.K. Bachmann and D.U. Wiechert, Diamond and Related Materials, Vol. 1, 422 (1992) Diamond and Related Materials, in press, (1994)

[15] P.K. Bachmann, H. Lade, D.Leers, D.U. Wiechert presented at "Diamond Films´93" , paper 16.2, Albufeira, Portugal, Sept. 20-24, 1993

[16] P. Pongratz, M. Joksch, P.K. Bachmann, D.Leers to be published (1994).

[17] P.K. Bachmann, H. Lade, D.Leers, D.U. Wiechert presented at "Diamond Films´93", paper 12.062, Albufeira, Portugal, Sept. 20-24, 1993.

[18] P.K.Bachmann, H.J.Hagemann, H.Lade, D.Leers, D.U.Wiechert, H. Wilson, submitted for presentation at "Diamond Films ´94", Castelvecchio, Italy, Sept. 25-30, 1994.

Epitaxial Growth of Diamond on Foreign Substrates

T. Inuzuka
Department of Electrical Engineering and Electronics, Aoyama Gakuin University
Chitosedai 6-16-1, Setagaya-ku, Tokyo 157, Japan

The initial growth process of diamond on cBN surfaces will be described in details considering the nucleation and epitaxy of crystals from vapor phase. At the quite early growth stage of diamond deposition, thin carbon layers start to grow prior to the daiamond growth. The nucleation of diamond takes place on this thin carbon layer selectively.

This layer will have the structure close to that of diamond and plays a significant role for the nucleation and epitaxy of diamond.

1. Introduction

Recently,polycrystalline diamond thin films are quite easily formed from the vapor phase on a variety of substrates by using several kinds of chemical vapor deposition (CVD) methods.[1-3] These films,however,contain some amonunts of graphitic components and hydrogen at the grain boundaries and/or crystal surfaces.[4] They may act as the reason for the degradation of the superior electronic and opto-electronic properties of diamond. To fabricate the elctronic- and optical- devices by using CVD diamond,it is required to grow the films with the high crystal perfection. Considering these requirements,it is significant to be able to grow diamond thin films epitaxially on foreign substrates.

Heteroepitaxial growth of diamond hss been reported on single crystal surfaces of cubic boron nitride(cBN), Ni, SiC and Si.[5-8] On single crystal or epitaxially grown Ni surfaces,it is quite difficult to form the epitaxial thin films(the growth of epitaxial islands has been confirmed), bacause the solubulity of carbon(diamond) into Ni is relatively high at the elevated substrate temperature. It is reported that the epitaxial nucleation of diamond can be successfully performed by impinging the positively charged particles (probably carbon ions) on substrate surfaces such as SiC(100) and Si(100). The growing films,however,show a textured structure with the tilt and/or twist of diamond island. This is a serious problem cosidering the application of diamond films to electronic devices.

On cBN surfaces,the epitaxial growth of diamond islands and the coalescence of the islands are observed and the epitaxial diamond films can be obtained as reported in the previous papers.[9-11] Now,cBN single crystal is the most promising candidate as a substrate for the fundamental investigation of heteroepitaxy of diamond.

In this paper,the initial growth process of epitaxial diamond thin films on (111) and (100) cBN surfaces will be described in details and the epitaxy and nucleation of diamond on foreign substrates will be discussed briefly.

2.Morphology of cBN single crystal

cBN single crystal synthesized under high pressure has been used as a substrate as shown in Fig.1. On (100) surface,the growth striations are observed by SEM alomg [110] direction. The crystal plane (111) located at the position parallel to the growth striation is correspond to (111) nitrogen plane and perpendicular one is to (111) boron plane. These are confirmed by using Rutherford back scattering method.[9] The (100) surface of cBN is not flat due to the growth striations, the (111)nitrogen is relatively flat and the(111)boron has pits and/or steps.

3. Growth of diamond on (111)boron surface

The initial growth processes of diamond on (111)boron surface are investigated and typical examples of the growth manner on the stepped and the flat surfaces are shown in Fig.2 (a) and (b)respectively.

In Fig.2(a),the step decoration of carbon layers (< 1nm) is observed at the quite early stage of deposition and this white bands grow wider forming a continuous carbon layer on the substrate surfaces. It can be also seen that diamond starts to grow slectively at the lower edge of the white bands. This side of the white bands correspond to the bunched step edges with the height of about 2 nm as measured by AFM.(Fig.3)

On the other hand,the formation of the continuous carbon layer can be seen on the flat region of the substrate as shown in Fig.2(b),and the growth of diamond islands is also observed. Observing the SEM photograph presicely(Fig.4 and Fig.2(a)),it is found that the numerous small and thin diamond islands are growing on the thin carbon layer with nearly the same contrast. The most of the small islands grow epitaxially without twinning and the smallest size of the islands resolved by high resolution SEM is about 5nm. It is considered that the carbon thin layer will play an important role for the nucleation of diamond on cBN (111) surfaces. The epitaxial islands grow laterally and the coalescences take place showing the various contrasts due to theformation of structural defects.(Fig.5)

On cBN(111)nitrogen surface,the formation of the thin carbon layer is not observed at the initial stage of deposition and epitaxial growth of diamond cannot be found under the various experimental conditions.

4. Growth of diamond on cBN(100)surface

On (100)suface,a complicated structure of the order of nm can be observed at the initial growth stage of diamond as shown in Fig.6. This structure was not observed on cBN(100) surface before deposition or after exposure to hydrogen plasma. By AES mesurements,it is found that this layer is the thin carbon layer which is similar to that observed on (111)boron surface. Continuing the deposition,the facetted diamond islands start to grow on the carbon layer and it is observed that the diamond islands show deformation relating to the small carbon particles in the carbon layer..

The growth process of epitaxial diamond thin film on (100) surface is shown in Fig.7. Fig.7(a) shows the small diamond islands and coalesced islands. The black and white stripes along [110]direction are due to the contrast by growth striations on cBN (100) surfaces. In (b),coalescence of the islands and the formation of (100) facets are observed. Finally, the continuous diamond thin film is formed as shown in(c).

5. Summary

Initial growth process of epitaxial diamond thin films has been investigated on single crystal cBN (111) and (100) surfaces. It is found that thin carbon layers start to grow on cBN(111)boron and (100) surfaces at the quite early growth stage. Continuing the deposition,the formation of epitaxial diamond islamds is observed selectively on thin carbon layers. These results suggest that a certain carbon rich state is formed on thin carbon layers and the nucleation of diamond takes place with the aids of hydrogen atoms. Although the structure of this layer is not determined yet, the thin carbon layer will have the structure close to diamond, and play the significant role for the nucleation of diamond from vapor phase. The structure determination of thin carbon layers and also the analysis of the nucleation process of diamond are now in progress by using STM and AFM.

Acknowledgment

This work is partly supported by a Grant-In-Aid for General Scientific Research No.04805003 from the Ministry of Education,Science and Culture.

References

1]S.Matsumoto,Y.Sato,M.Kamo and N.Setaka:Jpn.J.Appl.Phys.21 (1982)L183
2]M.Kamo,Y.Sato,S.Matsumoto and N.Setaka:J.Cryst.Growth 62 (1983)642
3]K.Suzuki,A.Sawabe and T.Inuzuka:Jpn.J.Appl.Phys.29 (1990) 153
4]Y.Sato and M.Kamo:Surf.and Coating Technol.39/40 (1989)183
5]S.Koizumi,T.Murakami,T.Inuzuka and K.Suzuki:Appl.Phys.Lett. 57 (1990)563
6]W.Zhu,P.C.Young and J.T.Glass:Äppl.Phys.Lett.63 1640(1993)
7]B.R.Stoner and J.T.Glass:Appl.Phys.Lett.60 (1992) 698
8]S.D.Wolter,B.R.Stoner,J.T.Glass,P.J.Ellis,D.S.Buhaenko, C.E.Jenkins and P.southworth:Appl.Phys.Lett.62(1993)1215
X.Jiang,K.Schiffman,A.Westphal and C.-P.Klages:Appl.Phys. Lett.63(1993) 1203
9]T.Inuzuka and S.Koizumi:Proc.SPIE 1325 (1990)1
10]T.Inuzuka,S.Koizumi and K.Suzuki:Diamond & Relat.Mater.1 (1992) 175
11]S.Koizumi and T.Inuzuka:Jpn.J.Appl.Phys.32 (1993)3920

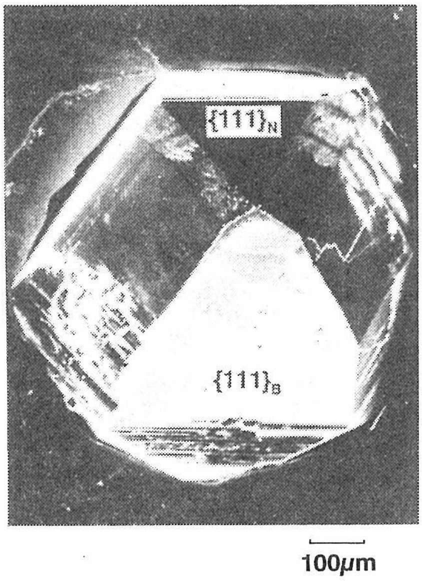

Fig.1 cBN single crystal after diamond deposition.

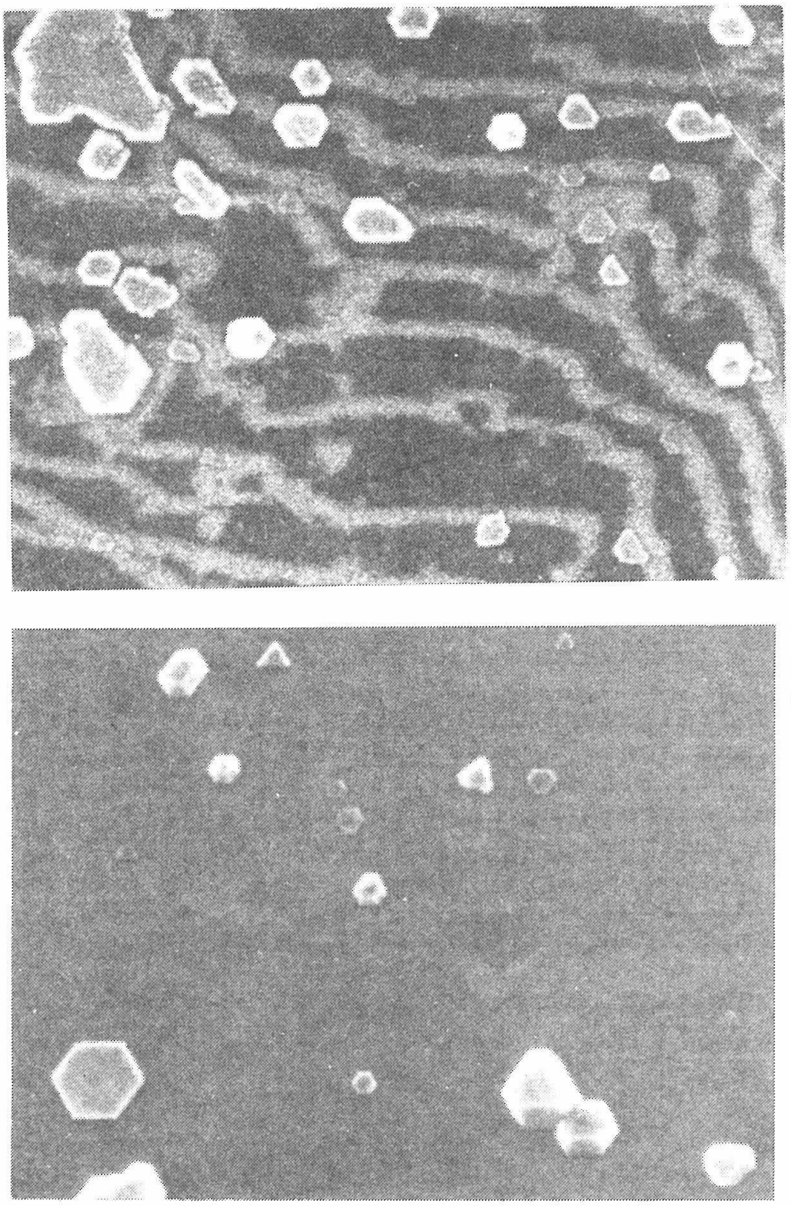

Fig.2 Early growth stage of diamond on cBN($1\bar{1}\bar{1}$), (a)step decoration of thin carbon layer,(b)thin carbon layer on flat substrate region.

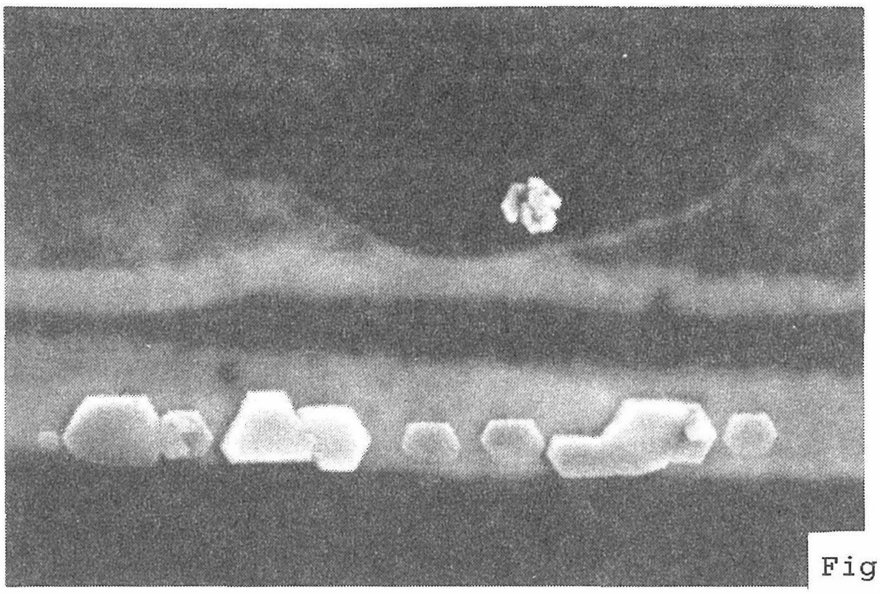

Fig.3 Growth of diamond islands on bunched step edge.

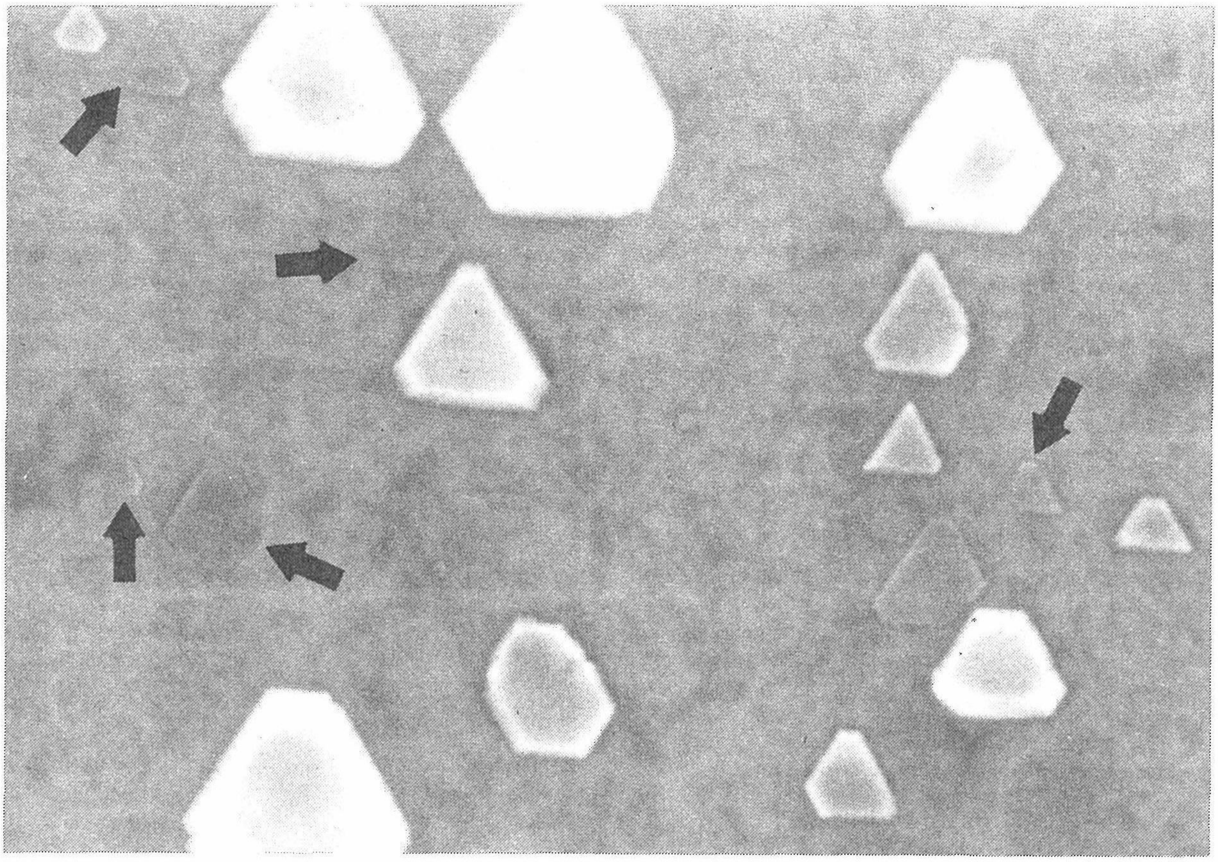

Fig.4 Small and thin diamond islands on/in thin carbon layer.

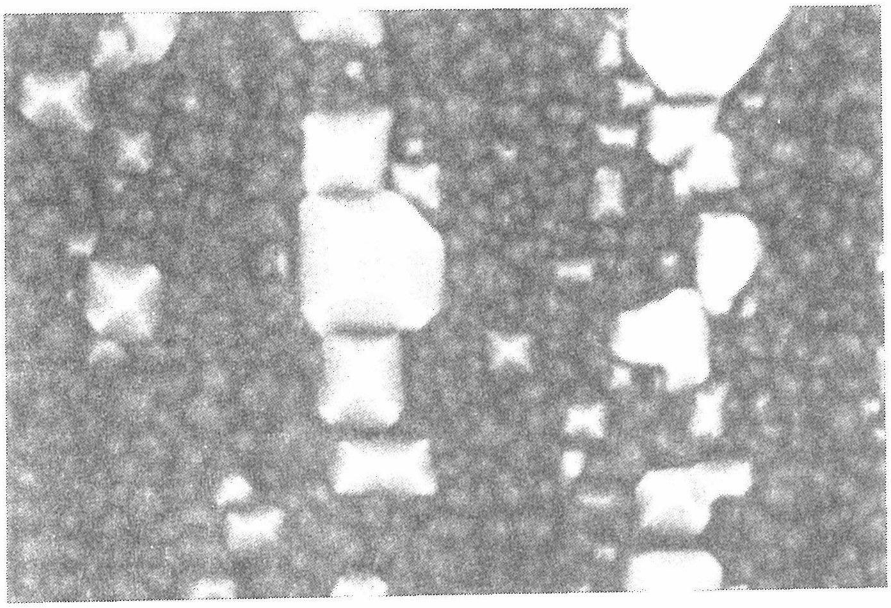

Fig.6 Initial growth stage of diamond on cBN(100).

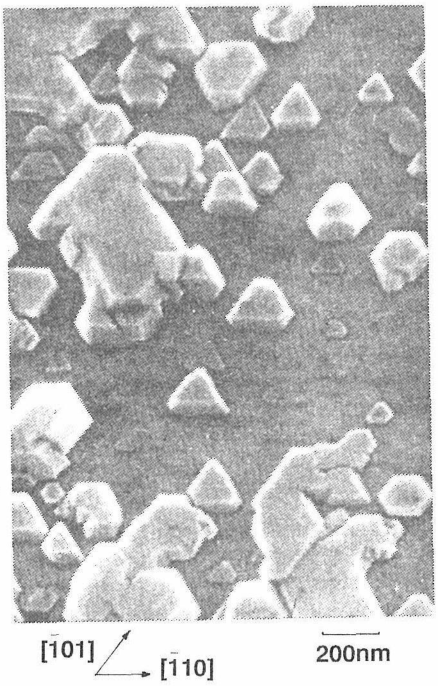

Fig.5 Coalescence stage of epitaxial diamond islands.

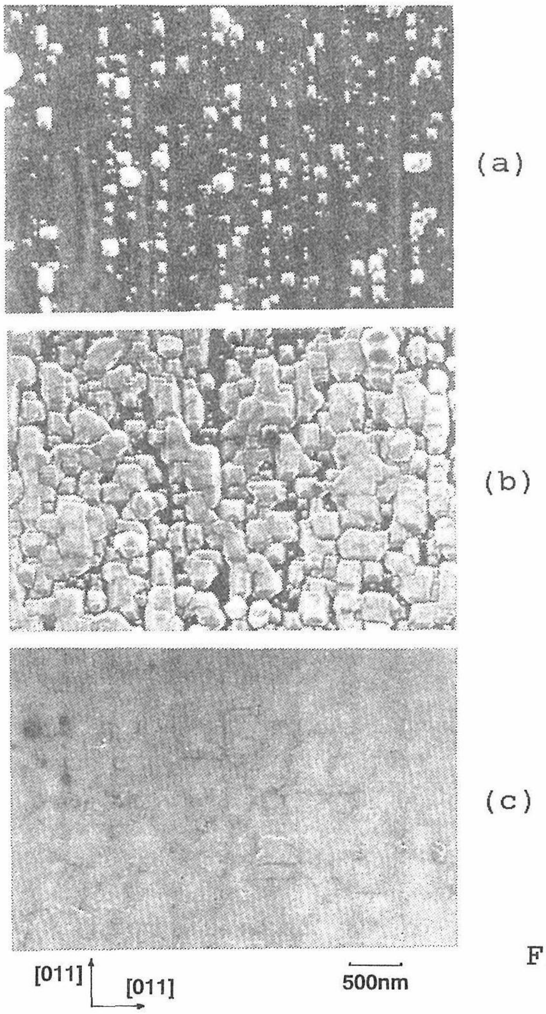

Fig.7 Growth process of epitaxial diamond thin films.

Growth and Electronic Properties of CVD Diamond

Jeffrey T. Glass,[+] Bradley A. Fox, Dean M. Malta and Brian R. Stoner,
Kobe Steel USA Inc., Electronic Materials Center, 79 Alexander Drive, 4401 Building
Research Triangle Park, NC 27709, U.S.A.
*Peichun Yang, Fimy R. Sivazlian and Wei Zhu**
Department of Materials Science and Engineering, North Carolina State University
Raleigh, NC 27695-7919, U.S.A.

Introduction

Diamond's exceptional properties have made it an excellent candidate for electronic devices for many years. Some early devices have been demonstrated using natural diamond while others have simply been speculated based on diamond's unique properties. Excellent reviews of this work and the potential devices are given in Ref. 1 and 2. Some applications of particular note include: radiation detectors; high temperature/high power diodes; and high temperature/high power transistors.

Unfortunately, these and many other applications will require high quality electronic grade diamond. Even natural stones with their impurity levels and defects are unlikely to yield sufficient properties, except in rare circumstances. In addition, the cost of this high quality diamond must be competitive with other emerging electronic materials. Thus, the only viable alternative for economic high quality diamond for many electronic applications is the development of heteroepitaxial thin films. Of course, the elimination of a primary defect hindering the electronic properties, grain boundaries, is only one of the developments necessary for diamond electronics. Looking farther into the future, the elimination of other defects such as dislocations, twins, stacking faults, and vacancies will also be necessary. However, the purpose of the present manuscript is to briefly review the status of progress towards heteroepitaxial growth and the observed improvement of the electronic properties.

The following section deals with highly oriented diamond films grown on silicon, which is by far the most advanced technology towards heteroepitaxial thin films. Complete films have been prepared, structural analysis has been underway and electronic properties have been measured. The subsequent section deals with a relatively new promising technology of diamond growth on nickel. Due to the much better lattice match between the nickel and the diamond, grain misorientation is expected to be significantly lower than that observed for diamond on silicon. However, the chemistry of such systems is much more difficult due to the tendency for graphitization on nickel. The process improves diamond particle quality and orientation on nickel, but has not yet allowed the development of complete films.

Diamond Growth on Silicon

Experimental

Highly oriented, (100) textured intrinsic diamond films have been grown in a microwave plasma chemical vapor deposition (MWCVD) reactor where the chamber was modified to allow *in situ* biasing.*[3]* Diamond growth occurred by a multistep process where bias-enhanced nucleation was used to grow heteroepitaxial diamond particles on (100) silicon substrates and the (100) texture was generated by control of the relative growth rates of each crystal direction according to the van der Drift texture evolution theory.*[4]*

To understand the potential benefits of heteroepitaxial nucleation and growth of highly oriented diamond films, the electronic properties of boron-doped diamond films grown on highly oriented (100) textured diamond films were compared to boron-doped diamond films grown on standard polycrystalline diamond films and on (100) type IIa natural diamond substrates. All three substrates were simultaneously deposited with a boron-doped diamond film to compare the role of the underlying substrate on the carrier concentration and the mobility. The electrical characterization was performed with temperature dependent resistivity and Hall effect measurements between 80 and 600K where all samples were vacuum annealed before characterization.

Results

The surface morphology of a highly oriented, (100) textured film grown on silicon is shown in Figure 1 where ~100% of the grains are oriented relative to the (100) silicon substrate. Additionally, the similar growth direction and rates for each grain produced a relatively smooth surface morphology.

[+] On leave from North Carolina State University

* Present address: AT&T Bell Labs, Murray Hill, NJ

Although a high degree of orientation between the (100) textured film and the (100) silicon substrate was observed, there was some degree of misorientation between the grains. The use of X-ray diffraction pole figures has been employed to quantify the misorientation of the individual diamond grains. The FWHM of the (220) peaks are typically 5-8°. The small FWHM indicated that the film had both small tilt about a <110> in the plane of the substrate and a small azimuthal rotation about the surface normal.

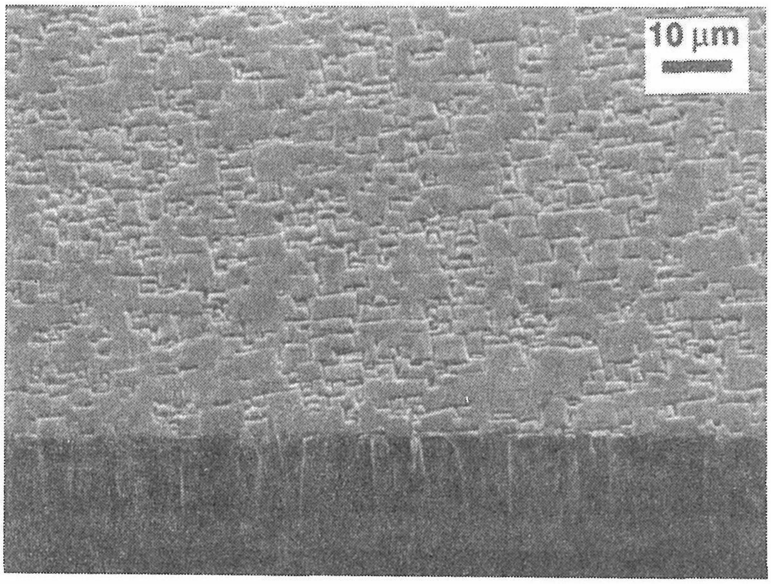

Figure 1: A SEM micrograph of a highly oriented (100) textured diamond film on a (100) silicon substrate.

A grain boundary between two highly oriented diamond grains imaged in a transmission electron microscope (TEM) is shown in Figure 2. The misorientation between the grains forms a network of parallel dislocations along the grain boundary. This dislocation structure is characteristic of a low angle grain boundary where an array of periodic dislocations forms to accommodate the misorientation. The dislocation spacing observed in Figure 2 was approximately 20 nm. An electron diffraction pattern of both grains was not able to detect the misorientation between these two grains and suggests a misorientation of less than 1°. Additional comparisons of the diffraction patterns between other adjacent grains determined misorientations less than 6° across the film.

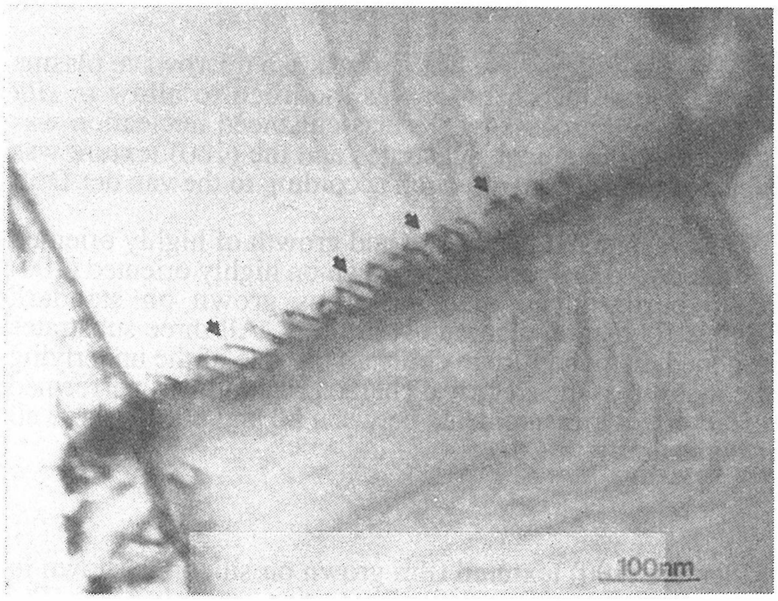

Figure 2: A TEM micrograph of a low angle grain boundary between two adjacent highly oriented grains.

The approximate thickness of the simultaneously deposited, boron-doped diamond film on a polycrystalline diamond film, a highly oriented (100) textured diamond film and a type IIa natural diamond substrate was 1.7µm. The carrier concentration as a function of temperature for each boron doped film was measured by the Hall effect and is shown in Figure 3a. Each sample exhibited two types of conduction mechanisms where a minima in the carrier concentration indicated the transition temperature between conduction mechanisms. At temperatures above the transition temperature, valence band conduction occurs where holes in the valence band are primarily responsible for charge transport. In this regime, the carrier concentration of the highly oriented film was similar to both the polycrystalline film and the monocrystalline homoepitaxial film. At temperatures below the transition temperature, the carrier concentration differed for each film. In this temperature regime, nonvalence band conduction dominated and has been discussed by other researchers.*[5,6]*

The corresponding mobility of the polycrystalline; highly oriented, (100) textured and homoepitaxial diamond films measured by the Hall effect are shown in Figure 3b. The room temperature mobility was 47.8 $cm^2/V\cdot s$, 135 $cm^2/V\cdot s$ and 427 $cm^2/V\cdot s$ for the polycrystalline, highly oriented (100) textured and the single crystal homoepitaxial diamond film, respectively. The mobility of the homoepitaxial film was always greater than the mobility of the highly oriented film which was always greater than the polycrystalline diamond film. At low temperatures, nonvalence band conduction dominated and the mobility was dramatically reduced for all three films.

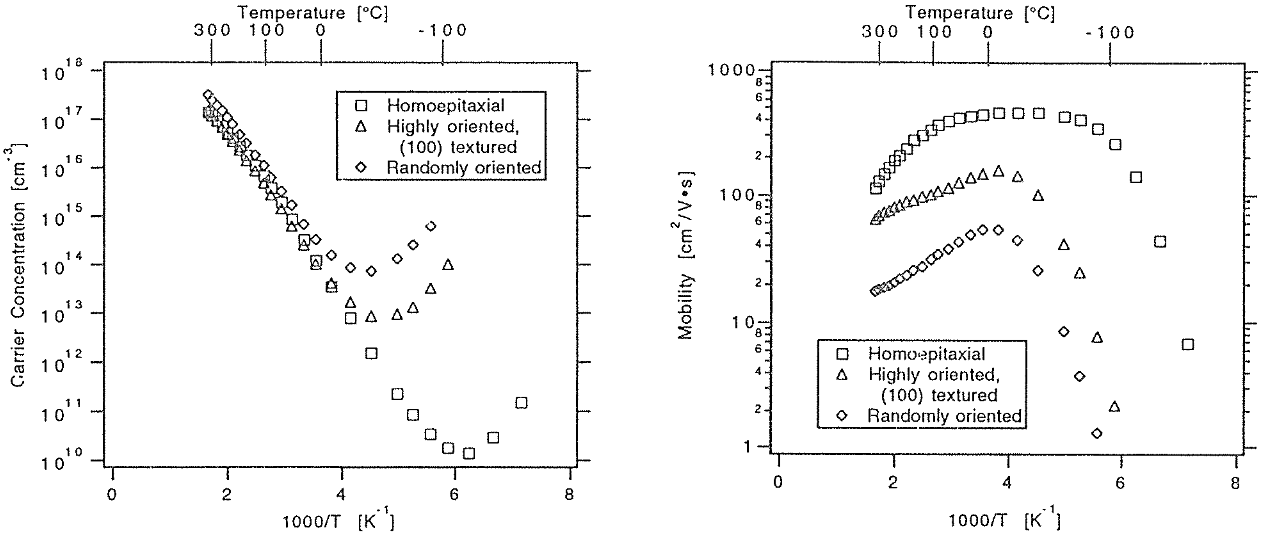

Figure 3: The a) carrier concentration and b) mobility of simultaneously deposited polycrystalline, highly oriented (100) textured and homoepitaxial diamond film.

Discussion

The mobility of the polycrystalline, highly oriented (100) textured and the homoepitaxial diamond film indicated a strong difference in hole transport with changes in the film morphology. However, the carrier concentration was relatively unaffected by the different morphology. This may be understood based on the grain boundary transport theories developed by Seto*[7]* and Baccarini*[8]* along with the observed grain boundary structure in Figure 2.

According to the grain boundary transport theory,*[7,8]* defects at the grain boundaries trap charge carriers and form a potential barrier at the grain boundary that impedes the motion of charge carriers. The trapping of charge carriers forms a depletion region around the grains where the fraction of the grain that is depleted of charge carriers depends on the grain size, the trap density and the dopant concentration in the grain. Since grain boundaries consist of dislocation networks, it is likely that dislocations are one source of traps at the grain boundary.

The difference in mobility of the polycrystalline and highly oriented diamond film suggests that there was a difference in the height of the potential barrier between grains for these films. The ratio of the polycrystalline mobility to the homoepitaxial mobility at elevated temperature was used to estimate the barrier height and trap density formed at the grain boundary.*[9]* For the randomly oriented polycrystalline diamond film, the barrier height was ~0.09 eV and the trap density was estimated to be 3.4×10^{12} cm^{-2}. The slightly lower carrier concentration of the highly oriented (100) textured film suggests an uncompensated acceptor concentration of $\sim 2 \times 10^{18}$ cm^{-3}; therefore, for a barrier height of ~0.07 eV, the trap density was 1.9×10^{12} cm^{-2}. The barrier height in the highly oriented (100) textured diamond film was ~20 meV less and the trap density was ~50% less than the corresponding values in the polycrystalline film. These calculations suggest the reduction in traps through low angle grain boundaries may account for the mobility improvement in highly oriented (100) textured films.

The grain boundary structure of a highly oriented film may be used to explain a possible source of reduction in traps of the highly oriented film. The reduction in traps can probably be attributed to the reduced dislocation density at low angle grain boundaries. A typical grain boundary consists of a dense network of dislocations that often cannot be resolved by TEM. For low angle grain boundaries, the dislocation density is proportional to the misorientation angle; therefore, lower angle grain boundaries generate fewer dislocations and wider dislocation spacings. The low angle grain boundary of the highly oriented film in Figure 2 exhibited a resolvable network of dislocations with a spacing of 20 nm. Since dislocations are the likely source of traps, the reduction in dislocation density at the grain boundaries of the highly oriented diamond film is the most likely cause for the reduction in the grain boundary traps and the substantial improvement in carrier mobility. Although this study quantified the improvement in the electronic behavior of highly oriented diamond films, it is likely that other properties may also be improved through heteroepitaxial nucleation and highly oriented diamond film growth.

Diamond Growth on Nickel

Experimental

The heteroepitaxy of diamond on Ni by chemical vapor deposition (CVD) has been the subject of intensive research both experimentally and theoretically*[10-19]*. Sato and co-workers have reported oriented diamond nuclei formed on both (100) and (111) Ni surfaces by microwave plasma CVD*[20,21]*. The present authors have also demonstrated recently the oriented nucleation and growth of diamond on Ni by multi-step hot filament CVD*[22-24]*. The process involves seeding the Ni surface with carbon, followed by high temperature annealing in atomic hydrogen. Diamond subsequently nucleates on such a seeded and annealed Ni surface with the same orientation as the underlying substrate, while the formation of graphite is inhibited. Diamond and non-diamond carbon powders were used as seeds on the Ni substrates prior to the annealing and growth. In addition, gaseous carbon in hydrogen was also used to generate a "seeded surface" by saturating the Ni at high substrate temperature prior to the growth.

A schematic of the thermal treatment is shown in Figure 4. The annealing time t_2, varied depending on the degree and type of seeding and the exact surface temperature. It is believed that the anneal must be held long enough to allow for sufficient reactions between the nickel, seeded carbon, and hydrogen to form Ni-C-H intermediate states which suppress graphite formation and promote diamond nucleation. On the other hand, the seeded substrates must not be over annealed because the diamond seeds will then completely dissolve and diffuse into the bulk of the Ni lattice with no effective nucleation centers left on the surface. After annealing, the temperature was lowered to 900°C for normal diamond nucleation and growth at a pressure of 20 Torr and a total gas flow rate of 800 sccm. The methane concentration in hydrogen was varied depending on the preferred orientation of the final film. For the (100) orientation, the methane concentration was set at 0.5% in H_2, and for the (111) orientation, the methane concentration was controlled at 0.3% in H_2.

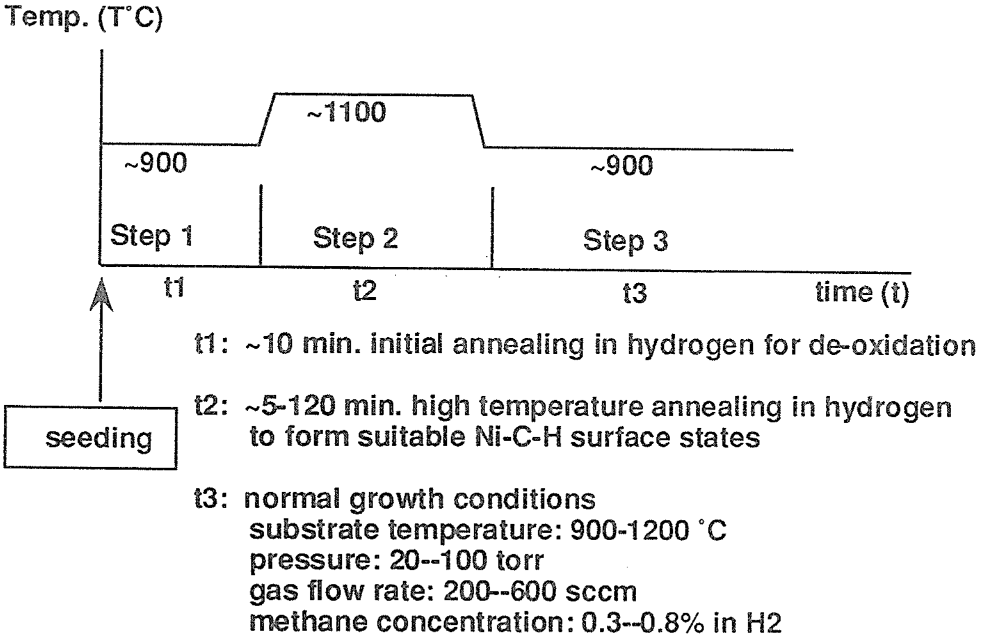

Figure 4: Schematic of the thermal treatment utilized for diamond deposition on nickel.

Results and Discussion

Figures 5 and 6 are scanning electron micrographs of diamond grown on Ni surfaces seeded with diamond powders prior to the thermal treatment. Both (100) and (111) oriented films could be grown under the above experimental conditions. It can be seen that in many areas, individual nuclei were grown together, where the grain boundaries are no longer discernible. This was encouraging because it indicated that there was very little misorientation among the neighboring nuclei. If the percentage of such oriented nuclei can be further increased and suitable growth conditions can be found to foster the selective growth of the preferred orientations, it appears that a complete single crystal film will develop with essentially no grain boundaries present, which is highly desirable for electronics devices applications. Currently, consistent orientations of about 85% of the diamond nuclei can be realized in an area of about 5×5 mm^2. The Raman spectra confirmed that the oriented diamond films possessed high structural quality, as evidenced by a strong diamond peak at 1330 cm^{-1} relative to the graphite peak at 1580 cm^{-1}.

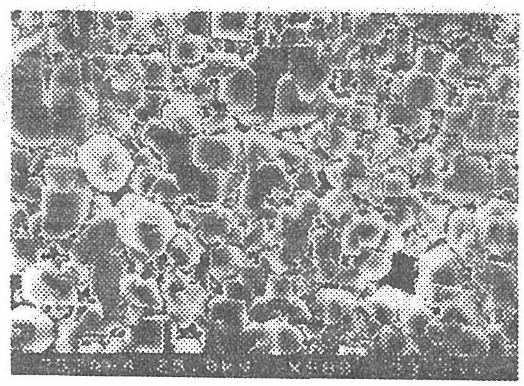

Figure 5: Scanning electron micrograph of diamond grown on (100) nickel surface seeded with diamond powder.

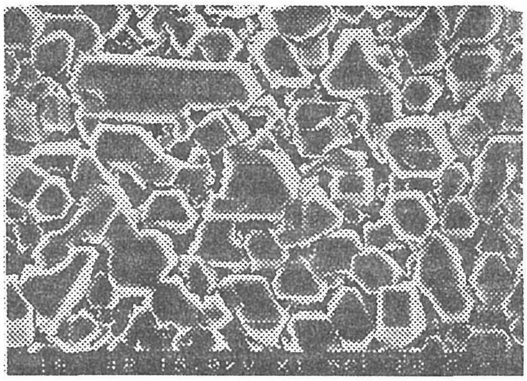

Figure 6: Scanning Electron micrograph of diamond grown on (111) nickel surface seeded with diamond powder.

The detailed chemical mechanisms responsible for the nucleation and growth of oriented diamond films are still not fully understood. It appears clear from the deposition experiments that graphite formation could be suppressed by forming either a nickel hydride or a nickel-carbon-hydrogen intermediate state through the annealing process. However, effective diamond nucleation required that the Ni surface was saturated with carbon. It has been postulated in the literature that the formation of Ni-C intermediate states in which carbon atoms are in a tetrahedral bonding configuration precedes the diamond crystallization from the Ni-C solvent media both under HPHT conditions*[11]* and in an atmospheric recrystallization process*[15]*. It was believed that similar intermediate states consisting of nickel, carbon, and hydrogen were formed in the CVD process which were responsible for the nucleation of diamond, not graphite, on the Ni surfaces. However, the exact nature of these intermediate states (structure and composition) is unknown at present.

In summary, the successful nucleation and growth of oriented diamond films on Ni substrates has been realized by a novel HFCVD process involving seeding, annealing, nucleation, and growth. It was found that heavy seeding followed by annealing resulted in high densities of both (100) and (111) oriented diamond nuclei on single crystal Ni surfaces which could subsequently grow together, where the grain boundaries are no longer discernible. With a better understanding of the fundamental mechanisms involved, complete, oriented diamond films on Ni substrates for electronics devices applications appear viable.

Acknowledgments:

The North Carolina State University authors wish to acknowledge partial financial support from the National Science Foundation through the Presidential Young Investigator Award and the Kobe Steel, Ltd. professorship at NCSU. The measurements of Raman spectra by A. T. Sowers and Professor R. J. Nemanich are greatly appreciated.

References:

1. I. M. Buckley-Golder and A. T. Collins, Dia. Rel. Mat. **1**, (1992)1083.
2. M. Seal, Dia. Rel. Mat. **1**, (1992)1075.
3. B. R. Stoner, C.-T. Kao, D. M. Malta, and R. C. Glass, Appl. Phys. Lett. **62**, (1993) 2347.
4. A. van der Drift, Philips Res. Rep. **22**, (1967) 267.
5. A. W. S.Williams, E. C. Lightowlers and A. T. Collins, J Phys. C: Solid St. Phys., **3**, (1970) 1727.
6. E. P. Visser, G. J. Bauhuis, G. Janssen, W. Vollenberg, W. J. P. van Enckevort and L. J. Giling, J. Phys.: Condens. Matter **4**, (1992) 7365.
7. J. Y.W. Seto, J. Appl. Phys., 46 (1975) 5247.
8. G. Baccarani, B. Ricco and G. Spadini, J. Appl. Phys. **49**, (1978) 5565.
9. B. A. Fox, B. R. Stoner, D. M. Malta, P. J. Ellis, R. C. Glass and F. R. Sivazlian, Dia. Rel. Mat., (in press)
10. R. H. Wentorf, Jr., Adv. Chem. Phys. **9**, 365 (1965).
11. J. C. Shelton, H. R. Patil, and J. M. Blakely, Surf. Sci **43**, 493 (1974).
12. J. F. Mojica and L. L. Levenson, Surf. Sci. **59**, 447 (1976).
13. M. Eizenberg and J. M. Blakely, Surf. Sci. **82**, 228 (1979).
14. K. A. Cherian, Sur. Coat. Technol. **47**, 127 (1991).
15. H. M. Strong, Acta Metallurgica **12**, 1411 (1964).
16. A. R. Badzian and T. Badzian, in *Materials Research Society Symposium Proceedings on Chemical Vapor Deposition of Refractory Metals and Ceramics*, edited by T. M. Besmann, B. M. Gallois, and J. Warren (Materials Research Society, Pittsburgh, PA, 1992), **250**, p.339.
17. V. I. Klykov and N. N. Sheftal, J. Cryst. Growth **52**, 687 (1981).
18. V. I. Klykov, N. N. Sheftal, and E. Hartmann, Acta Phys. Acad. Sci. Hung. **47**, 167 (1979).
19. H. I. Smith, M. W. Geis, C. V. Thompson, and H. A. Atwater, J. Cryst. Growth **63**, 527 (1983).
20. Y. Sato, I. Yashima, H. Fujita, T. Ando, and M. Kamo, in *New Diamond Science & Technology*, edited by R. Messier, J. T. Glass, J. E. Butler, and R. Roy (Mater. Res. Soc. Symp. Proc. **250**, Pittsburgh, PA 1992), p. 339.
21. H. Fujita, T. Ando, M. Kamo, T. Tanaka, and Y. Sato, in *Proc. 1991 Spring Jpn. Appl. Phys. Meeting,* edited by Jpn. Phys. Soc. (Tokyo, Japan, 1991), p. 13.
22. W. Zhu, P. C. Yang, and J. T. Glass, Appl. Phys. Lett. **63** (12), (1993), p. 1640-1642.
23. P. C. Yang, W. Zhu, and J. T. Glass, J. Mater. Res., **8** (8), (1993), p.1773-1776.
24. P. C. Yang, W. Zhu, and J. T. Glass, J. Mater. Res., **9** (5), (1994), in press.

Structure and Morphology of Oriented Diamond Films

Peter Koidl, Christof Wild and Nikolaus Herres
Fraunhofer-Institut für Angewandte Festkörperphysik
Tullastrasse 72, D-79108 Freiburg, Germany

Abstract

Fibre textured als well as heteroepitaxially textured diamond films have been grown by microwave plasma assisted CVD on silicon substrates. The texture axis is determined by the growth parameter $\alpha = \sqrt{3}\, V_{100}/V_{111}$, which in turn depends on the growth temperature and the gas composition. The overgrowth of heteroepitaxially oriented nuclei also depends on α. Growth under $\alpha \approx 3$ improves the orientation of heteroepitaxially textured films on {100} substrates, whereas much smaller α leads to a complete loss of the epitaxial orientation. It is shown that twinning causes this instability. The twin formation for various α values has been modelled giving full explanation of the observed growth morphologies.

1. Introduction

There has been considerable progress over the last decade in the low pressure deposition of diamond. An important achievement has been the development of oriented growth on non-diamond substrates. Two types of structural orientation may be considered. i) Fibre textured films have been demonstrated with various directions of the fibre axis [1,2]. Of special importance are <100> fibre textures, where a flat surface consisting of almost coplanar {100} facets can be achieved. ii) More recently, heteroepitaxial nucleation on easily available single crystalline substrates has been demonstrated leading to polycrystalline diamond films with preferential grain alignment both in normal and azimuthal direction [3,4].

In the present paper we consider both types of oriented diamond films as shown in Fig. 1. Their structural properties will be discussed. It will be shown that twinning has a pronounced influence on structure and morphology. This motivated us to perform growth simulations. Modelling of twin formation is shown to explain the observed growth features.

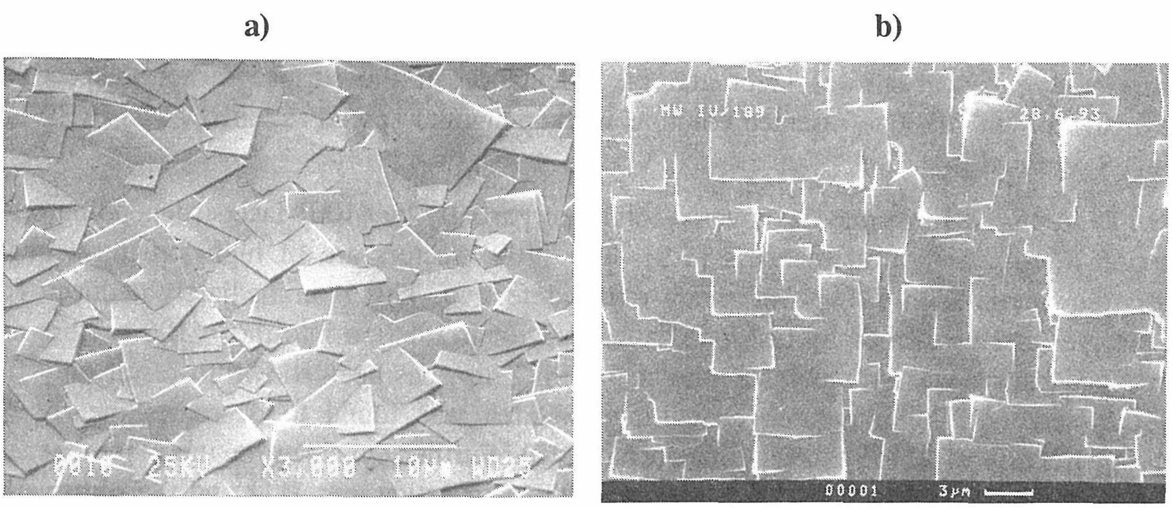

Fig. 1. a) 100 fibre textured diamond films with coplanar {100} surface facets
b) epitaxially oriented diamond film grown on {100} silicon

2. Experimental

The diamond films were prepared by microwave plasma assisted CVD from CH_4/H_2 gas mixtures. A NIRIM-type tubular reactor with a 40 mm diam. quartz tube was used for deposition. An optical two-colour pyrometer was utilized to measure and control the deposition temperature. In situ laser interferometry was used to monitor film nucleation and growth [5].

The heteroepitaxial nucleation was achieved by bias-enhanced CVD. A positively biased counter-electrode was introduced into the plasma and the substrate was connected to ground. Most of the nucleation and growth experiments were performed at 50 mbar pressure.

For random nucleation and growth of textured diamond films, silicon substrates dry-polished with diamond powder were used. The heteroepitaxial nucleation was performed on untreated {100} Si substrates.

3. Fibre-textured growth

The growth of polycrystalline diamond from randomly oriented nuclei generally results in a thickness dependent structure. Once the thickness is larger than the average seed to seed distance, a preferential grain orientation (texture) develops as a result of growth competition between differently oriented grains [6]. Columnar grain structures with the column axis parallel to the fastest growth direction, i.e. fibre textures, are common. The direction of fastest growth is determined by the (idiomorphic) equilibrium shape of individual diamond crystallites which depends on a growth parameter $\alpha = \sqrt{3}\, V_{100}/V_{111}$, i.e. essentially the ratio of growth rates on {100} and {111} faces [5]. The fastest growing direction and thus the direction of the fibre axis is given by [7]:

$$\begin{array}{ll} <1, 3/\alpha\text{-}2, 1> & \text{for } 1 \leq \alpha \leq 1.5 \\ <1, 0, 3/\alpha\text{-}1> & \text{for } 1.5 \leq \alpha \leq 3. \end{array}$$

A variety of fibre textures has been reported, including <100>, <110> and (less frequently) <111> fibre textures [1,2]. Generally, textured growth results in rough surfaces, however, for the <100> fibre texture, the film surface may consist of almost coplanar {100} facets resulting in a smooth surface as shown in Fig. 1a.

The film structure and surface morphology of textured diamond films has been characterized using X-ray diffraction, fast ion channelling, and angle resolved optical reflection [5]. These techniques give information on the crystal orientation averaged over the film thickness, the structure within a near-surface layer and the orientation of the surface facets, respectively. Fibre textures with <100> oriented columns with an angular spread as narrow as 1° (FWHM) have been reported [5].

<100> textured films may be covered totally or partially by {100} facets depending on the nucleation density and film thickness [5,9]. The {100} sectors are of high structural quality whereas the surrounding {111} sectors are rather defective. This is immediately deduced from SEM pictures and confirmed by fast ion channelling for irradiation into the <100> fibre axis. The reduced backscattering yield, i.e. the channelling dip, has been shown to result only from the {100} sectors. The integrated chanelling dip area was found to decrease linearly with increasing fraction of {111} facets at the surface [10]. Further evidence for the inhomogeneous defect distribution was given by high resolution TEM investigations [11] and the observation, that {100} sectors in <100> textured films are much more etch resistant than the surrounding material [12].

It has been shown that the texture formation and the direction of the fibre axis depends on the deposition conditions. Fig. 2 shows the dependence of the film texture and morphology on the methane concentration and deposition temperature. Three different growth regimes can be distinguished in Fig. 2. At low methane concentrations and increased temperatures, the films exhibit pronounced <110> textures. The surface consists of {111} facets, inclined with respect to the surface normal by 35.5°. At medium methane concentrations and medium deposition temperatures a transition of the fibre axis from <110> to <100> occurs, corresponding to a change in α from 1.5 to 3. The further increase of the methane concentration or decrease in temperature leads to a sudden deterioration of the film morphology. The films prepared under the latter conditions are fine-grained with surfaces showing hardly any crystalline facets. Thus the $\alpha=3$ line demarcates the sudden transition from sharply <100> textured films to a disordered fine grained material, most probably due to the disappearance of {100} sectors for $\alpha \geq 3$. The various directions of the fibre axis in Fig. 2 have been determined by X-ray diffraction. The α values were deduced from the above relations. The tilt angle τ_{100} indicates the average angle between the sample normal and the <100> directions of the crystallites.

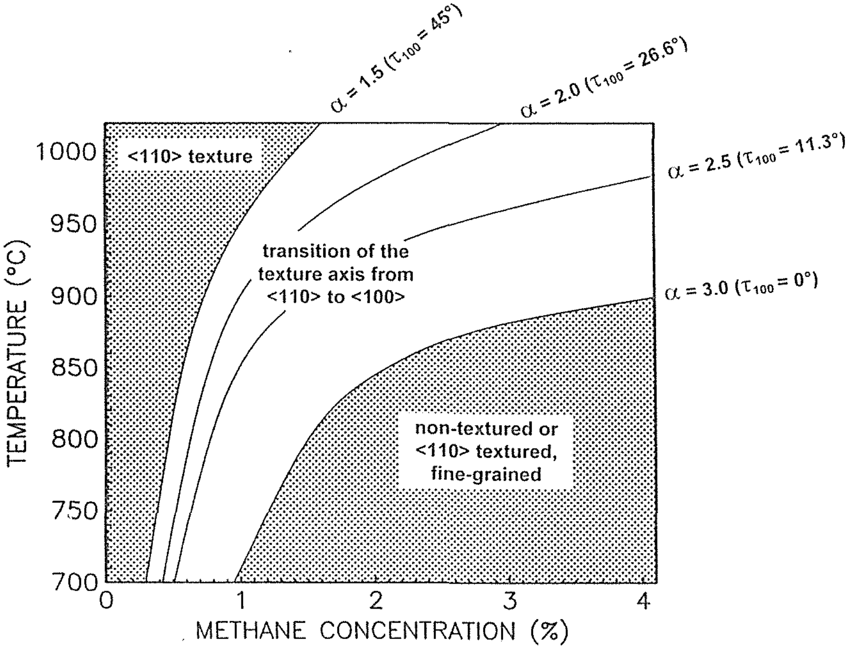

Fig. 2. Dependence of film texture on methane concentration and deposition temperature; the α values have been deduced from the direction of the fibre axis

Apart from the methane concentration and temperature other growth parameters may be considered. The addition of oxygen has been shown to shift the quantitative relationship given in Fig. 2, but qualitatively, very similar structural changes are observed when the carbon content in the process gas and the deposition temperature are varied [7]. Even minor gas contaminations, e.g. boron, are able to change the film structure and morphology. This suggests that those impurities - probably due to their facet-dependent incorporation rate - change the relative growth rate on {100} and {111} faces.

4. Heteroepitaxial nucleation and overgrowth

Recently, bias assisted microwave plasma CVD has been applied to grow diamond films via oriented nucleation on ß-SiC and Si [3,4]. In contrast to the fibre textured films discussed above, these films show a preferential *azimuthal* orientation of the crystallites relative to the substrate orientation. We have grown those "heteroepitaxial" films on {100} Si substrates and characterized their morphology and structure by SEM and X-ray diffraction. Fig. 1b shows an oriented diamond film deposited on Si by bias-assisted microwave plasma CVD. A nucleation layer was first deposited from 4% CH_4 diluted in H_2 at a negative substrate bias of 350 V. Subsequent growth took place under our standard conditions for diamond CVD (1.5 % CH_4, no bias).

A comparison of the X-ray pole figures for a fibre-textured and "heteroepitaxially" aligned film is shown in Fig. 3. The columnar alignment with rotational symmetry of the grain orientation in the fibre textured film becomes evident in contrast to the normal *and* azimuthal preferential alignment of the sample grown from oriented seeds. There is however a considerable degree of residual misorientation in the latter film with a spread of the grain orientation in both normal and azimuthal direction of approximately 7-12 degrees [13].

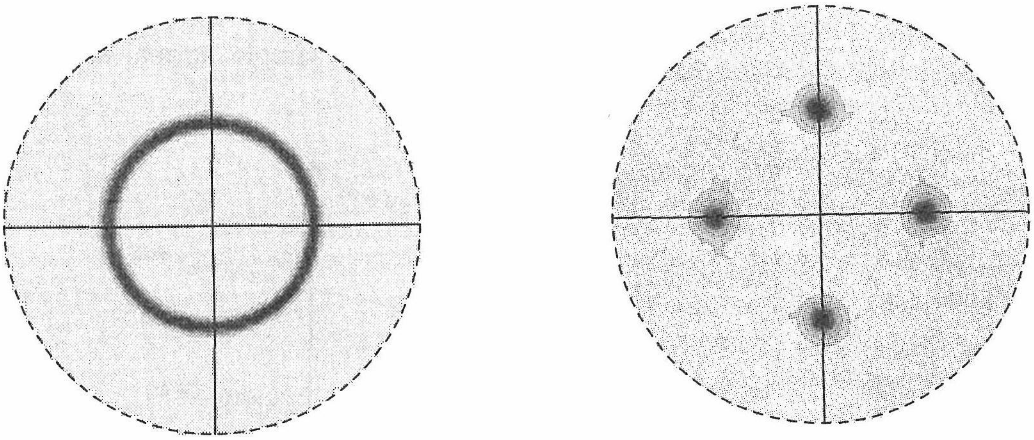

Fig. 3. X-ray pole figures of the 220 reflection for a fibre textured diamond film (left) and a heteroepitaxially textured diamond films grown on {100} silicon (right)

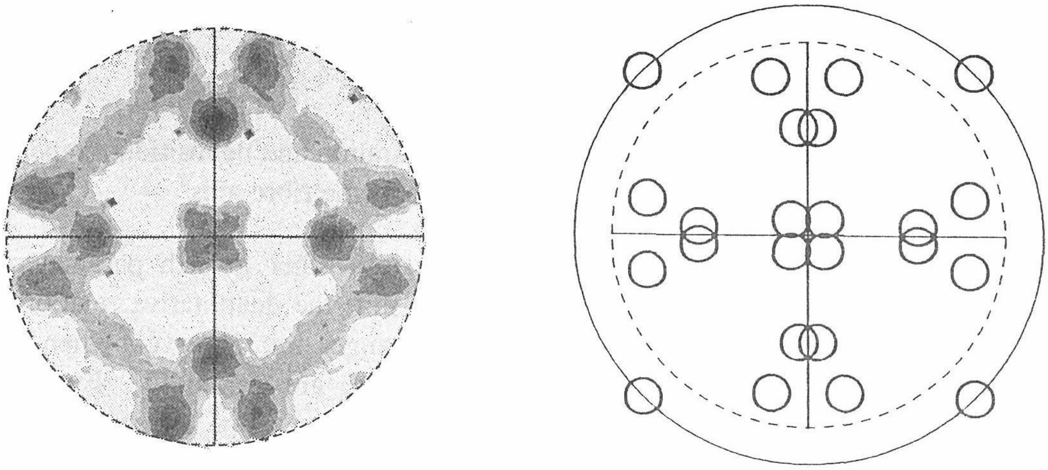

Fig 4. 220 pole figure of an oriented diamond film grown on epitaxially oriented nuclei under $\alpha \approx 1.5$ conditions (left) and theoretical positions of the pole density maxima for first order twins (right)

The orientational spread relative to the growth direction may be reduced by overgrowing under conditions favourable for the development of a <100> texture, i.e. $\alpha=3$. If however overgrowth is performed under conditions leading to much lower α values, the <100> heteroepitaxial texture is destabilized. It has been shown that twinning (first order and higher order) occurs such that the resulting crystals are oriented with their fastest growing direction closer to the substrate normal [7]. As an example Fig. 4 shows the X-ray pole figure of the 220 reflection of a film grown under $\alpha\approx1.5$ conditions on heteroepitaxially oriented nuclei deposited on {100} silicon. The pole figure can be explained by first order twins relative to the epitaxial orientation. An extra 6° rotation of the <110> direction towards the substrate normal had to be assumed to fit the data. This tilt of 6° is within the angular spread of the original seed orientations and may result from growth competition effects which favour crystals with <110> directions closer to the substrate normal.

5. Twin formation

It has been shown that twin formation may drastically influence the structure and morphology of epitaxially textured diamond films. It appears further that twinning is one mechanism leading to the deterioration of the {111} growth sectors for α close to or above 3 as shown for <100> fibre textured films. A better understanding of twin formation is therefore required.

Wild et al. recently have modelled the growth behaviour of twinned crystals [7]. The calculations assumed a cubo-octahedral crystal with a small twin attached to one of the primary faces. The temporal evolution of the shape of this bicrystal was calculated for different α values. Three types of twins had to be distinguished: twins on {100} faces, twins on {111} faces with the twin plane parallel to this face, and twins on {111} faces with an inclined twin plane. These twin types will be called $T_{\{100\}}$, $T_{\{111\},p}$, and $T_{\{111\},i}$, respectively. Fig. 5 shows the result of growth simulations for the above three twin types and α values from 1 to 3.

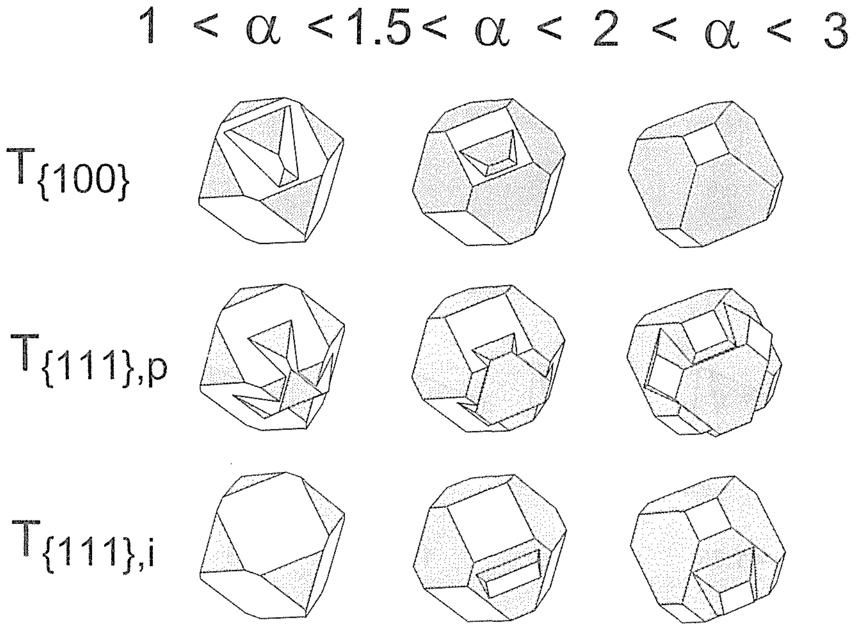

Fig. 5. Results of numeric growth simulations for different twin configurations (indicated on the left) and α values from 1 to 1.5, 1.5 to 2 and 2 to 3 (indicated on top)

The simulations indicate that: i) $T_{\{100\}}$ twins disappear for $\alpha>2$; for $\alpha<2$ these twins increase in size and cover part of the $\{100\}$ facet. ii) $T_{\{111\},p}$ twins propagate at first laterally. If restricted to the primary $\{111\}$ face, they do not lead to a significant increase of the surface roughness. However, for $\alpha>2$ they can reach the adjacent $\{111\}$ facet and for $\alpha<2$ the adjacent $\{100\}$ facets. On these adjacent facets the $T_{\{111\},p}$ twin propagates as $T_{\{111\},i}$ or $T_{\{100\}}$ twin, respectively. iii) $T_{\{111\},i}$ twins vanish for $\alpha<1.5$; they grow larger and cover part of the $\{111\}$ facet if $\alpha>1.5$.

These simulations predict the stability of particular crystal faces against twinning. A facet may be regarded stable if an infinitesimally small twin attached to it disappears. It is unstable if the twin grows larger. Fig. 5 shows that $\{100\}$ faces are stable against twinning for $\alpha>2$ and that $\{111\}$ facets are stable against $T_{\{111\},i}$ twin formation for $\alpha<1.5$. $T_{\{111\},p}$ twins grow larger for any α; however, for $\alpha<1.5$ they do not affect any neighbouring $\{111\}$ facets. The computer simulations thus predict that $\{111\}$ facets remain smooth for $\alpha<1.5$ and $\{100\}$ facets remain smooth for $\alpha>2$.

It has been shown that α is an important parameter determining the structure and morphology of both fibre textured and heteroepitaxially textured diamond films and the effect of twinning. An independent determination of α would thus be highly desireable. The shape of twins turns out to indicate the prevailing α value. To demonstrate this relation, we have grown a homoepitaxial film on a $\{100\}$ diamond substrate under conditions favouring $\alpha=1.5$ according to Fig. 2. The resulting film shows many growth steps and isolated $T_{\{100\}}$ twins, as shown in Fig. 6. A comparison of the twin shape with the model calculations (Fig. 6) in fact confirmes that α is very close to 1.5.

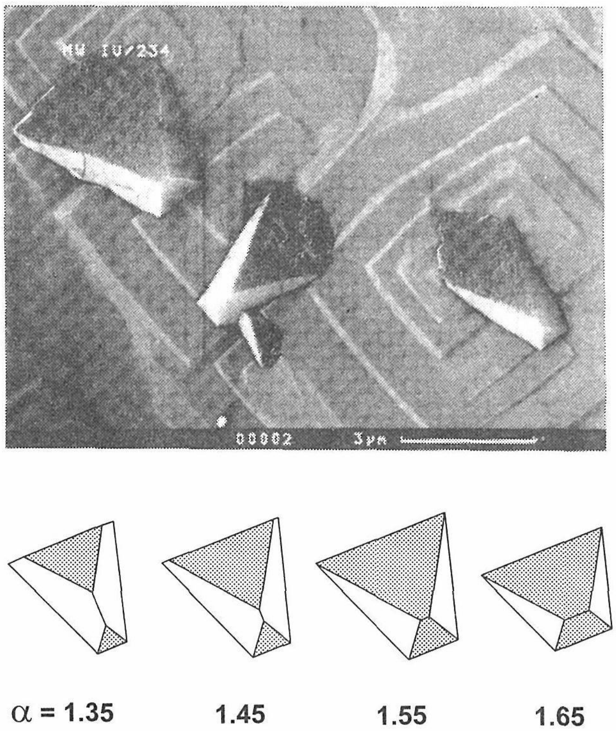

Fig. 6. SEM micrograph of twins formed during homoepitaxial growth on $\{100\}$ diamond under $\alpha\approx1.5$ conditions (top) and theoretical shape of $T_{\{100\}}$ twins for α around 1.5 (bottom)

6. Conclusion

It has been shown that the structure and morphology of CVD diamond films is largely determined by the ratio of growth rates on {100} and {111} faces, described by the growth parameter $\alpha = \sqrt{3}\, V_{100}/V_{111}$. The preferential orientation of fibre textured films is described by α and empirical relations between α and the growth conditions have been deduced from the analysis of differently textured films. Also the twin formation depends strongly on α, as predicted by numerical simulations. The evaluation of twin shapes provides an independent method to determine α and confirmes the underlying model concept. Finally, it has been shown that growth of heteroepitaxially textured diamond films also depends on α. The structural alignment may be improved by growing under appropriate α values, whereas inadequate α values promote twin growth which results in a degradation of the preferential epitaxial grain orientation.

7. Acknowledgments

We would like to acknowledge valuable contributions of R. Dian, R. Kohl, R. Locher and W. Müller-Sebert.

8. References

1. C. Wild, P. Koidl, N. Herres, W. Müller-Sebert and T. Eckermann: Electrochem. Soc. Proc., Vol. 91-8 (1991) 224.
2. R.E. Clausing, L. Heatherly, L.H. Horton, E.D. Specht, G.M. Begun and Z.L. Wang: Diamond and Related Mat. 1 (1992) 411.
3. B.R. Stoner and J.T. Glass: Appl. Phys. Lett. 60 (1992) 698.
4. X. Jiang and C.P. Klages: Diamond and Related Mat. 2 (1993) 1112
5. C. Wild, P. Koidl, W. Müller-Sebert, H. Walcher, R. Kohl, N. Herres, R. Locher, R. Samlenski and R. Brenn: Diamond and Related Mat. 2 (1993) 158
6. A. Van der Drift: Philips Res. Rep. 22 (1967) 267.
7. C. Wild, R. Kohl, N. Herres, W. Müller-Sebert and P. Koidl: in *Proc. Diamond 1993, Albufeira*; Diamond and Related Mat., *in print*
8. C. Wild, N. Herres and P. Koidl: J. Appl. Phys. 68 (1990) 973.
9. P. Koidl, C. Wild, R. Locher and R. Kohl: in *Proc. 2nd Intern. Conf. on the Applications of Diamond Films and Related Materials*, MYU Tokyo, 1933, p. 87
10. R. Samlenski, G. Flemig, R. Brenn, C. Wild, W. Müller-Sebert and P. Koidl: in *Proc. Diamond 1993, Albufeira*; Diamond and Related Mat., *in print*
11. Z.L. Wang, J. Bently, R.E. Clausing, L. Heatherly and L.L. Horton: Materials Science Monographs (Elsevier) Vol. 73 (1991) 489
12. Y. Sato and M. Kamo: in J.E. Field (ed.), *The Properties of Natural and Synthetic Diamond*, Academic Press, London, 1992, p. 423
13. R. Kohl, C. Wild, N. Herres, P. Koidl, B.R. Stoner and J.T. Glass: Appl. Phys. Lett. 63 (1993) 1792

Crystal Growth of Diamond and Nickel Carbide in the Ni-C-H System

Andrzej Badzian and Teresa Badzian
Materials Research Laboratory, The Pennsylvania State University, University Park, PA 16802, U.S.A.

ABSTRACT

The growth of diamond and nickel carbide was studied using microwave plasma chemical vapor deposition. The microwave hydrogen plasma contains a large concentration of atomic hydrogen, which alters the phase equilibria in the Ni-C-H system and actively participates in the growth process which helps the formation of organometallic molecules. These molecules take part in transport of Ni from Ni metal onto the graphite. Non-stochiometric nickel carbide possessing NaCl-type structure was obtained by this process. Diamond nucleation on graphite proceeds through an intermediary phase of hydrogenated nickel carbide.

1. INTRODUCTION

Experiments described in this paper indicate, that atomic hydrogen plays an important role in formation of crystal phases in the ternary system Ni-C -H. Although there is no thermodynamic data available for this ternary system, binary phase diagrams for Ni-C and Ni-H_2 systems have been reported (1). The Ni-H_2 system was studied at high pressures of molecular hydrogen and conditions of thermodynamical equilibrium (2). It is known that hydrogen can be dissolved in Ni using electrical discharge but because of its non-equilibrium nature this process did not attract much attention (2).

The primary motivation for the study of the crystallization phenomena in the Ni-C-H system arose from diamond heteroepitaxy in a CVD process. The crystal structure of Ni closely matches that of diamond with a lattice mismatch of about-1.3%. This suggests that Ni is suitable substrate for diamond heteroepitaxy but unfortunately both C and H react with Ni, and both dissolve in this metal. Consequently it is necessary to have just the right composition of $Ni_xC_y H_z$ phase which can provide nucleation sites for diamond. This requires that the nucleation and growth of graphite fibers on nickel be controlled. The common CVD process results in nucleation of graphitic fibers and Ni acts as a catalyst. Using the mirowave plasma process it is possible to inhibit the the nucleation of graphite by proper treatment of Ni by atomic hydrogen as it was reported in our previous paper (3). The presence of atomic hydrogen also effects catalytic hydrogenation process of hydrocarbons by nickel. This paper describes results on the formation of Ni-C phase and diamond nucleation where both rely on the active participation of atomic hydrogen.

2. TRANSPORT OF Ni FROM Ni FOIL ONTO GRAPHITE

Microwave plasma assisted chemical vapor deposition technique was used for nucleation and growth within Ni-C-H system. The apparatus was consisted of a silica tube reactor which crosses a microwave cavity as shown in Fig. 1. Gases (H_2 or 1% CH_4 in H_2) are fed into the top of the tube and a plasma ball is created at the center of the cavity. The introduction of this particular apparatus was a milestone in CVD diamond history (4).

The created plasma consists of molecules, ions, electrons and radicals such as atomic H˚, CH_3 and other hydrocarbons. Because of quantitative determination of concentration of H˚ in this microwave plasma is difficult, only a rough estimate could be made at a few atomic %.

The melting of Ni was observed where plasma ball contacts a strip of Ni, due to the metal interaction with the plasma and the electromagnetic field. The melting point of Ni saturated with hydrogen was about 200° C lower then that of pure Ni (1455°C), and for the eutectic point of the Ni-H_2 system it is only 50°C below 1455° (1).

Addition of CH_4 to hydrogen plasma causes further decrease in the melting point to 1150°C (3), which is lower than the 1326.5°C assign to Ni-C eutectic (1), and intensive evaporation accompanied this melting at 1150°C.

Another feature of metal-hydrogen interaction is permeation of hydrogen across metallic membranes, a phenomenon which is utilized in catalysis and purification of hydrogen (5).

The permeation of hydrogen was utilized in the following crystallization experiment. A sandwich of Ni foil (0.1mm thick) and a highly oriented pyrolytic graphite plate were exposed to a hydrogen plasma. The distance between the Ni foil and the graphite was less than 1 mm. The sandwich was heated up to the temperature close to 1150°C for 2 hours in hydrogen at 80 Torr

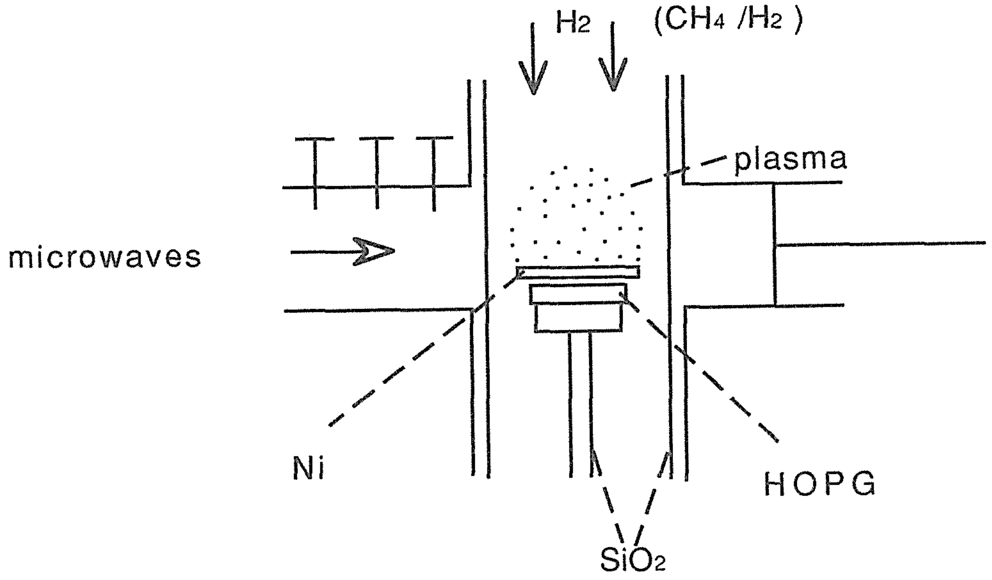

Fig. 1. A schematic of microwave plasma CVD system

where the temperature was measured on the top surface of the Ni foil. Next the temperature was decreased to 950°C and a mixture of 1% CH_4 in H_2 was introduced for 5 hours. As a result of this, Ni was transported from the Ni foil onto the graphite as shown schematically in Fig. 2. Transport of Ni was also observed in a different configuration where the Ni foil was hanging perpendicularly to the graphite. In these experiments the bottom surface of Ni foil became etched. The new crystals on graphite are shown in Fig. 3 where some crystals look cubic while some are rounded. The graphite surface was not noticeably etched however, at the edges of graphite plate etch pits are clearly visible due to plasma penetration around the edge of the foil.

Chemical analysis of the microcrystals on graphite was carried out using electron microprobe analysis and both Ni and C were detected. In the case of the small objects the results are rather qualitative but the content of C in Ni was estimated in the range of 5-8 atomic %.

X-ray diffraction analysis was performed by Debye-Scherrer method using 114mm diameter camera and Cu radiation. The crystals removed from the graphite were analyzed and X-ray diffraction patterns were found to consist of sharp diffraction lines. The lines correspond to Ni fcc structure, but they are shifted indicating lattice expansion which is caused by the incorporation of carbon. The 331 and 420 lines are clearly resolved as the $K\alpha_1$ and $K\alpha_2$ doublets. We believe the carbon is quite uniformly distributed in the different crystals because of this resolution. The lattice parameter for the carbide phase is 3.5271 ± 0.0004Å compared to the nickel metal standard which is 3.5238 ± 0.0001Å.

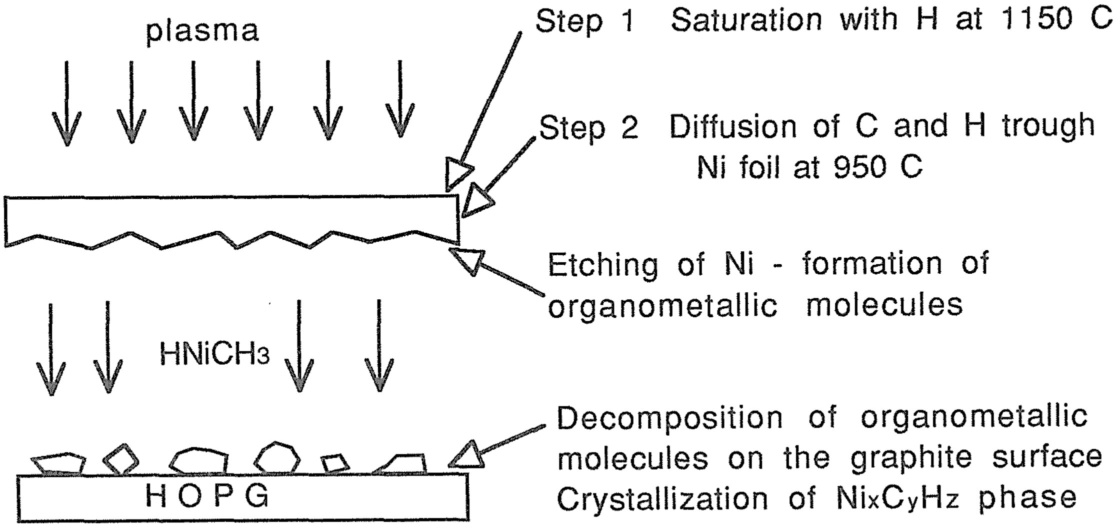

Fig. 2. Processes anicipated for transport experiment

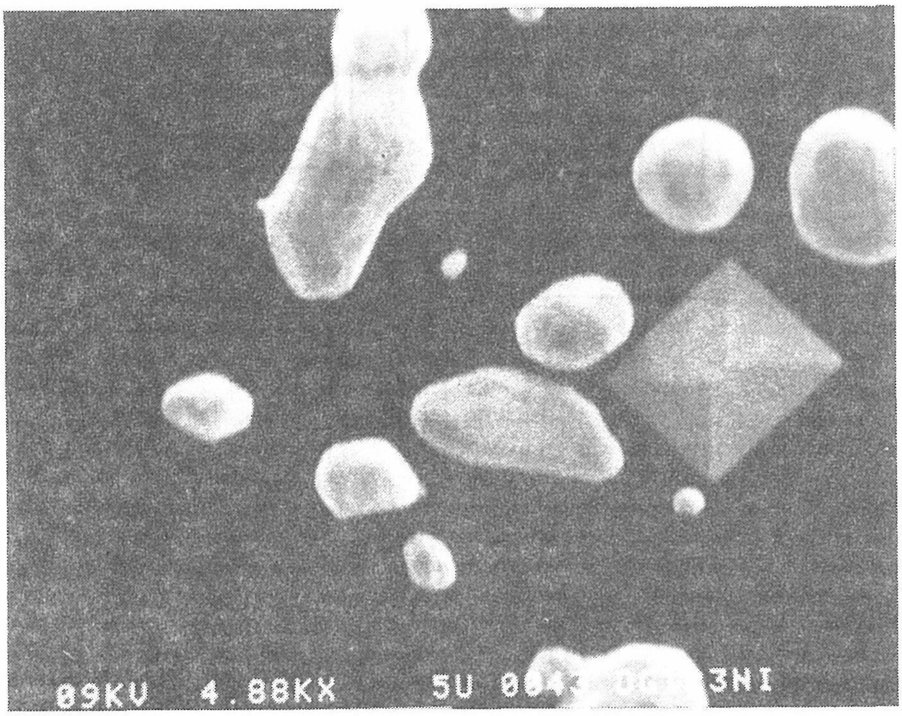

Fig. 3. Nickel carbide crystals grown on graphite

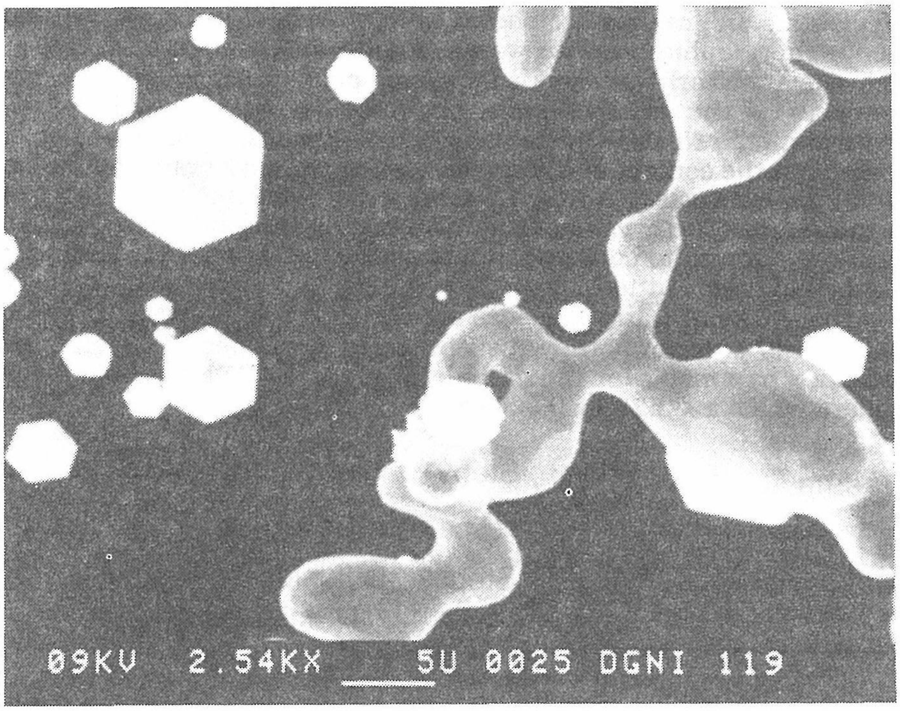

Fig. 4. Growth of diamond crystals and coalescence of $Ni_x C_y H_z$

Chemical analysis for hydrogen in this phase was not carried out on the microcrystals shown in Fig. 4. However combustion analysis for a bulk Ni sample, which underwent hydrogen plasma treatment as the first step and CH_4/H_2 plasma as a second step, indicated presence of 4% of C and did not detect H. It is known that the fugacity coefficient of H is high so that the ternary phase $Ni_xC_yH_z$ could be present in the plasma environment, but hydrogen leaves crystal lattice as soon as the plasma is terminated.

The crystal structure of this phase at room temperature can be described as defected NaCl type structure. One sublattice is occupied by Ni atoms and in the second sublattice a certain fraction of the lattice sites is occupied by C atoms.

In summary we have found that the cubic Ni-C phase can be formed during the process in which atomic hydrogen is involved.

3. NUCLEATION OF DIAMOND ON Ni CARBIDE SEEDED GRAPHITE

Study of diamond nucleation was conducted in direct connection to the experiments described above. HOPG plate (Fig .1) with nickel carbide crystals on it was used as substrate in diamond CVD process. The CVD process was carried out in the system shown in Fig. 1 where plasma ball was sticking to the substrate. The input gas was a mixture of 1% CH_4 in H_2 and the substrate temperature was 950°C. The process was run for 5 hours at 80 Torr pressure which were the typical conditions for CVD diamond growth. The result of the process is shown in Fig. 4. The Ni-C crystals are transformed and the diamond crystals appeared on the graphite and on Ni-C crystals while the graphite substrate underwent etching.

3.1 Ni-C crystals. The most striking change is a transformation of the Ni-C crystals. The crystals coalesce at temperature 500° C below the melting point of Ni and 200° C below the Ni-C-H eutectic point. Fig.4 shows how the Ni-C crystals shown in Fig. 3 coalesce forming long snake-like forms indicated that intensive mass transport takes place in this process. We believe that a interaction of microwave plasma with the metal crystals and graphite is responsible for this pseudo-melting phenomenon. A scheme shown in Fig. 2 can be helpful in explaining this transport. A combination of gas phase transport and surface diffusion seems to be responsible for the coalescence. The graphite substrate is etched by H° thus forming hydrocarbon radicals. The hydrocarbons and H° interact with Ni-C crystal surface forming organometallic molecules. These molecules decompose on graphite and on the surface of Ni-C crystals releasing some hydrocarbon radicals. The growth of Ni-C then proceeds on the existing crystals which explains snake-like forms. In addition new seeds of Ni-C phase are formed on graphite substrate. The surface of Ni-C phase seems to be unstable so that etching and deposition take place. Chemical composition of organometallic molecules which participate in this process is still an open issue.

3.2 Diamond nucleation. Diamond nucleates on both the graphite and on the Ni-C crystals. However the nucleation on Ni-C crystals is less frequent in this particular case (Fig. 4). A majority of the diamond crystals have cubo-octahedron form, the others represent different forms of (111) twins. We would like to point out that both diamond and $Ni_xC_yH_z$ crystals grow side by side from the same gas environment.

We believe that diamond crystals nucleate on a seed of an intermediary phase $Ni_xC_yH_z$ which is rich in C. Whereas the continuous etching of the graphite looks to be helpful in the formation of such seeds, some diamond crystals show <111> orientation related to the basal plane of graphite. Our reasoning is based on the observations of nucleation on pure graphite exposed to 1% CH_4/H_2 plasma. When the growth environment is clean (exclusively C and H) only etching of graphite appears and nucleation of diamond is rare (6). When the Ni foil is introduced into the plasma nucleation of diamond increases in multitude.

3.3 Growth of diamond on Ni substrates. Prior to the understanding of the Ni-C-H system we were trying to grow diamonds on polycrystalline nickel. Cubooctahedral single crystals (occasionally up to 160 μm) could be grown at the Ni substrate grain boundaries. Studies on the influence of Ni on hemoepitaxial growth were also carried out and cathodoluminescence (CL) spectra and topography were published (7). The results indicated that Ni atoms are incorporated into diamond lattice during growth via organomettalic molecules. In addition the CL spectra indicated a peak located close to the GR-1 peak assigned to a neutral vacancy. We think that the new peak (analogous to the Si peak) is related to an octahedral interstitial - vacancy complex. Many researchers have attempted to grow diamond on Ni, but oriented growth over only an limited area was achieved on single crystal Ni substrates (8). The concept of atomic hydrogen treatment of Ni to hinder graphite nucleation (3) was helpful in initiating new approaches. W. Zhu et al. (9) explored diamond micro crystals seeding of single crystal (100) and (111) surfaces of Ni and achieved oriented diamond growth (9). R. Roy et al. developed a new method of diamond growth--low pressure solid state source synthesis (10). One version of this method utilizes a mixture of nano scale form of carbon with Ni powder and Fig. 2 is helpful in understanding this new process.

4. DISCUSSION

Our improved understanding points to the critical role of H° in the crystallization processes described above. Hydrogenation of Ni inhibits nucleation of graphitic fibers. Effective hydrogenation of bulk Ni occurs at temperature ~1150°C, but sputtered Ni films require lower temperatures e.g. 1000°C because of their columnar structure. Also formation of a solution made up of H in Ni and volatile NiH takes place (3,11). These findings gave a new insights into the control of nucleation of diamond on Ni, but also contribute to related issues which are discussed below:

4.1 H° enables dissolution of carbon in Ni. According to the phase diagram Ni fcc structure can accommodate 2.7 at% of carbon at the eutectic temperature of 1326.5°C, but below 1000K° less than 1% of carbon is dissolved. In the experiments described above Ni was melted in a hydrogen plasma, then melted again in CH_4/H_2 plasma and then slowly cooled. The resultant material contains 4 at% of C (obtained from Rutherford Back Scattering) which is substantially higher then predicted by the phase diagram. We think that diffusion of carbon into Ni lattice is enhanced by the presence of hydrogen in the lattice. An independent theoretical study on the effects of subsurface H and C on CH_3 absorption on Ni (111) concludes that interstitial H helps to bind strongly tetrahedral CH_3 while interstitial C may make it easier for a carbon overlayer to revert to a planar graphite structure (12).

4.2 Transport of Ni by organometallic molecules. Transport of Ni in pure hydrogen plasma proceeds through volatile NiH which is partially decomposed when deposited. The rate of transport is increased when CH_4 is present in the plasma. We believe thus that transport occurs by organometallic molecules, which are decomposed when deposited, thus leaving solid interstitial phase $Ni_x\, C_y\, H_z$. This phase decomposes further when H leaves the lattice.

We are not able to recommend any chemical formula for the gas species. The role of atomic hydrogen in formation of organometallic molecules is not clear. In general it is known that C-H bond can be activated by transition metal reagents . The special type of bonding, namely three-center intra-molecular Metal-H-C interactions are now well characterized (13). The complexion of C-H bond by metal ions (so-called agostic) results in two-electron three center bonds. C-H bonds can interact with metal atom-ligands e.g. activating inert saturated hydrocarbons. In the case of experiments with Ni we hypothesize that complexes like CH_3NiH (14) and clusters with CH_4 are possible (15).

Metal surface-alcane interactions have an extensive literature in catalysis, with for example, dissociative adsorption on Ni. The catalysis leads to hydrogenation of unsaturated hydrocarbons where acetylene can undergo selective semihydrogenation (16). The Ni-C-H environment can influence diamond growth process because the gas phase reaction equilibria could be altered towards the saturated hydrocarbons.

Our previous experiments on Ni influence on the (001) epitaxial growth of diamond, like these reported in (3,7), indicated some structural improvement of the films. For example full width at half maximum of the 1332 cm-1 Raman peak was 1.7 cm-1 (equal to the lowest value measured for natural diamond) and the spectra showed low background. We speculate that catalysis hydrogenation of hydrocarbons can be beneficial for diamond growth.

We should like to mention a new aspect of diamond growth in liquid phase in connection to Ni chemistry and to transport of carbon in the Ni-C-Na OH system (17,18).

4.3 Formation of an interstitial carbide. Nickel carbide inclusions occur in HP/HT synthetic diamond crystals. Nickel carbide is non-stoichiometric (e.g. $NiC_{0.25}$) and possesses cubic structure (19). Some inclusions have the same orientation as the diamond matrix. (20,21) These facts indicate that carbide formation is essential to HP/HT nucleation and growth. According C-Ni phase diagram there are no stable carbides (1). The CVD experiment described above showed that NaCl-type phase was crystallized in the presence of atomic hydrogen and demonstrate that dissolution of carbon is enhanced by H°. The question now is how much carbon can be accommodated in the octahedral holes of Ni fcc structure.

4.4 Growth of graphite fibers. Catalytic growth of graphite fibers is easy to achieve by microwave plasma CVD. When Ni substrate is exposed to CH_4/H_2 plasma graphite fibers nucleate and no H° pretreatment is necessary in this case. The growth mechanism of graphite fibers includes formation of a particle of metal on the top of the growing fiber (22,23), but the chemical composition of this metal ball is still an open issue. We think that the "nickel" ball has chemical composition similar to the ternary phase $Ni_xC_yH_z$ (Fig . 4) where the model shown in Fig 2 can be helpful in solving this problem.

4.5 Nucleation and growth of diamond. Nucleation of diamond on $Ni_xC_yH_z$ phase is less frequent than on graphite. We hypothesize that an intermediate phase $Ni_xC_yH_z$ formed on graphite is richer in C so that in order to form more nucleation sites on Ni it must be saturated with C.

Growth of the $Ni_xC_yH_z$ phase and diamond crystals proceeds in the same environment, where the, concentration of organometallic molecules is the same over the growing surfaces of both phases (Fig. 4). This is an indication of the catalytic role that Ni has in CVD diamond growth process.

CONCLUSIONS

1. Microwave plasma containing atomic hydrogen enables dissolution of hydrogen in Ni and decreases melting temperature of Ni by about 200°C.
2. Presence of hydrogen in the Ni lattice increases carbon diffusion and $Ni_x C_y H_z$melts at 1150° C.
3. A new phase NiC_y (NaCl-type structure) is observed with the growth of this phase being reported for the first time.
4. The solid phase $Ni_x C_y H_z$ recrystallizes on graphite during interaction with CH_4/H_2 plasma where a pseudo-melting forms appear.
5. Nucleation sites for diamond are created on graphite by an intermediary phase $Ni_x C_y H_z$.

ACKNOWLEDGMENTS

This work was supported by the Office of Naval Research (with funding from BMDO under the contract No. 00014-92-J-1421) and by the National Science Foundation under Grant No. DMR -9104072. We extend our thanks to Diamond and Related Materials Consortium at the Pennsylvania State University to whom the experiments described above were reported on the meeting held in September 1991. We extend our thanks to Professor B. Baranowski for discussions.

REFERENCES

1. Binary Alloy Phase Diagrams, ed. T.B. Massalski, W. W. Scott, 2nd ed. Materials Park, Ohio, ASM International, (1990), pp 886 and 2047.
2. B. Baranowski, in Metal Hydrides, ed. G. Bambakidis, Plenum Press, New York and London (1980) 193.
3. A. Badzian and T. Badzian, in T.M. Besman, B.M. Gallois and J.W. Warren (eds.) Material Research Soc. Symp. Proc. Vol 250 (1992) 339.
4. M. Kamo, Y. Sato, S. Matsumoto and N. Setaka, J. Crystal Growth 62 (1983) 642.
5. V.M. Gryaznov and M.G. Slinko, Discuss. Faraday Soc. 72 (1981) 73.
6. A. Badzian, T. Badzian, R. Roy, R. Messier and K.E. Spear, Mat. Res. Bull. 23 (1988) 531.
7. B.G. Yacobi, J. Lebens, K.J. Vahala, A. Badzian and T. Badzian, Diamond and Related Materials, 2 (1993) 92.
8. Y. Sato, I. Yashima, H. Fujita, T. Ando and M. Kamo, in R. Messier, J.T. Glass, J.E. Butler and R. Roy, ed., New Diamond Science and Technologhy (1991) MRS Int. Conf. Proc. p. 371
9. W. Zhu, P.C. Yang and J.T. Glass, Appl. Phys. Lett. 63 (1993) 1640.
10. R. Roy, H.S. Dewan and P. Ravindranathan, Mat. Res. Bull. 28 (1993) 861.
11. A. Badzian and T. Badzian in J.P. Dismukes and K.V. Ravi, Diamond Materials, Proceedings Volume 93-17, The Electrochemical Society (1993) 441.
12. H. Yang, J.L. Whitten, R.E. Thomas, R.A. Rudder and R.J. Markunas, Surface Science Letters 277 (1992) L95.
13. J.A. Davies, P.L. Watson, J.F. Liebman and A. Greenberg, eds. Selective Hydrogen Activation, VCH Publishers, New York, (1990).
14. ibid p. 436,443,458 nn.
15. P.R. Kemper, J. Bushnell, P. Van Koppen and M.T. Bowers, J. Phys. Chem. 97 (1993), 1810.
16. W. Palczewska, in Hydrogen Effects in Catalysis, Z. Paal and P.G. Menou, Vol 31,M. Dekker, New York 1998, 373.
17. A. R. Patel and K.A. Cherian, J. Crystal Growth 46, (1979) 706 and Surf. Coat Technol. 47 (1991) 127.
18. E. Pavel, Diamond and Related Materials 2 (1993) 505.
19. K. Lonsdale and H.J. Milledge, in R. Berman ed. Physical Properties of Diamond Clarendon Press, Oxford, 1965, 37.
20. A. Badzian and A. Klokocki, J. Crystal Growth 52 (1981) 843
21. A. Badzian , in Advances in X-ray Analysis, C.S. Barret et al eds. Plenum Press, New York, 1987, vol. 31, 113.
22. R.T.K. Baker, in Chemistry and Physics of Carbon, P.L. Walker Jr. and P.A. Thrower eds. Vol 14 (1978) 83.
23. M.S. Dresselhaus, G. Dresselhaus, K. Sugihara, I.L. Spain and H.A. Goldberg, Graphite Fibers and Filaments, Springer-Verlag, Berlin, 1988.

Study of Homoepitaxial Growth of Diamond

Naoji Fujimori
Itami Research Laboratories, Sumitomo Electric Industries
1-1, 1-chome Koyakita, Itami, Hyogo 664, Japan

Abstract

Diamond epitaxial films were studied by scanning tunneling microscopy (STM), electron diffraction, cathodeluminescence (CL), X-ray diffraction (XRD) and Raman spectroscopy. STM observation revealed the dominated growth of dimer-row-extension on (001) and the kink growth on (111). Single-domain 2x1 surface was obtained using an off-angle (001) substrate. Epitaxial films thicker than 100μm usually contained un-epitaxial particles, which were found to be originated in the twin nucleation. However, the normal epitaxial region was found to have crystallinity as good as or better than natural IIa crystal.

1. Introduction

The study of diamond epitaxial growth is interested both as the way to the elucidation of diamond growth mechanism and as the alternating method of obtaining single-crystal diamond. In order to obtain good crystallinity and flat surface, many attempts have been performed and diamond MESFET was fabricated using homo-epitaxial films.[1,2)

The observation of homo-epitaxially grown diamond surface has been carries out using STM and electron diffraction,[3-5) which contributed to the understanding of the growth mechanism. Especially, atomic image of the surface helped to make an atomic model for computer simulation.[6)

On the other hand, homo-epitaxial films are suitable sample for characterization of CVD grown diamond, because it dose not contain a crystal boundary.

In this report, the author would like to summarize the studies of homo-epitaxial growth by micro-wave plasma assisted CVD (MPCVD). Surface structures and characteristics of thick diamond films are reported.

2. Surface Observation by Scanning Tunneling Microscopy

2-1. (001) Surface

Typical STM image of as-grown diamond(001) after the epitaxial growth is shown in Fig. 1. There are seen many rows along two directions that are perpendicular to each other. The distance between the adjacent rows corresponds to that of the longer side of the 2x1 unit. The observed step height was 0.9Å, which is as same as the height of a mono-atomic step of diamond(001), 0.89Å.

The probable atomic structure of the 2x1 structure is a dimer-type reconstruction, similar to the confirmed structure of clean (001) of Si or Ge. This reconstruction reduces dangling bonds by bonding of adjacent dangling bonds. Considering that the CVD growth was performed in a plasma whose main component was hydrogen, the hydrogen-adsorbed dimers are more probable.

In Fig. 1, significant extension of dimer rows is observed. Only single dimer row extends on the lower terraces. There exist two types of mono-atomic steps on diamond(001); i.e. S_A step at which dimer rows run parallel to the step edge and S_B step at which dimer rows run perpendicular to the step edge.[7] It is considered that he extension of the dimer rows occurs at S_B steps. The STM showed the difference of two types of steps, i.e. S_A steps are straight, while S_B steps are ragged due to the extension of the dimer rows.

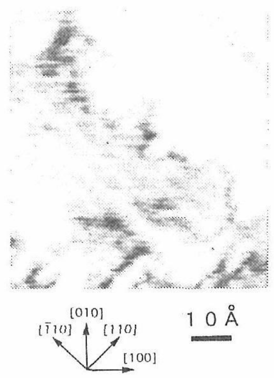

Fig. 1 STM image of diamond(001) epitaxial film.

2-2. (111) Surface

Fig . 2(a) is an STM image of the (111) epitaxial film, showing 1x1 periodicity observed by LEED. The majority of the observed steps were the bi-layer steps in the <112> direction. These steps showed very straight in atomic scale and kinks of 1x1 units were observed at the intervals of more than several 10Å. A typical image of the kink

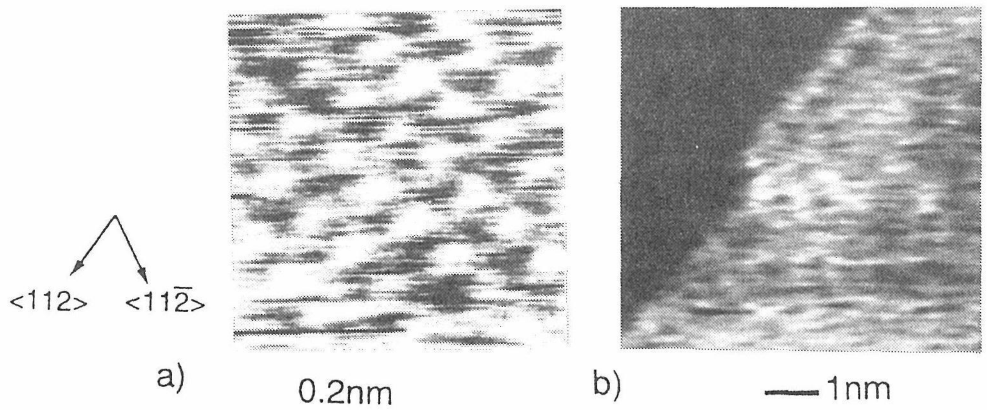

Fig. 2(a)(b) STM images of diamond(111) epitaxial film.

is shown in Fig. 2(b). These results suggest that the steps are very stable and that bi-layer kink growth can be carried out at the step.

3. Epitaxial Growth on Off-cut (001) Substrates

On the (001) surface, the boundaries of the two domains, 2x1 and 1x2, are mono-atomic height steps and the two domains form layer by layer. Therefore, single-domain is formed on the surface with no steps or on the surface with bi-atomic steps, as was reported for MBE-grown Si(001) surface on off-cut substrate.

In this section, the results of epitaxial growth on diamond (001) off-cut substrates are reported. The normal of the substrate surface was mis-oriented from [001] toward [110] direction by the angle from 1 to 5°. The epitaxial growth was carried out by MPCVD with methane concentration from 1% to 6%.

The LEED pattern of the sample grown on 4.3° mis-cut substrate with the methane concentration of 2% is shown in Fig. 3. The superstructure spots from one domain are far brighter than those from another domains, indicating a nearly perfect single-domain 2x1 surface. STM image also suggested that almost all dimer rows align in the same direction and that the bi-atomic height steps are formed all over the sample. On the other hand, the double-domain surface was observed after the growth with the 6% methane concentration. The formation of single-domain and double-domain surface with various methane concentration are summarized in Table 1. Single-domain 2x1 surface was formed after the growth with the lower methane concentration on the substrate with larger off-cut.

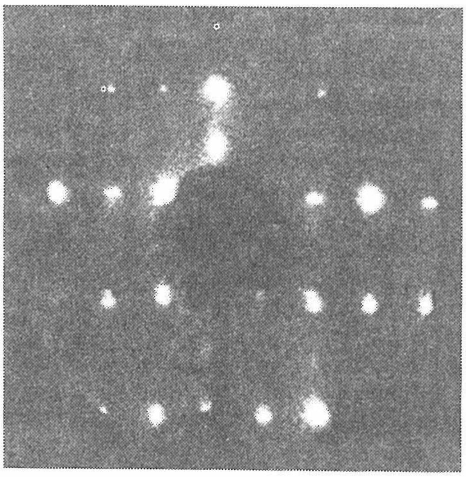

Fig. 3 LEED pattern of diamond(001) showing nearly perfect single-domain.

Table 1. Formation of single and double domain surface grown on mis-cut (001) substrates.

CH_4 conc. off-cut	1 %	2 %	4 %	6 %
1~2°	D	D	D	D
2.9°	-	-	D	-
4.3°	S	S	-	D
5.0°	S	S	-	D

S: single-domain
D: double-domain
-: no data

These results can be explained by the difference of nucleation density with methane concentration. The higher density of two-dimensional nucleation for the growth with higher methane concentration make it impossible to grow by the step-flow. In the growth with low methane concentration on the substrate with large off-cut, it is considered that the growth is performed with the step-flow and that the two-dimensional nucleation plays negligible contribution for the growth. The S_B steps catch up the S_A steps, resulting in the single-domain surface.

4. Activation Energy of Epitaxial Growth

The activation energy is one of the most fundamental information in chemical reactions. The energy is generally known from the temperature dependence of the reaction rate. In order to obtain the activation energy for diamond CVD growth, the measurement of the epitaxial growth on single-crystal substrates is the appropriate experiment, because the growth of poly-crystal films is quite complex.

Figures 4(a)-(c) show the Arrhenius plots for the growth rate using (001), (111) and (110) substrates. There can be found the temperature having a maximum growth rate in (001) and (111). Lower than these temperature, activation energies can be determined as 47, 100 and 61 kcal/mol for (001), (111) and (110), respectively. Larger activation energy of (111) growth suggests the smaller amount of growth site which can be derived from the STM observation.

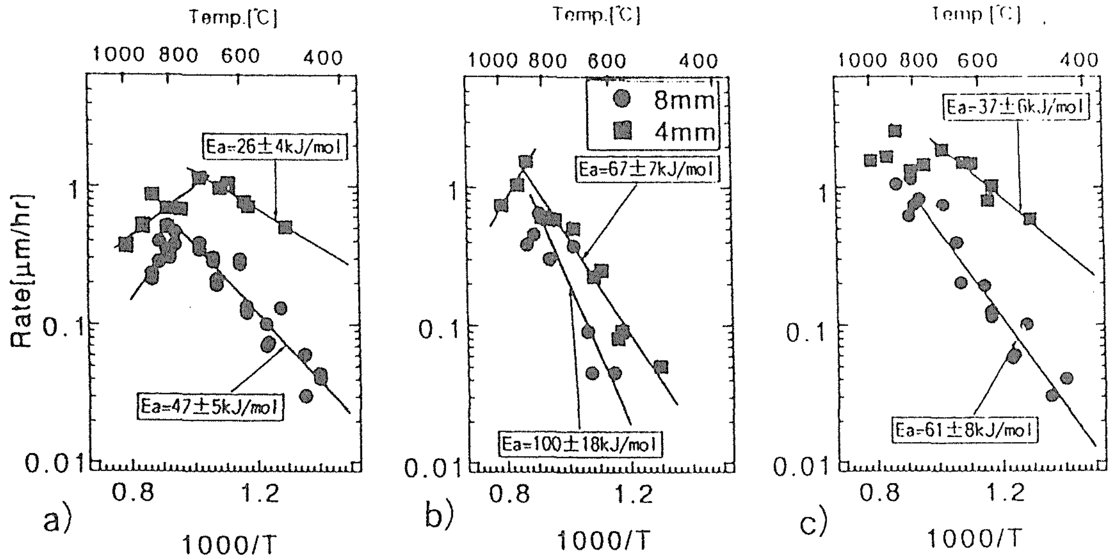

Fig. 4 The Arrhenius plots of diamond homo-epitaxial growth.
(a) (001), (b) (111) and (c) (110).

5. Growth of Thick Epitaxial Films

The epitaxial film thicker than 100μm was grown on (001) substrates by MPCVD, and the surface and bulk characterization were carried out.

Formation of un–epitaxial crystallites and growth hillocks were formerly reported by Kamo et al.[8)] for thick epitaxial films. It was found that the majority of the un–epitaxial crystallites was {111} penetration twins, which were considered to be originated by the twin nucleation on {111} facet on substrates or epitaxial films (Fig. 5(a)). The penetration twins with 4–fold symmetric location were also observed by SEM and they are attributed to the twin nucleation in reverse–pyramid pits on the substrate surface.

It is also found that the growth hillocks are induced by the twinning structure with a pair of parallel {111} twinning plane. Fig. 5(b) shows the schematic of the growth hillock induced by the twinning structure. The twinning structure is accompanied with reentrant corner on the surface where the growth rate is enhanced, resulting in the formation of growth hillock.

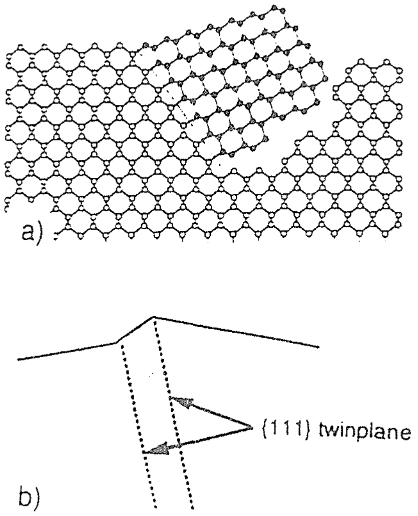

Fig. 5 Schematic of (a) unepitaxial crystallite and (b) growth hillock induced by twinning structure.

After the observation, the growth surface was polished and the substrate crystal was removed by mechanical polishing. Thus, the single–crystal CVD diamond was obtained and characterized it by various methods.

The Raman spectrum of 1332 cm^{-1} for the un–epitaxial crystallites found to be broad with high background, indicating worse crystallinity. On the other hand, the normal epitaxial region confirmed to be good crystallinity by Raman spectroscopy, CL, XRD and optical transparency. The high–resolution Raman spectrum showed sharp peak at 1332cm^{-1}, whose FWHM was 1.7cm^{-1} which is the same as that of natural and of synthesized IIa single crystal. In the CL spectrum, the strong emission assigned as the free exiton was observed at room temperature. The FWHM for (400) reflection in the measurement of double–crystal XRD was 35", which is smaller than that of natural IIa diamond. Optical transparency in infrared was quite good and showed no absorbance other than C–C bonding and small amount of C–H bonding. The transparency in the visible and in the ultraviolet region was also good and the absorption edge at 225nm, assigned to band–edge absorbance was clearly observed.

6. Conclusion

The surface observation and the characterization of the thin and thick diamond homo–epitaxial films were carried out and the results obtained are summarized as follow,

1) The observation with atomic order resolution revealed the dominated growth of dimer–row–extension on (001) and the kink growth on (111). Single–domain 2x1 surface was obtained using an off–angle (001) substrate.

2) Single–domain 2x1 surface of (001) was obtained using several degree mis–oriented substrate and the methane concentration less than 2%.

3) Thick epitaxial films had good crystallinity, which was confirmed by Raman spectroscopy, X–ray diffraction and cathodeluminescence.

4) Thick epitaxial films contain un–epitaxial crystallites, which were formed by twin nucleation on the {111} facets.

Reference

1) H. Shiomi, K. Tanabe, Y. Nishibayashi and N. Fujimori: Jpn. J. Appl. Phys. 29, (1990) 34.

2) H. Shiomi, Y. Nishibayashi and N. Fujimori: Jpn. J. Appl. Phys. 28 (1989) L2153.

3) T. Tsuno, T. Imai, Y. Nishibayashi, K. Hamada and N. Fujimori: Jpn. J. Appl. Phys. 30 (1991) 1063.

4) T. Tsuno, T. Tomikawa, S. Shikata, N. Fujimori: J. Appl. Phys. 75 (1994) 1526.

5) T. Tsuno, T. Tomikawa, S. Shikata, T. Imai and N. Fujimori: Appl. Phys. Lett. 64 (1994) 572.

6) T. Imai, T. Ueda, Y. Yamamoto, T. Tsuno and N. Fujiomori: To be published in *Proc. of IU–MRS* (1993, Tokyo, Japan).

7) D. J. Chadi: Phys. Rev. Lett. 59 (1987) 1691.

8) M. Kamo, H. Yurimoto and Y. Sato: Appl. Surf. Sci. 33/34 (1988) 553.

High Resolution Electron Microscopy of CVD Diamond Film

*J.L. Hutchison and D. Shechtman**
Department of Materials, University of Oxford, Parks Road, Oxford OX1 3PH, U.K.
*Department of Materials Engineering, Technion, Haifa, Israel

ABSTRACT

Growth defects in diamond films grown by plasma-assisted CVD have been studied and characterised by high resolution electron microscopy. The main defects are shown to be based on twinning and different twin boundaries of the type $\Sigma=3$, $\Sigma=9$, $\Sigma=27$ and $\Sigma=81$ have been identified. The higher order boundaries form by the interesection of lower order twins. By considering the geometry of the higher order boundaries it is shown that they are indicators for local growth directions, and their significance for possible growth mechanisms is discussed. The central nucleation point in some grains can be traced back to a five-fold twin centre which acts as a preferred nucleation site for new planes as the crystal grows.

INTRODUCTION

The majority of naturally occurring diamonds (type Ia), whilst containing abundant planar defects on {100} planes ("platelets"), have a very low density of other planar lattice defects such as twins and stacking faults. However, these defects are abundant in synthetic diamond films grown by chemical vapour deposition (CVD). They are present as growth defects and careful characterisation of these defects and their interactions can provide important information about growth mechanisms, and may give clues about ways to improve film quality.

Intermediate voltage high resolution electron microscopy with structure resolution in the 0.15 - 0.2 nm range is an ideal technique for the study of lattice defects in diamond, since it is capable of imaging both the {111} and {200} lattice planes in <110> oriented sections.

A number of groups have been applying HREM techniques to CVD diamond films, and have succeeded in identifying a wide range of defect structures (e.g. 1 - 4). In this contribution we describe some recent results obtained at Oxford, some of which may shed light on the growth processes involved in CVD diamond film growth.

EXPERIMENTAL

The films used in our studies were prepared by microwave plasma-assisted CVD, on both silicon (5) and molybdenum substrates. Details of the growth conditions have given elsewhere (5). After film growth the substrates were removed chemically, and the free-standing diamond films cut into 3mm squares, sandwiched between copper grids and ion-milled to perforation. They were examined in a JEOL 4000 EXII operating at 400 kilovolts, with a resolution of 0.16 nm. Images were recorded at primary magnifications of 500,000 or 600,000X.

The films had a dominant <110> texture normal to the substrate; grains were therefore sought which could be oriented into exact <110> orientations. Selected area electron diffraction patterns and atomic-resolution lattice images were recorded, under conditions appropriate for the optimum resolution of the instrument.

RESULTS

Electron diffraction

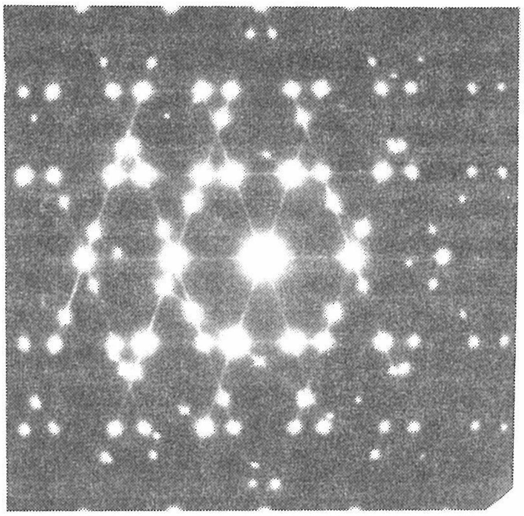

The <110> selected area difraction patterns revealed a high degree of disorder. An example of this is shown in Fig.1 opposite. In spite of the apparent complexity of this pattern it may be explained entirely as a consequence of five-fold lattice twinning. This will be discussed later in the text. It is noticeable that there is at first sight a five-fold symmetry in the pattern. Close examination however shows that this is not the case. Again, the implications of this for sub-grain boundary structures will be discussed.

Lattice defects

The structure images also showed considerable lattice disorder. The simplest boundaries correspond to first order twinning on {111} planes and give rise to $\Sigma=3$ boundaries, using the coincidence site lattice notation (6). The twins were frequently present as large domains, sometimes also as narrow lamellae only a few layers in thickness. Recurrent twinning on successive (111) planes occasionally generated small portions of hexagonal stacking - forming Lonsdaleite. In regions where $\Sigma=3$ twins overlap within the foil thickness with inclined boundaries Moiré interference effects give rise to complex contrast, similar to that found in Si and other fcc structures (7). It was found that $\Sigma=3$ twins increased in concentration towards the surfaces of grains.

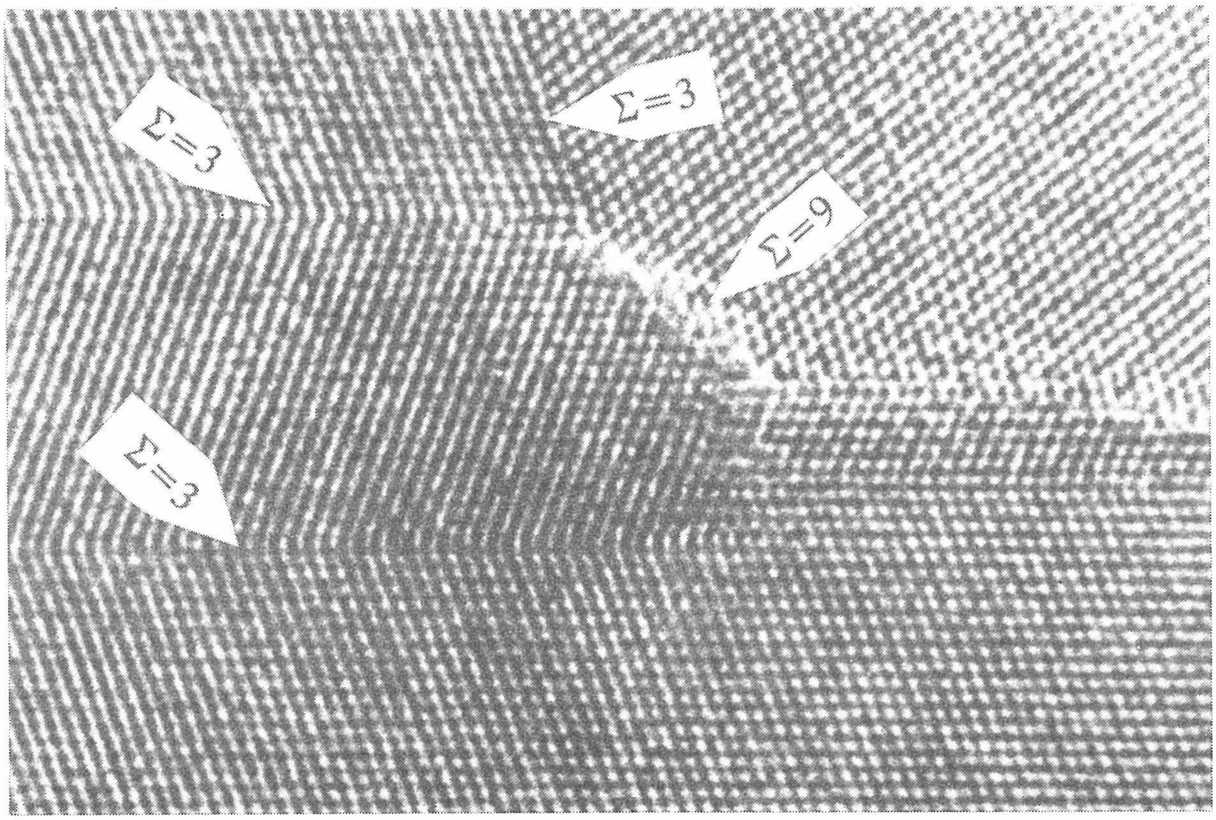

Figure 2. Complex boundaries in a <110> CVD diamond grain.

Other boundaries, identified by the rotation angle between the two components, according to the CSL notation, were also found. They arise from the interaction of the simpler configurations. Thus the interaction of two $\Sigma=3$ boundaries generates a $\Sigma=9$ boundary , and the interaction of a $\Sigma=3$ with a $\Sigma=9$ boundary gives rise to a $\Sigma=27$ boundary. The highest order boundaries we have identified so far correspond to $\Sigma=81$, with a twinning angle of 77.9°. These arise in two ways: the relatively rare interaction of a $\Sigma=3$ with a $\Sigma=27$ boundary, or as a result of the closure gap of 7.36° around a five-fold twin centre. The former case is a chance result of local growth conditions, the latter often propagates to the crystal surface as a topological fault. Examples of complex boundaries are shown in Fig. 3.

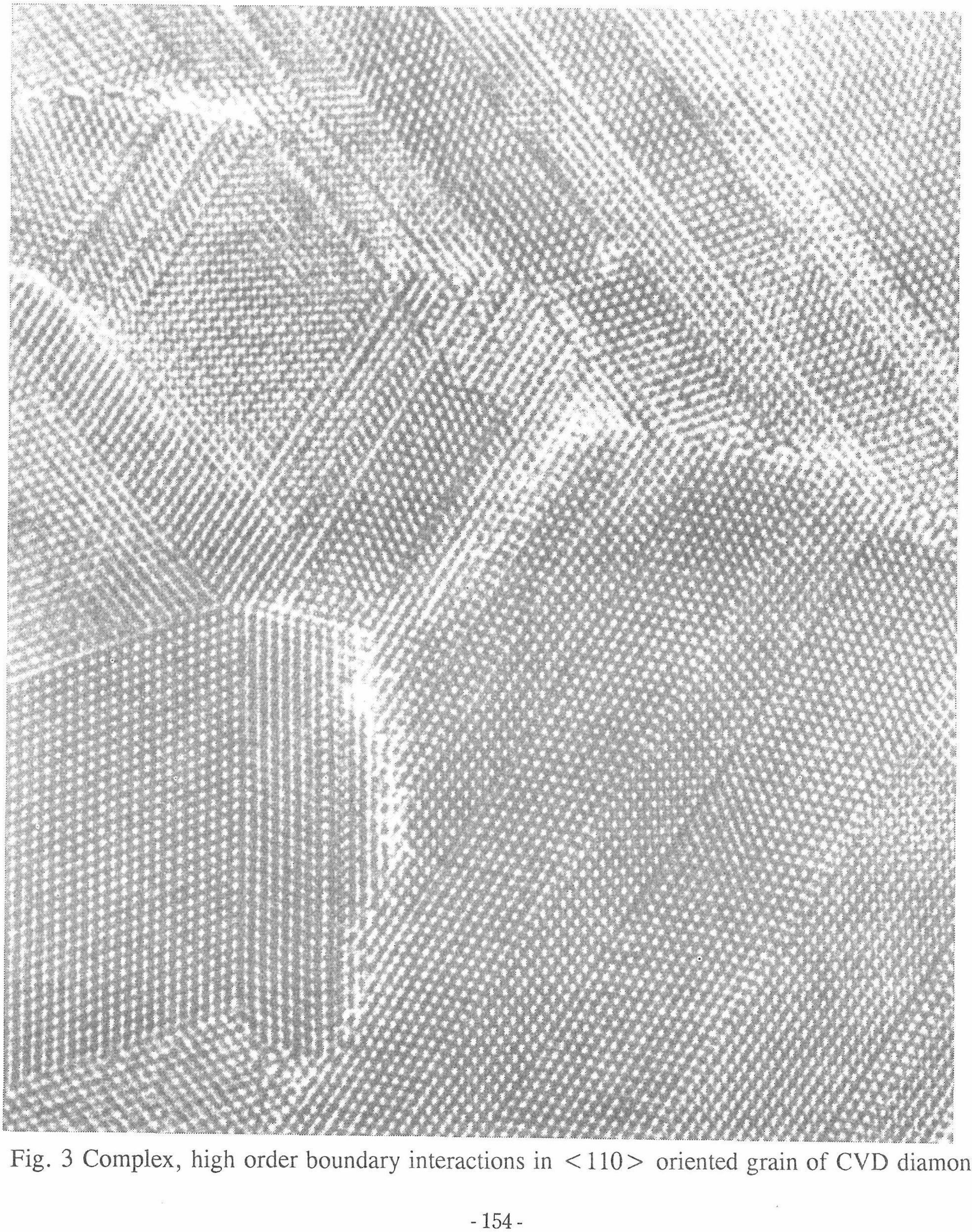

Fig. 3 Complex, high order boundary interactions in <110> oriented grain of CVD diamond.

In the case of five-fold twin centres, these have been shown to be planar, 5-membered carbon rings (8), which act as preferred growth nuclei, generating twin domains within the {110} planes, and also propagating along the <110> directions by a cage structure, as suggested by Matsumoto and Matsui (9). An image containing a 5-fold centre is shown in Fig. 4.

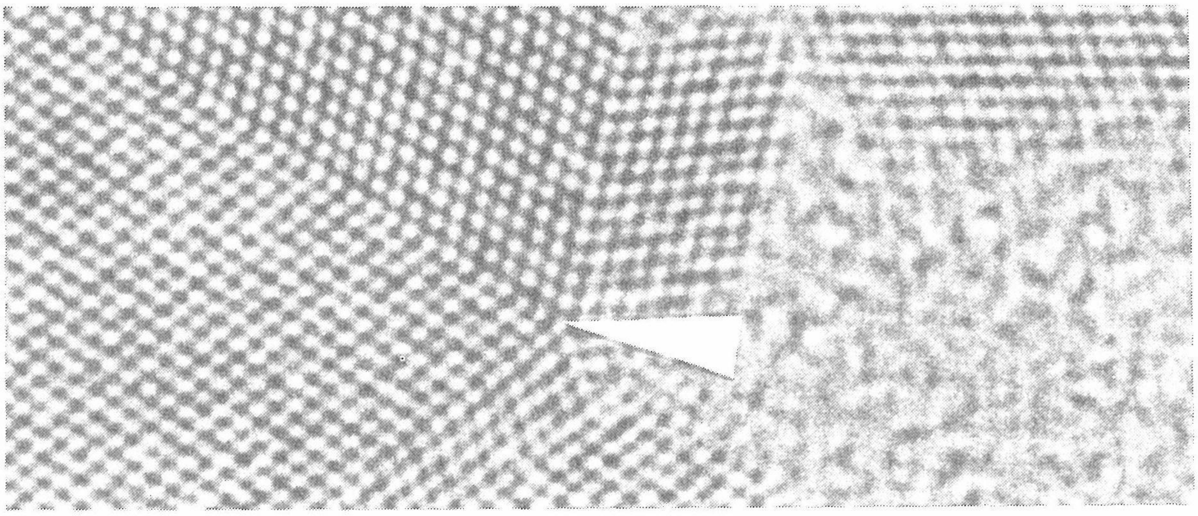

Fig.4. 5-fold twinning centre (arrowed) in CVD diamond grain.

Amorphous layers

At incoherent, high order boundaries we have often found evidence for non-crystalline material; also, such layers also occured in otherwise "coherent" boundaries, probably as a result of trapped impurities. An example of this is shown in Fig. 5. Such layers may be understood in terms of growing impinging on one another. As they approach, any local impurities will be incoroporated, and become trapped in the grain boundary.

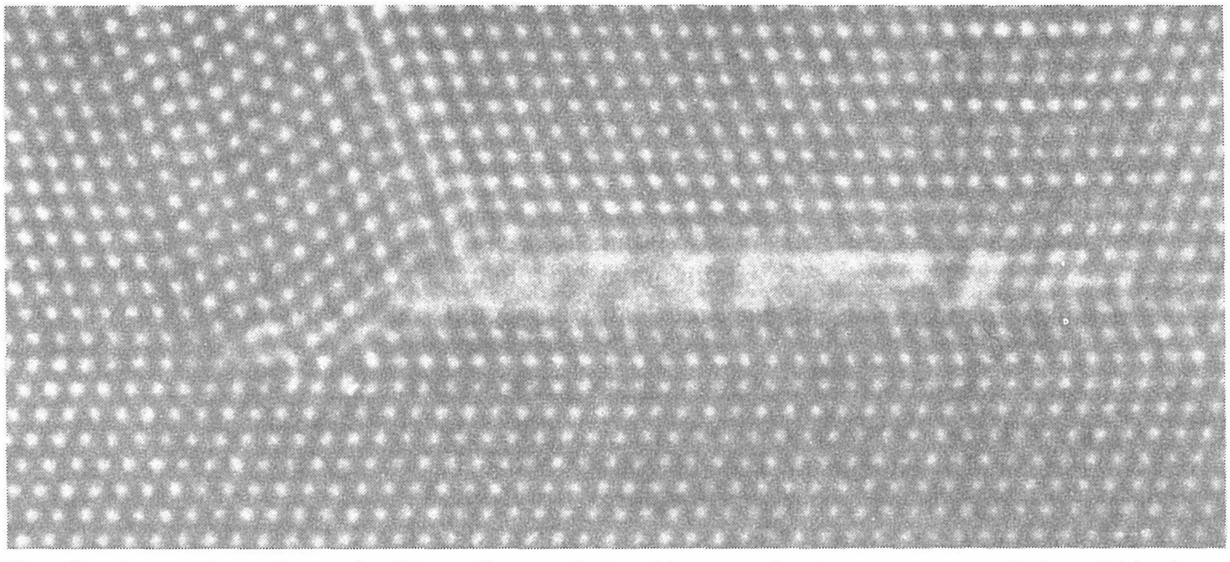

Fig. 5. Amorphous layer in CVD diamond. In this case the layers are parallel to 111 planes.

Intergranular amorphous carbon has been identified by electron energy-loss spectroscopy (10) and shown to contain almost completely sp^2 bonding. Similar analyses have not yet been carried out on the intragranular boundaries described here.

DISCUSSION

Misfit boundaries represent the locus of points of intersection of growing planes from two adjacent, non-matching twins. They are thus aligned along the local growth direction, and can provide clues about local growth. An earlier analysis of a complete grain section has been used to demonstrate that many such boundaries lead back to a 5-fold twin centres, preferred sites for nucleation and growth (5). It was argued (5) that $\Sigma=3$ twinning is crucially important to CVD diamond growth because a pair of parallel twin boundaries form a reentrant angle at the surface, stabilising incoming carbon atoms and forming growth steps. This is similar to the model postulated previously for the dendritic growth of germanium from the melt (11). An interesting feature of CVD diamond film surfaces is the large number of twin grooves present. Also, the small nuclei present at the start of film growth are frequently icosahedral in shape, with grooved edges, and pentagonal indents at their vertices.

Scanning electron microscope studies of film cross-sections and surfaces reveal the types of twins present (12). They are predominantly $\Sigma=3$, implying that these variants favour fast growth, whilst the higher order twinning appears to be eliminated during growth of the film.

It would thus be reasonable to suggest that $\Sigma=3$ twinning is an important factor in encouraging fast growth. Higher order boundaries which are also present, particularly at the centres of grains (corresponding to early stages in growth), are likely to hinder growth and they (or even the grains containing them) tend to be eliminated as the film develops.

ACKNOWLEDGEMENTS

This work was partly supported by the Office of Naval Research.

REFERENCES

1. B E Williams and J T Glass J. Mater. Res. **4** 373 (1989)
2. J. Narayan J. Mater. Res. **5** 373 (1989)
3. W Luyten, G Van Tendeloo, S Amelinckx and J L Collins Phil. Mag. A **66** 899 (1992)
4. P Wurzinger, M Joksch and P Pongratz Inst. Phys. Conf. Ser. No. **133** 157 (1993)
5. D Shechtman, J L Hutchison, L H Robins, E N Farabaugh and A Feldman J Mater. Res. **8** 473 (1993)
6. S Ranganathan Acta Cryst. **21** 197 (1966)
7. D Shechtman, A Feldman, M Vaudin and J L Hutchison Appl. Phys. Lett. **62** 487 (1993)
8. J L Hutchison and D Shechtman Proc 10th Eur. Congr. on Electron Microscopy (Granada) **II** 713 (1992)
9. S Matsumoto and Y Matsui J Mater. Sci. **18** 17785 (1983)
10. R G Seidensticker and D R hamilton J Appl. Phys. **34** 3113 (1963)
11. D Shechtman, J L Hutchison, E N Farabaugh and L H Robins Proc. TMS Symposium on Twinning in Advanced Materials (Pittsburg) 1993
12. P J Fallon and L M Brown Diamond and Related Materials **2** 1004 (1993)

Spectroscopic Studies of Point Defects in CVD Diamond and High-Pressure Synthetic Diamond

Alan T. Collins
Wheatstone Physics Laboratory, King's College London
Strand, London WC2R 2LS, U.K.

Perfect diamond, free from chemical impurities or structural defects, would exhibit no electronic transitions apart from the absorption edge at 5.49 eV and the free-exciton luminescence at around 5.3 eV. In fact most diamonds exhibit absorption and luminescence associated with the presence of point defects. These systems cover the energy range from about 1.2 eV in the near infrared spectral region to around 5.3 eV in the ultraviolet. In this article we will consider the optical centres in CVD diamond, paying particular attention to the silicon-related 1.681 eV defect, and the absorption and luminescence bands in high-pressure synthetic diamond produced by the presence of nickel.

1. INTRODUCTION

Optical spectroscopy has proved one of the most fruitful techniques for characterising point defects in diamond. Even so, although well over 100 different systems are known, atomic models have only been established with any certainty for about a dozen. Davies (1977) listed all the absorption and luminescence bands known at that time, and Clark *et al.* (1992) have provided the most recent update to that information. In this article we will consider work recently completed, or currently in progress, in two different, but vitally important areas. We will examine the absorption and luminescence spectroscopy of CVD diamond, and present the evidence which suggests that one of the most common optical bands, with a zero-phonon line at 1.681 eV, is associated with the presence of silicon and probably involves a vacancy trapped at the silicon impurity. We will also investigate the considerable number of optical centres in high-pressure synthetic diamond which involve the incorporation of nickel. These are two particularly appropriate topics for the present symposium since research workers from NIRIM have participated in many of these studies in collaboration with King's College London and the University of Reading, UK.

The major spectroscopic techniques used for studying point defects in diamond are absorption, cathodoluminescence, photoluminescence and luminescence-excitation. Additional information can be provided by photoconductivity measurements. All these techniques have been applied successfully in the infrared, visible and ultraviolet spectral regions. The majority of the optical systems in diamond are associated with vibronic centres. These centres have their ground and excited energy levels situated somewhere in the forbidden gap between the valence band and the conduction band. The absorption process produces a sharp zero-phonon line and a band at higher energy; in luminescence a sharp zero-phonon line and a band at lower energy are observed. Absorption spectroscopy is the only truly quantitative technique; if a particular defect produces an absorption band then the absorption coefficient is directly proportional to the concentration of centres present.

The photoluminescence and cathodoluminescence techniques as applied to diamond have previously been described in detail (Collins 1992). Here we simply note that photoluminescence can be a semi-quantitative technique if the intensity of the luminescence is compared to the intensity of the first-order Raman spectrum, and different optical centres can be selectively excited by changing the wavelength of the excitation. Cathodoluminescence, on the other hand, is not a selective process and the intensity of the luminescence bears no simple relationship to the concentration of defects present in the sample.

Luminescence-excitation provides a convenient method of investigating the shape of an absorption band when the absorption is too weak to measure directly. It also provides information about higher excited states of an optical centre. The luminescence from the sample is monitored while the wavelength of the light incident on the sample is scanned using a monochromator or dye laser; a long-wavelength-pass filter prevents the exciting light from reaching the detector. Examples of luminescence-excitation spectra from diamond, recorded using a monochromator or a dye laser, are shown by Clark *et al.* (1992) and Collins *et al.* (1987), respectively.

2. SPECTROSCOPY OF CVD DIAMOND

In a study of polycrystalline diamond films grown by the microwave plasma method at NIRIM, Collins *et al.* (1989) documented a number of cathodoluminescence lines that were not known in natural or synthetic diamond, as well as lines known from studies of conventional diamond to be associated with defect centres involving vacancies or interstitials. In a more recent investigation Khong and Collins (1993) have shown that cathodoluminescence lines at 2.33, 2.42, 2.48, 2.57 and 2.99 eV are characteristic of CVD diamond, whether grown by the microwave, hot filament or combustion flame techniques. In addition many specimens of CVD diamond exhibit a cathodoluminescence line at 1.681 eV. This optical system was first reported by Vavilov *et al.* (1980) in the cathodoluminescence spectra of CVD diamond grown by the thermal decomposition of gaseous carbon compounds in a closed system. From ion-implantation measurements on natural diamond they reached the conclusion that this emission line is associated with a centre containing two interstitial silicon atoms. Vavilov *et al.* also presented evidence to show that the line at 2.33 eV involves nitrogen and vacancies.

Because the 1.681 eV system is seen so frequently in CVD diamond it is one of the most studied optical centres in that material. Collins *et al.* (1990) reported for the first time that the 1.681 eV system could be seen in absorption in some samples, indicating that the defects were present in appreciable concentration. They also repeated the Si-ion implantation measurements of Vavilov *et al.* (1980) and confirmed that this led to the appearance of the 1.681 eV luminescence in natural and synthetic diamonds. In these measurements the 1.681 eV system was most intense in synthetic diamonds with a high substitutional nitrogen concentration, but more recent work (Collins *et al.* 1994), showing that the 1.681 eV absorption can be strong in CVD diamond with a negligible nitrogen concentration, rules out the involvement of nitrogen.

Clark and Dickerson (1991) have shown that the 1.681 eV photoluminescence increases substantially following electron irradiation and annealing at 600° C. The electron irradiation produces vacancies which become mobile at about 600° C, and these measurements suggest strongly that this optical centre is due to a vacancy trapped at the silicon impurity. (Clark and Dickerson have also confirmed that the 1.681 eV system is produced in natural diamond by implantation with Si ions.) Collins *et al.* (1994) have subsequently shown that the 1.681 eV absorption coefficient is greatly increased by electron irradiation and annealing. This measurement provides substantial support for the model proposed by Clark and Dickerson.

The width of the 1.681 eV line in early specimens of polycrystalline CVD diamond was of the order 10 meV at 77 K (See, for example, the absorption and luminescence spectra in Collins *et al.* (1990).) More recently the line width in high-quality CVD material has approached 0.7 meV at temperatures below 50 K, and this has enabled Collins *et al.* (1994) to demonstrate that the 1.681 eV "line" appears to be a doublet with an energy splitting of 0.8 meV. Temperature dependence measurements of the relative intensities of the two components, in the temperature interval 1.7 to 50 K, have indicated that the splitting is in the excited state (Collins *et al.* 1994).

In a collaborative investigation between NIRIM and the University of Reading , photoluminescence measurements have been carried out on high-pressure synthetic diamonds doped with silicon during growth. The 1.681 eV emission system is observed in these crystals, again confirming the rôle played by silicon in this defect, but the linewidths are much sharper (< 0.3 meV at 77 K) than those observed in the polycrystalline CVD diamond studied by Collins *et al.* (1994). Clark *et al.* (1993, 1994) also find that at 77 K the zero-phonon transition is a doublet, with components at 1.6822 and 1.6831 eV, and they, too, find that the higher energy component decreases in intensity as the temperature of the diamond is reduced to 1.7 K. However, the temperature dependence appears more complicated than that observed by Collins *et al.* (1994). Below 60 K each line in the doublet splits into two sub-peaks with a width ≤ 0.1 meV, and the intensity of the higher energy pair does not decrease as rapidly with decreasing temperature as predicted by the Boltzmann distribution used by Collins *et al.* Figure 1 compares the photoluminescence spectra from the CVD diamond used by Collins *et al.* and the silicon-doped high-pressure synthetic diamond studied by Clark *et al.*

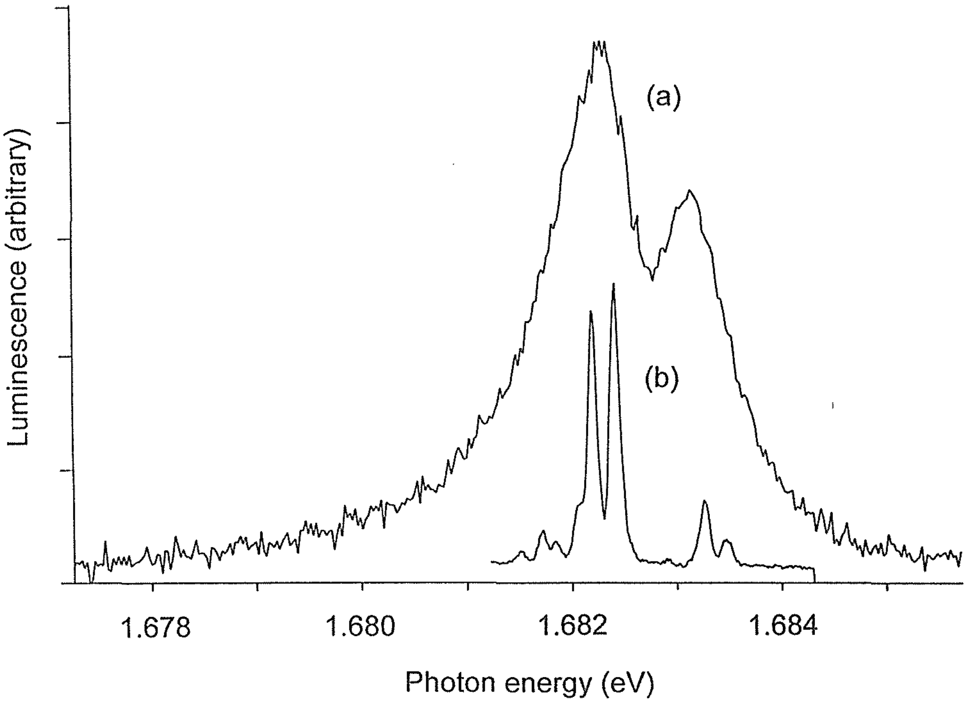

Figure 1. Photoluminescence spectra from (a) a De Beers polycrystalline CVD diamond film at 50 K and (b) a high-pressure synthetic diamond, doped during growth with silicon, recorded with the specimen at 4.2 K.

3. SPECTROSCOPY OF NICKEL IN SYNTHETIC DIAMOND

In a study of synthetic diamond abrasive grit Collins and Spear (1982, 1983) observed a number of absorption and luminescence bands that occurred only in specimens grown using nickel, or a nickel alloy, as the solvent-catalyst. In particular there were vibronic absorption bands with zero-phonon lines at 1.40, 1.883 and 2.51 eV, and a broad featureless band with a maximum near 1.4 eV. The dominant cathodoluminescence in the visible region was a vibronic band with a zero-phonon region at 2.56 eV. The 1.40 eV system observed using CL, for which the zero-phonon transition is clearly resolved as doublet, was also very intense in these diamonds. The 2.56 eV and 1.40 eV CL systems had first been observed in synthetic diamond grit many years previously, but the association with the presence of nickel had not been established.

In a few specimens Collins and Spear (1983) were able to resolve the doublet nature of the 1.40 eV transition in absorption. The relative intensities of the two peaks is constant in CL, but the lower energy peak is "frozen out" in absorption as the temperature is decreased. This shows that the splitting is in the ground state, and Collins and Spear (1983) showed that the thermal activation energy is equal to the spectroscopic splitting. In CL measurements on one large high-quality specimen the zero-phonon region around 2.56 eV (484 nm) appeared to be made up of four overlapping peaks, each with a separation of about 1.6 meV, and Collins and Spear showed that the temperature dependence of this luminescence was consistent with the splitting being in the excited state.

An improved understanding of the nickel-related centres was reached by a collaborative investigation between NIRIM, De Beers and King's College (Collins *et al.* 1990). In that work the optical bands described above were studied in specimens grown using different concentrations of nitrogen. It was found that the 1.883 and 2.51 eV absorption bands were dominant, and the 1.40 eV absorption was very weak, in diamonds with a high nitrogen concentration (~ 250 ppm); the broad 1.4 eV band was the major absorption at intermediate nitrogen concentrations (~ 30 ppm) and at lower nitrogen concentrations (~ 5 to 10 ppm) the 1.40 eV vibronic absorption band was very strong and the 1.883 and 2.51 eV systems were very weak. These measurements suggested that the different absorption bands were associated with different charge states of the nickel impurity. With a high nitrogen concentration the centres are expected to be in a negative charge state, and this appears to be borne out by an approximate correlation between the intensity of the 2.51 eV absorption band and the concentration of negatively charged substitutional nickel atoms detected using electron paramagnetic resonance (Kanda *et al.* 1990). Conversely, diamonds with a low nitrogen concentration give an ESR signal due to Ni^+ (Isoya *et al.* 1990).

Vishnevskiy *et al.* (1975) and Lang (1980) had shown, respectively, that the 2.56 and 1.40 eV CL can be produced only in the {111} growth sectors of synthetic diamond. Collins *et al.* (1990) showed further that all the absorption and luminescence bands that they attributed to nickel occurred exclusively in the {111} growth regions. Lang had also shown that the 1.40 eV emission is strongly polarised, with the $\mathbb{E}$-vector of the emission preferentially aligned with the growth planes, and the polarisation dependence of the zero-phonon doublet was examined in more detail by Collins (1989).

The synthetic diamonds examined in these recent studies have been grown by the temperature gradient method which has the potential to grow large (up to a few mm) diamonds of high crystal quality and controlled impurity incorporation. In specimens grown from an iron-nickel alloy with "getters" to reduce the the nitrogen concentration to a few ppm the components of the 1.40 eV doublet are very sharp, and at low temperatures (10 K) structure due to the 5 stable isotopes of nickel can be detected (Davies *et al.* 1989). In these diamonds the substructure in the 2.56 eV zero-phonon region is also very sharp (Collins *et al.* 1990) but this does not appear to be isotope-related.

Using luminescence-excitation Spear (1990) has demonstrated that the 2.56 eV centre can be very efficiently photo-excited using wavelengths less than 400 nm. In figure 2 we show the photo-luminescence excited by the ultraviolet lines of an argon ion laser at a series of temperatures from 1.8 to 16 K. We see that each of the peaks originally detected by Collins and Spear (1983) is, in fact, a doublet. The lowest energy doublet, not detected in that early work, behaves in a different manner to the other four doublets. At temperatures below 4.2 K the relative intensities of the components in that doublet change, and it is clear that this pair of peaks is not the lowest energy doublet of a group of five, but has a temperature dependence which is unrelated to that of the other four. Work is currently in progress in this laboratory to try to understand this behaviour.

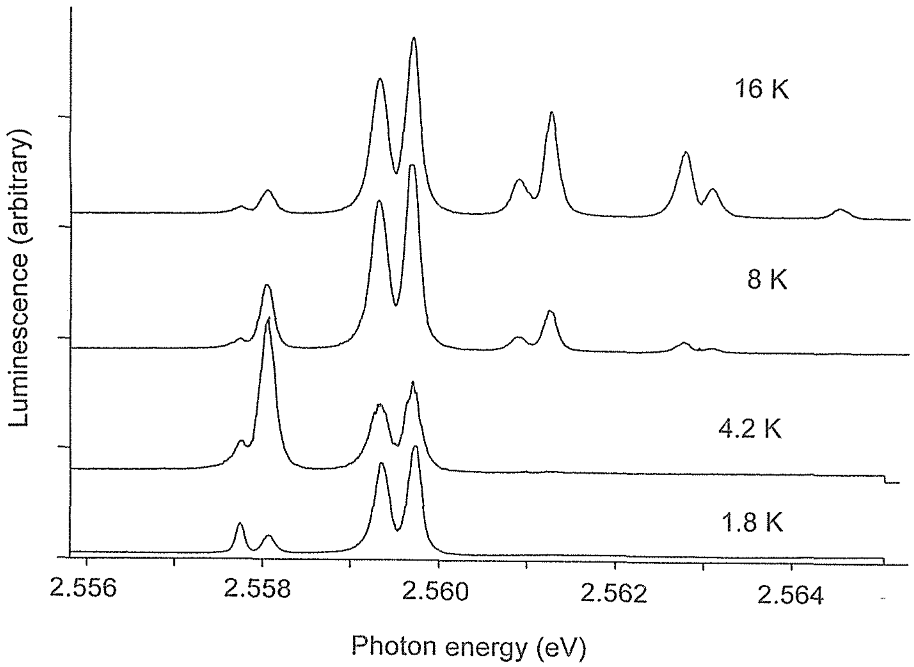

Figure 2
The 2.56 eV (484 nm) zero-phonon region recorded in photo-luminescence at four different temperatures from a high-pressure synthetic diamond grown using Fe-Ni and nitrogen getters to reduce the nitrogen content to around 10 - 20 ppm.

We conclude this section by mentioning briefly recent work at NIRIM on nickel in diamond. When virtually all the nitrogen is eliminated from a synthetic diamond grown using nickel the diamond has a brown colour which is associated with a continuum absorption which increases with increasing energy throughout the visible spectral region. In addition to the 1.40 eV absorption there is a complex zero-phonon region between 1.21 and 1.24 eV. Like the 1.40 eV absorption, this structure shows strong polarisation effects, and is detected only in the {111} growth regions. Furthermore, this absorption and the 1.40 eV absorption show related photochromic effects. Lawson *et al.* (1993) propose that this structure results from a different charge state of the 1.40 eV centre.

Lawson and Kanda (1993) have investigated the changes that occur in the 1.40, 1.883 and 2.51 eV absorption systems as synthetic diamonds grown from different nickel-containing alloys are progressively heated in the temperature range 1500 - 1900° C. They observe the decay of the 1.883 eV and 2.51 eV systems, and the concurrent growth of a complex array of absorption structure - most particularly a vibronic band with a zero-phonon line at 1.693 eV, and a series of sharp lines between 2.2 and 2.6 eV. The work of Lawson and Kanda indicates that the optical centres producing this absorption involve both nitrogen and nickel.

CONCLUSIONS

I have reviewed some of the work in two small areas of diamond physics, showing how spectroscopic measurements are leading to a better understanding of point defects in diamond - in particular silicon in CVD diamond and nickel in synthetic diamond. In both areas the gradual improvement in crystal quality has enabled more detailed spectra to be obtained allowing some phenomena to be interpreted more fully, but, inevitably, raising new issues requiring further investigation.

ACKNOWLEDGMENTS

I am grateful to Dr Colin Clark of the University of Reading for allowing me to show the data in figure 1(b) prior to publication, and to Lars Allers of this laboratory for recording the spectra shown in figure 2, and for his assistance with preparing the diagrams.

REFERENCES

C D Clark, A T Collins and G S Woods (1992) in *The Properties of Natural and Synthetic Diamond* (Ed. J E Field, Academic Press, London).
C D Clark and C B Dickerson (1991) Surface Coatings Technol. **47**, 336 - 43.
C D Clark, H Kanda, I Kiflawi and G Sittas (1993), Diamond Conference, Bristol (unpublished).
C D Clark, H Kanda, I Kiflawi and G Sittas (1994), personal communication.
A T Collins (1989) J. Phys.: Condensed Matter **1**, 439 - 50.
A T Collins (1992) Diamond Relat. Mater. **1**, 457 - 69.
A T Collins, L Allers , C J H Wort and G A Scarsbrook (1994) Diamond Relat. Mater. **3** (in press).
A T Collins, M Kamo and Y Sato (1989) J. Phys. D **22**, 1402 - 5.
A T Collins, M Kamo and Y Sato (1990) J. Mater. Res. **5**, 2507 - 14.
A T Collins, H Kanda and R C Burns (1990) Phil. Mag. B **61**, 797 - 810.
A T Collins and P M Spear (1982) J. Phys. D **18**, L183 - 87.
A T Collins and P M Spear (1983) J. Phys. C **19**, 6845 - 58.
A T Collins, J Szechi and S Tavender (1987) J. Phys. C **21**, L161 - 64.
G Davies (1977) Chem. Phys. Carbon **13**, 1 - 143.
G Davies, A J Neves and M H Nazaré (1989) Europhys. Lett. **9**, 47 - 52.
J Isoya, H Kanda and Y Uchida (1990) Phys. Rev. B **42** 9843 - 57.
H Kanda, A T Collins and J Isoya (1990) Unpublished work.
Y L Khong and A T Collins (1993) Diamond Relat. Mater. **2**, 1 - 5.
A R Lang (1980) Phil. Mag. B **41**, 689 - 98.
S C Lawson and H Kanda (1993) J. Appl. Phys. **73**, 3967 - 73.
S C Lawson, H Kanda and M Sekita (1993) Phil. Mag. B **68**, 39 - 46.
P M Spear (1990) Diamond Conference, Reading (unpublished)
V S Vavilov, A A Gippius, A M Zaitsev, B V Deryaguin, B V Spitsyn and A E Aleksenko (1980) Sov. Phys. - Semicond. **14**, 1078 - 9.
A S Vishnevskiy, V G Malogolovets, A F Nikityuk and L S Posun'ko (1975) Sinteticheskiye Almazy **3**, 215 - 219 (in Russian).

Homoepitaxial CVD Diamond Surfaces and Their Application to Electron Devices

H. Kawarada, H. Sasaki, M. Aoki and K. Tsugawa
School of Science & Engineering, Waseda University, Ohkubo 3-4-1, Shinjuku-ku, Tokyo 169, Japan

The hydrogen-termination effects on the surfaces of homoepitaxial diamonds have been investigated. Both (001) and (111) surfaces of homoepitaxial layers have been investigated by STM in an atomic scale. The surface dangling bonds are terminated by hydrogen atoms. In the metal contacts on the surfaces, the observed S factor, the SBH dependence on metal electronegativity, is 1.0 indicating that the contact properties obey the Schottky rule in p-type semiconductor. In the metals with higher electronegativity such as Au or Pt, ohmic contacts have been obtained. The drastic change from Schottky to ohmic contact on the same surface is one of the evidences of diminished surface states on the hydrogen-terminated diamond surfaces. The coexistence of ohmic and Schottky contacts is advantageous for the MESFET fabrication.

1. INTRODUCTION

The hydrogen-termination on diamond surfaces is expected to be effective in the reduction of the surface states. If the surface states are decreased, the diamond Schottky barrier heights (SBHs) might become metal-dependent. So far Schottky characteristics have no dependence on metal work function or electronegativity [1-3], because these diodes are usually fabricated on KNO_3 or CrO_3 treated surfaces [1-3] where oxygen atoms are adsorbed. The surfaces are called as 'oxygen adsorbed surface' later in this paper. The surface states are observed by valence electron spectra on the surface.

In our preliminary work [4] , on as-grown CVD diamond layers where the surfaces are terminated by hydrogen atoms, Schottky or ohmic contacts can be separately formed according to the metal electronegativity below or above 1.8. Since the samples are polycrystalline and the surfaces are not well-defined, the reliable SBHs could not be measured.

In this study, on both (111) and (001) surfaces of homoepitaxial films we have investigated the metal contacts based on the atomic scale characterization using scanning tunneling microscopy (STM). P-type semiconducting surfaces on the as-grown films are used for electric conduction. The surface conduction is considered to be hydrogen related, i.e., the deep level passivation due to hydrogen termination [5] or the band bending due to hydrogen termination at the surface [6]. The metal/diamond contact properties are linked with the result of the STM observation.

2. EXPERIMENTAL

The homoepitaxial diamond films were grown by microwave plasma CVD. The reaction gas was CO(5-10%) diluted with H_2. The total gas flow rate was normally 0.2 l/min and the pressure was 35 Torr. The substrates were high-pressure synthetic diamond (001) (1.5 x 2.0 x 0.3 mm in size). The substrate temperatures were kept around 800-900°C during deposition.

The depositions are completed with the pure hydrogen plasma treatment at 35 Torr for 1 min. to remove non-diamond carbon layers which are formed by residual carbon gas at the temperature descending process. The p-type surface conduction is observed on the surfaces. The popular surface oxidation treatment such as CrO_3 treatment was not carried out in our case. Tunneling currents in STM and metal contact properties are measured using the surface semiconducting layer of undoped epitaxial films.

The surfaces of homoepitaxial CVD diamonds have been characterized by atomic scale STM using Seiko SAM 3000 type. Macroscopic surfaces were observed by high energy reflection electron microscope.

Point contacts were formed by 14 kinds of metals and deposited contacts were fabricated by 5 kinds of metals on the homoepitaxial CVD diamonds. Ag paste as ohmic contacts covered a periphery of the surface and four sides of the sample. Hole conduction is limited in the surface p-type conductive layer. The current-voltage (I-V) characteristics were measured using a pico ampere meter combined with a voltage source (HP 4140B type).

3. STM OBSERVATION OF HOMOEPITAXIAL DIAMOND SURFACES

Both (111) and (001) surfaces of homoepitaxial diamond have been examined by atomic scale STM. The atomic scale image of (111) surface (Fig.1). shows a hexagonal pattern with a distance between the individual bright spot of 0.25 nm. Adsorbates are observed as bright protrusions on the terrace in addition to the hexagonal structure. The hexagonal pattern corresponds to the position of carbon atoms of the unreconstructed (111) diamond surface with a dangling bond per carbon atom. The surface dangling bonds are already terminated by hydrogen atoms in the hydrogen rich plasma as shown in the structure model shown in Fig.2. The individual spot of the STM images is due to hydrogen atom.

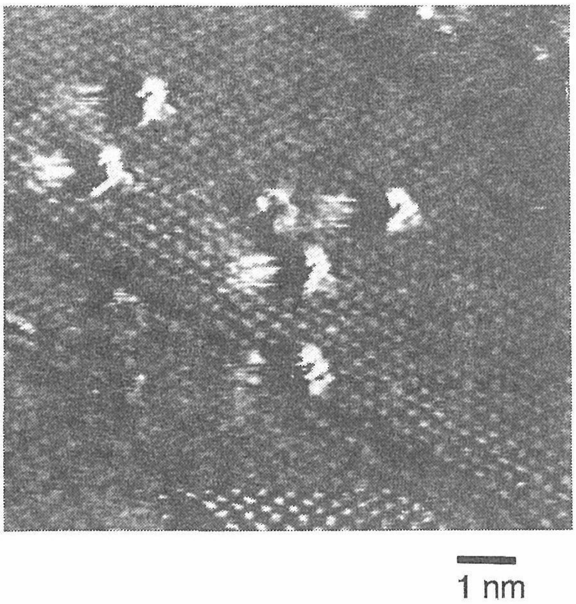

Fig.1 STM image of homoepitaxial CVD diamond (111).

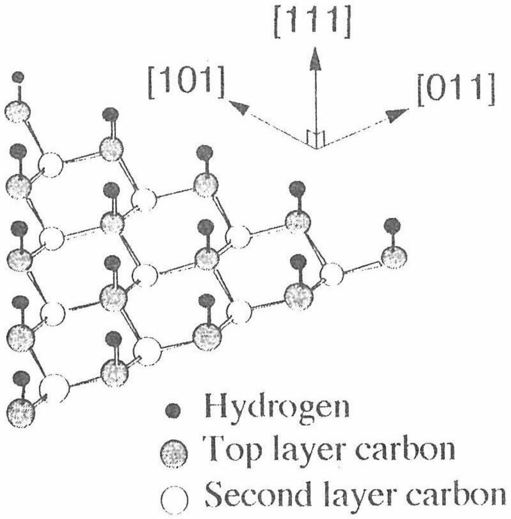

Fig.2 Schematic of hydrogen terminated diamond (111) 1x1 structure.

As grown (001) surfaces of homoepitaxial CVD diamonds exhibit 2x1 [7,8]. In the atomic scale STM images shown in Fig. 3, the dimer rows are reproducibly observed on the as-grown (001) surfaces if tip conditions are optimized [9]. Double domains are recognized by the two directional dimer rows observed in Fig. 3(a) as the white stripes oriented along perpendicular direction. The distance of the dimer rows is 0.5 nm. Each dimer is resolved in the enlarged view shown in Fig. 3(b). The distance of each dimer is 0.25 nm. The 2x1 reconstruction disappears after the popular surface chemical treatment using KNO_3 or CrO_3. The hydrogen termination is lost simultaneously at this stage.

From the tunneling spectroscopy measurement the as-grown (001) surface is p-type semiconducting from an asymmetric current-voltage curve of tunneling current and keeps a wide bandgap nature of diamond. Spectrum corresponding to surface states has not been found until now. The dangling bonds which cause surface states are thought to be terminated by hydrogen.

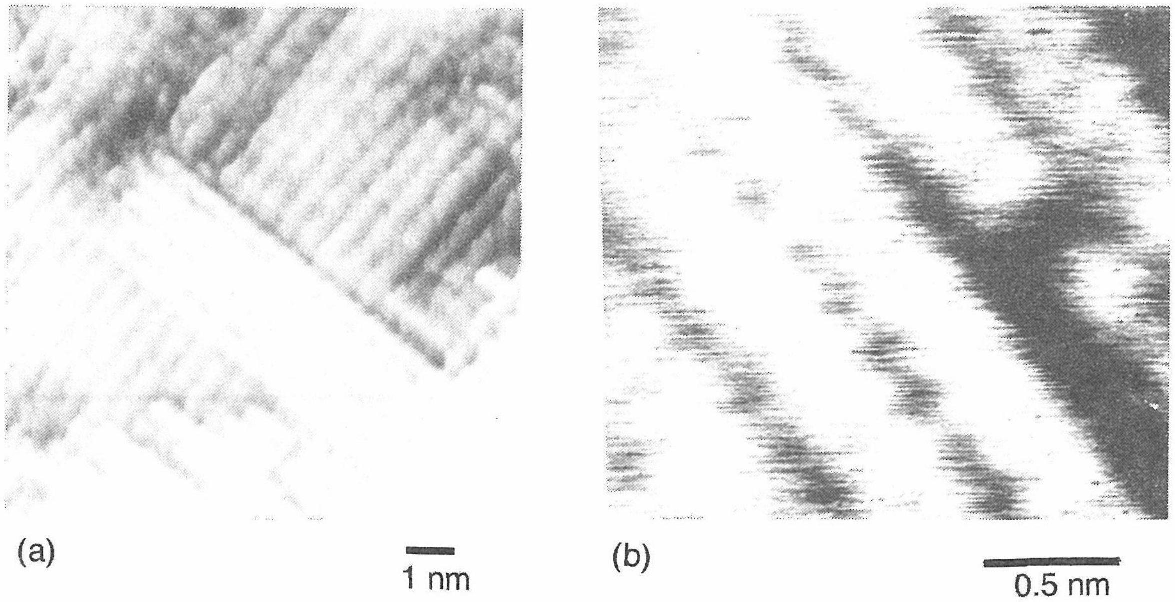

Fig.3 STM images of homoepitaxial CVD diamond (001).
(a) general area. (b) enlarged area. A white oval corresponds to a dimer.

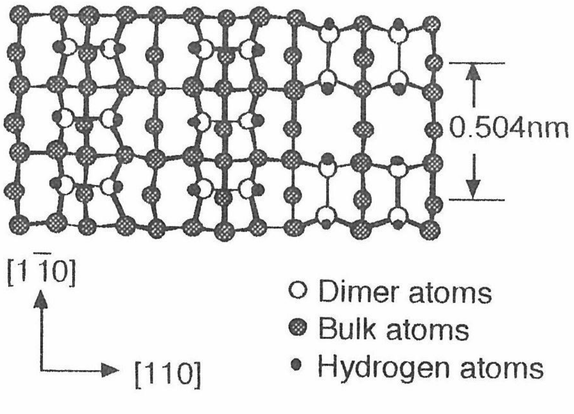

Fig.4 Schematic of hydrogen terminated diamond (001) 2x1 structure.

4. METAL CONTACTS ON HOMOEPITAXIAL DIAMOND SURFACES

The SBHs have been measured by I-V methods in 14 kinds of metals. The I-V characteristics of a Pb point contact and a Pb deposited contact on an undoped homoepitaxial diamond (001) are shown in Fig. 5. The surfaces are reconstructed to be the 2x1/1x2 structure. The linear region in the semilogarithmatic plots extend as much as 5 orders in the point contacts. The ideality factors are 1.04 in the point contact and 1.66 in the deposited contact. The ideality factors in point contacts using Al, Pb, and Zn are averaged 1.1-1.3 which is the nearest to unity ever reported in diamonds. And those of Al and Pb in evaporated contacts (0.3 mm in diameter) are averaged to be 1.6. The best ideality factors on the oxygen adsorbed surfaces are reported to be around 2. In the present experiments it is found that the metals having relatively lower electronegativities exhibit good Schottky characteristics from the points of ideality factor and rectification ratio. The improved ideality factors are due to the macroscopic surface flatness of the homoepitaxial films and the well defined (001) 2x1 structures in atomic scale.

The reason why the ideality factors of point contacts are better than those of evaporated contacts is not clear. We speculate that the reaction between metal and diamond at the deposition process leads to the destruction of C-H bondings on the surfaces and the formation of carbides. They are harmful for Schottky diode characteristics.

The properties of Schottky contacts on (111)1x1 surfaces are not as good as those of (001)2x1. The observed adsorbates on the (111) surfaces appeared in Fig. 1 are detrimental for the metal contacts. These adsorbates are not observed on (001) surfaces by STM.

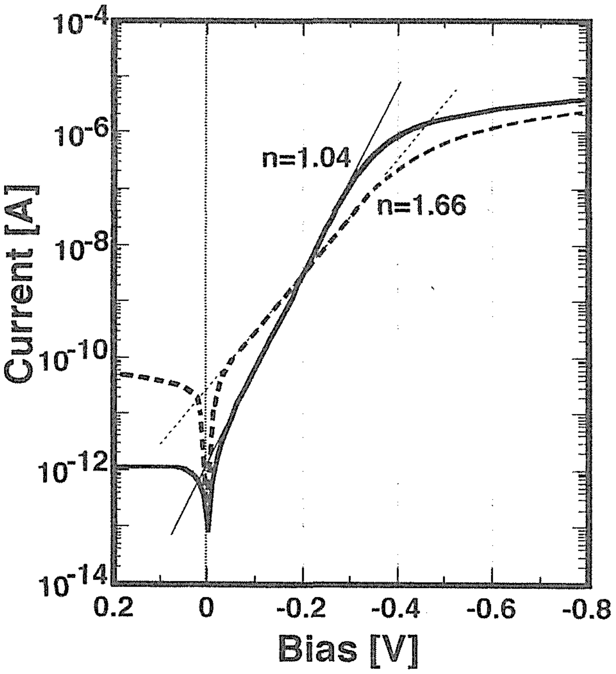

Fig.5 Current-voltage characteristics of Pb point contact (solid curve) and deposited contact (dotted curve) on homoepitaxial CVD diamond (001).

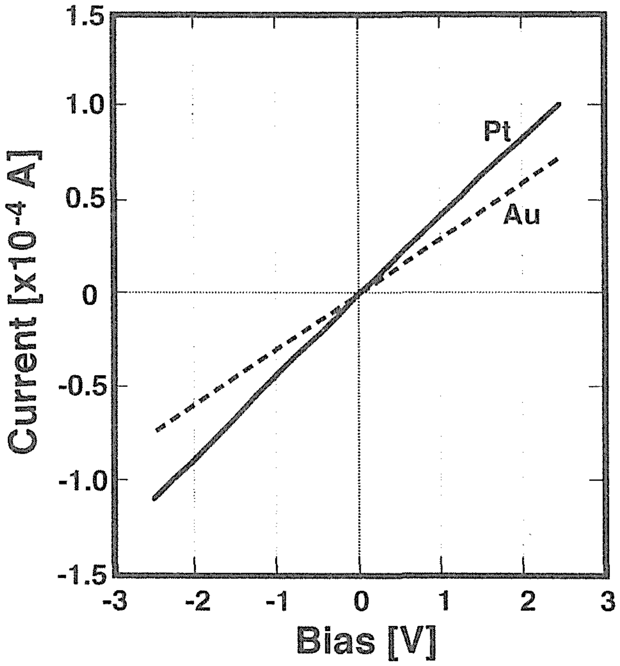

Fig.6 Current-voltage characteristic of Au and Pt contacts on homoepitaxial CVD diamond (001).

In the metals with higher electronegativities such as Au or Pt, ohmic contacts have been obtained. Au contact is shown in Fig. 6. This kind of ohmic contact has never been obtained on the oxygen adsorbed surfaces [4].

The relationship between the metal electronegativities and SBHs of corresponding metals is shown in Fig.7 [10]. As the metal electronegativities increases the SBH decreases. The S factor, the SBH Φ_{SBH} dependence on metal electronegativity χ_m ($S = d\Phi_{SBH}/d\chi_m$) [11], is 1.0 indicating that the contact properties comparatively obey the Schottky rule in p-type semiconductor. Moreover, the extrapolated SBH in Fig.7. become zero in the electronegativity above 2.2 corresponding to those of Au or Pt. The ohmic contact at higher electronegativities becomes reasonable considering this trend shown in Fig.7. The overall tendency in Fig. 7 implies that the surface states are effectively reduced at the hydrogen terminated diamond (001) surfaces for the first time.

The change from Schottky to ohmic contact by the variation of metal electronegativity can be explained if the electron affinity of the hydrogen terminated CVD diamond surfaces is near zero or minus [12] as reported previously. The coexistence of Schottky and ohmic contacts on the same surface is advantageous for the fabrication of metal semiconductor FET (MESFET). A very thin semiconducting layer on an insulating substrate is an ideal structure for the MESFET operation. In the present case, this kind of structure can be realized using the p-type semiconducting surface on undoped diamond as shown in Fig.8.

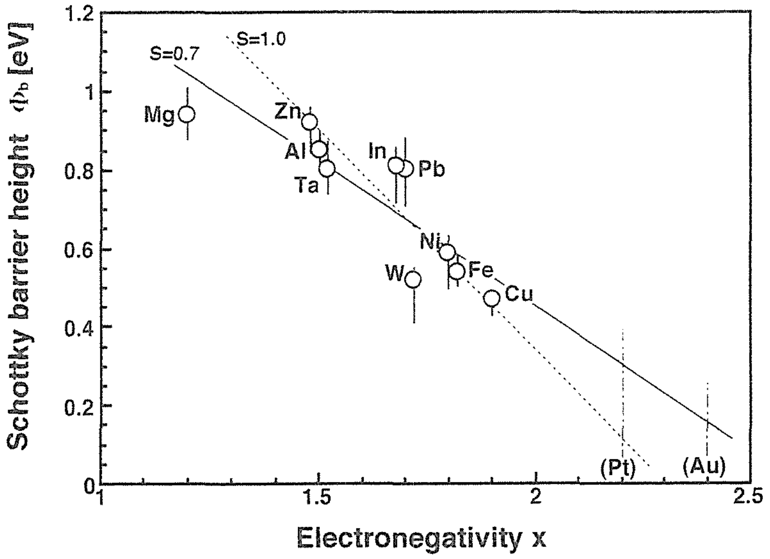

Fig.7 SBHs of various metals on homoepitaxial CVD diamonds as a function of metal electronegativity.

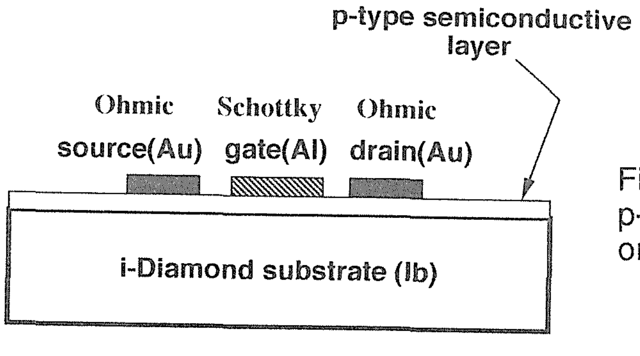

Fig.8 MESFET structure using a surface p-type semiconduciting layer on undoped homoepitaxial diamond.

5. CONCLUSIONS

On the homoepitaxial surfaces of (111) and (001) diamonds, the atomic surface structures and the metal contact properties have been investigated.

1) The hexagonal pattern due to (111) 1x1 structure and the dimer rows on (001) 2x1 structure have been reproducibly observed by the atomic scale STM images.. One dangling bond per carbon atom is terminated by one hydrogen atom in both cases.

2) On the (001) 2x1 surfaces, the highest quality Schottky diodes with the ideality factors being the nearest to unity ever reported in diamonds have been obtained using the metals with low electronegativities.

3) The SBH depends on the metal electronegativity and ohmic contacts have been obtained in the metals with higher electronegativities. It indicates that the surface states are effectively reduced by the hydrogen terminated (001) 2x1 surface. Moreover, the surfaces with p-type semiconducting property lead to an ideal structure for the fabrication of MESFET.

ACKNOWLEDGEMENTS

The authors are grateful to Mr. N. Fujimori of Sumitomo Electric Industries, Ltd. and Mr. S. Yamashita of Tokyo Gas Co., Ltd for their cooperation. They also wish to thank Mr. S. Morimoto and Mr. Y. Shimura of Micro Technology Lab. in Waseda University for their technical supports. This work was supported in part by a Grant-in-Aid for General Scientific Research (No. 04650658) from the Ministry of Education, Science and Culture of Japan.

REFERENCES

1) G.H.Glover, *Solid State Electron.* **16** (1973) 973.
2) C.A.Mead and T.C.McGill, *Phys. Lett.*, **58A** (1976) 249.
3) G.Sh.Gildenblat, S.A.Glot, and A.Badzian, *Proc. the IEEE,* 79 (1991) 647.
4) Y.Mori, H.Kawarada, and A.Hiraki, *Appl. Phys. Lett.* **58** (1991) 940.
5) M.I.Landstrass and K.V.Ravi, *Appl. Phys. Lett.* **55** (1989) 1391.
6) T.Sugino and J.Shirafuji, *Diamond Related Materials* 2 (in press).
7) H.Shiomi, K.Tanabe, and N.Fujimori, *Jpn. J. Appl. Phys.* **29** (1990) 34.
8) T.Tsuno, T.Imai, Y.Nishibayashi, K.Hamada, and N.Fujimori, *Jpn. J. Appl. Phys.* **30** (1991) 1063.
9) H.Kawarada and H.Sasaki , (submitted to J. Vac. Sci. Technol).
10) M.Aoki and H.Kawarada, (submitted to Jpn. J. Appl. Phys.)
11) S.Kurtin, T.C.McGill and C.A.Mead, *Phys. Rev. Lett.* **22** (1969) 1433.
12) F. J. Himpsel, J. A. Knapp, J. A. VanVechten and D. E. Eastman, *Phys. Rev.* **B20** (1979) 624.

Donor and Acceptor Diamond Film Doping

B.V. Spitsyn
Institute of Physical Chemistry, Russian Academy of Sciences, Leninsky
Prospekt 31, Moscow 117915, Russia

Abstract

There were considered goals and benefits of diamond doping in the course of its growth from vapor phase. There were indicated opportunities to get as equilibrium so nonequilibrium doping. In an approximation of carbon-element bond energy redistribution coefficient for boron and phosphorus between growing diamond film and gaseous crystallization medium have been calculated. The results of calculations became in the reasonable agreement with experimental data obtained by different techniques of diamond film growth. As acceptor so donor doping of diamond are possible. But by acceptor doping of diamond material by phosphorous its efficiency depends drastically from coexistence in diamond lattice intrinsic and impurity defects , particularly as chemically bonded hydrogen.

1. Introduction

Recent progress in diamond CVD open many ways to diamond and diamond films as high-tech materials. To-date activity in area of growth of single-crystalline and polycrystalline diamond films (DF) reveals many goals and benefits of diamond film doping. The prospects for the research and the development are very challengeable. Actually, diamond film doping open following opportunities:

- to study kinetics of homogeneous and heterogeneous (on growing diamond surface) reactions,
- to establish a growth mechanism of crystal (layer-by-layer, normal etc.),
- to change optimal range of parameters (e.s. crystallization temperature) for DF growth,
- to get as equilibrium so nonequilibrium doping,
- to use new chemical system for diamond CVD,
- precise control of dopant concentration, and it chemical and just energetic state before bonding to diamond lattice,
- to grow ultra-thin (till sub-micrometer thickness) uniformly doped diamond films,

– to synthesize diamond films with desirable spatial dopant distribution and also to grow multilayer diamond structures.

The putting in diamond intrinsic and impurity defects are sole ways to change in desirable direction physical, chemical and mechanical properties of diamond. Defect origination and its interaction proceeds usually in *nonequlibrium conditions. Generation of electrically active dislocations by* impulse laser action [1] and by driving in impurities by ion implantation[2] have been performing at extremely nonequilibrium and/or nonstationary conditions. It impedes the control of desirable defect formation.

It is why in the present time most attention paid to doping of diamond films in the course of it growth from vapor phase.

2. Geometrical and energetic factors for diamond doping

For estimation of opportunity of light element introducing as substitution impurity there were proposed to use the value of single bond length between carbon atom and of corresponding element atom and also value of the bond energy[3]. The corresponding values and it relative difference in the comparison with geometrical and energetical parameters of diamond lattice listed in the Table 1.

Table I. Geometrical and energetical parameters of single element-carbon bonds

Element	Covalent radius (A)	Relative radii difference $\frac{R_3 - R_C}{R_C}$x100, %	Element-carbon bond energy (kcal/mol)	E-C to C-C bond energy difference (kcal/mol)
C	0,77	0	83	0
B	0,85	+ 10,4	89	+ 6
N	0,70	– 9,1	73	– 10
P	1,10	+ 43	62	– 21
S	1,04	+ 35	63	– 20

By using of the Table 1 necessarily take in the mind that the accumulated data have been obtained on the base geometrical and energetic parameters such element-organic molecules like $B(CH_3)_3$, $N(CH_3)_3$, $P(CH_3)_3$ and $S(CH_3)_2$ with ordinarily element-carbon σ-bonds. But by introduction of corresponding atom in the substitution position in diamond lattice two serious peculiarities arise. Firstly the coordination number of impurity atom by its situation in substitutional position should be equal to four. Secondary as sequence of the first the atom could be to reveal donor (nitrogen, phosphorus, sulfur) or acceptor (boron) behaviour in the relationship to surrounding diamond lattice. It result to origination of permitted energetic level of donor or acceptor type in forbidden energetic gap of perfect single crystalline diamond (5.5 eV). The theoretical calculation of permitted levels of energy give not very save results to-date because not comprehensiveness of theory of solid state.

3. In-the-growth diamond doping

It is why the main hope in the solution now of dimond doping problem give mainly experimental techniques based on diamond CVD. Some of them will be shortly discussed in this communication.

Initial and very important steps of in the course of diamond growth doping are heterogeneous processes what involve breaking bonds in carbon and dopant precursors and formation of new chemical (carbon-carbon and carbon-element) bonds on diamond surface. At this step coordination number and energetics of dopant atom start to accommodate to its position in the bulk of diamond lattice.

In this stage, especially at low temperatures of chemical crystallization process, there is possible nonequilibrium doping. It means that excessive or deficient capture af impurity element proceeds (at crystallization temperature below about 800 °C). At the temperature ~900 °C obviously take place much more equilibrium conditions, and equilibrium destribution coefficient of most important impurities in diamond reasonable to estimate according to bond energy data (Table I). Qualitatively ratio:

$$K_E = (E/C)_{DF} \ / \ (E/C)_{\text{vapor phase}}$$

should be dependent from E_{C-E} to E_{C-C} difference.

Thermochemical calculation for 1200 K give distribution coefficients. They are for B and P equal to:

$$K_B \simeq \exp\ (6000 \ / \ 1.98 \cdot 1200) = 12.5$$

and

$$K_P \simeq \exp\ (- \ 210000 \ / \ 1.98 \cdot 1200) = 1.4 \cdot 10^{-4}$$

Above results are in reasonable agreement with experimental data [4-6,8]. Our results of diamond film doping in the chemical transport reaction summarized in Table II.

Table II. Some characteristics of in-the-growth doped diamond films

Dopant	Dopant concentration, atom·cm^{-3}	Specific resistence, Ohm·cm	Film thickness, um	E_a, e V	Conductivity type
Boron	$1.7 \cdot 10^{19}-4.5 \cdot 10^{21}$	$10^6-2 \cdot 10^{-3}$	0.1-2	0,37-0.05	p
Phosphorus	$5 \cdot 10^{18}-5 \cdot 10^{21}$	10^5-10^1	0.05-1	0.11-0.04	n
Sulfur	10^{20}	10^5-10^3	0.051	0.17	n*

*) according to high nonohmicity of electrical contacts to sulfur doped DF.

In more recent publications have been attained also high diamond film doping level by phosphorus [7,8]. Probably not high conductivity of diamond film [7] originates from bonded hydrogen [8] and another impurity and/or intrinsic defects. It is why necessary careful study of hydrogen concentration and bonding state in diamond films [9].

4. Conclusions

To summarize this paper we put forward following conclusions:

- diamond doping have many challengeable goals and benefits for fundamental science and new technology,
- as acceptor, so donor diamond film doping are possible,
- numerical estimations of redistribution coefficients between diamond film contained boron and phosphorous, and crystallization medium are in reasonable agreement with experimental data.

Donor doping by phosphorous obviously is very sensitive to presence of intrinsic and impurity (like bonded hydrogen) defect in diamond material,

- the effective and comprehensive solving of problems related to diamond doping requests interdisciplinary and international cooperation.

References

1. N.D.Samsonenko, V.V.Tokiy, S.V.Gorban, V.I.Timchenko, Diamond Films-90, Abstracts (1990) 14.17.

2. V.S.Vavilov, Phys.Stat.Solidi (a)31 (1975) 11.

3. B.V.Spitsyn and A.E.Alexenko, Arch.Nauki Mater. 7 (1986) 111.

4. A.E.Alexenko and B.V.Spitsyn, Diamond and Related Materials, 1 (Elsevier Science Publishers B.V., Amsterdam, 1992) p.705.

5. B.V.Spitsyn and A.E.Alexenko, Proc. 2-nd Symposium of Electrochem. Soc. on Diamond Materials (1991), p.597.

6. K.Nishimura, K.Das, J.T.Glass, K.Kobashi, R.J.Nemanich, In: R.Freer (ed.). The Physics and Chemistry of Carbides: Nirides and Borides (1990) p.183.

7. N.Setaka, Mat.Res.Soc.Symp.Proc. Vol.152 (1989) p.3

8. M.Kamo, H.Yurimoto, T.Ando, and Y.Sato, Proc. 2-nd ICNDST. Eds. R.Messier J.T.Glass, J.E.Butler, and R.Roy. MRS, Pittsburgh (1991) 637.

9. T.Sung, S.Khasawinah, W.H.Miller, B.Spitsyn, G.Popovici, M.A.Prelas, E.J.Charlson, E.M.Charlson, J.M.Meese, T.Stacy, G.Manning, S.K.Loyalka, and R.Tompson, Diamond Films'93, 4-th European Conference on Diamond, Diamond-like and Related Materials, Abstracts (1993) 9.113.

Polycrystalline Diamond Devices-Fabrication and Characteristics

Koji Kobashi, Kozo Nishimura and Koichi Miyata
Kobe Steel, Ltd., Electronics Research Laboratory, Takatsuka-dai 1-chome, Nishi-ku, Kobe 651-22, Japan

Abstract

Fabrication and characterization of two basic devices, diodes and field effect transistors, made of B-doped semiconducting polycrystalline diamond films, are described. The diode has a trilayer MiS structure consisting of an aluminum electrode, undoped diamond and semiconducting B-doped p-type diamond, fabricated on a low-resistivity Si substrate. The transistor has three electrodes for source, gate and drain with a linear configuration, where the gate region has the same structure as the MiS diode. The fabricated diodes showed a good rectification up to 300 °C, while the transistors exhibited a drain current modulation and cut-off up to 200 °C.

1. INTRODUCTION

Diamond is known to have many interesting properties for electronic applications, and feasibility studies of diamond devices are extensively carried out, including rectifying[1,2] and ohmic[3] contacts, and field effect transistors (FETs).[4-8] At the present stage of diamond device research, it is most important to establish microfabrication technologies such as selective deposition of diamond, doping, formation of ohmic and rectifying contacts, and reduction of contact resistance. To this end, polycrystallind diamond (PCD) films are most relevant because a relatively wide area is available.

In this paper, MiS-type diodes and FETs were fabricated using PCD films. It was demonstrated that MiS diodes exhibit a high rectification, while MS diodes showed only a poor rectification. On the other hand, it was not obvious at the beginning that FETs made of PCD films would be operational as PCD films have a low carrier mobility (on the order of 1 cm^2/V-s) due to grain boundaries and random orientation of diamond grains. However, in the present work, modulation and cut-off of the drain current were achieved for the first time in the PCD MiS-type FET.

2. METAL/INTRINSIC DIAMOND/SEMICONDUCTING DIAMOND (MiS) DIODE

2.1 Fabrication process

The MiS diode structure is shown in Fig. 1. It has a multilayer structure of a metal (Al) thin film electrode, an intrinsic semiconductor interlayer (undoped diamond), and a semiconductor layer (B-doped p-type diamond), fabricated on a low-resistivity Si substrate which is used as an opposite electrode.[9,10]

The substrate used was a 20 mm x 10 mm p-type Si with a resistivity of less than 0.1 Ω-cm, which were polished for 1 hour using 0.25 μm diamond paste. The B-doped PCD layer was deposited by microwave plasma chemical vapor deposition (MPCVD)[11] using 0.5% CH_4/H_2 and 1 ppm B_2H_6 as the source gas (the B/C ratio was 400 ppm). The substrate temperature, gas pressure, total gas flow rate, and deposition time were 800 °C, 35 Torr, 100 cc/min, and 7 hrs, respectively. The undoped diamond layer was deposited for 2 hours by MPCVD using 0.5% CH_4/H_2 and 0.1 % O_2. The estimated layer thicknesses was about 0.4 µm. The sample was then annealed at 850 °C for 30 min in vacuum, followed by CrO_3:H_2SO_4 and RCA cleanings. For electrodes, 0.2-µm thick Al film dots of 100 µm in diameter were photolithographically formed. Finally, the samples were pasted on a Cu plate with a silver paste.

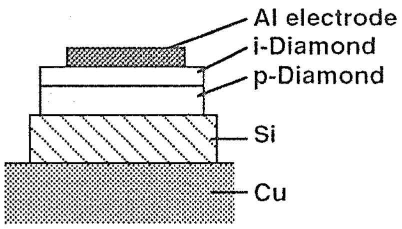

Fig. 1. Cross-sectional view of the MiS diode.

2.2 Current-voltage characteristics

Semi-logarithmic I-V characteristics of a MiS diode at room and high temperatures are shown in Fig. 2. In the forward bias state at room temperature, the turn-on voltage was 0.8 V, which decreased at elevated temperature. The rectification ratio at 5 V was 10^7 at room temperature, and decreased to 10^3 at 300 °C. From an Arrhenius plot of the reverse leakage current, an activation energy of 1.0 eV was obtained. This value is similar to that reported previously for undoped PCD films,[12] indicating that the undoped diamond layer is responsible for the potential barrier in the reversed bias state. By contrast, it was found (not shown) that the rectification ratio at 5 V was only 3 for a MS diode which were fabricated in a similar manner.

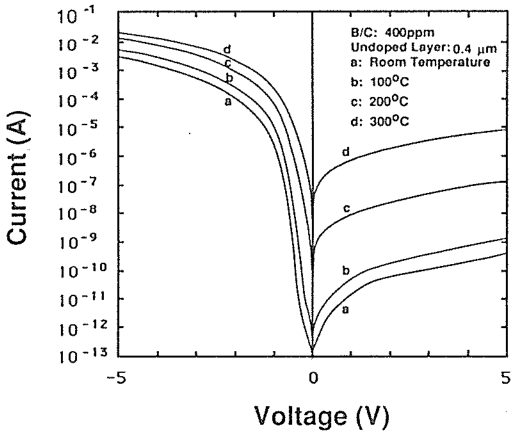

Fig. 2. I-V characteristics of a MiS diode at (a) room temperature, (b) 100 °C, 200 °C, and (d) 300 °C.

3. MiS FIELD EFFECT TRANSISTOR

3.1 FET structure

A schematic diagram of top and cross-sectional views of the fabricated MiSFET is shown in Fig. 3. It has a linear configuration with source and drain (Ti/Au) and gate (Al) electrodes. The gate length, the length of the undoped diamond layer under the gate electrode (gate insulator), the gate width, and the source-to-drain distance were 5, 10, 500 and 10 µm, respectively. Note that the gate structure is the same as the MiS diode, and the FET is operated in the depletion mode with a reverse bias voltage applied to the gate electrode.

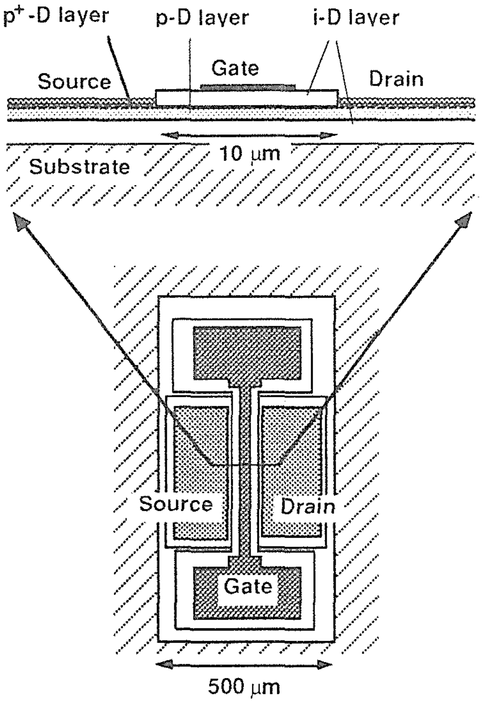

Fig. 3. Schematic diagram of MiSFET.

3.2 Fabrication process

For substrates, sintered, insulating Si_3N_4 was used, which had been polished with 1-µm diamond paste. First, 5-µm thick undoped diamond layer was grown on the substrate. Then a B-doped diamond layer was selectively deposited[13] by MPCVD using 0.5% CH_4/H_2 and 0.5 ppm B_2H_6. The estimated thickness of the B-doped layer was only about 0.03 µm with a doping concentration of about 5×10^{18} cm^{-3}. In order to reduce the contact resistance for the source and drain electrodes, a heavily B-doped (p^+) diamond layer with a thickness of 0.3 µm was selectively deposited in the source and drain electrode areas. The B-doping concentration in the p^+ layer was 10^{20} to 10^{21} cm^{-3} and the contact resistivity for Ti/Au electrodes was less than 10^{-4} Ω-cm^2. The gate insulator was selectively deposited to a thickness of 0.6 μm in the gate electrode region by MPCVD. The sample was annealed in vacuum, followed by CrO_3 and RCA cleanings. Finally, electrodes were formed by photolithography.

3.3 *MiSFET characteristics*

The drain current-voltage (I_D-V_D) characteristics of the fabricated MiSFET at room temperature and 200 °C are shown in Figs. 4. It is seen that I_D was modulated by the gate bias V_G and almost entirely cut off when V_G was greater than 24 V. The transconductance (g_m) was 43 and 530 pS/mm at room and 200 °C, respectively. The saturation in I_D at high V_D was not obvious because the series resistance of the channel layer is significantly high.

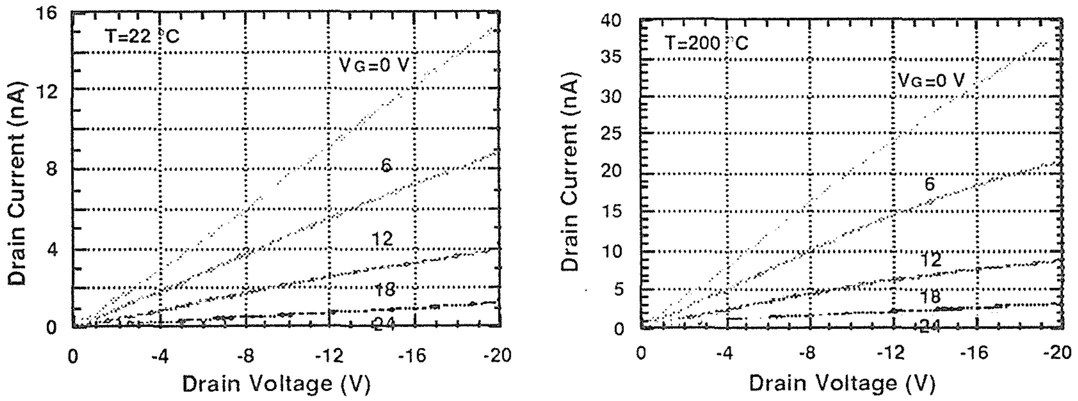

Fig. 4. I_D-V_D characteristics at room temperature and 200 °C.

4. CONCLUSION

MiS diodes and MiSFETs were fabricated using combinations of undoped and B-doped PCD films. The MiS diodes exhibited high rectification ratios of 10^5-10^6 at 5 V, which were significantly higher than the corresponding values for a MS diode. The rectification ratio of a MiS diode at 5 V was as high as 10^3 even at 300 °C. The MiSFET exhibited drain current modulation and cut-off from room temperature up to 200 °C. These results clearly indicate that CVD diamond films can be used for high-temperature electronic device applications.

ACKNOWLEDGMENTS

The author would like to thank K. Nishimura, K. Miyata, K. Kumagai, H. Koyama, K. Saito of Electronics Research Laboratory, Kobe Steel, Ltd., for input of information for this paper. He also acknowledges Dr. D. Dreifus of Electronic Materials Center, Kobe Steel USA Inc., for valuable discussion.

REFERENCES

1. M. W. Geis, D. D. Rathman, D. J. Ehrlich, R. A. Murphy and W. T. Lindley: IEEE Electron Device Lett. **EDL-8** (1987) 341.
2. S. A. Grot, G. Sh. Gildenblat, C. W. Hatfield, C. R. Wronski, A. R. Badzian, T. Badzian and R. Messier: IEEE Electron Device Lett. **11** (1990) 100.
3. K. L. Moazed, R. Nguyen and J. R. Zeidler: IEEE Electron Device Lett. **9** (1988) 350.
4. H. Shiomi, Y. Nishibayashi and N. Fujimori: Jpn. J. Appl. Phys. **28** (1989) L2153.
5. G. Sh. Gildenblat, S. A. Grot, C. W. Hatfield and A. R. Badzian: IEEE Electron Device Lett. **12** (1991) 37.
6. K. C. R. Zeisse, C. A. Hewett, R. Nguyen, J. R. Zeidler and R. G. Wilson: IEEE Electron Device Lett.**12** (1991) 602.
7. A. J. Tessmer, K. Das and D. L. Dreifus: Diamond and Related Mater. **1** (1992) 89.
8. R. J. Trew, J-B. Yan and P. M. Mock: Proc. IEEE **79** (1991) 598.
9. K. Miyata, D. L. Dreifus and K. Kobashi: Appl. Phys. Lett. **60** (1992) 480.
10. H. Shiomi, Y. Nishibayashi and N. Fujimori: Jpn. J. Appl. Phys. **29** (1990) L2163.
11. K. Kobashi, K. Nishimura, Y. Kawate and T. Horiuchi: Phys. Rev. **B38** (1988) 4067.
12. K. Miyata, D. L. Dreifus, K. Das and K. Kobashi: *Diamond Materials,* eds. A. J. Purdes, B. M. Meyerson, J. C. Angus, K. E. Spear, R. F. Davis and M. Yoder (The Electrochemical Society, Pennington, NJ, 1991) p. 543.
13. T. Inoue, H. Tachibana, K. Kumagai, K. Miyata, K. Nishimura, K. Kobashi and A. Nakaue: J. Appl. Phys. **67** (1990) 7329.

Diamond Substrate Interactions and the Adhesion of Diamond Coatings

Benno Lux and Roland Haubner
Technical University, Vienna, Austria

ABSTRACT

Formation of a diamond coating on a substrate requires a stable substrate surface, especially during early deposition stages.

In many cases hydrogen and/or carbon react with the substrate surfaces to form gases or solid carbide layers, to dissolve carbon, etc., leading to changes in the diamond nucleation and growth. Certain substrate elements with high vapor pressures can also cause detrimental effects.

All these interactions can affect the adhesion of the diamond coatings. Intermediate layers applied prior to diamond deposition might finally prove to be one of the best possible solutions for minimizing such detrimental substrate interface effects.

KEY WORDS: CVD diamond, nucleation and growth, vapor pressure, substrate/gas and diamond/substrate interactions, substrate surface treatments, intermediate layers, adhesion.

---

1. INTRODUCTION

Very few materials are inert to the aggressive gas atmosphere needed for low-pressure diamond synthesis. Changes in the substrate surface occurring during deposition can significantly influence diamond nucleation, growth and the adhesion of the final diamond coating [1-5].

Atomic (H^o), molecular hydrogen (H_2) and carbon species cause reactions, especially with ceramics, modify certain metallic substrates, and can form intermediate layers, thus delaying the onset of diamond nucleation, growth and the coating formation.

Atomic hydrogen is essential for avoiding the formation of non-sp^3 carbon. The C/H ratio and the amount of atomic hydrogen are critical parameters. For proper diamond nucleation and growth also the carbon supersaturation in the gas phase must be kept relatively low in order to prevent the formation of amorphous carbon or graphite.

The diamond nucleation can be heavily disturbed by the substrate chemistry. During the early diamond growth two stages - isolated crystal and layer growth - must be distinguished [6]. Only after formation of a diamond layer can the diamond growth become independent of substrate effects. The time needed to form a continuous film depends not only on nucleation density, but also on the parameters chosen, such as carbon flux, substrate surface temperature, etc.

The very early growth period is characterized by the increase in size of the small, isolated crystals originating from the nuclei. During this stage surface diffusion of carbon to the nuclei occurs from the relatively large diamond-free substrate surface areas surrounding them. Simultaneously the activated gas phase continues to react with the substrate surface. As the diamond crystals grow together, they form larger islands which spread until the entire substrate surface is covered by the diamond coating. The substrate is no longer affected by the aggressive gas phase but it can still dissolve the diamond coating at the substrate/coating interface [7,8].

2. INTERACTIONS AT THE SUBSTRATE SURFACES: EXAMPLES [9]

- Diamond as a substrate permits nucleation and growth without a nucleation step (homeo-epitaxial nucleation and growth). On high-pressure diamond particles with damaged facets the crystallographic habitus of diamond is rebuilt rapidly during CVD growth [10].

- c-BN : Hetero-epitaxial nucleation of diamond has been observed on cub-BN crystals [11].

- Silicon : Hetereo-epitaxial nucleation is difficult due to formation of a thin SiC layer prior to nucleation. Recently however special surface pretreatments have permitted epitaxial nucleation and growth [12,13].

- Silicon carbide : SiC, a typical representative of a covalent bonded carbide, is practically inert to the reactive gas atmosphere used for the diamond synthesis. Having also a very low thermal expansion coefficient it is a nearly ideal substrate for diamond coatings [14].

- Ceramic materials (oxides, nitrides, etc) : Thermodynamic calculations and experiments showed that substrate surfaces of ceramics, such as SiO_2, Al_2O_3, ZrO_2, AlN, etc., can be transformed by the hydrogen or the carbon into metals, hydrides or carbides. The high reactivity with atomic hydrogen even allows chemical reactions which would not occur with molecular hydrogen. Diamond nucleation usually starts only after a stable surface layer is formed [2,4].

- Pure metals : For the interactions occurring with metals the carbon species are most important. Both carbide formation and carbon dissolution into the bulk material take place.

* Carbide Formation

Refractory metals (Ti,Zr,Hf/ V,Nb,Ta/ Cr,Mo,W) form stable carbides in the presence of carbon or hydrocarbons. Due to their high stability and the low carbon solubility in these metals, intermediate carbide surface layers form. The layer growth rate is influenced mainly by the substrate temperature, the carbon concentration and diffusion coefficient in the particular carbide. The overall growth rate is relatively slow [3,15,16].

Diamond nucleation starts readily after the surface is carburized. Scratches leading to thin edges can accelerate local carbide formation, thus promoting the onset of diamond nucleation.

* Carbon Dissolution

On metallic substrates which do not form stable carbides but which can dissolve carbon (e.g. Fe,Co,Ni [4,5], Pt [17]), carbon diffusion into the substrate occurs until the entire substrate is saturated with it. The time needed to reach saturation increases with the substrate thickness. This carbon diffusion can significantly delay the onset of diamond nucleation, since a certain carbon concentration at the substrate surface must be reached before stable diamond nuclei can be formed.

3. INTERACTIONS AT THE GROWING DIAMOND/GAS INTERFACE

- Catalysis of Non-Diamond Carbon Formation due to a High Vapor Pressure of the Substrate

Certain elements can retard or even prevent the formation of a diamond coating if in direct contact with the diamond being formed. For example iron can lead to massive non-diamond carbon deposition at the substrate/diamond interface. Only after this carbon layer is thick enough to prevent the diffusion of Fe from the substrate can diamond nucleation and growth start on the intermediate carbon deposit [4].

An excessive substrate vapor pressure can interfere detrimentally with the growth of diamond crystals. The high vapor pressure of such substrates as Fe, Co, Ni, Cr, etc., lead to contamination not only of the growing diamond on these substrates but also to contamination of the surrounding area, including even neighboring depositions on substrates with low vapor pressures [5]. This effect has been observed for diamond growth on refractory metals, which (except for Cr) have a very low vapor pressure. There contamination by Fe, Co, Ni, Cr. etc., led to formation of numerous huge growth steps on the growing diamond crystal facettes [3,5]. Such growth steps occur when the impurities cannot be incorporated into the crystal and therefore interfere with the normal atomic attachment kinetics [18].

4. INTERACTIONS AT THE SUBSTRATE/DIAMOND COATING INTERFACE

In particular industrial wear protection as well as low-friction and specific structural applications of alloys can be improved by diamond coatings. The following two industrial alloy types would be of special interest for use as substrates:

- Fe-, Co- and Ni-based Alloys

Experiments with lamellar and spheroidal cast iron substrates - which are saturated with carbon -, showed that this saturation can help in achieving more rapid nucleation and growth of better adhering diamond coatings [4].

Prior to diamond deposition the substrate surfaces of pure iron or steel must be protected by "stable" intermediate layers in order to avoid the C dissolution at the diamond/substrate interface, - to prevent detrimental carburization of the alloys -, and - last not least - to counteract the effects of the high vapor pressures.

Recent experiments have confirmed their feasibilty for diamond coatings by special surface treatments. Diamond coatings adhered better on carbon- and silicon-saturated cast iron alloys than on untreated iron alloys [4]. More appropriate pretreatments for reliable stable substrate surface conditions during the coating process and intermediate layers with compatible expansion coefficients sufficient to produce the required coating adhesion must still be worked out.

The detrimental effect of the prolonged heat treatment must be solved by an appropriate choice of heat-resistant steel substrates.

- WC/Co-based Hard Metals

Hard metals (WC/Co), already having excellent properties for such applications, could be even further improved by a superhard diamond coating. The sintered alloys consist mainly of WC mixed with other refractory carbides which are bound usually by a Co binder (5-15 wt %). the Co however has a detrimental effect on diamond nucleation and growth [19-22]. The adhesion problem increases with increasing Co concentration in the binder and with the addition of refractory metal carbides other than WC [21]. The formation of non-diamond carbon due to the direct contact with Co and to the relatively high Co vapor pressure are supposedly the main reasons for the problems encountered [20-23].

Pretreatments of the hard metal to enrich locally the Co binder with Si or B at the substrate surface improved significantly the diamond coating adhesion [7,8].

Also applying very thin and reactive interfacial intermediate refractory metal layers (Ti, Cr), on a hard metal subtrate prior to the diamond deposition proved to increase the coating adhesion. These layers react at least partially during diamond deposition to form carbides and thus directly improve the adhesion, while simultaneously preventing undesirable surface reactions which would otherwise occur during deposition [24].

It was recently also shown that the Co binder dissolves the diamond coating during the prolonged heat treatment resulting from the diamond deposition conditions. Thus the interface diamond coating/hard metal is not stable during the diamond deposition [7, 8]. This can have also consequences on the coating adhesion.

5. CONCLUSION : INTERMEDIATE LAYERS to control SUBSTRATE SURFACE INTERACTIONS

Of the many approaches now being proposed to deal with these various problems, that of applying intermediate layers -which was articulated many years ago [25], - might well prove to be one of the most feasible possibilities for practical industrial solutions.

The idea of putting an inert or an at least "compatible" intermediate layer between the diamond coating and the substrate - prior to the coating deposition - is thus not new. It has been successfully applied for CVD coatings on cutting tools for decades [26].

Properly utilized, this technique not only prevents substrate interactions prior to the formation of a diamond coating, it also stops the diamond dissolution at the diamond/substrate interface during deposition, and it could even help to reduce the interfacial stress problems through the choice of an intermediate layer with an appropriate expansion coefficient.

6. ACKNOWLEDGEMENTS

This work was sponsored mainly by the Austrian "Fonds zur Förderung der wissenschaftlichen Forschung" and was carried out at the Technical University in Vienna under the auspices of the trinational German, Austrian and Swiss "D-A-CH" cooperation on the "Synthesis of Superhard Materials".

Balzers AG, Liechtenstein is also acknowledged for sponsoring specific parts of this work. In particular we thank also Dr.H.Kaufmann for his personal help and interest.

Last but not least, the authors thank all students and research Team members at the Technical University in Vienna who performed the numerous experiments summarized in this review.

7. REFERENCES

1. B.Lux, R.Haubner: Diamond and Diamond-Like Films and Coatings NATO-ASI Series B: Physics, 266 (1991) 579-609 Edited by R.E.Clausing et al., Plenum, New York 1991
2. A.Lindlbauer, R.Haubner, B.Lux: Wear, 159 (1992) 67-77
3. P.O.Joffreau, R.Haubner, B.Lux: J.Ref. Hard Metals, 7,(4),(1988) 186-194
4. A.Lindlbauer, R.Haubner, B.Lux: Diamond Films and Technology 2, No.2 & 3 (1992) 81-98
5. R.Haubner, A.Lindlbauer, B.Lux: Diamond and Related Materials (1993) (in press)
6. R.Bichler, R.Haubner, B.Lux: High Temperature-High Pressure Vol.21 (1989) 576-593
7. S.Kubelka, R.Haubner, B.Lux, R.Steiner, G.Stingeder, M.Grasserbauer: Diamond and Related Materials, (1994), (in press)
8. S.Kubelka, R.Haubner, B.Lux, R.Steiner, G.Stingeder, M.Grasserbauer: Diamond Films and Technology (1994), (in press)
9. R.Haubner, B.Lux: ADC'93, 2ndInt.Conf. on the Applications of Diamond Films and Related Materials, Omiya Saitama, Japan, Aug.25-27, 1993, 131-138, Editors: M.Yoshikawa, M.Murakawa, Y.Tzeng, W.A.Yarbrough, MYU, Tokyo
10. P.O.Joffreau, R.Bichler, R.Haubner, B.Lux: J.Ref.Hard Metals 7, No.2 (1988) 92-97
11. R.Haubner: J.Ref.Hard Metals, 9, No.2 (1990) 70-76
12. X.Jiang, C.-P.Klages: Diamond and Related Materials, 2 (1993) 1112-1113
13. T.Inuzuka: privat communication (1993)
14. P.K.Sen, IDR, Industrial Diamond Review 52 (1992)
15. A.Lindlbauer: Doctoral Thesis, TU Vienna (1992)
16. R.Litos, R.Haubner, B.Lux: High Temperature-High Pressure, 22 (1990) 90-118
17. S.J.Harris, D.N.Belton, A.M.Weiner, S.J.Schmieg: J.Appl.Phys., 66, No.11 (1989) 5353-5359
18. I.Minkoff, B.Lux: "The Metallurgy of Cast Iron" pp.474-493 Editors: B.Lux, I.Minkoff, F.Mollard Georgi Publ.Comp., St Saphorin, Switzerland
19. B.Lux, R.Haubner: Chapter 6 in "Diamond Films and Coatings" Editor: R.Davies, NOYES Publications, Mill Road at Grand Avenue Park Ridge, NJ 07656, USA, 1993
20. X.X.Pan: Doctoral Thesis, TU Vienna (1989)
21. R.Haubner, B.Lux: Journal de Physique, C5, 5 (1989) 169-176
22. H.Matsubara, J.Kihara: Science and Technology of New Diamond, 89-93 Editors: S.Saito, O.Fukunaga, M.Yoshiwara, KTK Scientific Publishers, Tokyo 1990
23. J.Oakes, X.X.Pan, R.Bichler, R.Haubner, B.Lux: Surface and Coatings Technology, 47 (1991) 600-607
24. S.Kubelka, R.Haubner, B.Lux, R.Steiner, M.Grasserbauer: Diamond Films'94 Il Ciocco, Italy, 25-30.Sept.1994 (in preparation)
25. H.Schachner, B.Lux, K.Stjernberg, A.Thelin, H.Tippmann: Swedish Patent, S 8403429-7 (Priority 27.06.1984) US Patent, US 4,734,339 (1988)

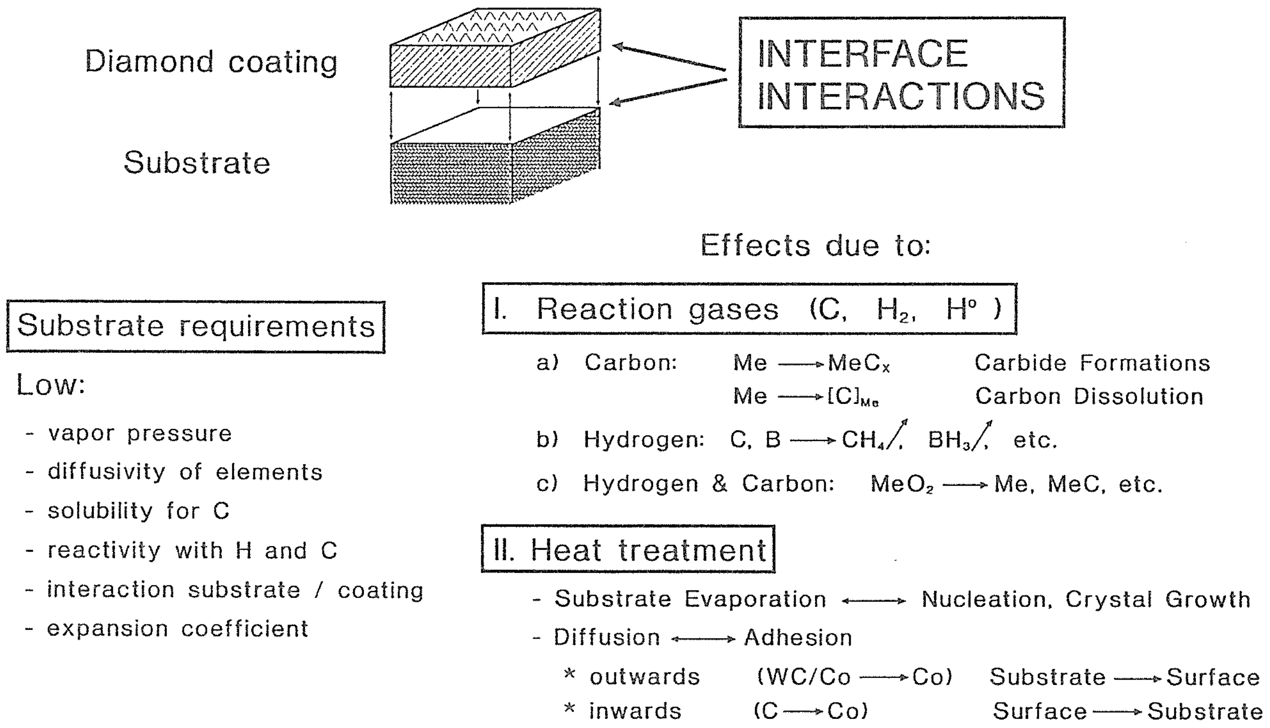

Effects due to:

Substrate requirements

Low:

- vapor pressure
- diffusivity of elements
- solubility for C
- reactivity with H and C
- interaction substrate / coating
- expansion coefficient

I. Reaction gases (C, H_2, H°)

a) Carbon: $Me \longrightarrow MeC_x$ Carbide Formations
$Me \longrightarrow [C]_{Me}$ Carbon Dissolution

b) Hydrogen: $C, B \longrightarrow CH_4\nearrow, BH_3\nearrow$ etc.

c) Hydrogen & Carbon: $MeO_2 \longrightarrow Me, MeC$, etc.

II. Heat treatment

- Substrate Evaporation ⟷ Nucleation, Crystal Growth
- Diffusion ⟷ Adhesion
  - * outwards (WC/Co → Co) Substrate → Surface
  - * inwards (C → Co) Surface → Substrate

Fig.1: Substrate / interface requirements and effects occuring during CVD diamond deposition.

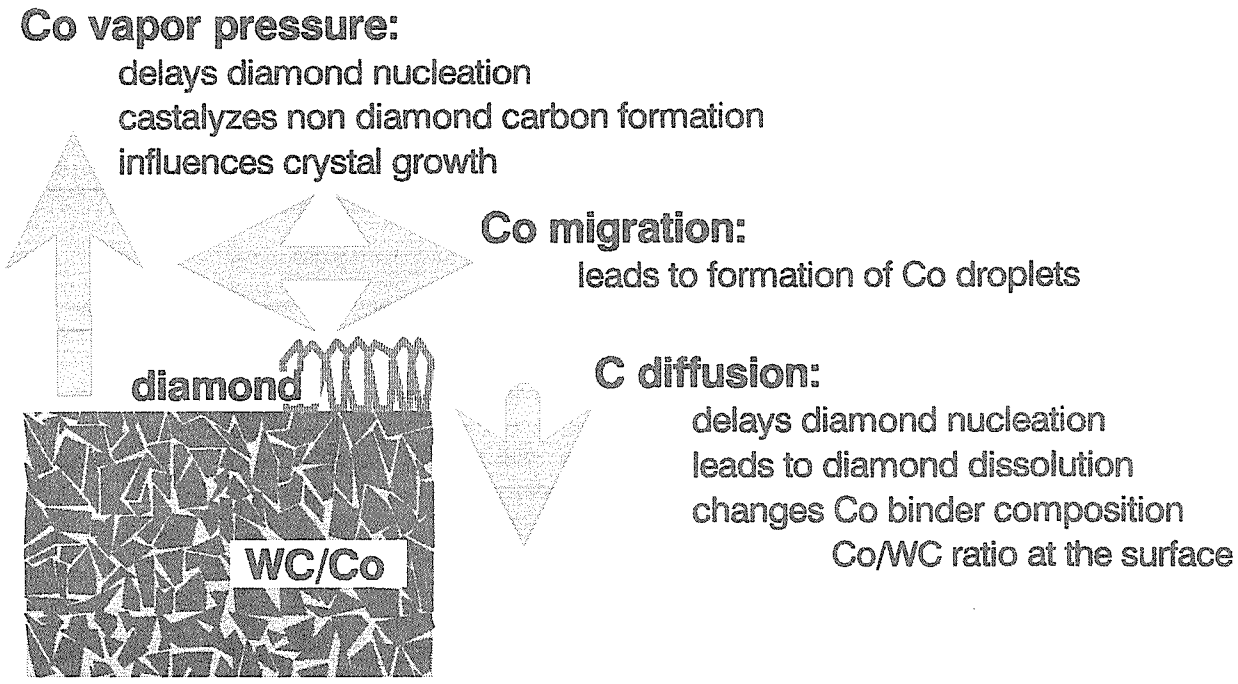

Co vapor pressure:
delays diamond nucleation
castalyzes non diamond carbon formation
influences crystal growth

Co migration:
leads to formation of Co droplets

C diffusion:
delays diamond nucleation
leads to diamond dissolution
changes Co binder composition
Co/WC ratio at the surface

Fig.2: Influence of the hard metal Co binder phase on the diamond deposition process [8]

Synchrotron X-ray Studies of Hexagonal Hard Materials under Pressure

Akifumi Onodera, Masaki Ueno and Minoru Yoshida*
Faculty of Engineering Science, Osaka University, Toyonaka, Osaka 560, Japan
Osamu Shimomura# and Ken-ichi Takemura
National Institute for Researches in Inorganic Materials, Tsukuba, Ibaraki 305, Japan

The room-temperature equations of state and pressure-induced structural phase transitions, as studied by *in situ* angle-dispersive x-ray diffraction using a synchrotron source to some extent and an imaging plate detector to a great part, are presented for AlN, GaN, and InN, all crystallizing in the hexagonal wurtzite-type structure at ambient conditions. Our studies on much harder materials, *w*-BN, 6*H*-SiC, and 3*C*-SiC, are also included. We find satisfactory agreement between the experiments and most of the existing first-principles calculations on the bulk moduli and transition pressures. The general trends in these parameters can reasonably be systematized by first-principles ionicity scales.

I. Introduction

Among binary octet $A^N B^{8-N}$ compounds, III-V nitrides and SiC are interesting semiconductors in that they have wide bandgaps, high hardness, and high thermal conductivities (see Table I). For these reasons, many of them are under current development for novel electronic devices.[1] Another point of interest is the high stability towards the hexagonal structure at ambient conditions. Indeed the wurtzite-type structure is possessed by each ambient-pressure phase of AlN, GaN, and InN. Boron nitride is an exception to the nitride family: it crystallizes at ambient pressure in the graphite-like form but one of the high-pressure phases is the wurtzite-type structure (*w*-BN). In SiC, 3*C*-type and 6*H*-type rather than the wurtzite (2*H*)-type are the most common forms among the various polytypes.

Like other $A^N B^{8-N}$ compounds, the III-V nitrides and SiC are expected to undergo pressure-induced structural phase transition. A naïve approach based on the Phillips ionicity [2] leads to an expectation that AlN, GaN, and InN would transform into the NaCl-type structure whereas the β-Sn-type structure is expected for SiC.[2,3] Recent first-principles calculations [4-7] show prevalence of the NaCl-type structure for the high-pressure phase of SiC, however.

Table I. Selected properties of III-V nitrides and SiC.

	6*H*-SiC	3*C*-SiC	*w*-BN	AlN	GaN	InN
Bandgap (eV)	2.9	2.3	6.4[a]	6.3	3.4	2.0
Microhardness (GPa)	23	19	70[a]	13	?	?
Thermal conductivity (W/m·K)	490	490	1300[a]	320	130	?
Axial ratio *c*/*a*	4.900	1.000	1.647	1.600	1.622	1.611

[a] Data for the zinc-blende form.

In the meantime, the Phillips ionicity[2] was questioned from first-principles approaches [6,7] on ionic charges and it was pointed out that upward revisions be needed in the ionicity of compounds containing first-row elements. The compounds of the present interest just fall in such cases. It is, in turn, of great importance to know how the revised ionicity can be applied to the problem of high-pressure transitions.

This study therefore aims at (i) reconnaissance of structural phase transition in BN, AlN, GaN, InN and SiC; (ii) comparison of the measurement with first-principles calculations; and (iii) systematization of the general trends in these materials in terms of ionicity.

II. X-ray diffraction

The experimental procedure pursued in this study was angle-dispersive x-ray diffraction technique *in situ* under pressure in a gasketed diamond-anvil cell employing, in most cases, an imaging plate (IP) detector.[8] The x-ray source used was either a monochromatized Mo$K\alpha$ or a synchrotron radiation (BL-3A or 6B at the Photon Factory, National Laboratory for High Energy Physics).

Figure 1 shows x-ray diffraction patterns of 3*C*-SiC recorded by IP on both up- and down-strokes.[9] The patterns in Fig.1(a) were taken using the Mo$K\alpha$ radiation while those in Fig.1(b) were from the synchrotron study. In the pattern at 36 GPa, peaks responsible for the zinc-blende (111), (200), and (220) reflections are recorded. Owing to hit of the Mo$K\alpha$ radiation, gasket lines (labeled by G) appear in each pattern in Fig.1(a) and eventually disturb the reflection(s) of interest. This occurs actually in the patterns taken at 85 and 105 GPa. Under such a difficult situation, we notice appearance of a new peak labeled by an arrow in the 105 GPa pattern. No further information can be obtained from this unless the gasket lines be eliminated. The small divergence of the synchrotron radiation enables to eliminate the gasket lines. The resulting pattern is shown at the top of Fig.1(b). It obviously demonstrates that the new peak is by no means spurious. This and the two additional peaks appearing at higher angles can be unequivocally assigned to the NaCl-type structure. Consequently, we find that 3*C*-SiC undegoes a structural phase transition into the NaCl-type by 105 GPa. On downstroke, this transformed high-pressure phase returns back to the ambient-pressure phase by about 35 GPa [Fig.1(b)].

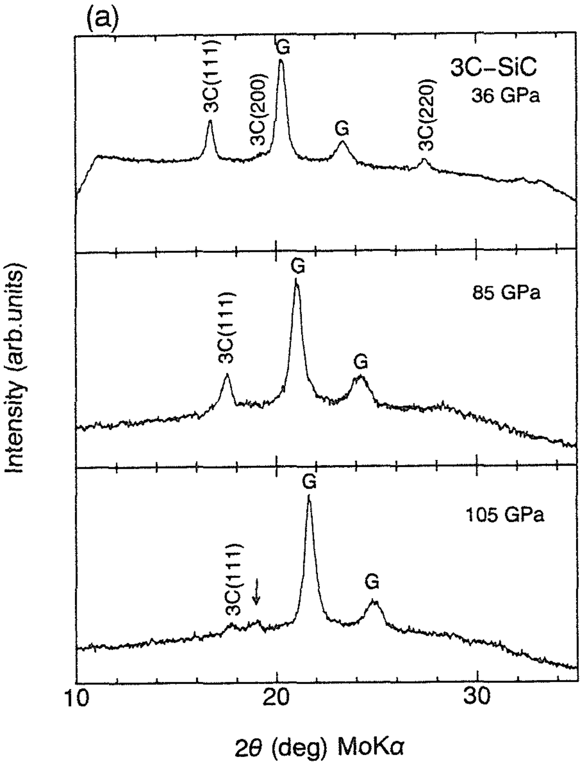

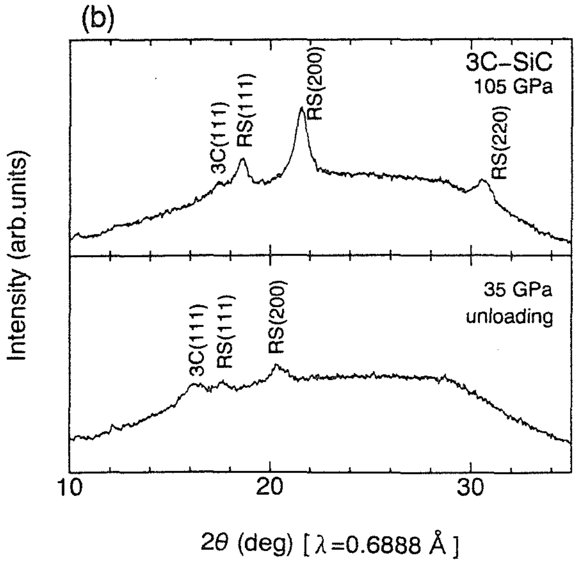

Fig.1 X-ray diffraction patterns for 3*C*-SiC. The letters 3*C* and RS respectively represent the 3*C* and NaCl phases.

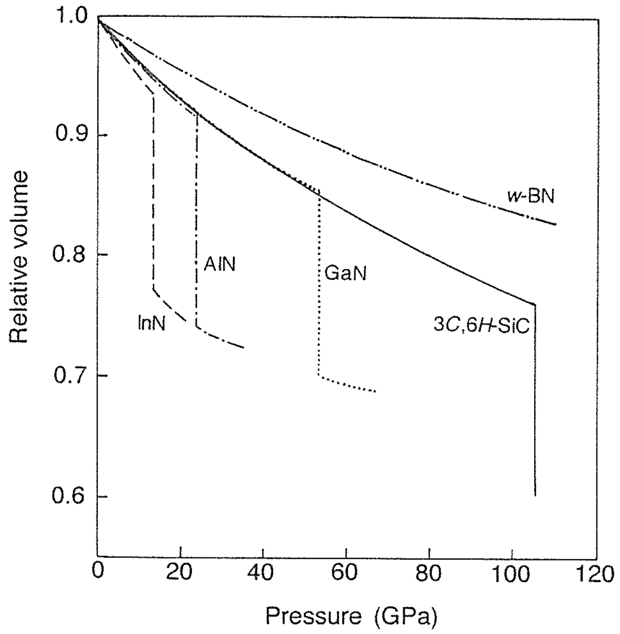

Fig.2 Room-temperature equation of state for nitrides and SiC.

Our studies on other compounds yielded the following results: 6*H*-SiC persists to about 95 GPa, with a premonition of phase transition presumably into the NaCl-type structure [9]; AlN (at 22.9 GPa; Ref.10), GaN (at 52.2 GPa; Ref.11), and InN (at 12.1 GPa; Ref.11) all transform into the NaCl-type structure; *w*-BN remains stable at least up to 106 GPa.[12] The equation-of-state curves for the nitrides and SiC are shown in Fig.2. The phase transitions in AlN, GaN, InN, and 3*C*-SiC take place at the discontinuities in volume. The bulk modulus (B_0) and its pressure derivative (B_0') deduced from Fig.2 (also Ref.13) are summarized in Table II. We also list in Table II the transition pressure (P_t) and volume change (ΔV) accompanied by the transition.

Table II. Elastic and transition parameters for III-V nitrides and SiC.

	B_0 (GPa)	B_0'	P_t (GPa)	ΔV (%)	Method	Reference
***w*-BN**	**390±3**	**3.5±0.8**	no transition	to 106 GPa	x-ray diffraction	12,13
	390	6.3			LCAO	14
AlN	**207.9±6.3**	**6.3±0.9**	**22.9±0.2**	**19.5**	x-ray diffraction	10,12,13
	195	3.74	12.9	22.5	psuedopotential	15
	221		16.6	18.1	LMTO-ASA	16
	205		12.5	19	LMTO-FP	17
GaN	**237±31**	**4.3±2.0**	**52.2±3.0**	**17.9**	x-ray diffraction	11-13
	239		65	10	LMTO	18
	244		55	11	psuedopotential	19
	190	2.92	55.1	14	psuedopotentail	20
InN	**125.5±4.6**	**12.7±1.4**	**12.1±0.2**	**17.6**	x-ray diffraction	11-13
	165		25.4		LMTO	21
6*H*-SiC	**260±9**	**2.9±0.3**			x-ray diffraction	9
3*C*-SiC	**260±9**	**2.9±0.3**	**105**	**20.3**	x-ray diffraction	9
	212	3.7	66	18.5	psuedopotential	5

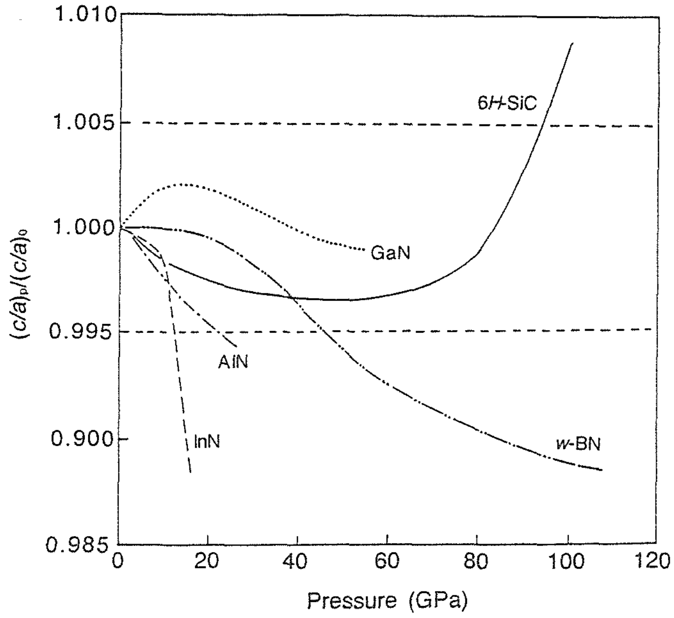

Fig.3 Presseure dependence of the axial ratio for the nitrides and 6*H*-SiC.

In the hexagonal crystal system the axial ratio c/a is an important parameter to know the distortion. Figure 3 shows the axial ratio normalized to the ambient-pressure value for *w*-BN, AlN, GaN, InN, and 6*H*-SiC, each in the hexagonal phase. The compounds in Fig.3 can be classified into four groups according to the changes in c/a: compounds exhibiting a marked decrease in c/a with pressure and undergoing the transitions at relatively low pressures (AlN and InN); compound which shows little pressure-induced change in c/a but undergoes the transition (GaN); compound showing a conspicuous increase in c/a in the vicinity of the premonition of phase transition (6*H*-SiC); and compound exhibiting a large change in c/a but, nevertheless, persisting in the hexagonal phase (*w*-BN). The axial ratios in AlN and InN at ambient pressure (see Table I) already deviate significantly from an ideal value, 1.633, for the hexagonal packing. The decrease in c/a in these two compounds indicates that the distortion from the ideal geometry is not redeemed but instead is enhanced with the application of pressure and, incidentally, the phase transitions take place when the normalized c/a reaches a value of 0.995. The phase transition in GaN occurs without such a change in c/a from the ambient-pressure value. In 6*H*-SiC, the axial ratio at ambient pressure is close to three times of the ideal value. It eventually shows a steep rise from about 80 GPa and crosses a value of 1.005 at 90 GPa where we find a premonition of phase transition. This situation is similar to the casses of AlN and InN in that each lattice becomes destabilized at the 0.5% change in c/a from the ambient values. Although the change is relatively large in *w*-BN, the axial ratio approaches 1.63 with increasing pressure. The approach to the ideal value probably gives rise to a further stabilization of *w*-BN in the wurtzite structure.

III. Comparison with calculations

Theoretical studies[5,14-21] for the elastic and transition parameters are joined in Table II. An excellent agreement is achieved between the measured and calculated elastic parameters of *w*-BN. The calcualtion[14] on the other hand predicts a phase transition to occur in BN from the zinc-blende to wurtzite-type at 133 GPa. In AlN and GaN, many of the calculations for B_0 agree reasonably well with the experiment. All the predictions underestimate P_t of AlN, whereas overestimations are met in P_t of GaN. The calculated B_0 and P_t are significantly higher than the measured values in InN. Underestimations occur in B_0 and P_t of 3*C*-SiC. We note that there is no problem in the underestimation because the calculations achieved on P_t are for the equilibrium pressure and, hence, that comparison of P_t between the calculation and experiment becomes valid after the transition pressures on up- and downstrokes are determined.

IV. General trends

Although the first-principles calculations shown in Table II can interpret the elastic properties and transition parameters reasonably well, the interpretation is limited to within each compound. No general trend or systematization is given for the nitrides we are studying.

Such arguments have been made from rather simple points of view. Cohen [22] put forth a relation between the bulk modulus (B_0) and the nearest-neighbor-distance (d) of tetrahedrally bonded solids to be $B_0 \propto d^{-3.5}$. Majewski and Vogl [23] tried to find trends in B_0 and also the transition pressures of $A^N B^{8-N}$ compounds in terms of unit cell volume V and showed $B_0 \propto V^{-1.6}$ in comparison to the experimental values $B_0 \propto V^{-1.14}$ to $V^{-1.0}$. No nitrides were treated in these reports. Instead of plotting B_0 against V or d, we show in Fig.4 plots of B_0 against charge asymmetry coefficient g derived by García and Cohen. [7] It was shown that g's for the nitrides are significantly higher than the Phillips ionicity (f_i). [2] In Fig.4 we find, in particular, the high values in B_0's in the nitrides. Also, very smoothed lines connecting respective series of Al, Ga, and In compounds can be delineated.

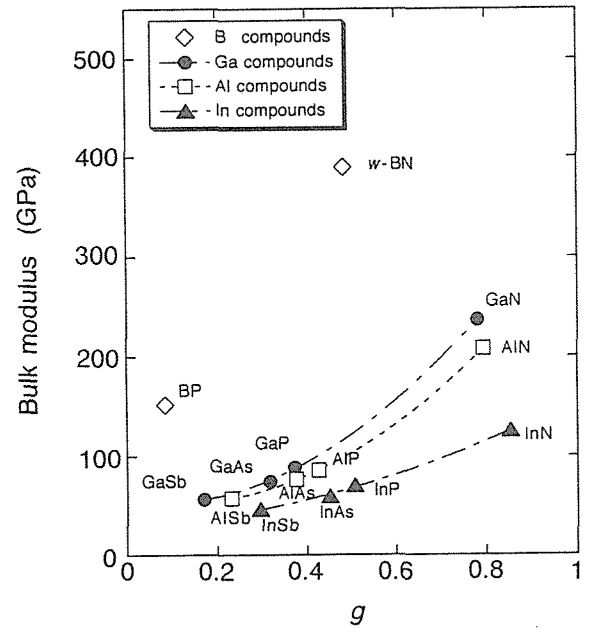

Fig.4 Plots of bulk modulus against g (Ref.7).

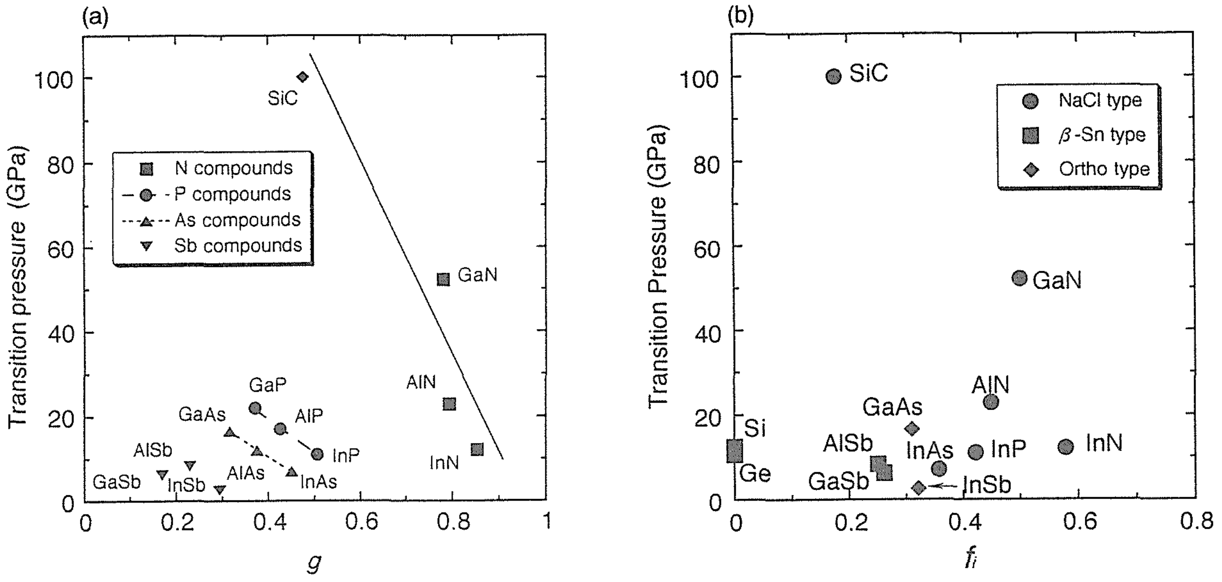

Fig.5 Plots of transition pressure against (a) g and (b) f_i.

Plots of transition pressure (P_t) against two ionicity scales are compared in Figs.5(a) and (b). In the P_t-vs-g plots, Fig.5(a), SiC falls close to the family of nitrides and, furthermore, the prevalence of the NaCl-type structure for SiC at high pressure can reasonably be interpreted. In addition, discrimination among the series of compounds as well as the smoothed plots within each series are better achieved in Fig.5(a) than those in Fig.5(b) which gives P_t-vs-f_i plots. Such plots can also be attained for the nitrides (see Ref.11) by first-principles ionicity scales of Christensen *et al.*[6] and Yeh *et al.*[24]

V. Summary

Our x-ray diffraction study has revealed that the trends in the bulk moduli as well as the transition pressures in III-V nitrides and SiC are in harmony with the trends in the first-principles ionicity scales.

Acknowledgment

Part of this work was performed under the approval of the Photon Factory Program Advisory Committee (Proposal Nos. 91090 and 93G295).

* Present address: Advanced Technology Research Laboratories, Sumitomo Metal Industries Co., Amagasaki, Hyogo 660, Japan.
# Present address: Photon Factory, National Laboratory for High Energy Physics, Tsukuba 305, Japan.

1. J.H.Edgar, J.Mater.Res. **7**, 235 (1992).
2. J.C.Phillips, *Bonds and Bands in Semiconductors* (Academic, New York, 1973).
3. J.R.Chelikowsky, Phys.Rev. B**35**, 1174 (1987).
4. K.J.Chang and M.L.Cohen, Phys.Rev. B**35**, 8196 (1987).
5. B.H.Cheong, K.J.Chang, and M.L.Cohen, Phys.Rev. B**44**, 1053 (1991).
6. N.E.Christensen, S.Satopathy, and Z.Pawlowska, Phys.Rev. B**36**, 1032 (1987).
7. A.García and M.L.Cohen, Phys.Rev. B**47**, 4215 (1993).
8. O.Shimomura, K.Takemura, H.Fujihisa, Y.Fujii, Y.Ohishi, T.Kikegawa, Y.Amemiya, and T.Matsushita, Rev.Sci.Instrum. **63**, 967 (1992).
9. M.Yoshida, A.Onodera, M.Ueno, K.Takemura, and O.Shimomura, Phys.Rev. B**48**, 10587 (1993).
10. M.Ueno, A.Onodera, O.Shimomura, and K.Takemura, Phys.Rev. B**45**, 10123 (1992).
11. M.Ueno, M.Yoshida, A.Onodera, O.Shimomura, and K.Takemura, Phys.Rev. B**49**, 14 (1994).
12. M.Ueno, M.Yoshida, A.Onodera, O.Shimomura, and K.Takemura, Jpn.J.Appl.Phys.Suppl. **32**, 42 (1993).
13. M.Ueno, M.Yoshida, A.Onodera, O.Shimomura, and K.Takemura, Proc.Joint AIRAPT/APS Conf. High Pressure Science and Technology (Colorado Springs, July 1993), in press.
14. Y.N.Xu and W.Y.Ching, Phys.Rev. B**44**, 7787 (1991).
15. P.E.Van Camp, V.E.Van Doren, and J.T.Devreese, Phys.Rev. B**44**, 9056 (1991).
16. I.Gorczyca, N.E.Christensen, P.Perlin, I.Grzegory, J.Jun, and M.Bockowski, Solid State Commun. **79**, 1033 (1991).
17. N.E.Christensen and I.Gorczyca, Phys.Rev. B**47**, 4307 (1993).
18. I.Gorczyca and N.E.Christensen, Solid State Commun. **80**, 335 (1991).
19. A.Muñoz and K.Kunc, Phys.Rev. B**44**, 10372 (1991).
20. P.E.Van Camp, V.E.Van Doren, and J.T.Devreese, Solid State Commun. **81**, 23 (1992).
21. P.Perlin, I.Gorczyca, I.Gregory, T.Suski, N.E.Christensen, and A.Polian, Jpn.J.Appl.Phys. Suppl. **32**, 334 (1993).
22. M.L.Cohen, Phys.Rev. B**32**, 7988 (1985).
23. J.A.Majewski and P.Vogl, Phys.Rev. B**35**, 9666 (1987).
24. C.Y.Yeh, Z.W.Lu, S.Froyen, and A.Zunger, Phys.Rev. B**46**, 10086 (1992).

Efficiency Characteristics of Diamond Synthesis / Review /

N.V. Novikov
Institute for Superhard Materials, Ukraine

The review presents the results, describing direction, the main tasks and place of researches in diamond synthesis, carried out at the Institute for Superhard Materials. A limited length of this lecture does not permit a wide presentation of the recent results, and there is no possibility to describe the methodical features. However, the author hopes, that the additional information can be found in editions of the Institute, as well as in the papers of our employees at International Conferences.

Contents of the review: 1. Computer simulation of fields of temperature and pressure in high pressure apparatuses (HPA). 2. Diamonds synthesized by spontaneous crystallization. 3. Large diamond crystals. 4. Physico-mechanical properties of diamond. 5.The use of diamond properties.

Computer simulation of fields of temperature and pressure in HPA: Diamond synthesis is performed in HPA, the efficiency of which is characterized by its service life (the number of working cycles before destruction), yield of diamonds (the productivity) in one cycle, cost of a set of HPA components, including a reaction cell. The magnitude of these characteristics depends on a combination of many factors. Thus, according to our data, in the case of a belt-type HPA with a hole 40 mm in diameter, the average service life of components of HPA, made by various European companies under certain conditions was in the range from 904 to 104 cycles. In terms of tungsten consumption per 1000 ct of synthetic diamond the distinction in durability have made from 2,0 up to 3.2 kg.

To find out the reasons of the distinctions, we use the analysis of fields of pressure and temperature in HPA. This characteristics permits the determination of the dependence of a diamond yield on main parameters (pressure, temperature, time), as well as on features of constructive fulfillment of a reaction cell and on physical properties of materials, used for its manufacturing. We have conducted numerous calculations of temperature fields in HPA of a recessed anvil-type and belt-type. Our programs permit us to solve coupled problems on electro- and heat conductivities and to determine the variation of a temperature field with electric heating of a cell depending on design features, electric conductivity and thermophysical characteristics of materials used. Solving nonlinear problems on the deformable solid mechanics it is possible to construct a field of distribution of pressures in HPA in compression by the force of a press. In calculations, additional thermal stresses are taken into account. In determining the pressure distribution in view of characteristics of elasticity and plasticity of materials used, the conditions of friction on contact surfaces when loading HPA and extruding a deformable gasket are taken into consideration.

Figure 1 gives calculated fields of temperature (a), pressure (b), excess of temperature of solvent metal melting at a given pressure (c) and excess of pressure above the equilibrium line for phases A and B at a given temperature.

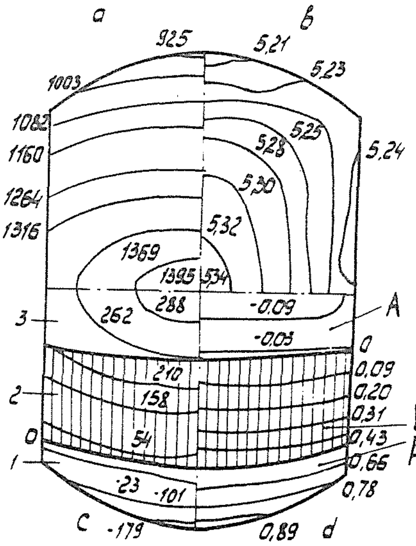

Fig. 1

In a similar way the concentration of diamonds, which are being crystallized during phase transformations in a reaction mixture can be calculated. The process of crystallization initiates in the zone indicated in Fig. 1 (crosshatched) from the moment (t_s) of the fulfillment of a given criterion of graphite - diamond phase transition.

Diamonds emerge in the centre, then the area of possible synthesis is expanded. Difference of temperature on the vertical axis is 4-5 times more than on the horizontal one. At an initial moment of diamond crystallization the pressure gradient does not exceed 0.15 GPa. With increase in diamond concentration the pressure drops owing to changes in density of the reaction mixture and the pressure gradient increases up to 0.75. It is necessary to maintain the pressure.

Kinetics of changes in thermostressed state of the reaction volume can be shown as p,T-parameters on the phase diagram of carbon and the melting of a solvent metal.

From positions of the nonlinear mechanics, we have executed the analysis of p,T-conditions of diamond nucleation in graphite and in a metal melt. Instant changes of the microvolume are analytically accounted for in graphite - diamond phase transition. It is found that for diamond nucleation in graphite and maintenance of equilibrium pressure (4.94 GPa and 1200 C) an external hydrostatic pressure of 16.7 GPa is needed. Formation of a metal melt reduces pressure, necessary for phase transition by a factor of 3.3.

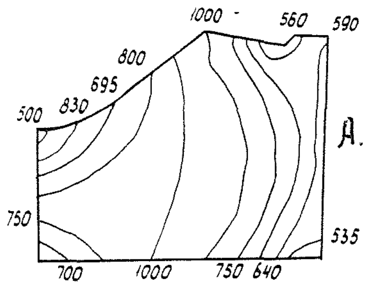

Fig. 2

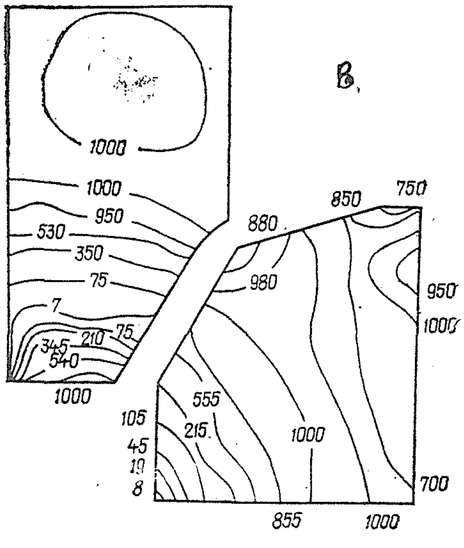

Fig.3

By applying the developed technique, it is possible to take into account the features of a HPA design, and changes in stresses when interference assembling of its components as well as to determine equivalent stresses and to plot isolines of allowable cyclic loads (Figs. 2, 3) for components of recessed-anvil (A) and belt (B) HPA (die-unit, punch, surrounding rings). In the calculation the criterion of a limiting mechanical state is given.

The calculated data derived on the basis of computer simulation point to the representativeness of the characteristics of fields of distribution of pressures and temperature in a HPA working zone in synthesis of diamond, sintering of polycrystals or composites of superhard materials, as well as in solving various technological problems. For example, for choice of materials for a reaction cell or optimization of its design.

Diamonds of spontaneous crystallization: The crystals of synthetic diamonds do not basically differ from natural ones in shape and crystallography. But the differences are found out when analyzing impurities, inclusions, and bulk and surface defects. This is revealed first of all by studies of thermophysical and optical characteristics as well as by evaluation of internal stresses and submicrostructure heterogeneity.

Consider now some results of studies of such characteristics as crystal habit, quantity of metal inclusions and level of internal stresses.

Figure 4 shows the relation between the diamond crystal habit and inclusion content. On axes relative values of pressure and temperature are indicated. P_s is the pressure, used to produce heat resistant diamonds, and T_e is the eutectic temperature for a two-component melt of metals with carbon at pressure P_s. The areas of p,T conditions are shown where the distribution of inclusions throughout the whole bulk of a crystal (■), half bulk (◩), the distribution of oriented inclusions (☒) and rare single inclusions are possible (☐).

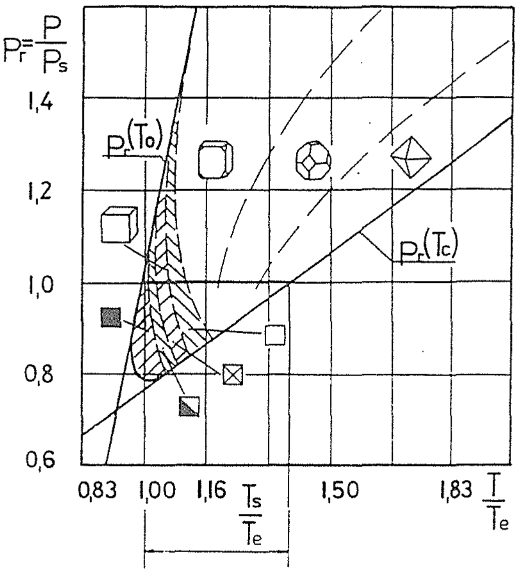

Fig. 4

The studies have confirmed a significant effect of alloying of a solvent metal with getters of nitrogen (titanium, zirconium, boron) which change the ratio between carbide-forming, graphitizing and inert with respect to carbon components. To obtain impurity-free crystals, the way of their accommodation in the reaction cell volume, and the degree of perfection of a graphite structure are important. So, it is shown, that the dissolution of graphite crystals due to the addition of alloying elements and resulting changes of the melt temperature can essentially hinder diamond crystallization.

The composition of a solvent metal influences also the metal inclusion content, and hence physico-mechanical properties of diamond grits. Their quantitative content and, accordingly, the degree of the influence are judged about from the data of measurements of a failure load on a grain as well as from electromagnetic properties of powders, and implicitly - from the results of thermal treatment. Thus, in laser processing of diamond powders 400/315 m in grit size, taken from various lots of synthetic diamonds, the strengthening factor K = 1.25 ÷ 1.45.

Lot of synthetic diamonds	Initial characteristics			K
	p, N	χ * 10^{-8} m^3/kg	ρ, Ohm * m	
5	60	3.7	2.3 * 10^{3}	1.08
9	71	11.5	9.3 * 10^{7}	1.23
11	64	12.8	1.1 * 10^{10}	1.45

It should be noted that the quantity of bulk defects in synthetic diamond (SD) influences the diamond magnetic susceptibility (χ), which varies from - 0.6 * 10^{-8} m^3/kg up to 160 * $10^{-8}$$m^3$/kg. Electrical resistance (ρ) decreases in the range from $10^{12}$to 10^{7}Ohm*m, the number of defects on grain surface of SD being increased.

To separate synthetic diamond grits to the degree of surface imperfection, and surface development, an efficient method of adhesion-magnetic separation was used. Ferromagnetic high dispersion particles are applied on diamond grits, the mass of the former makes 0.01-6.0 % of diamond mass. Their adhesion is the merit of the imperfection of diamond particle surface. The subsequent classification of diamond particles into a number of fractions is carried out in a controllable magnetic field. The method permits the obtaining of practically defectless synthetic diamond powders with increased uniformity of strength and electrical resistance. Large diamond crystals: When growing large diamond single crystals on seeds in variable temperature and pressure fields the choice of elements of a growth system as well as a solvent alloy and carbonaceous material is of major importance. As seed natural and synthetic diamonds crystals are equally used.

In experiments under consideration as seeds, AC 100 315/250 m synthetic diamond grits have been used with <111> and <100> without growth steps, traces of dissolution and mirror-smooth when examining. The choice of relatively small crystals was dictated by the necessity to reduce volume of a defective zone under a seed. Its effective diameter makes from 3.5 and to 1.2 a, where a is the average size of a seed's face.

As a result of computer simulation of a temperature field in the growth volume of HPA, the conditions for carbon concentration control in axial and radial directions were optimized. A feasibility was established of obtaining flattened and full-volumed crystals when alloying a main solvent metal. Depending on rate and conditions of growth the impurity content changed. In experiments single crystals, containing nitrogen in amount of 2 ÷ 4 * 10^{18}atoms/cm have been received. Heat conductivity of the crystals 1.5 - 4 mm in size was 1500 - - 1600 Wt/m.K. The ratio between the octahedron edge and a crystal height was 1.8 to 2. Depending on a given size, seven to thirty single crystals were grown simultaneously for 20-36 hours.

An optimum rate of single crystal growth with a minimum of a solvent metal inclusions makes 1-3 mg/h.

Carbon atoms diffusion to the surface of a growing crystal is given by:

$$D(C_R - C_{lim})/L = A(C_{lim} - C_K)[1-1/1+(C_{lim} - C_K/\Delta C_0)]$$

where D is the diffusion factor; L is the thickness of a diffusion layer; C_R, C_K, C_{lim} are the limited dissolution of carbon, respectively at the boundary between solvent and carbonaceous material, solvent and the crystal and in a layer of a solvent; ΔC_0 is the concentration of carbon which corresponds to the transition from a spiral growth mechanism on screw dislocations to a mechanism of growth on two-dimensional seeds.

The findings permit the calculated and experimental dependence to be found between the growth rate and temperature and concentration differences with thickness of a solvent layer. For a Ni-C sample the growth rate of a crystal height (h) made 1.5 mm/day. The results were as follows:

Height of a solvent layer H, mm	Difference of carbon concentration, mass %	Temperature difference, ΔT, K
2.0	0.120	8.4
4.0	0.137	9.6
6.0	0.154	10.8
8.0	0.160	11.2
10.0	0.190	13.2

Note the necessity to achieve a small error in calculated and experimental determination of temperature, no more than ± 1 K. With certain combinations of temperature and concentration gradients the crystal growth rate decreases sharply.

The results of growing of high-grade crystals have allowed the relation $\Delta T = 2.5\ (H-h)$ to be found. The computer simulation permits the calculation of the concentration gradient variation in a solvent layer in a real time of crystallization. The forthcoming solution of an equation for a three-dimensional model will allow the calculation of a probability of development of various faces of a diamond crystal as it grows and the search of the best technical decisions to grow single crystals of controlled habit and sizes.

Physico-mechanical properties: To optimize the technological parameters, it is important to use a wide spectrum of methods of diamond testing. Consider some results, adding the information, received with application of widespread tests, such as using a Friatester, tests on heat resistance and abrasive ability.

It is expedient that these characteristics of diamond, as of a high-strength, brittle material, should be added with determination of fracture toughness K_{Ic}, static and dynamic hardness (H), strength (σ) in view of quality of crystals. Below are the results derived when testing up to fifty natural (type 1a) diamond (ND) 315/250 um crystals, which were defect-free octahedrons of the highest purity, and up to three hundred synthetic (type 1b) diamond (SD) crystals, cubooctahedrons, 315/250 and 400/315 um in grit size.

The analysis of the experimental data permits the following conclusions (Fig. 5):

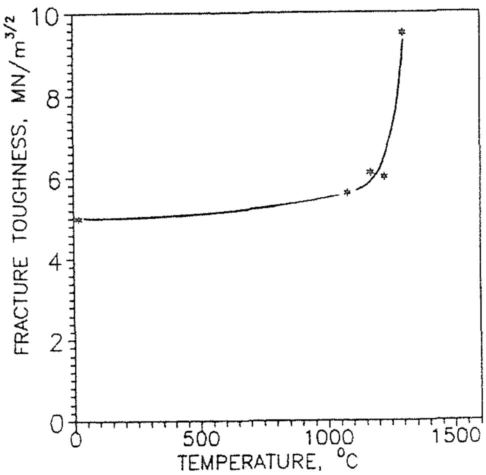

Fig. 5

Diamond grade	P, N	K_{IC} MN.m$^{3/2}$
Synthetic type 1b diamond	0.49 0.98 1.96 4.91 9.81	4.5 4.9 5.0 4.6 4.8
Natural type 1a diamond	1.96 4.91 9.81	5.4±0.6 4.5±0.4 4.9±0.4

- K_{IC} value for ND crystals varies only slightly up to 1225 C. At higher temperatures a rapid increase of K_{IC} is observed, as a result of formation of a quazi-plastic zone at the tip of a crack.

- A good agreement is observed between our results and the equations of Antis, et al. $K_{IC} = 0.16(E/H)^{1/2}(p/c)^{3/2}$ and Niihara $K_{IC} = 0.18(E/H)^{2/5}Ha^{1/2}/(c/a-1)^{1/2}$;

- K_{IC} values for ND and SD are practically identical at various loads on an indenter.

The data in Figs. 6 and 7 show a temperature dependence of static and dynamic hardness, and strength of diamond in view of temperature effect (77-300 K). The range of loading rate variations is $3 * 10^{-2}$ - $2.3 * * 10^{6}$ GPa/s. The strength variation of diamond as a brittle hard substance with a loading rate does not show itself at room temperature in defect - free crystals (without a crack, 1) and with a crack (at 300 K, 2; at 77 K, 3). In cooling the rate of a pre-existing crack propagation increases and the strength of diamond reduces. A brittle fracture mode of natural and SD is observed when being compressed at the temperature from 77 up to 1373 K. Fig. 7 shows a curve (dotted line), constructed according to Zhurkov's equation for diamond crystals of a perfect structure.

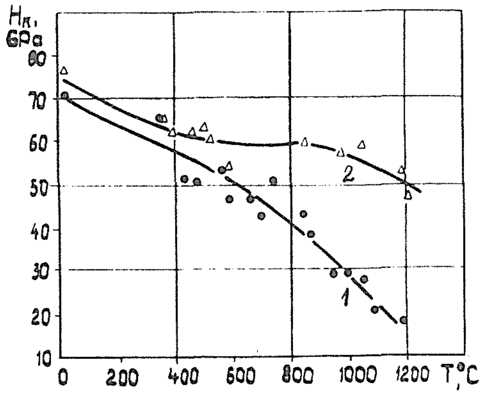

Fig. 6

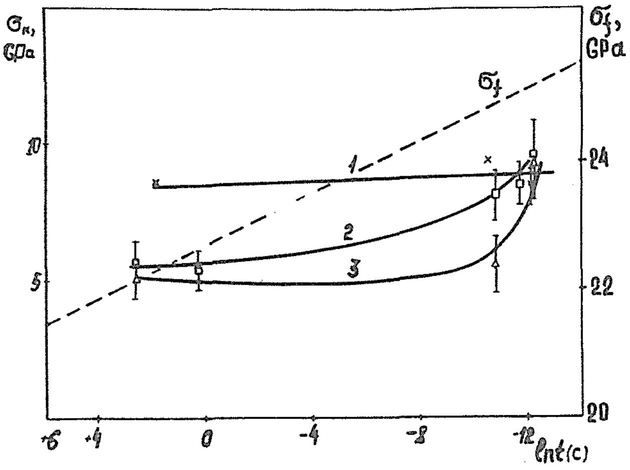

Fig. 7

The use of the characteristics. Synthetic diamond crystals of a perfect habit and high quality are needed for their effective use in wear resistant tools or diamond composites. An efficient application of diamond crystals in electronics is a special problem.

Consider a problem of manufacturing diamond-containing composites based on the requirements to characteristics of diamond powders. At our Institute, such composite materials as Slavutich, Tvesal, KAM have been produced and patented.

Tungsten carbides (WC-Co) are used as a matrix for diamond-containing materials for the manufacturing of working elements of rock-breaking cutters, drilling bits and augers. SD and ND powders of various grit sizes are used as fillers.

The problem resides in the fact that by a combination of two highly hard wear resistant materials one has to receive a composite with a higher wear resistance as compared with carbide and not to suffer losses in fracture toughness and dynamic strength in doing so. For this end, a high heat resistance of diamond is needed along with a minimum of metal impurity content, a high fracture toughness (the lowest K value), and optimal characteristics of a crystal surface to ensure its high retention in the matrix.

Figure 8 shows the compression strength $<\sigma>^*_c$ of KAM with a vitreous matrix as a function of a degree of a diamond damage (ε^*). The results of computer simulation at ε^* equal to 0 or 0.1 are compared with experimental findings.

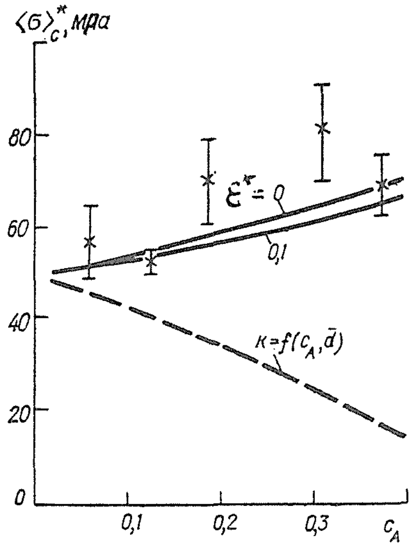

Fig. 8

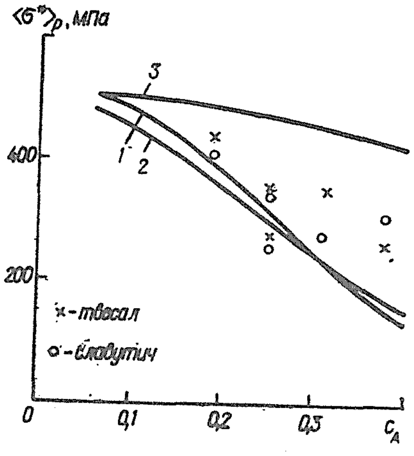

Fig. 9

Figure 9 shows the strength as a function of a degree of diamond damage conditioned by the means of diamond production (is taken into account by factor K) and sintering technology.

BK6 + ND 400/315 m are used in Slavutich material, whereas BK6 + AC82T 315/250 m in Tvesal. Curves 1, 2, 3 are calculated ones, and in KAM (3) a degree of diamond damage (ε^*) is taken to be zero.

Computer simulation permits us to calculate for a certain composition of a composite material, for example, BK6 + ND

500/400 m the conditions of damage to obtain the highest strength. The volume fraction of diamonds (SD) in the composite and the value of residual temperature stresses are taken into account. The latter are determined by a technological gradient of temperature $0< T < 770$.

An imitation computer analysis of various structures of composites, accounting for a level of internal stresses, a set of characteristics of the both phases, and some experimental results, has allowed us to establish the following:

- The formation of a rigid diamond skeleton at a large diamond concentration in a matrix and reduction of residual stresses increase the compression strength of a composite.
- The resistance to propagation of cracks, initiated on a working surface of a composite at friction against a counterbody (rock, abrasive) at large specific loads, is increased in the case of the increasing of a mechanical contact and adhesion between a diamond particle and a matrix material.

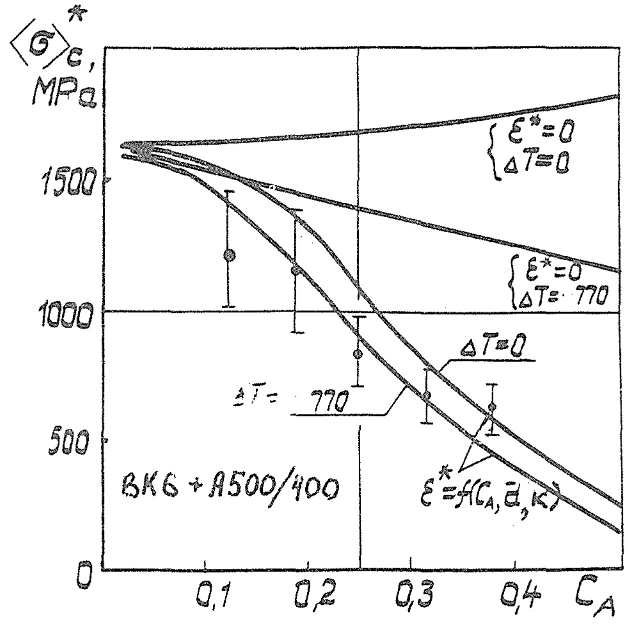

Fig. 10

Figure 10 shows the variation of the compression strength $<\sigma^*>_c$ of a diamond composite with a size of diamond grits $\bar{d}$. The analysis shows, that one of the main factors, determining strength, is the degree of damage of diamond grits. $\varepsilon^* = f(C_A, \bar{d}, K)$. This dependence can be expressed analytically as $\varepsilon^* = \pi^3 NKd (1+\nu^*)(5-4\nu^*) / 240$. Here, ν^* is Poisson's factor for a composite, N is the number of diamond grits per its unit volume. Obviously, that the reduction of grit sizes and increase in grit strength and heat resistance (a smaller K value) result in increase of a composite strength. Through experiments it has been found that by reducing grit size from 400/315 or 315/250 m down to 60/40 m, and optimizing sintering parameters (p, T, t) it is possible to lower the degree of grit damage by a factor of 6 and to increase the compression strength of a composite by a factor of 1.3.

Conclusion. The findings given above show the possibilities of further improvements in processes of diamond synthesis and sintering diamond-containing composites. A great number of characteristics and factors affecting them points to the necessity of further development of researches in this area of various scientific centres as well as of an active exchange of results, and collective discussion thereof.

The author is grateful for the given opportunity of such a discussion within the framework of cooperation between high pressure research centres of NIRIM and ISM.

Molecular Rearrangement and Chemical Reaction in Molecular Solids at Very High Pressure

K. Aoki
National Institute of Materials and Chemical Research, Tsukuba, Ibaraki 305, Japan

High-pressure structural study of molecular solids provide us a valuable insight into the nature of chemical bond. A number of molecules with triple bond such as acetylene and hydrogen cyanide have been found to undergo phase transition and chemical reaction in a pressure range up to several gigapascals. In a sub-terapascal region, polymerization or dissociation may be observed even for very stable molecules such as carbon dioxide and nitrogen. These high-pressure behaviors are interpreted in terms of changes in inter or intramolecular bonds. Recent high-pressure results for solid acetylene and carbon dioxide obtained by Raman scattering, infrared absorption, and x-ray diffraction are presented.

1. Introduction

Molecular arrangement in solid is interpreted in terms of intermolecular forces such as van der Waals and electrostatic forces. When condensed, molecules regularly algin in crystals to minimize the cohesive energy. The contribution of each intermolecular force to the cohesive energy varies with distances between the interacting molecules, and hence depends on pressure. Alternation of the contribution subsequently causes phase transitions with molecular rearrangement. As well as volume compression data, the structural data for high pressure phases provide us an insight into the intermolecular forces, and are of very valid for construction of the reliable theoretical models of intermolecular potentials.

Reconstruction of intramolecular bonds occurs in highly densified molecular solids. Intramolecular bonds, which are stronger than intermolecular bonds roughly by a factor of several tens, are influenced little on compression. This allows an assumption of rigid molecules in interpretation of high pressure effects on molecular solids. When molecules approach beyond a threshold distance at very high pressure, formation of new bonding between adjacent molecules is expected. Monomers polymerize into large molecules or dissociate into atoms. Polymerization of acetylene with *sp* to sp^2 rehybridization is the former example[1]; metallization of iodin is the latter example[2].

We can thus observe various changes in inter and intramolecular bonds with increasing pressure, and consequently extend and deepen our understanding of the nature of chemical bond.

Table I. Phase transitions and chemical reactions in molecules with double or triple bonds. Crystal structures are those of high-pressure phases appearing at room temperature. Reaction pressures are those at room temperature.

molecule	formula	crystal structure	reaction pressure	reference
acetylene	C_2H_2	*Pa3, Cmca*	3.5 GPa	3, 4
hydrogen cyanide	HCN	*I4mm, Imm2*	1.5 GPa	5, 6
cyanoacetylene	HCCCN	$P2_1/m$	1.5 GPa	7, 8
cyanogen	C_2N_2	*I(?), II(?), III(?)*	3.5 GPa, 10 GPa	9, 10
acetonitril	CH_3CN	$P2_1/C$, *Pbam or Pmmm(?)*	15 GPa	11
tetracyanoethylene	$(CN)_2CC(CN)_2$	*Im3*, $P2_1/n$	6 GPa	12
benzen	C_6H_6	*II(?), III(?), III'(?)*	20 GPa	13,14

2. Gigapascal Region

Several unsatulated molecules have been found to undergo phase transition and polymerization at high pressure (Table I). For study of rehybridization process, the simple molecules with triple bonds are of particular interest. Triple bond, which consists of one *sp* hybrid orbital and two π orbitals, likely converts into double bond and further into single bond as a consequence of rehybridization. For several molecules with CC and CN triple bonds, phase transition and chemical reaction have been investigated by Raman scattering, infrared (*ir*) absorption, and x-ray diffraction. The results for acetylene, C_2H_2, which seems to be most appropriate to show how phase transition and polymerization takes place under pressure, will be described below.

2.1 Phase Transition in Solid C_2H_2

The outline of the phase diagram for C_2H_2 is drawn using limited low-temperature and high-pressure experimental data (Fig.1). The low temperature phase appearing between 191 and 133 K at atmospheric pressure is cubic with *Pa3* space group[15]. Below 133 K an orthorhombic structure with *Cmca* space group becomes stable[16]. Their crystal structures are illustrated in Fig.2. Molecular axes are oriented along one of the body diagonals of the cube in the *Pa3* structure, whereas they are aligned in the same planes parallel to the base plane in the *Cmca* structure. They are converted to each other by rotation of the molecular axes. Along an isotherm at 298 K, the same sequential transitions take place: the liquid to the cubic phase at 0.7 GPa and to the orthorhombic phase at 0.9 GPa.

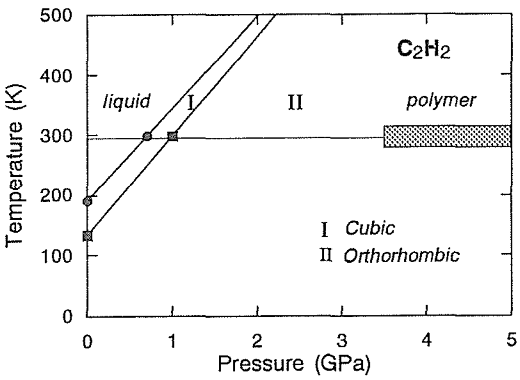

Fig.1. Phase diagram of C_2H_2.

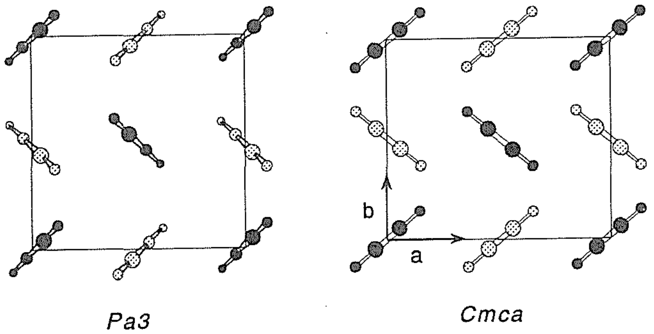

Fig.2. *Pa3* and *Cmca* structures of solid C_2H_2.

The intermolecular forces between C_2H_2 molecules have theoretically been studied[17,18]. Acetylene is a linear molecule having a large quadrapole moment ($+3.0 \times 10^{-26}$ esu cm^2). Lattice energy calculation for various linear molecules has shown that both the cubic *Pa3* and orthorhombic *Cmca* structures are favored for the molecules with a large quadrapole moment, and hence for C_2H_2. Another intermolecular force playing a major role in arrangement of C_2H_2 molecules is the hydrogen bond formed between the CC triple bond and the hydrogen atom[17]. This short-distance interaction tends to force molecules to algin in the T-shaped configuration, which can actually be recognized in the orthorhombic structure. Prior to the experimental observation, the cubic to orthorhombic transition under pressure has been predicted successfully by theoretical study in which the hydrogen bond is explicitly taken into account[18].

The variations of the cell dimensions with pressure are shown in Fig.3. The equivalent three cubic edges split into the *a,b,* and *c* edges at 0.9 GPa. Among them, the *c* edge shows a faster decrease with pressure. Since it corresponds to a half of the interlayer spacing, the large compressibility is attributed to the relatively weak bonding between the molecular layers. It is noted that the length of the *a* edge approaches that of the *b* edge; the rectangular base plane is gradually converted to a square. At 4.2 K and atmospheric pressure, the two molecular axes in the T-shaped configuration forms an angle of about 80 degree[16]. The resulting *a/b* ratio is 1.03. At 2.8 GPa and room temperature, the *a/b* ratio decreases to 1.01 very close to 1, suggesting the molecular rotation into the correct T-shaped configuration. This molecular rotation may be driven by strengthening of the hydrogen bonding as the molecules approach.

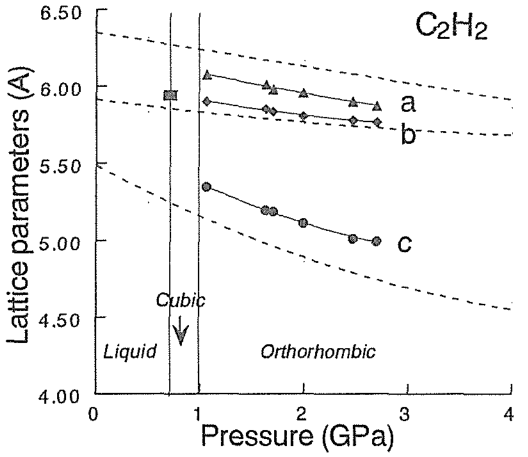

Fig.3. Variation of the lattice parameters of C_2H_2 under pressure. Broken curves are those of calculation[18].

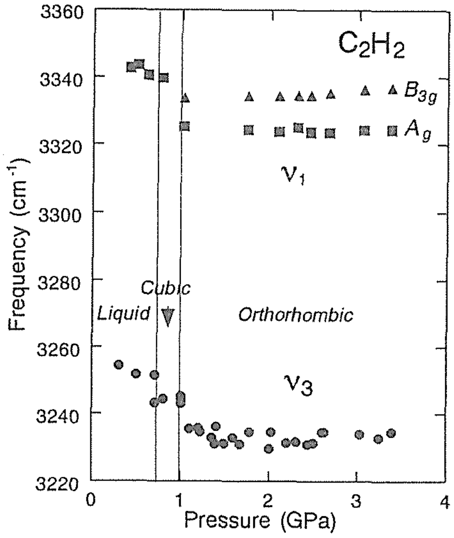

Fig.4. Variation of the CH stretching frequency of C_2H_2 under pressure.

It is interesting to see how the molecular rearrangement affects the vibrational property. Significant spectral change in the lattice vibrational region has been observed in associated with the phase transition by Raman scattering[3]. The intramolecular vibrational frequencies are rather insensitive to the phase transition, but particular intramolecular modes show drastic changes.

Figure 4 shows the variation of the C-H stretching frequencies with pressure. The ν_1 mode is the Raman-active symmetric stretch and ν_3 is the *ir*-active antisymmetric stretch[19]. These frequencies are very sensitive to the molecular arrangement since the C-H bond participates in formation of the hydrogen bond. Both the ν_1 and ν_3 frequencies discontinuously decrease at 0.9 GPa, indicating formation of the hydrogen bond in the T-shaped molecular arrangement. For the ν_1 mode of the orthorhombic phase, the A_g and B_{3g} splitting is shown to increase with pressure. This is also ascribed to strengthening of the hydrogen bonding as well as the variation of the *a/b* ratio described above.

2.2 Polymerization in Solid C_2H_2

Polymerization occurs at pressures above 3.5 GPa. As the reaction proceeds, the transparent solid turns yellow, red, and finally black. Raman spectra show that the reaction product contains conjugated linear polymers (polyacetylene)[4]; the Raman peaks at 1100 and 1500 cm^{-1} are those from the coupling vibration of C-C stretch and C-H deformation and the mainly C=C stretch, respectively. Presence of cis-polyacetylene, another isomer of polyacetylene, has also been shown in resonant Raman spectra.

The overall structural aspect of the reaction product has been obtained by *ir* absorption[19]. The *ir* spectra taken for the reaction process at 4.2 GPa show that new peaks are observed around 1000, 1600, and 3000 cm^{-1} in addition to the monomer peaks, indicating formation of polymers with conjugated backbone. While the pressure is increased to 10 GPa, the intensity of the absorption peaks related to C-H stretching of saturated carbon hydride increases but those from conjugated polymer backbone change little. Formation of sp^3 polymers is accelerated at higher pressures and the opaque sample returns transparent again. Thus the successive rehybridization from *sp* to sp^2, and finally to sp^3 can be seen in solid C_2H_2 as the pressure increases.

3. Sub-terapascal Region

At very high pressure beyond one megabar, chemical reaction is expected to occur even in very stable molecules such as nitrogen, N_2, and carbon dioxide, CO_2. Polymerization of N_2 has been suggested experimentally by shock compression[20], under which a high temperature exceeding a few thousand degrees is generated simultaneously with rapid compression, and theoretically predicted to occur around 100 GPa under hydrostatic compression[21]. A recent theoretical calculation for a newly proposed structure has bravely lowered the polymerization pressure to 55 GPa about a half of the previously predicted pressure[22]. Several experiments have already confirmed that N_2 molecule still exists at least up to 180 GPa[23,24]. One likely explanation for the discrepancy between the theory and the experiment is a presence of a large potential varier along the reaction pass. High temperature may be required to drive the inhibited reaction.

Neither experimental nor theoretical work has been made for the solid-state polymerization of CO_2. In contrast, phase transitions in the molecular phase have been extensively investigated both by theory and by experiment.

3.1 Phase Transition in Solid CO_2

Dry ice with a cubic *Pa3* structure has been the only known crystalline phase of CO_2 for a pressure range up to 20 GPa and a temperature range up to 300 K. This is very contrast to the high pressure behaviors of other simple molecules. Nitrogen, for instance, is found to exhibit six crystalline phases in the corresponding pressure and temperature ranges[25]. As well as C_2H_2, CO_2 has a very large quadrapole moment of -4.3×10^{-26} esu cm^2. So that the wide ranged stability of the *Pa3* structure can be interpreted in terms of the quadrapole-quadrapole interactions. Further more, a transition into an orthorhombic structure has been predicted intuitively by analogy with the phase transition observed for C_2H_2 and theoretically by cohesive energy calculation.

A structural transition into a high pressure phase was first observed at about 18 GPa and ambient temperature by Raman measurement[26]. Recent *ir* measurement has revealed that the transition occurs at about 12 GPa[27], which has been confirmed very recently by x-ray diffraction[28]. Low temperature Raman measurement has also confirmed appearance of the high pressure phase about 11 GPa at temperatures of 40 and 80 K[29], indicating that the transition pressure is little influenced on temperature. Such temperature insensitive feature of the cubic to orthorhombic transition is in agreement with the calculated results, although the agreement in the transition pressure with the experiment seems not satisfied[30,31].

The high pressure structure has been determined by x-ray diffraction to be an orthorhombic structure belonging to *Cmca* space group[28]. The cell dimensions containing four molecules are $a=4.330\pm0.015$, $b=4.657\pm0.005$, and $c=5.963\pm0.009$ Å at 11.8 GPa. The angle ϕ between the molecular axis and the crystallographic b axis is about 52°. (The arrangements of CO_2 molecules in the cubic *Pa3* and orthorhombic *Cmca* structures are same as those in the cubic and orthorhombic structures of C_2H_2, respectively. See Fig. 2) These lattice parameters are in good agreement with the calculation which gives $a=4.17$, $b=4.65$, $c=6.02$ Å, and $\phi=52°$ at 12 GPa[30].

The volume compression data show that the volume reduction associated with the transition is very small (Fig.5). The molar volume of the orthorhombic cell at 11.8 GPa is 18.03 cm^3/mol, whereas that of the cubic structure coexisting at 11.8 GPa is 18.10 cm^3/mol. The volume change can be considered to be zero within the experimental error. Another characteristic feature concerning with the phase transition is that the two phases coexist for a wide pressure range. The reflection peaks from the cubic structure are observed even at 18 GPa. This may be related to the very small volume difference between the two phases.

The phase transition has been detected by *ir* absorption measurement[27]. The CO_2 molecule has three normal vibrational modes, the symmetric stretching mode ν_1, the bending mode ν_2, and the antisymmetric mode ν_3. The frequency shifts of the normal modes, $\nu_i(P)-\nu_i(0)$, calculated from the observed combination *ir* frequencies are plotted in Fig.6. For the cubic phase, the calculated results agree well with the experimental data, reproducing the overall aspects of the frequency shifts measured. However, agreement is shown to be a little poor for the high-pressure orthorhombic phase. The calculation predicted frequency decrease for all the normal modes and a remarkably large change in the antisymmetric stretching mode ν_3[31]. The experiment has revealed that the frequency of the bending mode ν_2 increases and the symmetric stretching mode ν_1 shows the largest decrease at the phase transition.

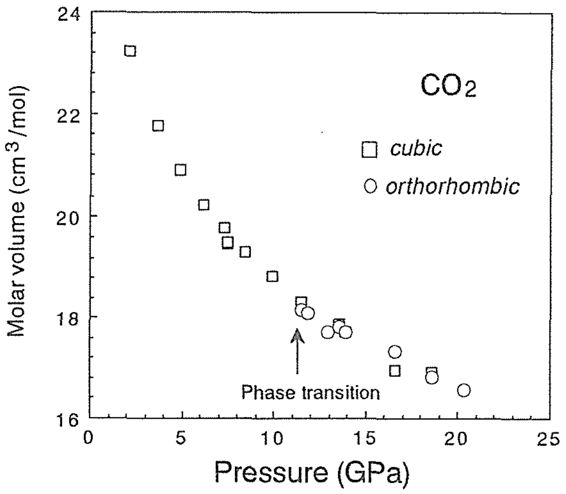

Fig.5. Variation of the molar volumes of solid CO_2 under pressure.

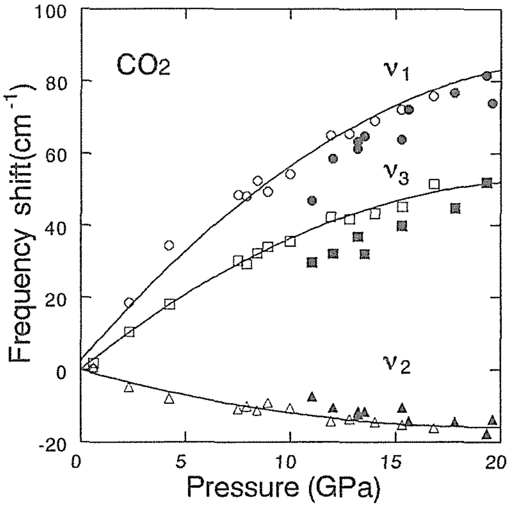

Fig.6. Frequency shifts of the normal vibrational modes of CO_2 with pressure: open and solid symbols represent the cubic and orthorhombic phases, respectively. Solid curves are fitted to the data of the cubic phase.

3.2 Polymerization in Solid CO_2

The presence of CO_2 molecule has been confirmed at least up to 50 GPa by x-ray diffraction[32]. No reaction has been observed (Fig.7). However, there still remains a possibility of polymerization of CO_2 as observed for CS_2, and it may occur at higher pressure and probably at very high temperature. Initiation of polymerization by laser heating is being examined.

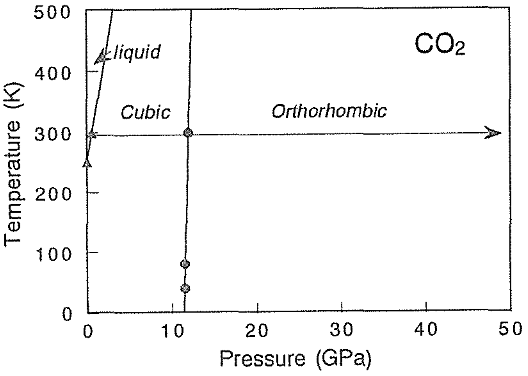

Fig.7. Phase diagram of CO_2

4. Summary

The high pressure experiments on solid C_2H_2 and CO_2 were described. The observed phase transition and chemical reaction were shown to be interpreted in terms of gradual or abrupt changes in chemical bonds between or within the molecules. Structural study by x-ray or neutron diffraction will be required to determine exactly molecular arrangement through phase transition or chemical reaction. Extension of temperature range up to a few thousand kelvin is also required to drive chemical reaction. Diffraction measurement with a use of intense synchrotron x-ray beam and high temperature generation by laser heating will be of essential techniques for advancing these measurement on molecular solids.

References

1. K. Aoki, Y. Kakudate, M. Yoshida, S. Usuba, K. Tanaka, and S. Fujiwara, *Sol. State Commun.* **64**, 1329(1987).
2. K. Takemura, S. Minomura, O. Shimomura, Y. Fujii, *Phys. Rev. Lett.* **45**, 1881(1980).
3. K. Aoki, Y. Kakudate, M. Yoshida, S. Usuba, K. Tanaka, and S. Fujiwara, *J. Chem. Phys.* **88**, 4565(1988).
4. K. Aoki, Y. Kakudate, M. Yoshida, S. Usuba, K. Tanaka, and S. Fujiwara, *ibid*, **89**, 529(1988).
5. K. Aoki, B. J. Baer, H. C. Cynn, and M. Nicol, *Phys. Rev.* **B42**, 4298(1990).
6. K. Aoki, B. J. Baer, H. C. Cynn, and M. Nicols, *Molecular Systems under High Pressure* (Edited by R. Pucci and G. Piccitto, Elesevier Science Publisers, North-Holland, 1991)p.283.
7. K. Aoki, Y. Kakudate, M. Yoshida, S. Usuba, and S. Fujiwara, *J. Chem. Phys.* **91**, 778(1989).
8. K. Aoki, Y. Kakudate, M. Yoshida, S. Usuba, and S. Fujiwara, *ibid*, **91**, 2814(1989).
9. C-S. Yoo and M. Nicol, *J. Phys. Chem.* **90**, 6726(1986).
10. C-S. Yoo and M. Nicol, *ibid*, **90**, 6732(1986).
11. H. Yamawaki, K. Aoki, Y. Kakudate, M. Yoshida, S. Usuba, and S. Fujiwara, *Chem. Phys. Lett.* **169**, 77(1990).
12. H. Yamawaki, K. Aoki, Y. Kakudate, M. Yoshida, S. Usuba, and S. Fujiwara, *ibid*, **198**, 183(1992).
13. Ph. Pruzan, J. C. Chervin, M. M. Thiery, J. M. Besson, J. P. Forgerit, and M. Revault, *J. Chem. Phys.* **92**, 6910(1990).
14. F. Cansell, D. Fabre, and J-P Petitet, *ibid*, **99**, 7300(1993).
15. G. J. van Nes and F. van Bolhuis, *Acta Crystallogr. Sect.* **B35**, 2580(1979).
16. H. K. Koski and E. Sandor, *ibid*, **B31**, 350(1975).
17. K. Sasaki, A. Koide, and T. Kihara, *Chem. Phys. Lett.* **47**, 416(1977).
18. R. LeSar, *J. Chem. Phys.* **86**,1485(1987).
19. M. Sakashita, H. Yamawaki, and K. Aoki (unpublished data).
20. W. J. Nellis, N. C. Holmes, A. C. Mitchell, and M. Van Thiel, *Phys. Rev. Lett.* **53**, 1661(1984).
21. A. K. McMahan and R. ReSar, *ibid*, **54**, 1929(1985).
22. C. Mailhoit, L. H. Yang, and A. K. McMahan, *Phys. Rev.* **B46**, 14419(1992).
23. R. Reichlin, D. Schiferl, S. Martin, C. Vanderborgh, and R. L. Mills, *Phys. Rev. Lett.* **55**, 1464(1985).
24. P. M. Bell, H. K. Mao, and R. J. Hemley, *Physica B+C* **139&140B**, 16(1986).
25. R. D. Etters, *Simple Molecular Systems at Very High Density* (Edited by A. Polian, P. Loubeyre, and N. Boccara, Plenum, New York, 1988) p.109.
26. R. C. Hanson, *J. Phys. Chem.* **89**, 4499(1985).
27. K. Aoki, H. Yamawaki, M. Sakashita, *Phys. Rev.* **B48**, 9231(1993).
28. K. Aoki, H. Yamawaki, M. Sakashita, Y. Gotoh, and K. Takemura, *Science*, **263**, 356(1994).
29. H. Olijnyk, H. Daufer, H. -J. Jodl, H. D. Hochheimer, *J. Chem. Phys.* **88**, 4204(1988).
30. B. Kuchta and R. D. Etters, *Phys. Rev. B*, **38**, 6265(1988), *Phys. Rev.* **B47**, 14691(1993).
31. R. D. Etters and B. Kuchta, *J. Chem. Phys.* **90**, 4537(1989).
32. L. Liu, *Earth Planet Sci. Lett.* **71**, 104(1984).

Spectroscopic and X-Ray Studies of Materials at High Pressure: Recent Developments

Malcolm Nicol[a], *Suzanna E. Gibson*[a], *Diane Reifschneider*[a], *Susanna W. Johnson*[a,b,†]
Bruce Baer,[a,*] *and David Schiferl*[b]
[a]Department of Chemistry and Biochemistry, University of California,
Los Angeles, CA 90024-1569, U.S.A.
[b]Los Alamos National Laboratory, Los Alamos, NM 87545, U.S.A.

Abstract. Recent studies of oxygen, sulfur, and nitroanilines illustrate some of the complex behaviors of nominally simple molecular solids at high pressures. We describe: a general method for analyzing diffraction patterns from a sample consisting of several small crystals used to characterize the structure of ϵ-O2; Raman spectra of sulfur at high pressures that further corroborate our impression that photoreaction mechanism at high pressures are not simple; and changes in the lattice, $-NH_2$, and $-NO_2$ regions of Raman and inelastic neutron scattering spectra of ortho- and para-nitroaniline which provide evidence of structural phase transitions at moderate pressures.

Simple molecular solids often behave in complex ways at high pressures as recent studies of oxygen, sulfur, and the nitroanilines show. Crystals of these materials are intensely chromatic at high pressures, with colors varying dramatically with crystal orientation and pressure.[1-5] Optical and infrared vibrational spectra in solid ϵ-O_2 indicate that its bonding and electronic structure are especially unique. Sulfur and the nitroanilines are photosensitive at pressures of the order of 5 GPa. Oxygen and sulfur are reported to become metals near 95 and 82 GPa, respectively.[6,7] In order to interpret the spectra, possible insulator-to-metal transitions, magnetic and transport properties of these solids on the atomic scale, the structures of the relevant phases must be established. Structure determinations are difficult for relatively simple crystals at high pressures, and work on these structures are further complicated because they cannot be prepared at ambient pressure and have relatively low-symmetry cells containing many light atoms. This report describes progress on defining the properties, spectra, phases, and structures of these solids at high pressures and understanding how the structures relate to the optical properties and dynamics of these systems.

Diffraction studies with single crystals usually provide the most accurate structural information on materials. For phases that are stable only at high pressures, however, it may be impossible to grow a crystal large enough and suitably oriented for collecting reliable structural data. Efforts to elucidate the structure of ϵ-O_2 illustrate some of the problems. Powder diffraction studies have provided structures for many high pressure phases but not for ϵ-O_2. While several groups have obtained powder patterns of ϵ-O_2 at pressures from 10 to 61 GPa,[8,9] these patterns have not been interpreted successfully. Crystals of ϵ-O_2 suitable for single crystal work have been grown only by heating samples under pressures above 16 GPa to or near melting in a Merrill-Bassett diamond-anvil cell with beryllium backing plates and slowly cooling the crystals to ambient temperature. The beryllium is highly stressed and prone to failure during heating, risking loss of both the sample and cell. Thus, when samples consisting of several 25-μm-diameter crystals with different orientations, as evident from different colors in polarized light, were obtained after one or two heating cycles,[10] we were

---

[†] Deceased January 21, 1994
[*] Current address: Department of Chemistry, University of California, Riverside, CA.

motivated to extend single-crystal procedures to several-crystal samples.

Our initial approach was to collect diffraction data from the sample using a Rigaku rotating Mo-anode generator and a Picker diffractometer. This source illuminated all of the crystals at the same time so that reflections were simultaneously collected from several different crystals with unknown, different orientations. This several-crystal approach is a mixed blessing which may be typical of high pressure-high temperature diffraction work. For any one crystal, the metal components of the diamond-anvil cell mask scattering from many reciprocal lattice points needed to solve the structure. With some luck, scattering from these points will points will not be masked for some other crystals with other orientations. The crystallographic challenge is then to identify reflections from crystals of the same structure with different, unknown orientations. Of course, one wants to avoid samples where reflections from different crystals overlap, for example, a twinned crystal.

Our general procedure for analyzing several-crystal diffraction patterns is described in detail elsewhere[11] and is only briefly outlined here. The first step of the analysis is to determine the centered diffractometer angles (θ, ω, χ, and ϕ) where each reflections appears. The Cartesian components of a jth reciprocal lattice vector, $\mathbf{v}_j$, in the ϕ-axis system[12] and the angle Ψ_{jk} between the jth and kth reflections can be expressed in terms of the X-ray wavelength, λ, and sines and cosines of θ, ω, χ, and ϕ.[11] The value of the angle Ψ_{jk} is significant if reflections corresponding to $\mathbf{v}_j$ and $\mathbf{v}_k$ originate from the same crystal; in this case, Ψ_{jk} relates directly to the angle between planes of atoms in real space. Certain values of Ψ_{jk} like 60°, 90°, 120°, 270° or the 35° angle between 111 and 100 reflection for a cubic structure are especially interesting because they suggest both that the jth and kth reflections may originate from the same crystal and that the unit cell may have higher than triclinic symmetry.

The tasks of identifying reflections from the same crystal involves searching for reflections, $\mathbf{v}_j$, $\mathbf{v}_k$, and $\mathbf{v}_m$, which are related by vector summation:

$$\mathbf{v}_m = c_{mj}\mathbf{v}_j + c_{mk}\mathbf{v}_k \qquad (1)$$

where c_{mj} and c_{mk} are constants, ideally small integers. The diffractometer angles for possible $\mathbf{v}_m$'s can be calculated from the measured diffractometer angles for $\mathbf{v}_j$ and $\mathbf{v}_k$, and the diffractometer can be driven to search for diffracted intensity in the vicinity of the appropriate angles. If intensity is observed, the reflection can be centered. If the centered reflections satisfy (1) within an acceptable uncertainty, the reciprocal lattice vectors, $\mathbf{v}_j$, $\mathbf{v}_k$, and $\mathbf{v}_m$, can be confidently assigned to a reciprocal lattice plane of the same crystal. Extension of the analysis to three dimensions to identify non-coplanar lattice vectors leads to the solution of the unit cell of the material in questions. The matches do not have to be developed from the same crystal. Once the required matches have been developed, the unit cell of the sample and orientation matrices of individual crystals can be determined. More complete intensity data sets can then be collected for individual crystals as a basis for solving the full crystal structure, including atomic positional and thermal parameters.

We used this approach to determine that ϵ-O_2 has an 8-molecule monoclinic cell with lattice constants: a = 3.649 Å; b = 5.493 Å; c = 7.701 Å; β = 116.11°. The space group could not be definitely determined because the several observed intensities were low; but systematic absences for three crystals in the ϵ-O_2 sample suggest that the space group is A2/m. The data collected with the rotating anode source also were insufficient to determine precise atomic positional and thermal parameters. Further work with more intense synchrotron sources collimated to illuminate individual crystals in the sample is needed to define these parameters. Again, the orientational information obtained from the several crystal work will be helpful here in reducing the amount of synchrotron time required to locate reflections from the individual crystals.

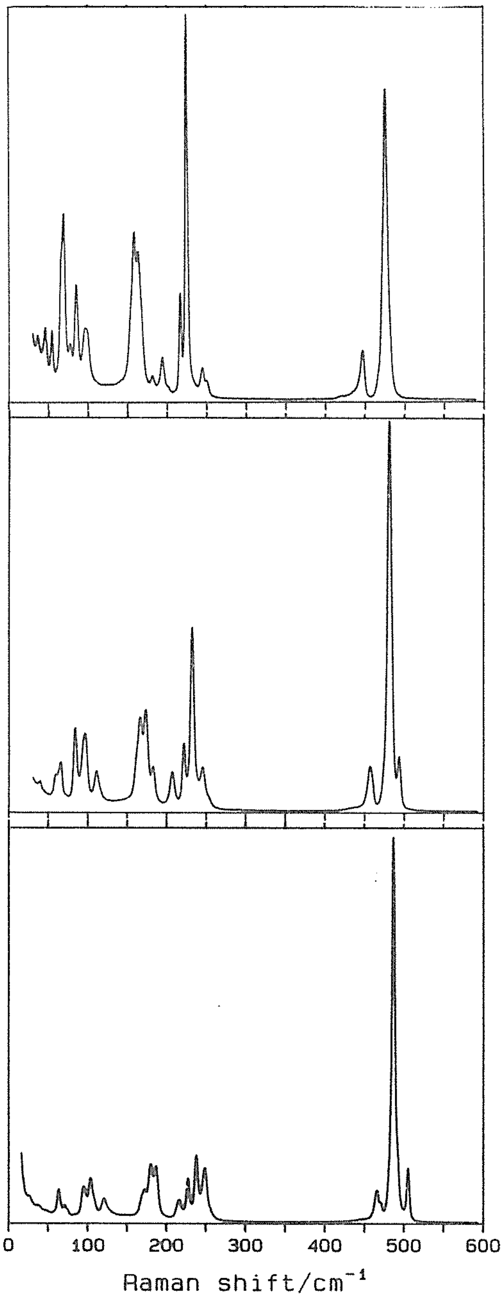

Fig. 1. Raman spectra of sulfur with 605-nm excitation at ambient temperature and 2.1, 4.8, and 7.3 GPa. These spectra show no evidence of the photoproduct.

Sulfur is the most complex Group VIA element at high pressures. More than 25 years after Vezzoli, Dachille, and Roy[13] comprehensively summarized sulfur at ambient and higher temperatures to 10 GPa, efforts to confirm and extend the diagram continue to yield serious discrepancies among studies using the same techniques, and contradictory results *between* techniques--even at ambient temperature. For example, Nagata et al.[14] recorded Raman spectrum showing a reversible phase transition at 5.2 GPa, while their X-ray diffraction patterns showed no sign of phase changes up to 8.3 GPa. Such persisting confusion surrounding the phase behavior of sulfur is less surprising in light of our discovery of the wavelength dependence of Raman spectra of sulfur at high pressures.[4] At higher pressures (> 20 GPa) without the complications of laser irradiation, recent X-ray results[15,16] have converged on a clearer view of the sequence of phase transitions at ambient temperature leading to metallic sulfur in the 100-GPa range.

The influence of photochemistry on sulfur to 10 GPa has been a focus of our work. Fig. 1 shows Raman spectra excited by a 605-nm dye laser of sulfur at ambient temperature at 2.1, 4.8, and 7.3 GPa which are characteristic of α-S_8 or phases V and IX of Vezzoli, Dachille, and Roy.[13] At this wavelength and these pressures, sulfur is not photoreactive. The photosensitivity of sulfur to 530.9-nm light at ambient temperature is shown in Fig. 2 by Raman spectra of powdered sulfur at 7.7 GPa obtained in sequence with 647.1, 568.2, 530.9, and 568.2-nm excitation. X-ray diffraction patterns of "phototransformed" sulfur have not been detected,[13,14] leading one group to conjecture that the product may occur only at the illuminated surface of the sample, although the intensities of features of transformed sulfur in Raman spectra likethe lowermost trace in Fig. 2 suggest that the extent of transformation may be high at least for powders. Preliminary Raman spectra of sulfur at high pressures and low temperatures further complicate the interpretation of the photomechanism.

Raman and inelastic neutron diffraction spectra of triaminotrinitrobenzene (TATB) at high pressures show that the nitro substituents are perturbed by hydrogen bonds to amine groups.[19] A strong deuterium isotope effect also is observed. The coupling between lattice phonon modes and higher energy vibrational modes, promoted by hydrogen bonding, also has been suggested as a mechanism for depositing the mechanical energy of a shock wave in a detonation.[20] Exactly how this is accomplished is not known.

Because these perturbations may be inter- or intra- molecular in origin, we have sought to compare these observations for TATB with properties of related nitroanilines with (o-nitroaniline, ONA) and without (p-nitroaniline, PNA) intramolecular hydrogen bonds to define more clearly the sources of the perturbations. These Raman and companion inelastic neutron scattering (INS) studies of ONA, PNA, and the ring or amine perdeuterated isotopomers (ONA-d_4, ONA-Nd_2, PNA-d_4, and PNA-Nd_2) at high pressures also detect phase changes and variations of the mode coupling between phases. Infrared spectra at ambient pressure of the nitroanilines in an argon matrix at 20 K or thin films at ambient to 20 K were collected to aid in interpreting the high pressure spectra.

The lack of good normal-mode bases is a major problem in interpreting the nitroaniline spectra. Previous studies have interpreted these spectra in terms of symmetry modes of benzene; however, the ring, nitro, and amine modes are so strongly mixed that this is not a good approximation.[21] Better symmetry

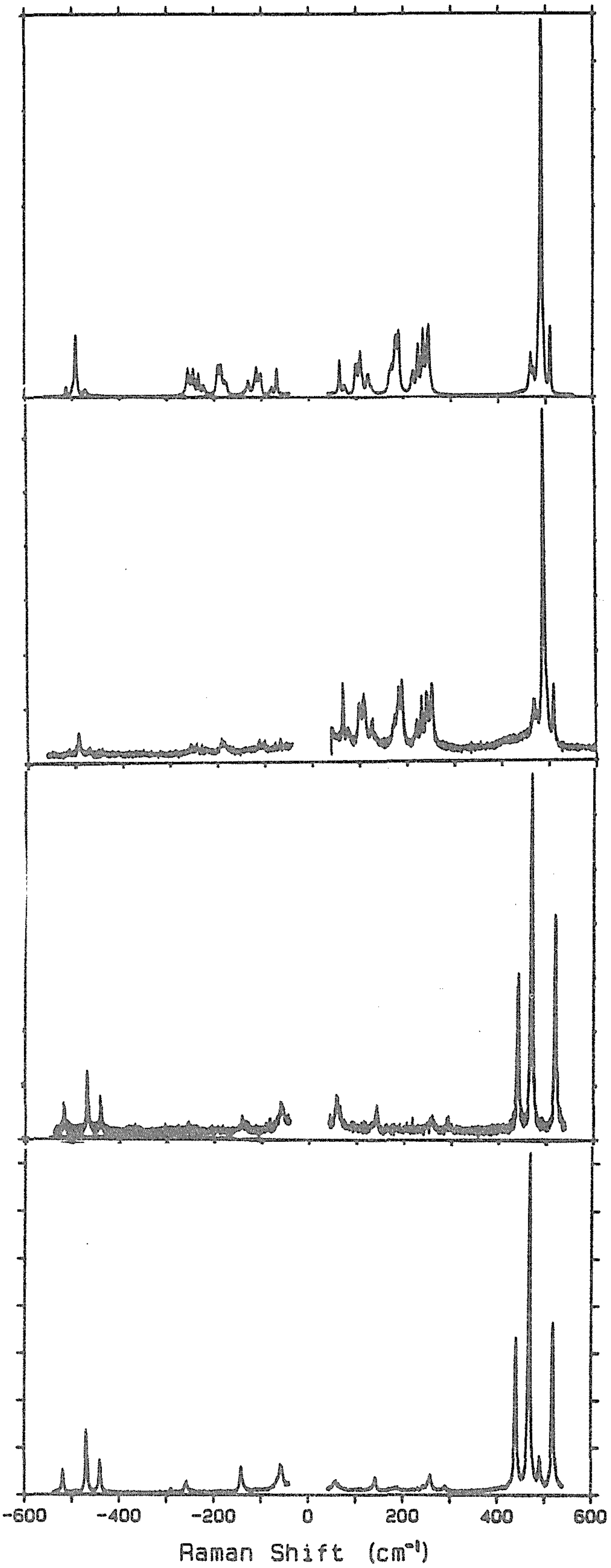

Fig. 2. Raman spectra of sulfur at 7.7 GPa taken in order with 647.1 (top), 568.2, 530.9, and 568.2-nm (bottom) excitation. The sample was phototransformed at 530.9 nm and shorter wavelengths. Features of untransformed sulfur very weak in the 568.2-nm spectrum after photoreaction.

modes have been determined for PNA; however, we used an *ab initio* routine, SPARTAN, to identify normal modes for these molecules. This routine first computes an optimal geometry for an isolated molecule and then calculates the normal modes and their approximate vibrational frequencies for this geometry. The calculations were done at the (restricted) Hartree-Fock level of theory using the 6-31G* basis set which allows for polarization so effects of hydrogen bonding are included. Computations for PNA were performed assuming the molecular symmetry to be C_s, which has the lower minimum energy, or the planar C_{2v}.

The computations yielded good vibrational assignments for the infrared spectra of ONA and PNA in Ar matrices. However, for PNA films at 20 K or INS spectra at 15 K, better assignments were obtained by assuming C_{2v} symmetry, suggesting that this is the molecular symmetry at low temperatures. Under ambient conditions, the crystal structure of PNA is layered, with chains of the molecules aligned head-to-tail in layers with the rings tipped slightly out of the layers.[23] At lower temperatures, the crystal axis in the layers and normal to the chains elongates. The other axes contract,[5] and the rings appear to flatten into the layers, forcing the amine group to be more co-planar with the ring and the molecule to adopt C_{2v} symmetry and improving intra-layer hydrogen bonding. The structure of ONA is not so layered which may explain why the assignment of modes for the infrared spectra of ONA isolated in Ar can be easily correlated with spectra of ONA crystals at ambient conditions.

Raman spectra of the ONA's were collected to nearly 6 GPa by which the material has turned from orange to black and spectra are of poor quality. Lattice-mode spectra like those in Fig. 3 locate a phase transition at 0.2 GPa which explains the many differences in intensities between INS patterns of ONA-d_4 at ambient pressure and 1 GPa. INS and Raman spectra of the internal modes show that the hydrogen bonds of these two phases are very different. Other splittings and changes of relative intensities in the lattice and internal mode spectra at 2 GPa and higher pressures do not appear to occur at a particular pressure as if there were another phase transition.

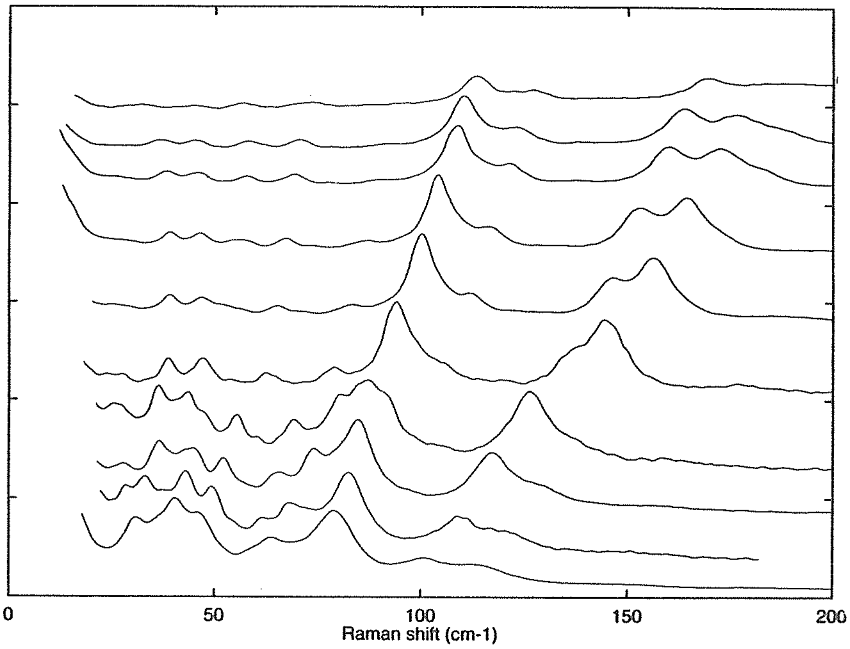

Fig. 3. Lattice-mode (30 to 200 cm^{-1}) Raman spectra of ONA-d_4 at (from bottom to top) ambient pressure, 0.3, 0.7, 1.1, 2.1, 3.1, 3.6, 4.5, 4.8, and 5.5 GPa. Differences between the spectra at ambient pressure and 0.3 GPa are attributed to a phase transition also detected in INS spectra.

Raman spectra of good quality have been collected for PNA to 8 GPa, where it is deep red. Changes of the lattice-mode spectra between 0.7 and 1.0 GPa, corresponding to changes reported at ambient pressure and low temperatures attributed to alignment of the rings in the layers.[24] Further changes between 3.0 and 4.6 GPa correlate with a phase transition established by Block and Piermarini.[6] At higher pressures, PNA is black (making Raman work difficult) and undergoes further chemical or phase changes. Raman spectra collected at pressures as low as 0.8 GPa from PNA samples that had been subjected to pressures above 10 GPa differ qualitatively from spectra of PNA samples that had not been so highly pressurized, suggesting that a different form of PNA or reaction product formed at higher pressure. The conditions where this species forms are not well established; however, the process is not photochemical. The material has not yet been recovered at ambient pressure. The lattice modes and several other features in the NH_2 and NO_2 regions of the Raman spectrum of this material differ from those of other PNA phases; and this material seems to undergo a phase transition below 1.6 GPa. A more complete description of the many detailed changes of ONA and PNA spectra at high pressures is in preparation.

Acknowledgments

Support provided by NSF grant DMR90-11076, IGPP-LANL, and the UCLA Research Committee and assistance from M. Chun, H. Cynn, W. Karney, A. Martin, M. Morgano and P. Wolf are gratefully acknowledged.

References

1. M. Nicol, K.R. Hirsch, and W.B. Holzapfel, *Chem. Phys. Letters* **68** (1979) 49.
2. M. Nicol and K. Syassen, *Phys. Rev.* **B28** (1983) 1201.
3. S.F. Agnew, B.L. Swanson, and L.H. Jones, *J. Chem. Phys.* **86** (1987) 5239.
4. P. Wolf et al., in P. Pucci and G. Piccitto, eds., *Molecular Systems Under High Pressure* (North-Holland, Amsterdam, 1991), 263-271.
5. S. Block and G.J. Piermarini, *SPIE Proceedings* **878** (1988) 21.
6. H. Luo and A.L. Ruoff, *Phys. Rev.* **B48** (1993) xxx.
7. S. Desgrenies, Y.K. Vohra, and A.L. Ruoff, *J. Phys. Chem.* **94** (1990) 1117.
8. B. Olinger, R. L. Mills, and R.B. Roof, Jr., *J. Chem. Phys.* **81** (1984) 5068-5073.
9. S. Desgrenies, Y.K. Vohra, and A.L. Ruoff, *Bull. Amer. Phys. Soc.* **33** (1988) 521.
10. A.S. Zinn, D. Schiferl, and M. Nicol, *J. Chem. Phys.* **87** (1987) 1267.
11. S.W. Johnson, M. Nicol, and D. Schiferl, *J. Appl. Cryst.* **26** (1993) 320.
12. W.R. Busing and H.A. Levy, *Acta Cryst.* **22** (1967) 457.
13. G. Vezzoli, F. Dachille, and R. Roy, *Science* **166** (1969) 218.
14. K. Nagata et al., *Jpn. J. Appl. Phys.* **31** (1992) 1078-1084.
15. Y. Akahama, M. Kobayashi, and H. Kawamura, *Bull. Amer. Phys. Soc.* **38** (1993) 1598.
16. H. Luo and A.L. Ruoff, *Bull. Amer. Phys. Soc.* **38** (1993) 1570.
17. B.J. Baer, D. Schiferl, and M. Nicol, (unpublished).
18. B. Eckert et al., in H.D. Hochheimer and R.D. Etters, eds., *Frontiers of High-Pressure Research* (Plenum, New York, 1991), 143.
19. S.K. Satija et al., *J. Phys. Chem.* **95** (1991) 10103.
20. D. Dlott and M. Fayer, *J. Chem. Phys.* **92** (1990) 3798.
21. See, for example, D. Kumar et al., Vibrational Spectros. **4** (1992) 39.
22. E.W. Schmid et al., Z. Elektrochemie **64** (1960) 940.
23. K. Trueblood, *Acta Cryst.* **14** (1961) 1009.
24. G.S.R. Krishna Murti, *Indian J. Phys.* **31** (1957) 353.

NMR Characterization of Shocked Quartz*

M.B. Boslough, R.T. Cygan, R.A. Assink and R.J. Kirkpatrick[†]
Sandia National Laboratories, Albuquerque, NM 87185 U.S.A.,
[†] University of Illinois, Urbana, IL 61801, U.S.A.

ABSTRACT

We have characterized experimentally and naturally-shocked quartz (both synthetic and natural samples) by solid state nuclear magnetic resonance (NMR) spectroscopy. Relaxation analysis of experimentally-shocked samples provides a means for quantitative characterization of the amorphous/disordered silica component. NMR spectra demonstrate that magnetization in both the amorphous and crystalline components follows power-law behavior as a function of recycle time. This observation is consistent with the relaxation of nuclear spins by paramagnetic impurities. A fractal dimension can be extracted from the power-law exponent associated with each phase, and relative abundances can be extracted from integrated intensities of deconvolved peaks. NMR spectroscopy of naturally-shocked sandstone from Meteor Crater, Arizona (USA) led to the discovery of a new amorphous hydroxylated silica phase. Solid state NMR spectra of both experimentally and naturally-shocked quartz were unexpectedly rich in microstructural information, especially when combined with relaxation analysis and cross-polarization studies. We suggest solid state NMR as a potentially useful tool for examining shock-induced microstructural changes in other inorganic compounds, with possible implications for shock processing of structural ceramics.

INTRODUCTION

Identification of shocked minerals and determination of their degree of shock metamorphism has become an increasingly important problem in earth and planetary science as the relative importance of hypervelocity impact processes has been recognized. Diagnostic methods for examining shock features in minerals have traditionally relied on qualitative examination of microstructures by optical and electron microscopy. Silicon-29 NMR spectroscopy offers the potential for quantitatively assessing the degree of shock metamorphism in silicates by probing the local bonding environment of silicon. We have performed NMR analysis of both laboratory-shocked synthetic quartz powders, and of naturally-shocked quartz from Meteor Crater, Arizona, USA.

NMR analysis of the recovered products from controlled explosive shock-loading experiments was performed to investigate shock-induced amorphization processes. Si-29 NMR spectroscopy is an excellent probe of the local bonding environment of silicon in minerals and is capable of detecting and characterizing amorphous and disordered components. NMR spectra obtained for the recovered materials exhibit a narrow resonance associated with the shocked crystalline material, and a broad component consistent with an amorphous phase, despite the absence of evidence for glass from optical microscopy. The NMR measurements were performed over a range of recycle times from 1 second to 83 hours.

We have also collected spectra from five naturally-shocked Coconino Sandstone samples from Meteor Crater, with the goal of examining possible correlations between NMR spectral characteristics and shock level. We had previously found a strong correlation between the width of the Si-29 resonance and peak shock pressure for experimentally-shocked quartz, due to the shock-induced formation of amorphous silica, which increases as a function of shock pressure between 7.5 and 22 GPa [1,2]. We had suggested that NMR spectra could be used as a "shock barometer", or at least as a screening tool and sensitive method for identifying shocked quartz. However, because the duration of shock loading can be many orders of magnitude longer for natural impacts than for laboratory experiments, we examined the naturally-shocked specimens as well.

EXPERIMENTAL

The shock recovery experiments using quartz powder samples were carried out in the same manner as those for the study of Cygan *et al.* [1]. The experiment made use of the Sandia National Laboratories "Momma Bear" explosive loading fixture to achieve a well-characterized shock state. These recovery fixtures allow samples to be shocked in a controlled, reproducible manner. Shock pressure and temperature histories were determined numerically by two-dimensional computer simulations [3]. The peak shock pressure was 22 GPa. The starting material was synthetic α-quartz sieved to a mean grain size of less than 38 μm (-325 mesh). The quartz was annealed at 900°C for 20 hours to minimize the initial defect densities that initially broadened the (101) X-ray diffraction peak [1].

The NMR spectra of the experimentally-shocked samples were recorded on a Chemagnetics spectrometer, which detects radio-frequency re-emissions from active Si-29 nuclei that have been excited to a high-energy state while the sample is immersed in a magnetic field of 4.7 T. Direct polarization, a comb saturation sequence, and magic angle spinning (MAS) at 4 kHz were employed to provide spectra with significantly reduced dipolar interactions and improved signal-to-noise ratio. The number of scans ranged from 36,000 for short pulse delays to 1 for long pulse delays.

The five samples of shocked Coconino Sandstone were obtained from Meteor Crater to represent the range of shock pressures associated with the impact. The samples are identical to those first examined by Kieffer using X-ray diffraction and optical microscopy [4]. The NMR spectra were obtained at a frequency of 71.5 MHz with an applied magnetic field of 8.45 T. The MAS frequencies were typically at 3.5 kHz, and the pulse recycle time was 30 s. Approximately 200 to 300 mg of sample powder was used for each NMR analysis.

RESULTS

Experimentally-Shocked Synthetic Quartz: Representative spectra collected at two widely different pulse delay times are shown in Figure 1 for the unshocked and shocked synthetic quartz samples. Resonance frequencies are provided in terms of chemical shift (ppm relative to an external standard) and are related to the local bonding environment of silicon-29 nuclei and to the Si-O-Si bond angle distribution. The two spectra of the unshocked sample have qualitatively similar features, independent of recovery time. The spectra for the shocked sample, however, appear quite different for short and long recovery times. For short recovery times, the spectra of the shocked sample exhibit both broad and narrow components. The narrow component corresponds to the normal ordered phase and is similar to that observed for the unshocked sample, while the broad component corresponds to a disordered phase produced by the shock wave. For short recovery times the narrow component dominates to the extent that the contribution of the broad component is not observed. These spectra illustrate the importance of recognizing the relaxation characteristics of complex material.

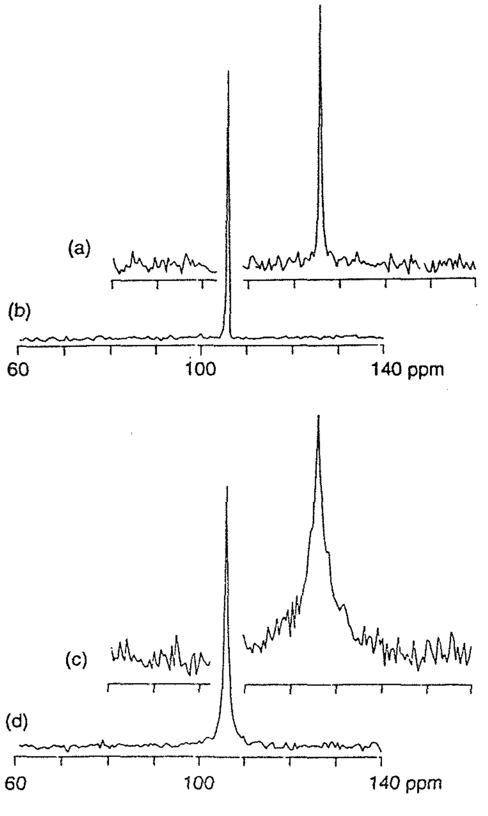

Figure 1. Spectra of unshocked α-quartz at (a) 10 s and 100,000 s and of shocked α-quartz at (c) 10 s and (d) 90,000 s delay time.

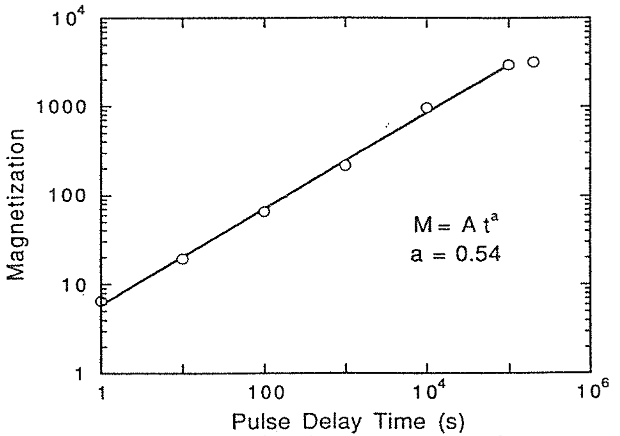

Figure 2. The magnetization recovery of an α-quartz sample on a log-log scale, which follows power-law behavior over 5 decades of time.

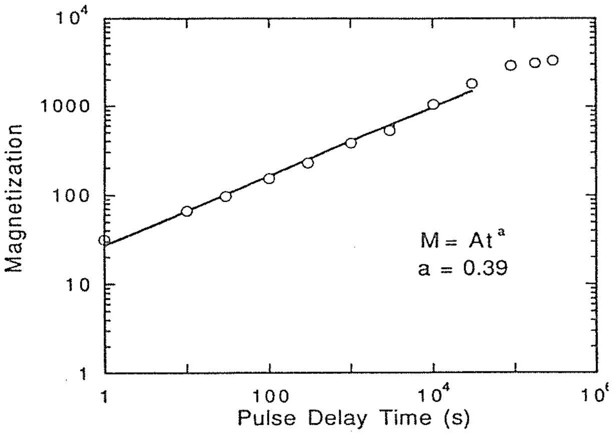

Figure 3. The magnetization recovery of α-quartz shocked to 22 GPa, which consists of components with differing relaxation behavior.

Figure 2 shows the magnetization recovery for a sample of the unshocked α-quartz. The recovery is plotted as a function of pulse delay time on a log-log plot, from which it is clear that the magnetization follows a power-law behavior over 5 decades of time. Calibration of the spectrometer with other silicate samples having shorter relaxation times confirms that the magnetization is near equilibrium for the longest pulse delay times recorded. A least-squares fit to the magnetization data yields a power-law exponent of 0.54. Figure 3 shows the magnetization recovery of an α-quartz sample which has been subjected to a 22 GPa shock wave. The recovery again displays a power-law dependence on pulse delay time, only now the exponent has been reduced to 0.39.

Naturally-Shocked Quartz Sandstone: Figure 4 provides the MAS NMR spectra for the five naturally-shocked samples; numbers in the figures are the same as those used by Kieffer [4]. The spectra are presented in relative order of increasing shock pressure. The ability of MAS NMR to discriminate among the silica polymorphs and amorphous phases is demonstrated by these results. The following is a summary of our observations: Sample #8: mostly quartz, small amounts of coesite and possibly amorphous silica, no stishovite. Sample #4: mostly quartz, more coesite than sample #8, some amorphous silica, and stishovite. Sample #33: same as sample #4, but with an additional peak, due to Q3 (one OH) silicon sites in a dense form of hydroxylated amorphous silica. Sample #7: mostly amorphous silica, with some quartz and coesite, no stishovite, contains a less intense peak associated with the same Q3 site as in sample #33. Sample #9: almost entirely amorphous silica, no stishovite. A representation of the different tetrahedral silicon sites is presented in Figure 5.

DISCUSSION

Experimentally-Shocked Synthetic Quartz: By analyzing the spectra of the experimentally-shocked quartz, we were able to estimate the ratio of disordered to ordered phase and determine the fractal dimension of each phase. The spectra of the shocked quartz were numerically fit with two components: a narrow Lorentzian component corresponding to an ordered crystalline phase and a broad Gaussian component corresponding to a disordered phase. A Lorentzian lineshape provides the best fit for the entire spectrum of the unshocked material as well as the best fit for the narrow component of the shocked material. A Gaussian lineshape provides the best fit for the broad component of the shocked material. Figure 6 shows the relative intensity of each component as a function of pulse delay time. As stated earlier, each component can be described with a power-law pulse delay time dependence. The exponent of the broad Gaussian component equal to 0.32 and the exponent of the narrow Lorentzian component equal to 0.49.

Power-law behavior of the magnetization recovery has been observed previously for paramagnetically doped sol-gel derived silicate samples [5]. Power-law dependence for spin-1/2 nuclei is

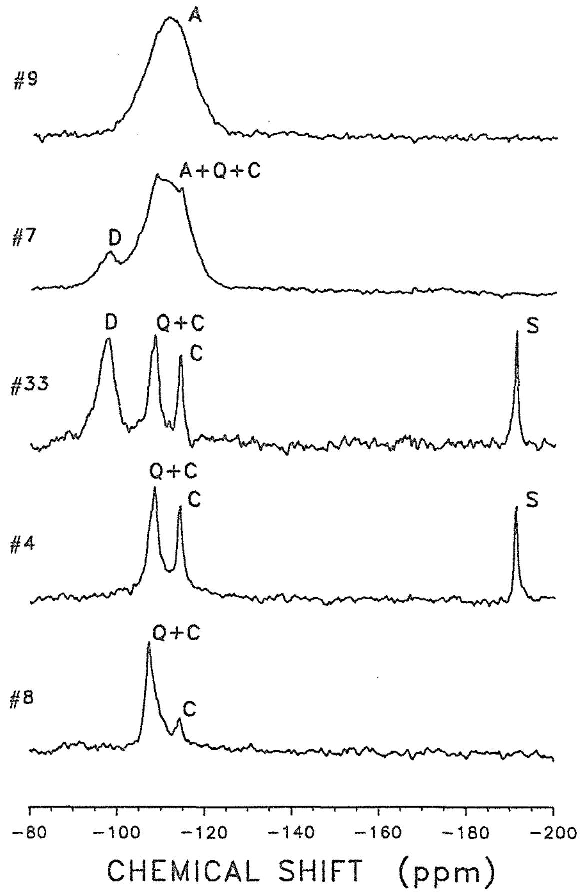

Figure 4. Si-29 NMR spectra of shocked sandstone, where Q=quartz, C=coesite, S=stishovite, A=amorphous (Q4 sites), and D=densified form of hydroxylated amorphous silica (Q3 sites). Sample numbers are those of Kieffer [4].

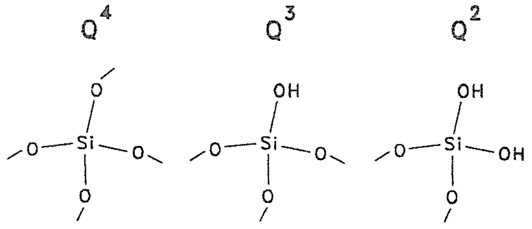

Figure 5. Silicon sites that are distinguished by Si-29 NMR spectroscopy using MAS and CPMAS methods

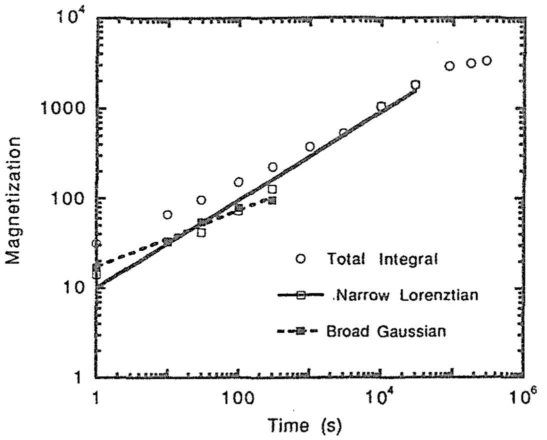

Figure 6. Magnetization recovery of α-quartz sample shocked to 22 GPa. Each spectrum was deconvolved into a narrow Lorentzian (ordered phase) and a broad Gaussian (disordered phase) component.

expected whenever the sample is undergoing MAS and its relaxation is dominated by randomly-distributed paramagnetic impurities. Although the samples in this study were not intentionally doped, they contain low levels of paramagnetic impurities [6]. The power-law exponent was shown by Devreux et al. [5] to be equal to 1/6 of the fractal dimension of the material containing the observed nuclei. The power-law exponent of 0.54 for unshocked quartz is reasonably close to the value of 0.50 predicted for a three-dimensional material. The narrow Lorentzian component, corresponding to relatively undisturbed crystalline material, has a power-law exponent of 0.49--consistent with relaxation controlled by a three-dimensional morphology. By contrast, the power-law exponent of 0.32 for the broad Gaussian component is suggestive of relaxation in a two-dimensional system, implying the amorphous phase is lamellar in structure.

The equilibrium intensities of each component are proportional to the amounts of material in each phase. For times of 10,000 s and above, the broad resonance was a fairly minor component of the total signal and could be ignored. Thus, a reasonable estimation can be made of the equilibrium signal corresponding to the ordered phase. The intensity of the equilibrium signal corresponding to the disordered phase can not be quantitatively determined; however, because the spectra were difficult to fit in the 1000 to 3000 s time regime. We estimate that the disordered phase accounts for less than 10% of the shocked quartz.

Naturally-Shocked Quartz Sandstone: Of particular interest in these results are the strong stishovite resonances in samples #4 and #33; the stishovite peak observed by Yang et al. [7] is significantly weaker. We also observe a more intense X-ray diffraction line ($2\theta = 30.2^0$) for stishovite, implying there is more of this phase in our samples. The only samples for which we observe stishovite are those from the intermediate shock pressures.

The presence of the resonance with a chemical shift of about -98 ppm in two of our samples (#33 and #7) is especially noteworthy. There is no X-ray diffraction evidence for significant amounts of any crystalline material other than the three silica polymorphs. There are several lines of evidence that this resonance corresponds to silicon in tetrahedra with one hydroxyl group in a dense form of hydroxylated amorphous silica: 1) Variable recycle time NMR experiments indicate the resonance has a very short relaxation time (T$_1$), consistent with previous observations for shock-produced amorphous silica. 2) The shift to higher frequency (smaller negative ppm value) is consistent with a denser phase than a similar phase formed at one atmosphere for a given silicon coordination. A dense amorphous phase has been identified in NMR spectra obtained by Nellis et al. [8] from crystalline quartz shocked to 33 GPa, with a resonance centered at about -106 ppm, an upfield shift of about 6 ppm from -112 ppm for normal-density silicon glass [9]. The resonance for Q3 (one OH) silicon sites in a normal-density gel is at about -102 ppm [10]. Our observed peak position of about -98 ppm would be consistent with densification by roughly the same amount as the amorphous silica associated with shocked quartz. 3) The peak is broad, indicating a wide range of Si-O-Si bond angles typical of amorphous material, and is inconsistent with silicon in clay or feldspar. 4) The target Coconino Sandstone was wet, and there is TEM evidence for vesicular "froth" (consisting of amorphous material produced by steam separation) in the intermediate shock samples [11]. 5) We have observed in a previous NMR study of clinoptilolite that shock loading can generate hydroxyl groups [12].

The strongest evidence for the existence of a densified form of hydroxylated amorphous silica is provided by cross-polarization NMR experiments, referred to as CPMAS when using magic-angle spinning. Cross polarization transfers nuclear spin from protons to other NMR-active nuclei, thereby providing additional structural information and preferentially eliminating spectrum signal from anhydrous phases. Figure 8 provides a comparison of the CPMAS and MAS spectra for sample #33. The enhanced CPMAS signal for the -98 ppm resonance confirms the occurrence of the hydroxylated tetrahedral silicon (identified as Q3). A less intense peak at -86 ppm associated with Q2 silicon is also observed in the CPMAS spectrum. No significant CPMAS signal is observed for sample #9; the "A" peak is due to Q4 silicon in amorphous silica.

CONCLUSIONS

The silicon-29 NMR spectra of experimentally-shocked synthetic quartz consist of two components corresponding to ordered and disordered phases. The spin-lattice relaxation of each phase exhibits power-law behavior which suggests that the disordered phase has a two dimensional morphology while the ordered phase is three dimensional. The relative intensities of the fully relaxed spectra yield relative abundances of each phase; by this means, we found that the disordered phase accounts for less than 10% of the total material.

Silicon-29 NMR spectroscopy can also provide considerable microstructural information on high pressure crystalline and amorphous phases resulting from natural impacts. Cross-polarization techniques can be used to enhance silicon resonances near protons to analyze hydrated phases. Using this approach

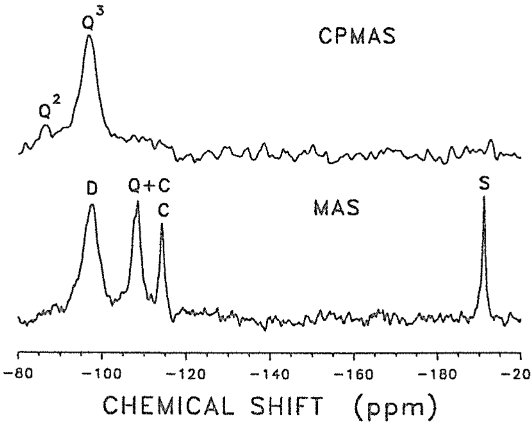

Figure 8. MAS and CPMAS SI-29 NMR spectra for Meteor Crater sample #33 exhibiting the hydroxylated Q3 and Q4 sites for silicon.

we have identified a new naturally-occurring shock-produced phase--a densified hydroxylated amorphous silica.

It is clear from these results that solid state NMR is an extremely powerful tool for examination of shock-induced microstructural changes in quartz, yielding quantitative information on existence of phases, their relative abundances, morphology, and relaxation behavior. Application of similar NMR spectroscopic techniques to the examination of shock-induced microstructural changes in other inorganic compounds--particularly structural ceramics--would be likely to yield similarly useful information.

ACKNOWLEDGMENTS

This work was performed at Sandia National Laboratories, supported by the Department of Energy under contract DE-AC04-94AL85000, with partial funding by the National Aeronautics and Space Administration's Planetary Materials and Geochemistry program. Susan Kieffer and John McHone kindly provided us with well-documented samples from Meteor Crater. Gary Turner obtained the NMR spectra on the shocked sandstone.

REFERENCES

[1] R. T. Cygan, M. B. Boslough, and R. J. Kirkpatrick, "NMR spectroscopy of experimentally shocked quartz: Shock wave barometry," in *Proceedings of the Twentieth Lunar and Planetary Science Conference*, 1990, pp. 451-457.

[2] R. T. Cygan, M. B. Boslough, and R. J. Kirkpatrick, "NMR spectroscopy of experimentally shocked quartz and plagioclase feldspar powders," in *Proceedings of the Lunar and Planetary Science Conference*, Volume 22, 1992, pp. 127-136.

[3] R. A. Graham and D. M. Webb, in *Shock Waves in Condensed Matter*, Y. M. Gupta, ed., New York, Plenum, 1985, pp. 831-36.

[4] S. W. Kieffer, *Journal of Geophysical Research* 76, pp. 5449-5473 (1971).

[5] F. Devreux, J. P. Boilot, F. Chaput, and B. Sapoval, *Physical Review Letters 65*, 614 (1990).

[6] E. L. Venturini, private communication.

[7] W.-H. Yang, R. J. Kirkpatrick, N. Vergo, J. McHone, T. I. Emilsson, and E. Oldfield, *Meteoritics 21*, pp. 117-124 (1986).

[8] W. J. Nellis, A. J. Gratz, P. S. Fiske, and J. F. Stebbins, *Eos 73*, p. 594 (1992).

[9] R. Oestrike, W.-H. Yang, R. J. Kirkpatrick, R. L. Hervig, A. Navrotsky, B. Montez, *Geochimica et Cosmochimica Acta 51*, pp. 2199-2209 (1987).

[10] B. Pfleiderer, K. Albert, E. Bayer, L. van de Ven, J. de Haan, and C. Cramers, *Journal of Physical Chemistry 94*, pp. 4189-4194 (1990).

[11] S. W. Kieffer, P. P. Phakey, and J. M. Christie, *Contributions to Mineralogy and Petrology 59*, pp. 41-93 (1976).

[12] R. T. Cygan, M. B. Boslough, and R. J. Kirkpatrick, *Eos 73*, p. 360 (1992).

Materials Synthesis and Processing at Ultrahigh Pressures: Applications of the Diamond-Anvil Cell

Raymond Jeanloz
University of California, Berkeley, CA 94720-4767, U.S.A.

INTRODUCTION

The development of the diamond-anvil cell over the past quarter century has made it possible to synthesize, process and fundamentally study materials at sustained ultrahigh pressures of the Megabar (10^{11} Pa ~ 10^6 atm) range.[1, 2] Such pressures are significant for at least two basic reasons. First, the pressure–volume work done in compressing matter to the 10^{11} Pa range is on the order of electron volts; that is, comparable to the energies of chemical bonding.[2] Thus, one expects profound changes in the chemical properties of materials at ultrahigh pressures, the archetypal example being the transformation of hydrogen to the metallic state first predicted theoretically more than 50 years ago.[3] This transition is of broad scientific interest, with the single most abundant material in the Universe probably being metallic hydrogen located deep within stellar and giant planetary interiors. Though not yet fully confirmed, and still an active topic of experimental and theoretical research, it does appear that metallic hydrogen has been produced in the laboratory in the past few years.[3, 4]

The second reason is that the strengths of materials are typically far smaller than the stresses achieved in ultrahigh-pressure experiments, even the strongest solids yielding under differential stresses of the order of 10^{9-10} Pa. Therefore, deformation (plastic flow) associated with slightly nonuniform pressures, typical at ultrahigh-pressure conditions, results in full-density, super-hard polycrystalline aggregates of even the strongest and most brittle materials. Large strains achieved during compaction produce textures of closely interlocking crystals, the grain boundaries being physically welded together to yield an ultrastrong compact that is optically clear if the constituent grains are transparent. The ability to produce high-strength aggregates at ultrahigh pressures has yet to be fully recognized by the research community, yet may have far-reaching implications for the synthesis and production of novel materials at these extreme conditions.

A significant motivation for research at ultrahigh pressures has been the "applied" reason that such conditions exist deep inside planets, the pressure at the Earth's center being 365 GPa, for example.[2] Thus, the diamond cell has revolutionized our understanding of planetary materials, for instance revealing that a single phase -- the perovskite high-pressure form of $(Mg,Fe)SiO_3$ -- comprises nearly half our planet.[5] Despite more than 10^{21} tons being present at depth, however, this phase was not discovered until 1976 and is only available in µg-mg quantities in the laboratory.[6]

TECHNIQUES

The basic design of the diamond-anvil high-pressure cell is simple, with the sample being compressed between the points of two gem-quality diamonds.[1, 2, 7, 8] Small dimensions of the sample area ensure that high pressures (~10^{10-11} Pa) can be achieved even with a relatively modest force (~ kN) on the anvils. The geometry is essentially uniaxial, meaning that a gasket must be used to contain the sample between the anvils. In fact, two of the key advances that were required to achieve Megabar pressures with the diamond cell were the recognition that a gasket is essential and parallel alignment of the culet faces is critical; these factors serve to maintain adequate sample thickness between the anvils and to minimize stress concentrations in the diamonds.

An obvious reason for using single-crystal diamond for the anvils, high strength, is matched by other distinct advantages: the transparency of diamond to a wide range of electromagnetic radiation and its refractory, chemically inert nature. The high thermal conductivity of diamond also means that the anvils can remain relatively cold and unaffected, even if the sample is heated to temperatures of thousands of kelvin.[9] Consequently, materials are not only effectively contained at extreme conditions of pressure and temperature, during synthesis or processing, but can also be examined in situ, directly through the anvils.[1, 2, 8-10]

Due to the transparency of the anvils, it is especially convenient to use optical probes with diamond cells. Examples range from infrared and visible spectroscopy (including Raman and

Brillouin scattering) through x-ray diffraction and Mössbauer (γ-ray) spectroscopy, all of which can be used to examine the sample at ultrahigh pressures. Moreover, calibration of pressure and temperature is often accomplished by fluorescence spectroscopy and spectroradiometry, respectively.[1]

Maintaining alignment of the anvils, critical to reaching ultrahigh pressures, is one of the most tedious aspects of using the diamond cell. With improved capabilities in machining, however, it is becoming possible to construct pre-aligned (non-alignable) diamond cells that can achieve Megabar pressures.[11] In addition to improved convenience of use, current efforts in diamond-cell techniques are concentrating on expanding the range and improving the accuracy of pressure–temperature calibrations, as well as extending the ability to probe the sample in situ at extreme conditions. For example, x-ray diffraction has been carried out to over 200 GPa at 300 K, whereas electrical resistivity and Seebeck coefficient measurements have been performed over temperatures of 150-3000 K at pressures above 60-80 GPa.[1, 11-14]

Among static techniques, multi-anvil devices sacrifice pressure in order to compress larger samples ($\sim 10^{-6}$ - 10^{-3} l vs.$\leq 10^{-12}$ l typical for the diamond cell).[8] Also, the geometry is intrinsically more suited to generating uniform pressures than is the uniaxial configuration of the diamond cell. Therefore, a design concept for the future is to merge these approaches into a multi-anvil diamond cell, the gasket between the diamond anvils being replaced by four metal anvils in order to achieve both a larger sample volume and the ability to independently control the 3 normal stresses on the sample, while retaining the diamond cell's advantages of optical access and ultrahigh pressures.

MATERIALS SYNTHESIS AND PROCESSING AT ULTRAHIGH PRESSURES

Synthesis of Novel Amorphous Phases

Most crystalline substances transform to one or more denser phases when compressed to high pressures. Complex crystals, such as those typical of many ceramic and alloy systems, usually exhibit a rich diversity of phases as functions of pressure or temperature, and much work has gone into determining the equilibrium transitions among these polymorphs.

An interesting question arises, however, when experiments are carried out at such low temperatures or during such short time intervals that phase transitions cannot occur: What is the fate of a crystal compressed to ultrahigh pressures while being kinetically prevented from transforming to its equilibrium structure? To be sure, the equilibrium transition pressure and temperature are surpassed as the kinetically blocked sample is taken to increasingly metastable conditions. But the surprising result, recognized only in the past decade, is that a new type of transition can ultimately take place; once it becomes sufficiently metastable, the original crystal undergoes an instability and collapses to a dense amorphous structure.[15]

The initial discovery of this pressure-induced amorphization came from shock-compressed materials, with the observation of "diaplectic" glass in samples that had been subjected to hypervelocity impact, either in the laboratory or, due to meteorite impact, in nature.[16] The characteristic feature of diaplectic glass is that it retains the original shape of the crystal from which it was formed. After shock compression, certain polycrystalline materials are thus a mixture of crystalline and glassy phases, both of which exhibit their original crystal boundaries. The unmodified crystal shape provides convincing evidence that the glass is not formed in the classical manner, by quenching from the melt, but is produced by amorphization in the solid state.[16, 17]

The nature of pressure-induced amorphization was significantly clarified by the discovery that three tetrahedrally bonded systems, H_2O Ice I_h at 80 K, and SnI_4 and SiO_2 quartz at 300 K, become amorphous under hydrostatic pressures.[18-20] Prior to this, it was thought that shock amorphization might occur on decompression, or that perhaps shearing was a necessary ingredient. The static compression experiments proved, however, that uniform compression under hydrostatic pressures suffice for converting a crystal to the amorphous state.

Subsequently, a wide variety of ionic, covalent and metallic crystals have been shown to amorphize under compression (Table 1). Two types of amorphization transitions have been found, reversible and irreversible. In the first case, the amorphous state created on compression reverts back to the original crystalline structure on decompression, whereas in the second the amorphous material can be retrieved metastably to ambient conditions.

It is unclear what kinetic or other factors determine whether a given material exhibits reversible or irreversible amorphization. For example, SiO_2 quartz amorphizes irreversibly, whereas the isomorphous $AlPO_4$ berlinite exhibits a reversible transition. The reversibility suggests a close

Table 1: Examples of Pressure-Induced Amorphization

System			Transition Pressure (GPa)		Reference
Reversible					
SnI_4			12 (±2) up, 4 (±1) down		*19*
GeI_4			23 (±10) up, 1.0 (±0.7) down		*42*
S_8	Sulfur		25 up, > 0 down		*43*
$LiKSO_4$			14 (±2) up, > 0 down		*44*
$Al(PO)_4$	Berlinite		15 (±3) up, 5 (±2) down		*23*
$Ca(NO_3)_2/NaNO_3$			9 up, > 0 down		*45*
$Ca(OH)_2$	Portlandite		12 (±1) up, 4 (±1) down		*46*
$Co(OH)_2$			11-40 up, 7-11 down		*47*
$Mg_3Si_2O_5(OH)_4$	Serpentine		18 (±4) up, > 0 down		*29*
α-$SrZrF_6$			10 up, > 0 down		*48*
β-$BaZr_2F_{10}$			4 up, > 0 down		*49*
poly(4-methyl-pentene-1)			0.2		*50*
Irreversible (Glass is Quenched)					
H_2O (80 K)	Ice I_h	(stable < 0.5 GPa)	1.0		*18*
	Ice VIII	(stable > 2 GPa)	≤ 0.3	on decompression	
SiO_2	Quartz	(stable < 3 GPa)	25-30		*20*
	Coesite	(stable < 7 GPa)	30-35		
GeO_2	Quartz	(stable < 1 GPa)	7		*21*
$CaAl_2Si_2O_8$	Anorthite	(stable < 3 GPa)	22-28		*28*
$MgAl_2O_4$	Spinel	(stable < 25 GPa)	30-40		*51*
Fe_2SiO_4	Fayalite	(stable < 5 GPa)	35-45		*32*
$CaSiO_3$	Wollastonite	(stable < 3 GPa)	25		*52*
	Perovskite	(stable > 20 GPa)	≤ 1	on decompression	
R-Al_5Li_3Cu			23		*53*
GaAs			≥ 0	on decompression	*54*
C_{60}	High-P Phase	(stable > 20 GPa)	≥ 6	on decompression	*35*

similarity in short- to intermediate-range structures between the crystalline and amorphous states. In contrast, irreversible transitions have played an important role in the initial studies of amorphization: because the glassy state formed at high pressures is recuperated to ambient conditions, it can be examined in minute detail by electron microscopy and other techniques.[21, 22] This was significant in proving that the pressure-amorphized state is not a microcrystalline state, but is truly a glass in possessing no long-range structural order.

Due to the system being kinetically blocked, one would expect that amorphization involves only small movements of the ions away from the original crystal structure. Proof of this is dramatically illustrated by the crystal structural "memory" effect discovered in $AlPO_4$, in which a single crystal, amorphized under hydrostatic conditions, is found on decompression to revert back to a single crystal having the same orientation as the starting sample.[23] That is, despite a loss of long-range order, the structure of the amorphous state apparently remains close enough to that of the original crystal to revert back to the exact configuration of the starting material.

These observations suggest that different amorphous structures are formed depending on the crystal structure of the starting material. Indeed, different crystalline polymorphs of a given compound should transform to distinct "polymorphs" of the amorphous state. This has, in fact, been established by spectroscopic investigations.[24] Moreover, a first-order phase boundary has been observed between distinct amorphous phases of H_2O Ice.[25]

Based on limited experimental observations and molecular dynamics simulations, pressure-induced amorphization itself appears to be a first-order transition involving a finite volume change.[18, 26, 27] Furthermore, there is both theoretical and experimental evidence suggesting that the collapse of the crystal structure is driven by a phonon instability, perhaps involving elastic destabilization; if there is a volume change, the bulk modulus must be among the vanishing moduli.[26-29] Little more is currently known about the specific process causing amorphization, although it seems plausible that several mechanisms operate, in detail, depending on the initial crystal structure, strain rate, temperature heterogeneity of stress, and other variables involved.

It does appear, however, that the amorphization taking place under static conditions is closely related to the formation of diaplectic glass under shock compression (differences in strain rate and thermal histories probably cause the greatest differences between shock- and statically amorphized samples). The high strain rates and short durations of shock experiments are apparently mimicked by the kinetically low temperatures of the static experiments in preventing the sample from transforming to its equilibrium high-pressure (crystalline) phase. Thus, current thinking is that the "high-pressure phase" branch of the shock Hugoniot -- the densified state achieved at peak pressure under dynamic loading -- is actually a pressure-amorphized material that can be recovered as diaplectic glass on decompression.[28, 30-32] Hence, the study of pressure-induced amorphization illustrates the manner in which static experiments can help reveal the processes occurring in materials under shock compression.

Two of the more novel amorphous phases created in this manner are antiferromagnetic Fe_2SiO_4 and "collapsed" C_{60}. Crystalline Fe_2SiO_4 (fayalite), which becomes antiferromagnetic at temperatures below 65 K, amorphizes when compressed above 40 GPa at room temperature.[32] Magnetic susceptibility and Mössbauer spectroscopy demonstrate that the amorphized material exhibits antiferromagnetic ordering at the same temperature as the crystalline Néel transition; that is, with surprisingly little "frustration" despite the loss of long-range order.[33] Indeed, this appears to be the first example of true antiferromagnetism in a glassy material, and serves to emphasize the close relationship between the atomic configurations in the crystalline and the pressure-amorphized sample.

When C_{60} buckminsterfullerene is compressed at 300 K, it transforms to a new crystal structure above 30 GPa.[34, 35] On decompression, the high-pressure phase transforms to a new amorphous phase of carbon, a "collapsed" fullerene.[35, 36] Little is yet known about the properties of this amorphized carbon phase, but the rich behavior of crystalline fullerenes suggests promising possibilities. Incidentally, this is not the first instance of a crystalline high-pressure phase becoming amorphous on decompression (Table 1); metastability appears to be the key to amorphization, whether for a low-pressure phase on compression or a high-pressure phase on decompression.

High-Temperature Experiments

Elevated temperatures facilitate the synthesis and processing of new materials at ultrahigh pressures. Chemical reactions are typically found to proceed rapidly at temperatures exceeding 1000 K, and stress variations across the sample are reduced or eliminated during the thermal annealing. Few laboratories have so far explored the pressure–temperature regime above 30-50 GPa and 1000-2000 K, however, so there are only a limited number of illustrative examples to consider.

One set of investigations has concentrated on nitride compounds. For example, new transition-element nitrides can be formed by reacting the metal with fluid nitrogen at pressures of 30-100 GPa; in particular, high-pressure Fe-nitrides have been formed in this way.[37] Similarly, cubic structured (diamond-like) compounds have been investigated in the B-C-N ternary system, the objective being to create materials harder than diamond. Although cubic B-C-N compounds have been successfully created at elevated pressures and temperatures, these have so far proven to have bulk moduli no greater than that of diamond; instead, they appear to be nearly intermediate in properties between cubic BN (borazon) and C (diamond).[38]

An especially interesting direction for materials synthesis is to use pressure to modify the chemical bonding in the sample, in this way enabling altogether new types of compounds to be formed. Thus, oxygen transforms from an essentially ionic constituent at ambient conditions -- the primary component of traditional ceramic crystals -- to a metallic alloying component at ultrahigh pressures (indeed, some evidence suggests that elemental O_2 becomes metallic above 100 GPa).[39]

A prime example of this bonding transformation is FeO, which becomes metallic when taken to simultaneous pressures and temperatures exceeding 70 GPa and 1000 K; in contrast, it is a non-metallic ceramic at zero pressure.[13, 40] The change in bonding character, thought to involve a Mott-like transition, explains why it is that oxides are found to react vigorously with liquid Fe above ~30-50 GPa, the oxygen combining with (alloying into) the metallic phase at high pressures.[41]

Qualitatively, it appears that oxygen takes on a chalcogenide-like behavior at high pressures. The resulting chemical reactivity of liquid iron alloys with respect to oxides at ultrahigh pressures is of particular geophysical interest because it implies that vigorous chemical reactions take place between the metallic core and rocky mantle deep inside large terrestrial planets, such as Earth and Venus.[41]

SIGNIFICANCE AND CONCLUSIONS

Because the effect of compression is to alter the chemical properties of matter, ultrahigh pressures offer a special means of synthesizing novel materials. Entirely new compounds can be formed, and retained metastably to ambient conditions. Thus, pressure can play a role analogous to that of chemistry; it provides an alternative means, instead of changing composition, for tuning the bonding properties of materials. The primary disadvantage, the difficulty of achieving ultrahigh pressures, is at least partly mitigated by the fact that condensed-matter theory is far better suited to modelling the effects of varying pressure than of varying composition. At the same time, the stress- and thermal-processing of materials at ultrahigh pressures can lead to novel polycrystalline textures, including super-dense and strong aggregates. Further developments of such aggregates will no doubt help produce the anvils required for large-scale synthesis at these extreme conditions.

So far, research at ultrahigh pressures has emphasized basic principles, rather than the development of new technological materials. This trend is likely to change, however, with more attention being focused on synthesis. The discovery of pressure-induced amorphization has already led to the discovery of novel materials, while also revealing some of the key processes taking place during shock-compression of materials.

More significantly, amorphization under hydrostatic compression is the simplest example of a wide class of crystal-structural instabilities now being recognized.[17, 55-57] These instabilities occur due to a strong driving stress being imposed under kinetically blocked conditions. Indeed, shearing seems to help trigger the amorphization instability, and computer simulations indicate that similar instabilities take place under large tensional strains, as well.[55-58] This general form of strain-induced amorphization appears to define the stability limits of crystals, and includes the Born criterion for instability.[55-57]

In fact, the stress-strain conditions with which crystals amorphize under pressure are close to the local conditions achieved in dislocation cores and the "process zone" at fracture tips.[59] Because dislocation cores involve a complex stress field that is heterogeneous on the atomic scale, however, their formation and dynamics are far more difficult to characterize than the lattice instability achieved under hydrostatic compression. In this sense, pressure-amorphized material is an ideal bulk sample of dislocation core, and the amorphization transition appears to be a large-scale model for the instability that ultimately leads to the failure (yielding) of materials at the microscopic level.

Acknowledgements

This work was supported by the U. S. National Science Foundation and NASA.

REFERENCES

1. Jayaraman, A., *Rev. Mod. Phys.* 55, 65 (1983); *Rev. Sci. Instrum.* 57, 1013 (1986).
2. Jeanloz, R., *Ann. Rev. Phys. Chem.* 40, 237 (1989).
3. Mao, H. K., and R. J. Hemley, *Am. Scientist* 80, 234 (1992).
4. Mao, H. K., and R. J. Hemley, *Rev. Mod. Phys.*, in press (1994).
5. Knittle, E., and R. Jeanloz, *Science* 235, 668 (1987).
6. Hemley, R. J., and R. E.Cohen, *Ann. Rev. Earth Planet. Sci.* 20, 553 (1992).
7. Jephcoat, A. P., H. K. Mao and P. M. Bell, in *Hydrothermal Experimental Techniques*, edited by H. E. Barnes and G. C. Ulmer (Wiley-Interscience, New York), 469 (1987).
8. Williams, Q., and R. Jeanloz, in *Molten Salt Techniques 4*, edited by R. J. Gale and D. G. Lovering (Plenum, New York), 193 (1991).
9. Bodea, S., and R. Jeanloz, *J. Appl. Phys.* 65, 4688 (1989)
10. Heinz, D., and R. Jeanloz, in *High-Pressure Research in Mineral Physics*, edited by M. H. Manghnani and Y. Syono (Am. Geophys. Union, Washington, DC), 113 (1987).
11. Mao, H. K., personal communication; Jeanloz, R., unpublished results.
12. Mao, H. K., Y. Wu, R. J. Hemley, L. C. Chen, J. F. Shu and L. W. Finger, *Science* 246, 649 (1989).
13. Knittle, E., and R. Jeanloz, *J. Geophys. Res.* 96, 16169 (1991).
14. Li, X., and R. Jeanloz, *J. Geophys. Res.* 95, 5067 (1990); unpublished results.
15. Jeanloz, R., and Q. Williams, *Nature* 350, 659 (1991).

16. Stöffler, D., *Fortschr. Miner.* 49, 50 (1972); *ibid* 51, 256 (1974).
17. Johnson,W. L., *Progress in Materials Science*. 30, 81 (1985).
18. Mishima, O., L. D. Calvert and E. Whalley, *Nature*, 310, 393 (1984).
19. Fujii,Y., M. Kowaka and A. Onodera, *J. Phys. C*, 18, 789 (1985); Sugai, S. *ibid*, 799 (1985).
20. Hemley, R. J., in *High-Pressure Research in Mineral Physics*, edited by M. H. Manghnani and Y. Syono (Am. Geophys. Union, Washington, DC), 347 (1987).
21. Wolf, G. H., S. Wang, C. A. Herbst, D. J. Durben, W. Oliver, Z. C. Kang and K. Halvorson, in *High-Pressure Research: Application to Earth and Planetary Sciences*, edited by Y. Syono and M. H. Manghnani (Am. Geophys. Union, Washington, DC), 503 (1992).
22. Winters, R. R., A. Garg and W. S. Hammack, *Physical Review Letters* 69, 3751 (1992).
23. Kruger, M. B., and R. Jeanloz, *Science* 249, 647 (1990).
24. Hemley, R. J., L. C. Chen and H. K. Mao, *Nature* 338, 638 (1989).
25. Mishima, O., L. D. Calvert and E. Whalley, *Nature* 310, 393 (1985); Mishima, O., K. Takemura and K. Aoki, *Science* 254, 406 (1991).
26. Tse, J. S., and D. D. Klug, *Phys. Rev. Lett.* 67, 3559 (1991); Tse, J. S., and D. D. Klug, *Science* 255, 1559 (1992); Tse, J. S., *J. Chem. Phys.* 96, 5482 (1992).
27. Chelikowsky, J. R., H. E. King, N. Troullier, J. L. Martins and J. Glinnemann, *Phys. Rev. Lett.* 65, 3309 (1990); Binggeli, N., and J. R. Chelikowsky, *ibid* 69, 2220 (1992).
28. Williams, Q., and R. Jeanloz, *Nature* 338, 413 (1989).
29. Meade, C., and R. Jeanloz, *Science*, 252, 68 (1991).
30. Jeanloz, R., *J. Geophys. Res.* 85, 3163 (1980).
31. Tan, H., and T. J. Ahrens, *J. Appl. Phys.* 67, 217 (1990).
32. Williams, Q., E. Knittle, R. Reichlin, S. Martin and R. Jeanloz, *J. Geophys. Res.* 95, 21549 (1990); Richard, G., and P. Richet, *Geophys. Res. Lett.* 17, 2093 (1990).
33. Kruger, M. B., R. Jeanloz, M. P. Pasternak, R. D. Taylor, B. S. Snyder, A. M. Stacy and S. R. Bohlen, *Science* 255, 703 (1992).
34. Duclos, S. J., K. Brister, R. C. Haddon, A. Kortan and F. A. Thiel, *Nature* 351, 380 (1991).
35. Nguyen, J. H., M. B. Kruger and R. Jeanloz, *Solid State Commun.* 88, 719 (1993).
36. Kosowsky, S.D., C. H. Hsu, N. H. Chen, F. Moshary, P. S. Pershan and I. F. Silvera, *Phys. Rev. B* 48, 8474 (1993).
37. Dillon, T., and R. Jeanloz, *EOS, Trans. Am. Geophys. Union* 73 (suppl.), 64 (1992).
38. Knittle, E., R. B. Kaner, R. Jeanloz and M. L. Cohen, *Phys. Rev. B*, in press (1994).
39. Desgreniers, S., Y. K. Vohra and A. L. Ruoff, *J. Phys. Chem.* 94, 1117 (1990).
40. Knittle, E., R. Jeanloz, A. C. Mitchell and W. J. Nellis, *Solid State Commun.* 59, 513 (1986).
41. Knittle, E., and R. Jeanloz, *Science* 251, 1438 (1991); *Geophys. Res. Lett.* 16, 609 (1989).
42. Pasternak, M. P., R. D. Taylor, M. B. Kruger, R. Jeanloz, J. P. Itié and A. Polian, *Phys. Rev. Lett.*, in press (1994).
43. Luo, H., and A. L. Ruoff, *Phys. Rev. B* 48, 569 (1993).
44. Sankaran, H., S. K. Sikka, S. Sharma and R. Chidambaram, *Phys. Rev. B* 38, 170 (1988).
45. Winters, R.R., G. C. Serghiou and W. S. Hammack, *Phys. Rev. B* 46, 2792 (1992).
46. Meade, C., and R. Jeanloz, *Geophys. Res. Lett.* 17, 1157 (1990).
47. Nguyen, J. H., M. B. Kruger and R. Jeanloz, *Phys. Rev. B*, in press (1994).
48. Serghiou, G.C., and W. S. Hammack, *J. Chem. Phys.* 96, 6911 (1992).
49. Serghiou, G.C., R. Winters and W. S. Hammack, *J. Phys.: Cond. Matter* 4, 7617 (1992).
50. Rastogi, S., M. Newman and A. Keller, *Nature* 353, 55 (1991).
51. Kruger, M. B., J. H. Nguyen and R. Jeanloz, *EOS, Trans. AGU* 74 (suppl.), 675 (1993)
52. Serghiou, G.C., and W. S. Hammack, *J. Chem. Phys.* 98, 9830 (1993).
53. Winters, R.R., and W. S. Hammack, *Science* 260, 202 (1993).
54. Vohra, Y.K., X. Hui and A. L. Ruoff, *Appl. Phys. Lett.* 57, 2666 (1990).
55. Wolf, D., P. R. Okamoto, S. Yip, J. F. Lutsko and M. Kluge, *J. Mater. Res.* 5, 286 (1990).
56. Hsieh, H., and S. Yip, *Phys. Rev. Lett.* 59, (1987); *Phys. Rev. B*, 39, 7476 (1989).
57. Wang, J. H., S. Yip, S. R. Phillpot and D. Wolf, *Phys. Rev. Lett.* 71, 4182 (1993).
58. Kingma, K. J., C. Meade, R. J. Hemley, H. K. Mao and D. R. Veblen, *Science* 259, 666 (1993).
59. Hoagland, R. G., M. S. Daw, J. P. Hirth, *J. Mat. Res.* 6, 2565 (1991).

Structures and Properties of Perovskite-type Compounds Synthesized Under Very High Pressures

Takehiko Yagi
Institute for Solid State Physics, University of Tokyo, Japan

1. Introduction

Perovskite structure is one of the most common crystal structures among ABO_3-type compounds. In this structure, one of the cations together with the oxygen ion form face centered cubic close packing lattice and hence this structure has very high density. At atmospheric pressure, only the large cations, such as Ca and Sr, can form perovskite structure. Under high pressure, however, oxygen ions are compressed more than the cations and even a small cations can form perovskite structure. Figure 1 shows the synthesis pressure vs unit cell volume of many perovskite-type compounds formed at elevated pressures. With increasing pressure, compounds containing smaller cations transform into perovskite structure and the resulting unit cell volume decreases as well. The perovskite-type compound with the smallest unit cell volume so far synthesize is $MgSiO_3$[1,2], which can be formed above about 24 GPa.

Perovskite-type compounds are widely used as important materials in many fields, yet the variety is rather limited at atmospheric pressure. It is clear that using pressure, much variety of compounds can be crystallized into perovskite structure. With the aid of a laser heated diamond anvil technique, which can cover very wide range of pressure and temperature, variety of perovskite-type compounds have been so far synthesized. In this paper, the properties of perovskite-type compounds synthesized under very high pressures are reviewed.

2. Mg and Ca bearing silicate perovskites

Because of its geophysical importance, $MgSiO_3$ perovskite is one of the best studied high pressure minerals. It has orthorhombic symmetry and is quenchable to ambient condition, although it transforms back into a low pressure enstatite phase or into an amorphous state when it is heated above several hundred degrees centigrade at atmospheric pressure. An important mineral containing Ca in the mantle, $CaSiO_3$, transforms also into perovskite structure above 14 GPa[3,4]. Both of these two perovskites have similar structures but there are two distinctly different properties in $CaSiO_3$ perovskite. One is that it has cubic symmetry, instead of orthorhombic, and the other is that it is unquenchable on release of pressure and transforms into an amorphous phase at room temperature. The structural analysis of $CaSiO_3$ perovskite, however, has been made only at high pressures and there are still some ambiguities. The solubility of $MgSiO_3$ and $CaSiO_3$ are very limited and diopside, $CaMgSi_2O_6$, decomposes into two perovskites assemblage, $MgSiO_3$ + $CaSiO_3$, when it is heated above 24 GPa[4,5,6].

Compared to these silicate perovskites formed from pyroxene compositions, much less is known about the perovskites formed from garnet compositions. Pyrope ($Mg_3Al_2Si_3O_{12}$), for example, transforms into perovskite above about 27 GPa, but the transformation pressure and the unit cell dimension differ significantly depending on the studies[7,8]. Another characteristic feature of garnet is the slow transformation rate. In case of $MgSiO_3$ and $CaSiO_3$, a complete transformation into high pressure phase occurs easily just above the transition pressure. On the other hand, when garnets are converted into perovskite using a laser heated diamond anvil, the low pressure phase always remains even when the heating was made more than 10 GPa above the transition pressure[9].

Very recently, a new high pressure phase of grossular ($Ca_3Al_2Si_3O_{12}$) was found using an in situ x-ray observation[10]. Fig. 2 is the x-ray diffraction patterns obtained at 5.4 GPa and at atmospheric pressure after the crystalline grossular was heated above 1000 °C at about 30 GPa. In this study, in order to get hydrostatic environment, argon was used as a pressure transmitting medium. In the lower figure, diffraction pattern from the high pressure phase can be observed together with those from solid argon and unreacted starting material. On complete release of pressure, diffractions from the high pressure phase and argon disappeared completely, as shown in the above figure. The diffraction profile of the high pressure phase is very similar to that of $CaSiO_3$ perovskite. However, some of the diffraction lines of this high pressure phase are wide and there are some

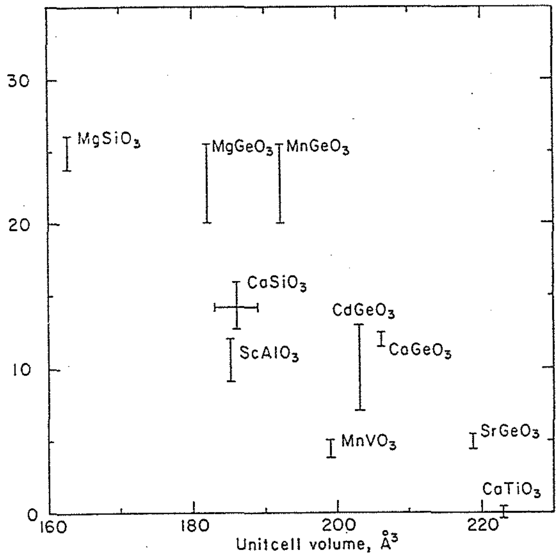

Fig.1. Synthesis pressure vs unit cell volume of perovskite-type compounds.

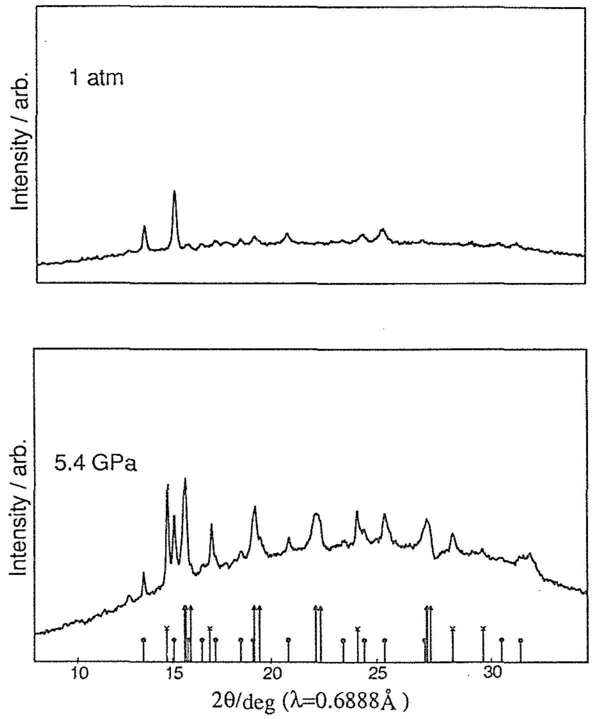

Fig. 2. $Ca_3Al_2Si_3O_{12}$ perovskite observed at 5.4 GPa (below) and after complete release of pressure (below). Diffractions from the unreacted starting material (circle), and solid argon (cross) are also observed together with those of the orthorhombic perovskite (triangle). It is clear that the high pressure phase is unquenchable on release of pressure.

extra lines which cannot be explained by a cubic perovskite structure, which indicates that the structure is slightly distorted from cubic symmetry. Among many possible distortions, the orthorhombic perovskite similar to that of $MgSiO_3$ explains the observed diffraction pattern well. Although no direct measurement of the chemical composition was made yet, it is believed that the high pressure phase has the same composition from the starting material because of the two reasons. One is that no diffraction lines other than this perovskite phase was formed at high pressure. The other is that the unit cell volume of the unreacted starting material remain unchanged. The result of this study is quite different from the previous studies[5,11]. At this moment the reason of this discrepancy is not clear but the differences of the starting material and the way of observation are the possible explanations. This study has clarified the existence of a new type of perovskite compound which is unquenchable but has distorted from cubic. However, the distortion from the cubic symmetry became clear only when the experiment was made under hydrostatic condition using argon as a pressure transmitting medium, otherwise all the diffractions are very broad and it was impossible to notice the broadening of the lines caused by the distortion of the structure. So far, no precise analysis of the structure of $CaSiO_3$ was made under hydrostatic environment and it may be necessary to reinvestigate it carefully.

Unit cell volumes and the bulk moduli of silicate perovskites are summarized in Table 1. When the unit cell volume of Mg perovskite and Ca perovskite with the same chemical composition are compared, it is clear that the substitution of Mg into Ca increases the unit cell volume about 11%. This is because the ionic radius of Ca is much larger compared to Mg. In

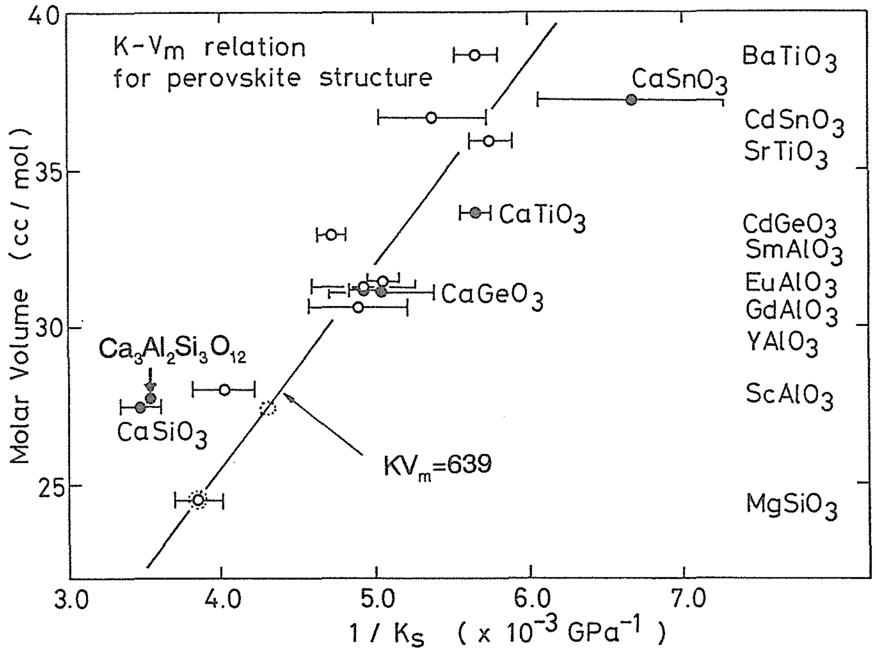

Fig. 3. Molar volume vs inverse of the bulk modulus for many perovskite type compounds. The product KVm is almost constant for many perovskite but those containing Ca has different trend.

spite of the expansion of the unit cell volume, the bulk modulus of Ca perovskite increases compared to that of Mg perovskite. It is known that in many compounds having the same structure, the products of bulk modulus, K, and molar volume, V, is almost constant. In Figure 3, molar volume is plotted as a function of inverse of the bulk modulus for many compounds with perovskite structure. It is clear from this figure that the product KV is about 640 GPa·cm^3/mol for most of the compounds. As is clear in Fig.3, however, if the compounds containing Ca, including present $Ca_3Al_2Si_3O_{12}$, are selected, it has clearly different trend. This fact indicates that the elastic property of Ca containing perovskite is slightly different from other compounds.

3. Other unquenchable compounds with perovskite structure

Properties of perovskite-type compounds seem to vary systematically with the ionic radios of the component ions. Figure 4 shows crystal structures of ABO_3-type compounds as a function of cation radius[12]. The parameter t is a Goldschmidt tolerance factor in perovskite structure which is defined as $t=(A+O)/(2(B+O))^{1/2}$, where A+O is the sum of the radii of the divalent cation and oxygen, and B+O is the sum of the radii of the tetravalent cation and oxygen[13]. In the region where tolerance factor is larger than 0.84, we can synthesize perovskite-type compounds under high pressure and quench it to ambient condition. For the compounds with smaller t, the high pressure phase was believed to have $LiNbO_3$ type structure, based on the quench experiments. High pressure in situ x-ray observations on $MnSnO_3$ and

Table 1. Crystallographic data of silicate perovskites[9].

composition	V_0(Å^3)	K_0(GPa)	K_0'
$Ca_3Al_2Si_3O_{12}$	183.96	283 ±7	4
$Ca_4Si_4O_{12}$	182.32	288±13	4
	181.48	281±4	4
$Mg_3Al_2Si_3O_{12}$	165.34		
$Mg_4Si_4O_{12}$	162.35	260±20	3-5
	162.75		

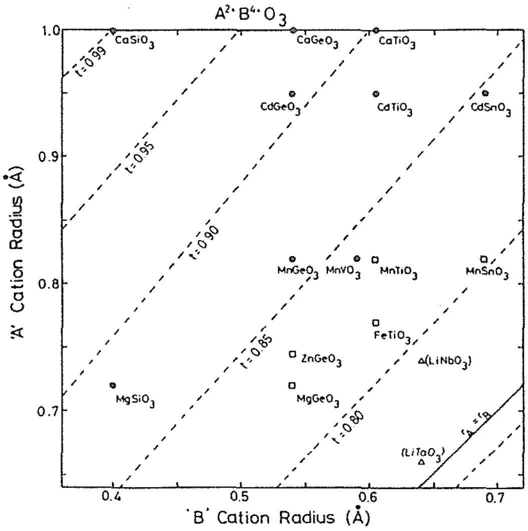

Fig. 4. Goldschmidt diagram for selected perovskite-forming compounds. "A" is the divalent cation radius in sixfold coordination, "B" is the tetravalent cation radius in sixfold coordination. Dotted lines are contours of the perovskite tolerance factor. Filled circles: perovskite-forming compounds. Open squares: lithium niobate quench products. Triangles: stable lithium niobate compounds (trivalent cations only)[12]

$FeTiO_3$, however, clarified that the real high pressure phase has a perovskite structure and $LiNbO_3$ structure observed in a quench product was a metastable phase formed retrogressvely from the perovskite phase during the pressure release.

Compounds which has $LiNbO_3$ structure from the beginning, such as $LiNbO_3$ and $LiTaO_3$, transform into much denser phase above 32 GPa[13]. The density increase is as much as 20 %, although $LiNbO_3$-type structure is already a very dense structure. X-ray diffractions from this high pressure phase is well observed, as shown in Figure 5[14], but the analysis of the crystal structure is so far unsuccessful. The diffraction pattern has some similarity to that of perovskite structure but the difference between observed and calculated d values are larger than the uncertainty of the experiment when the indexing are made based on the perovskite structure.

It is quite interesting to note that the diffraction pattern of the high pressure phases of $LiNbO_3$ and $LiTaO_3$ are very similar to that obtained from the high pressure phase of Fe_2O_3(Fig.6), which is formed above 60 GPa at room temperature[15]. Mössbouer study on this phase suggests that the irons in this structure have two different electronic state and are placed in two different environment, which means that the chemical formula should be expressed as $FeFe'O_3$. If so, this unknown structure seems to be an important structure which can be stabilized under very high pressures for many ABO_3 type compounds and its structural analysis is strongly desired.

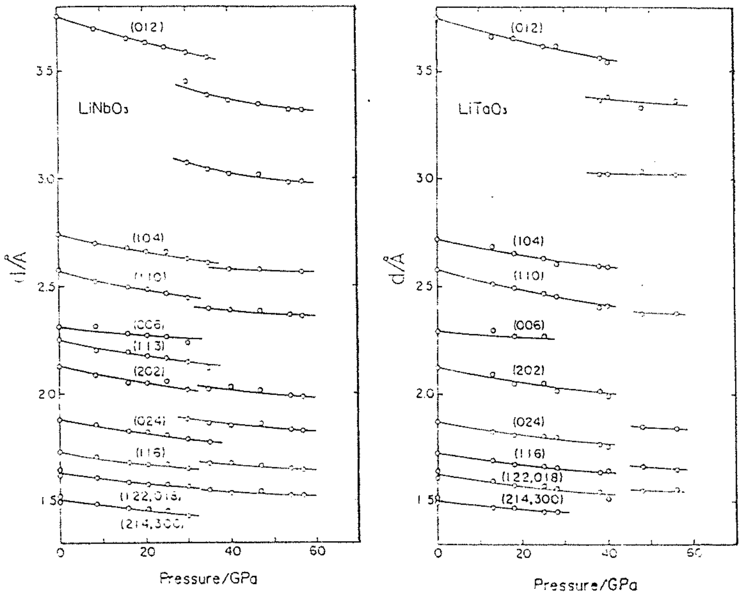

Fig. 5. D-values observed in $LiNbO_3$ (left) and $LiTaO_3$ (right) as a function of pressure.[14]

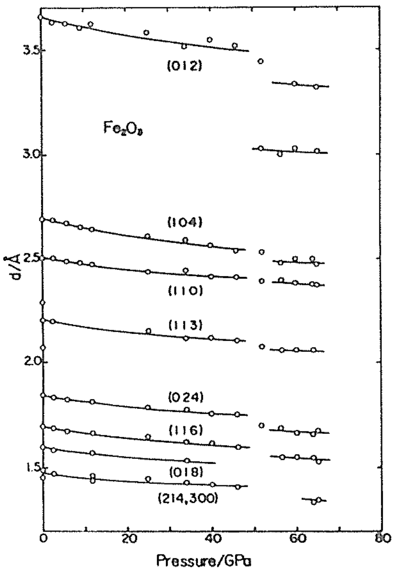

Fig. 6. D-values of Fe_2O_3 as a function of pressure.[15]

5. Conclusions

High pressure is a powerful tool to synthesize variety of compounds having perovskite structure. The nature of the perovskite-type compounds are largely controlled by its constituent ions and there are many compounds which cannot be quenched to ambient conditions. In situ x-ray observation plays essential role to study the nature and behavior of these compounds. High pressure phase of $LiNbO_3$ seems to be an important structure as a very dense structure of ABO_3 type compounds.

Acknowledgments

This is a review of the works carried out in my laboratory with many of my colleagues. The author is grateful to H. Yusa, K. Leinenweber, T. Suzuki, W. Utsumi, and many other people for the cooperations of these researchs.

References

1. Yagi, T., Mao, H. K., & Bell, P. M. (1978) Phys. Chem. Minerals, **3**, 97-110.
2. Ito, E. and Matsui, Y. (1978) Earth Planet. Sci. Lett., **38**, 443-450.
3. Liu, L. and Ringwood, A. E. (1975) Earth Planet. Sci. Lett., **28**, 209-211.
4. Tamai, H. and Yagi, T. (1989) Phys. Earth Planet. Inter., **54**, 370-377.
5. Mao, H. K., Yagi, T., and Bell, P. M. (1997) Carnegie Inst. Yearb., **76**, 502-504.
6. Irifune, T., Susaki, J., Yagi, T., & Sawamoto, H. (1989) Geophys. Res. Lett., **16**, 187-190.
7. Liu, L. (1974) Geophys. Res. Lett., **1**, 277-280.
8. Irifune, T. et al. (1992) in"High Pressure Research: Application to Earth and Planetary Sciences", edited by Y. Syono and M. H. Manghnani, TERRAPUB, Tokyo, pp.43-50.
9. Yusa, H. (1994) Ph. D. thesis, Univ. of Tokyo.
10. Yusa, H. and Yagi, T. (1994) Phys. Earth Planet. Inter., in preparation.
11. Liu, L. (1980) Earth Planet. Sci. Lett., **47**, 1079-1082.
12. Leinenweber, K., Utsumi, W., Tsuchida, Y., Yagi, T., & Kurita, K. (1991) Phys. Chem. Minerals, **18**, 244-250.
13. Goto, T. and Syono, Y. (1982) Program and Abstract, 23rd High Pressure Conference of Japan, PP.170-171.
14. Suzuki, T., Akimoto, S., Goto, T., and Syono, Y. (1982) ibid., pp. 70-71.
15. Suzuki, T., Yagi, T., Akimoto, S., Ito, A., Morimoto, S., & Syono, Y. (1985) in "Solid State Physics Under Pressure" ed. S. Minomura, 149-154, KTK/Reidel, Tokyo/Dordrechit.

Material Science at Ultrahigh Pressures

Ho-kwang Mao and Russell J. Hemley
Geophysical Laboratory and Center for High-Pressure Research,
Carnegie Institution of Washington, 5251 Broad Branch Rd. N.W., Washington, D.C. 20015, U.S.A.

ABSTRACT — The use of pressure to alter physical states of materials is as fundamental as the use of temperature or chemical composition. With recent breakthroughs in diamond-cell technology, a wide range of physical measurements can be conducted *in situ* at ultrahigh pressures to several hundred gigapascals. In the small number of systems investigated, a variety of pressure-induced transitions have been observed in solids under ultrahigh pressures. Examples of materials with interesting or potentially useful properties include pressure-amorphized solids, pressure-induced metals, van der Waals compounds, new dense clathrates, high-T_c superconductors, and the high-pressure phases of hydrogen.

INTRODUCTION

Pressure, temperature, and chemical composition are three fundamental variables controlling physical state of materials. Historically the impact of high pressure on the condensed-material physics had been negligible in comparison to that of temperature and composition. This does not reflect the relative significance, but rather reflects the experimental capability. Intrinsically, the temperature variable is limited by the melting and boiling points of the material, and the composition variable is limited by the number of compatible elements in it. The pressure variable is not bounded by these limitations; it thus complements these other parameters and could cover a potentially greater field. In contrast to the evolution of techniques exploiting temperature or composition, the development of the pressure capability had been very recent.

With breakthroughs in diamond-cell technology, static pressures of several hundred gigapascals (GPa), an order of magnitude higher than the previous maximum, can be reached routinely in the laboratory. Even more significantly, physical properties of materials can be characterized accurately in-situ at high pressures [1]. The newly acquired capabilities enable us to explore the full power of the pressure variable. An average of two or more high-pressure transitions has been observed in each solid in this wide range of pressures. The added dimension is particularly exciting to material science. It provides the prospect, for example, of potentially tripling the number of known materials. Discoveries of new materials, perhaps with novel physical and chemical properties, are within sight.

HIGH-PRESSURE DIAMOND CELL

Since pressure is force divided by area, enormous pressures can be generated by opposing anvils with a very small tip (culet), providing that the anvil material is strong enough to withstand the pressure without yielding. Flawless single-crystal diamond is chosen for its strength. The anvils exert pressure on a thin metallic gasket within which a circular sample chamber is confined (Fig. 1). Samples immersed in pressure-transmitting media are sealed in the chamber. The gasket also functions as a supporting belt without which the anvils will fail at a maximum pressure of only 35 GPa.

Diamond is transparent to much of the electromagnetic spectrum – including high energy x- and γ-radiation above 10 keV and low energy ultraviolet-visible-infrared (UV-VIS-IR) radiations below 5 eV. Numerous diffraction, scattering, and absorption probes can be employed for determination of electronic, dynamic, and structural properties of samples under pressure. A main constraint of the diamond cell technology is the limited anvil size (~0.2-0.4 carat, 1 ct. = 0.2 gm). At a constant anvil size, higher pressures are reached with a reduction in sample volume: there is a tradeoff between the maximum pressure and the maximum volume of the compressed sample. For instance, diamonds with 1-mm large culet diameter are generally limited to pressures below 5 GPa; diamonds with 20-μm small culet diameter are needed for pressures above 300-400 GPa. The diamonds with 20-μm small culet diameter are needed for pressures above 300-400 GPa. The diameter of the sample chamber is approximately one half of the culet diameter, and the thickness, one tenth. Studying minute samples requires development of microsampling techniques.

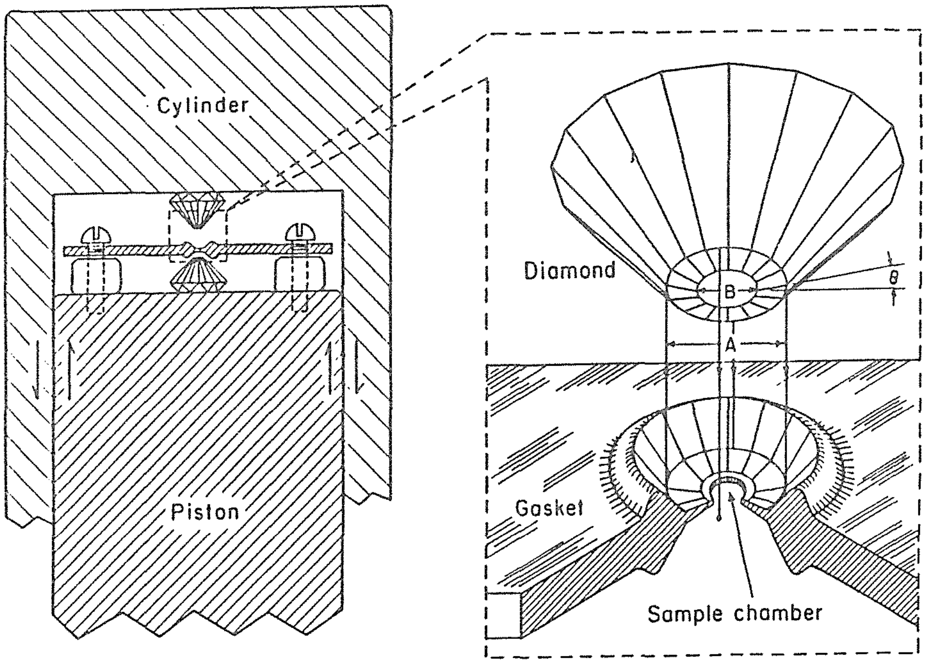

Figure 1. Schematic diagram of diamond-anvil cell.

Great progress in microsampling spectroscopies has resulted from recent advancement in two fronts – radiation sources and the detector systems. Lasers and synchrotrons provide collimated beams of electromagnetic radiations many orders of magnitude more brilliant than those from conventional light sources. Multichannel detector technology – such as energy dispersive x-ray detectors, two-dimensional position sensitive x-ray detectors, storage-phosphorous x-ray imaging plates, image intensifiers, intensified diode array detectors, charge-coupled detectors, and new Fourier-transform interferometer techniques – allows simultaneous detection in thousands of channels, thus providing sufficient measurement sensitivity for studying ultrasmall samples at ultrahigh pressures.

PRESSURE TUNING OF PHYSICAL PROPERTIES

When pressure is applied to matter, atoms are brought closer together. Interactions among atoms increase, and physical and chemical properties of the material change accordingly. Pressure provides the ideal means of such continuous tuning of interactions and properties. In contrast, changing interatomic distances by varying composition is restricted by the discrete nature of chemical elements, and tuning by temperature is complicated by thermal excitations (i.e., vibrations). Measurements of physical properties tuned over extended pressure range provide crucial experimental basis for testing and developing new theories of condensed matter.

Physical properties of fundamental and technological interest, such as superconductivity, can also be favorably tuned or enhanced by pressure. For example, the mercury-based oxides $HgBa_2Ca_{n-1}Cu_nO_{2n+2+\delta}$ (n = 1, 2, 3) have superconducting onset temperatures (T_c) of 94, 128, and 135 K, respectively. Their T_c's were found to increase with pressure [2]. When studied in a diamond cell with the four-lead electrical conductance technique (maximum pressure of 45 GPa) [3], record high T_C's of 164, 154, and 118 K were reached (Fig. 2).

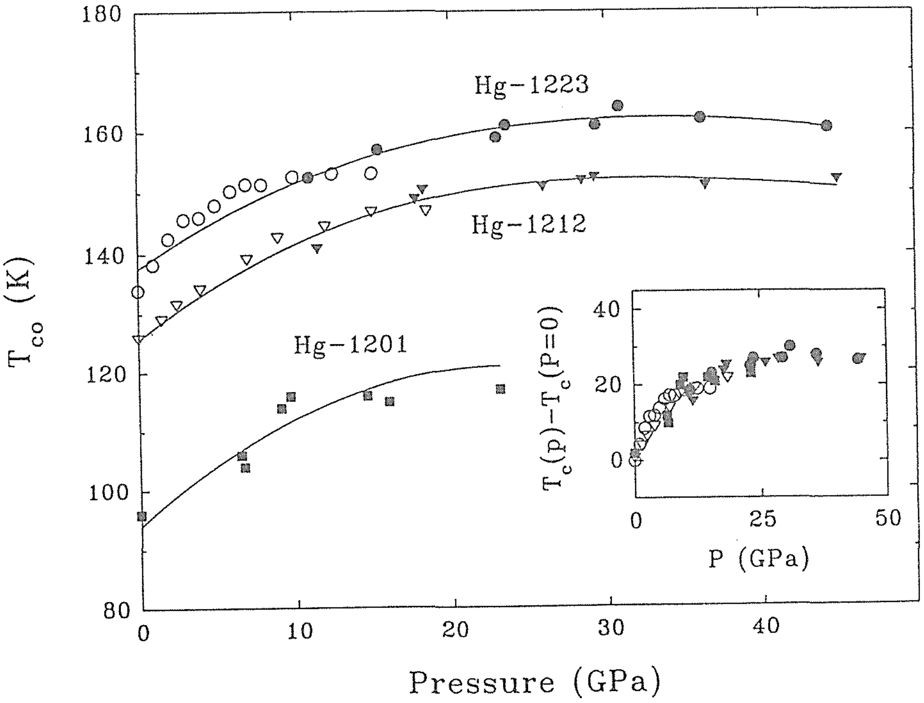

Fig. 2. T_C vs P. Open symbols, from Ref.[2]; solid symbols, diamond-cell data from [3].

NOVEL TRANSITIONS

At several hundred GPa, the density increases as much as 50% for the most incompressible materials, and 1000% for very soft ones. Numerous transitions occur in this compressional space, including novel types of pressure-induced transitions.

Insulator-Metal Transitions — In general with increasing density, electrons in a material become increasingly unstable localized in bonds and near atomic cores. From the early days of quantum theory it was predicted that above a critical density electrons in all materials must delocalize into conduction states thus forming a metal. The metallization process could involve, for example, a change in molecular or crystallographic structure, or an overlap of electronic valence and conduction bands. The insulator-metal transition occurs in iodine at 16 GPa is well established, and has become a classic an example of such a pressure-induced transition of this type [4]. Recently, its phase transitions, crystal structures, and electronic properties were studied by and optical and x-ray diffraction measurements and band-structure calculations to 276 GPa [5].

Pressure Amorphization — When a crystalline material is compressed to pressures well outside of its stability field, it may convert to an amorphous material if the temperature is too low for it to recrystallize to the equilibrium high-pressure crystalline phase. This phenomenon was first documented in ice-I, which transforms to a high-density amorphous form at 1 GPa and 77 K [6]. Such pressure-induced amorphization transformations have been observed in a growing number of materials during the past ten years [7, 8]. Such transformations may access unusual metastable states with varying degrees of disorder and possibly unique properties.

Phonon Localization Transitions — Most solids can be described by harmonic approximation; in some others, anharmonicity prevails. In the harmonic case, noninteracting phonons couple strongly and form a broad continuum band. In the anharmonic case, strong interaction of phonons leads to the formation of states of bound quasiparticles only weakly coupled in the crystal. For example, in two-phonon vibrational spectroscopy, the quasiparticle is a biphonon acting as a molecular oscillator. The biphonon forms a sharp peak separated from the origin of the broad two-phonon continuum band by the quantity of its anharmonicity. The condition that the harmonic and anharmonic cases overlap has been a problem of great interest in condensed systems. It was postulated that if the relative magnitudes of the continuum band width and the anharmonicity could be varied so that the former would exceed the latter, the bound biphonon would disappear into the continuum band. Such a transition has been observed for the first time by varying pressure in solid deuterium [9]. As shown in Fig. 3, at ambient condition the anharmonicity is 60 cm^{-1} while the continuum band width is only 2.2 cm^{-1}, so that the bivibron is well separated from the continuum. At high pressures, the anharmonicity remains nearly constant, while the continuum band width, which is a measure of the intermolecular coupling, increases sharply. The two become equal at 36 GPa, and indeed, the bivibron vanish into the continuum. Calculations with a parameter-free model Hamiltonian agree exactly with the experimental results.

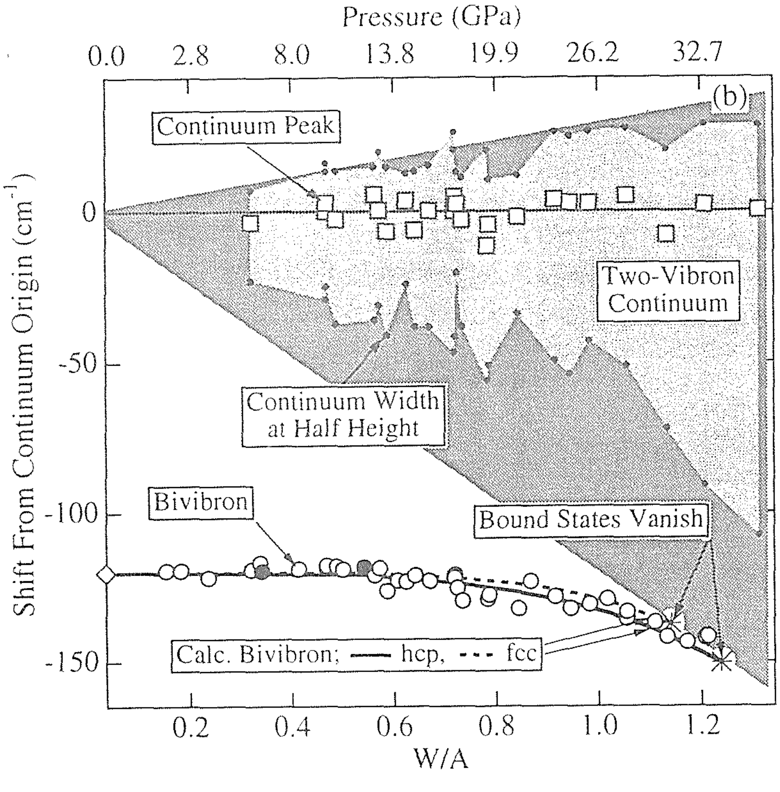

Fig. 3. Shaded area denotes the continuum band width, W. A is anharmonicity.

NEW MATERIALS

In general bonding properties in materials can be altered considerably under pressure, in some cases drastically as the relative energies of the valence electrons change in response to compression. Thus, chemical affinities of the elements can become very different from those at ambient pressure. For example, above 200 GPa, the inert-gas solid Xe with van der Waals bonding and the alkali halide CsI with ionic bonding become very similar; both have metallic bonding [10, 11] and transform to the same hcp-like structure [12, 13, 14].

Van der Waals Compounds — Inert-gas molecules interact weakly at low density through van der Waals force. They also do not readily form stoichiometric compounds at ordinary pressure. However, we now know that such solid compounds can be made at high pressures, as was first demonstrated with the synthesis of $He(N_2)_{11}$ [15]. Since then, two more compounds of this novel type, $NeHe_2$ [16] and $Ar(H_2)_2$ [17] have been observed at high pressures. Their crystal structures and stoichiometry can be rationalized in terms of molecular packing efficiency arguments.

High-Density Clathrates — Clathrate hydrates consist of hydrogen-bonded networks of cages in which large guest molecules are contained, interacting with the lattice by van der Waals forces. They are unstable at moderate pressures as the open networks break down under compression. In a high-pressure study of H_2-H_2O binary system, a novel type of clathrate with 1:1 ratio was discovered [18]. In this high-pressure clathrate, H_2O and H_2 form two interlocking networks, both with the diamond structure (Fig. 4). With the efficient packing of molecules afforded by the structure, the new type of clathrate is stable to at least 30 GPa.

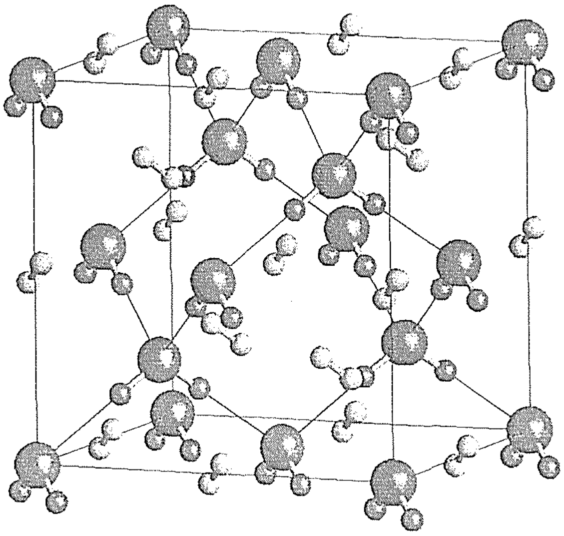

Fig. 4 . Crystal structure of the high-density clathrate. The dumbbells are idealized representations of the rotationally disordered hydrogen molecules; the large spheres denotes the oxygen of the H_2O molecules.

ULTRAHIGH-PRESSURE HYDROGEN

Study of highly condensed hydrogen is an archetypal problem which may contribute to understanding problems described above [19]. At low pressures and temperatures, hydrogen is an insulating molecular solid. Elementary theory predicts that at extreme pressures, the molecules will dissociate to form a monatomic metal. Between these two diametrically opposed types of solids, a number of unexpected transitions and new phenomena have been documented experimentally.

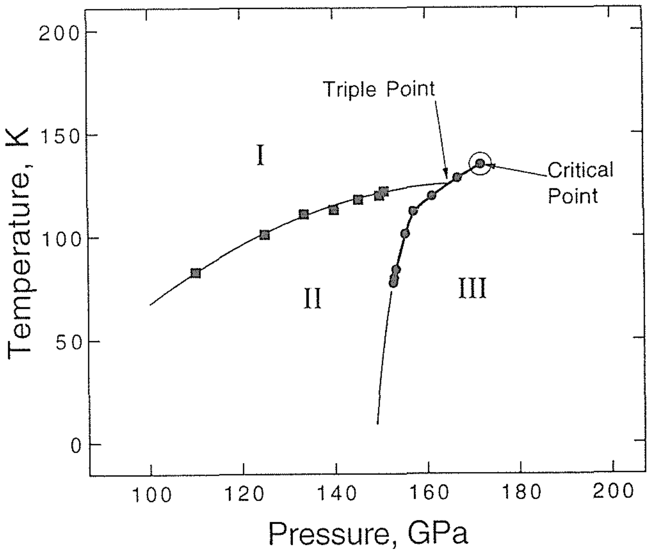

Fig. 5. Phase diagram of normal hydrogen at megabar pressures.

Ultrahigh pressures above 250 GPa have been reached with minute hydrogen samples in diamond-anvil cells [20]. However, due to the strong absorption of the probe laser radiation by the diamond anvils and the sample, properties of hydrogen in this pressure region have yet to be unambiguously characterized. At lower pressures where the experimental difficulties are less severe, micro-Raman and infrared spectroscopies have been applied to probe hydrogen successfully. Some of the most profound transitions in hydrogen are observed around 150 GPa. A symmetry-breaking transition occurs at low temperature and very high pressures (phase I to II; Fig. 4). At higher pressures, phase III shows a precipitous drop in Raman vibron frequency and an enormous increase in infrared vibron absorption [21]. The results reveal the electronic nature of the transition.

The boundary between I and III terminates at a critical point, above which the transition becomes continuous, The topology is strikingly similar to that associated with a Mott transition [22], in which there is an electron spin-ordered antiferromagnetic phase (Phase II for hydrogen) at low temperatures, a disordered phase at high temperatures (Phase I), and an electron delocalized phase at high pressure (Phase III), with both a triple point and a critical point in the phase diagram.

NOVEL PHYSICS

It is conceivable that novel physical phenomena may emerge with detailed study of matter in the new pressure dimension made possible by the development of new techniques. Analogy could be drawn to the discoveries of superfluidity and superconductivity. These properties were unpredicted and unexpected, and could only be found with the application of extreme temperature conditions and careful experimental observations. Searching for novel physical phenomena that is unique to the extreme pressure condition requires similar efforts.

ACKNOWLEDGMENT — This work is supported by NSF, NASA, and C.I.W.

REFERENCES

1. H. K. Mao, in *Simple Molecular Systems at Very High Density,* A. Polian, P. Loubeyre and N. Boccara, Eds. (Plenum, New York, 1989), pp. 221.
2. C. W. Chu *et al.*, Nature **365**, 323 (1993).
3. L. Gao *et al.*, Phys. Rev. Lett. in press.
4. A. S. Balchan and H. G. Drickamer, J. Chem. Phys. **34**, 1948 (1961).
5. R. Reichlin *et al.*, Phys. Rev. B**49**, 3725 (1994).
6. O. Mishima, L. D. Calvert, E. Whalley, Nature **310**, 393 (1984).
7. M. Kruger and R. Jeanloz, Science **249**, 647 (1990).
8. R. J. Hemley, A. P. Jephcoat, H. K. Mao, L. C. Ming, M. Manghnani, Nature **334**, 52 (1988).
9. J. H. Eggert, H. K. Mao, R. J. Hemley, Phys. Rev. Lett. **70**, 2301 (1993).
10. K. A. Goettel, J. H. Eggert, I. F. Silvera, W. C. Moss, Phys. Rev. Lett. **62**, 665 (1989).
11. R. Reichlin *et al.*, Phys. Rev. Lett. **62**, 669 (1989).
12. H. K. Mao *et al.*, Science **246**, 649 (1989).
13. H. K. Mao *et al.*, Phys. Rev. Lett. **64**, 1749 (1990).
14. A. P. Jephcoat *et al.*, Phys. Rev. Lett. **59**, 2670 (1987).
15. W. Vos *et al.*, Nature **358**, 46 (1992).
16. P. Loubeyre, M. Jean-Louis, R. LeToullec, L. Charon-Gerard, Phys. Rev. Lett. **70**, 178 (1993).
17. P. Loubeyre, R. LeToullec, J. P. Pinceaux, Phys. Rev. Lett. **72**, 1360 (1994).
18. W. L. Vos, L. W. Finger, R. J. Hemley, H. K. Mao, Phys. Rev. Lett. **71**, 3150 (1993).
19. H. K. Mao and R. J. Hemley, Am. Scientist **80**, 234 (1992).
20. H. K. Mao and R. J. Hemley, Science **244**, 1462 (1989).
21. M. Hanfland, R. J. Hemley, H. K. Mao, Phys. Rev. Lett. **70**, 3760(1993).
22. N. Mott, *Metal-Insulator Transitions, 2nd Edition* (Taylor & Francis, London, 1990).

Author Index